MOLECULAR PATHWAY ANALYSIS OF BIOCRUDE FORMATION IN HYDROTHERMAL LIQUEFACTION

A Thesis Presented

by

HEATHER ORISE LECLERC

Submitted to the Graduate School of
Worcester Polytechnic Institute in partial fulfillment
of the requirements for the degree of

DOCTOR OF PHILOSOPHY

March 2023

Department of Chemical Engineering

MOLECULAR PATHWAY ANALYSIS OF BIOCRUDE FORMATION IN HYDROTHERMAL LIQUEFACTION

A Thesis Presented

by

HEATHER ORISE LECLERC

Approved as to style and content by:

Dr. Andrew R. Teixeira, Advisor Chemical Engineering, WPI	Dr. Michael T. Timko, Co-advisor Chemical Engineering, WPI
Dr. Nikolaos Kazantzis, Member Chemical Engineering, WPI	Dr. Harold Walker, Member Civil & Environmental Engineering, WPI
Dr. Prashant Deshlahra, Member Chemical Engineering, Tufts	Dr. Susan Roberts, Department Head Chemical Engineering, WPI

ACKNOWLEDGEMENTS

Throughout my PhD, there have been *countless* people who have made a positive impact on both me and my research. I am particularly grateful to my advisors, Andrew Teixeira and Mike Timko for their unending support, guidance, and continual feedback (despite my high level of sass). You two have pushed me to new heights and have provided me with more opportunities than I could ever have imagined possible. No matter what crazy idea I came to you both with, you accepted it and encouraged me to pursue my passions whether its end goal be personal growth or scientific knowledge. Thank you for sharing your expertise and knowledge with me regarding hydrothermal liquefaction, the life of an academic, and all of the seemingly very random questions that constantly popped into my head!

A big thank you to my loving boyfriend, Jeffrey. You have continued to support me from my "Masters", the transition to the PhD program, and beyond. Without your support I would not have made it through my PhD. Thank you for continuing to lift me up when things aren't going right and the weight of all my responsibilities felt endless. You provided laughter and love throughout the entire process, and I cannot thank you enough for supporting my crazy endeavors and encouraging me to spend 10 months in Denmark to benefit my future, despite meaning I had to leave you behind. Your continual acts of selflessness will never cease to amaze me.

I also want to acknowledge the members of the Teixeira and Timko labs for all their assistance throughout my PhD including Cam Armstrong, Jacob Crislip, Liz Belden, and David Kenney, whose research discussions and complaining sessions I could not do without. Cam and Jacob, I will always look back fondly on all of our dance parties and the times spent hitting balloons around the lab in 017 until all hours of the night. I also cannot forget all of the others who have

come before and after me and have helped to make my graduate school experience unforgettable including Maddie Reed, Avery Brown, Maksim Tyufekchiev, Karen Agro, Esai Lopez, Fatou Diop, and Kevin Keating. The undergraduate students who have assisted me in my research endeavors and have helped in collecting data throughout the years, including but not limited to: Lexi Harrison, Kathryn Carlson, Karen Agro, Skyler Kauffman, and Emily Toala. Also, an excessively big thank you to Dr. Geoff Tompsett and Dr. Alex Maag for all of their amazing assistance in the lab, providing me with trainings and hands-on guidance and for serving as mentors for me both in the lab and in life, helping me manage my time in graduate school and having two advisors! Walking into 020 to be greeted by you two was always a highlight of my day and I applaud you both for putting up with me so often and letting me complain about any dumb thing. I am forever grateful for the hours you both have spent training me in the lab and talking with me about research ideas.

Additionally, I would like to acknowledge all of the friends and mentors I gained from my Fulbright experience in Denmark. Thomas and Daniele, despite all of the research-related challenges I encountered during my stay, I am so grateful for the opportunity to stay and collaborate with you both. Not only did I gain valuable technical experience and knowledge regarding the transition from batch to continuous processing, but also gained new worldviews and ways of approaching problems. This experience allowed me to meet some of the most wonderful people and greatest friends from a diverse set of backgrounds and ideologies that I am grateful to be able to consider lifelong friends. To Swanand and Antonio, no matter where life takes us, I know you both will never hesitate to reach out for an adventure, and I will always be ready to go! Thank you for helping me to transition to life in Denmark when things were not going smoothly and for always being there when I needed assistance. To Eliana, Diogo, Maria, and Komeil, the

rest of the ‘squad,’ looking back at photos and thinking back to all of the memories that we have made together across Aalborg and Denmark in general never fails to bring a smile to my face. You all have been the greatest friends a girl could ask for and have reminded me of the importance of maintaining a work-life balance and the impact that taking breaks and having fun can have on you as a person as well as on the quality of your work. I cannot wait to return to Denmark and visit you all.

In the beginning I said I had countless people to thank, and it’s still going! Next, I would like to acknowledge my collaborators and my committee members for their assistance in teaching me new techniques, critiquing my writing, and all of their efforts in making me a better scientist, researcher, and engineer. Amy McKenna has fostered my immense love for advanced mass spectrometry techniques, specifically FT-ICR MS and has taken the time to teach me how to properly analyze data, interpret it, and is always available to answer any quick questions I may have. I look forward to continuing my works with FT-ICR MS and Amy as I begin my postdoctoral (and hopefully) individual research career. Richard West, Hal Walker, Nik Kazantzis, and Prashant Deshlahra have all provided feedback to my research questions and ideas to ensure that it has reached the highest quality possible, to which I am eternally grateful.

Last, but not least, I need to thank my parents. Without their support and encouragement I would not have made it this far. Thank you for always encouraging me to follow my dreams and to pursue the path I wanted, regardless of challenges. Since I was little, I was always encouraged to be a ‘nerd’ and explore chemistry, despite you failing it countless times mom. You have helped me to balance my scientific curiosity, life, and ambitions and have always supported my dreams and decisions, even when they took me thousands of miles across the Atlantic Ocean.

ABSTRACT

Hydrothermal liquefaction (HTL) is a process utilized to convert high water content feedstocks into a usable biocrude oil at temperatures between 250 – 350 °C and pressures in excess of one hundred bar. Despite HTL's prevalence as a research topic since the turn of the century, the majority of research until recently focused on improving oil yields from single-source algal feeds. In recent years, the focus has shifted towards waste-based feedstocks to address feedstock availability and prohibitive cost issues plaguing early HTL research. Food, yard, and wood wastes from municipal solid waste (MSW) account for 223 million tons of waste annually. These energy-dense waste feeds have the potential to produce spatially distributed and usable biocrude oil across the United States.

Despite research interest in this area, hydrothermal liquefaction has yet to realize commercialization due to insufficient biocrude yields and a lack of fundamental understanding regarding heteroatom distribution and subsequent removal. Due to the complexity of waste feedstocks as well as the severe reaction conditions, the chemistry of waste HTL is poorly understood and colloquially referred to as a black-box process. To uncover the governing chemical pathways towards biocrude production from waste, experimental research coupled with advanced analytical chemistry techniques is required.

Mass spectrometry (MS) is an analytical technique used to measure the mass-to-charge ratio (m/z) of individual molecules. The most common MS technique is gas chromatography mass spectrometry (GC-MS), which measures the volatile portion of a sample (boiling point ≤ 325 °C). In typical bio-oil samples from waste HTL, less than 40% of the biocrude can be analyzed using GC-MS. In addition to GC-MS, further high-resolution mass spectrometry techniques are available

with increased resolution and the ability to distinguish between mass-to-charge ratio changes on the order of parts per billion. One such technique, Fourier transform ion cyclotron resonance mass spectrometry (FT-ICR MS) allows for this ppb resolution due to the use of a superconducting magnet at strengths of 9 – 21 Tesla.

In this work, a detailed chemical understanding and pathway analysis is developed to describe the effect of feedstock composition and catalysts on biocrude formation and heteroatom distributions. HTL chemical pathways are experimentally assessed through batch reactions and subsequent mass spectrometry analysis and further confirmed using density functional theory and kinetic model simulations. Research included in this thesis utilizes analytical and computational chemistry to determine the effects of feedstock composition, catalysts, and pretreatment conditions on resultant hydrothermal liquefaction molecular pathways. Enhanced chemical knowledge of biocrude formation pathways was then applied to determine sub-mechanisms for real-world waste feedstocks.

AUTHORSHIP

The work included in this thesis would not have been possible without collaborations and the assistance of the people listed below in the development of ideas and publication of Chapters 2 – 5. Further collaborators have assisted in data collection for Chapters 6 and 7 in the hopes that they will be published in the near future. A summary of additional contributors and their affiliations are provided below.

Chapter 2- Elucidating the role of reactive nitrogen intermediates in hetero-cyclization during hydrothermal liquefaction of food waste

Rasha Atwi[1], Sydney F. Niles[2], Amy M. McKenna[2,3], Richard H. West[1], Michael T. Timko[5], Andrew R. Teixeira[5]

Chapter 3- Emergent chemical behavior in mixed food and lignocellulosic green waste hydrothermal liquefaction

Jeffrey R. Page[4], Geoffrey A. Tompsett[5], Sydney F. Niles[2], Amy M. McKenna[2,3], Julia A. Valla[4], Michael T. Timko[5], Andrew R. Teixeira[5]

Chapter 4- Quantifying lignin structural impacts on its monomer yields in hydrothermal liquefaction

Ronish M. Shrestha[5], Feng Cheng[5], Alex R. Maag[5], Geoffrey A. Tompsett[5], Charles M. Cai[8], Brent Scheidemantle[8], Klaus Schmidt-Rohr[9], Amy M. McKenna[2,3], Andrew R. Teixeira[5], Michael T. Timko[5]

Chapter 5- Hydroxyapatite catalyzed hydrothermal liquefaction transforms food waste from an environmental liability to renewable fuel

Geoffrey A. Tompsett[5], Alex D. Paulsen[6], Amy M. McKenna[2,3], Sydney F. Niles[2], Christopher M. Reddy[7], Robert K. Nelson[7], Feng Cheng[5], Andrew R. Teixeria[5], Michael T. Timko[5]

Chapter 6- Effects of feedstock flexibility parameters on biocrude yields from hydrothermal liquefaction

Geoffrey A. Tompsett[5], Alex R. Maag[5], Karen F. Agro[5], Kathryn R. Carlson[10], Michael T. Timko[5], Andrew R. Teixeira[5]

Chapter 7- Developments in the transition from batch to continuous processing for hydrothermal liquefaction

Geoffrey A. Tompsett[5], Alex R. Maag[5], Skyler Kauffman[5], Thomas H. Pedersen[11], Daniele Castello[11], Michael T. Timko[5], Andrew R. Teixeira[5]

Affiliations

1. Department of Chemical Engineering, Northeastern University, 360 Huntington Ave., 201 Cullinane, Boston, MA
2. National High Magnetic Field Laboratory, 1800 Paul Dirac Dr., Tallahassee, FL 32310
3. Department of Soil and Crop Sciences, Colorado State University, Fort Collins, Colorado 80523
4. Department of Chemical and Biomolecular Engineering, University of Connecticut, 191 Auditorium Rd., Storrs, CT 06269
5. Department of Chemical Engineering, Worcester Polytechnic Institute, 100 Institute Rd., Worcester, MA 01609
6. Mainstream Engineering Corporation, 200 Yellow Pl., Rockledge, FL 32955
7. Woods Hole Oceanographic Institute, 86 Water St., Falmouth, MA 02543
8. Bourns College of Engineering- Center for Environmental Research and Technology, University of California Riverside, Riverside, CA 92507
9. Department of Chemistry, Brandeis University, 415 South St., Waltham, MA 02453
10. Department of Chemical Engineering, University of New Hampshire, 33 Academic Way, Durham, NH 03824
11. Energy Engineering, Aalborg University, Pontoppidanstræde 111, Aalborg Øst, 9220 Denmark

TABLE OF CONTENTS

TABLE OF FIGURES

TABLE OF TABLES

CHAPTER 1

BACKGROUND AND MOTIVATION

1.1 MUNICIPAL SOLID WASTE ABUNDANCE

In 2018, 292.4 million tons of municipal solid waste (MSW) was generated in the United States.[1] MSW is also known as trash or garbage, and constitutes items that the average person will dispose of in their daily life. It can be divided into ten primary categories and 'other,' as shown in **Figure 1-1**. While recycling efforts have increased in recent years, the paper and paperboard category benefits the most from these efforts with 66.5% of paper waste being recycled in 2018 as opposed to 12.6% of metals, the second-highest recycled category.[1] Second to paper and paperboard, food waste accounts for 21.6% of total MSW, wherein yard trimmings and wood wastes account for 12.1 and 6.2%, respectively.[1, 2]

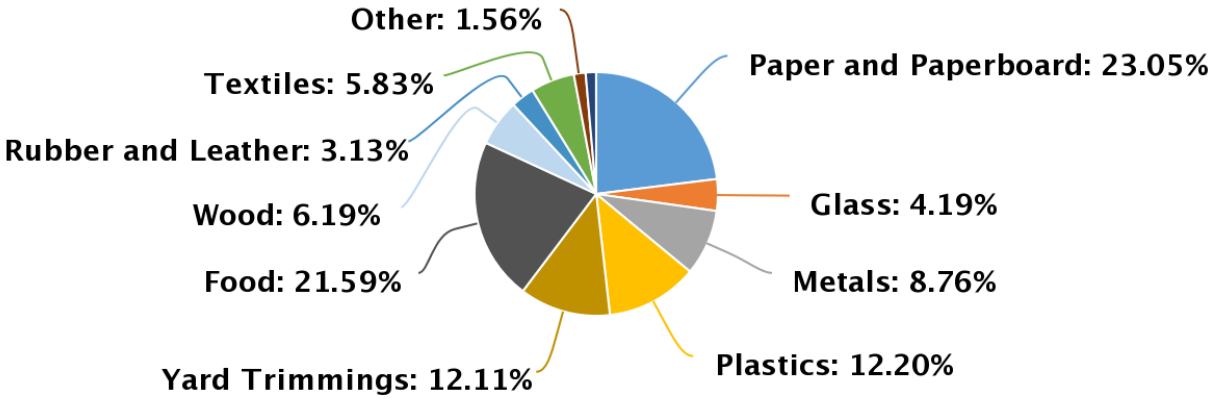

Figure 1-1. Distribution of municipal solid waste materials. Data obtained from the U.S. Environmental Protection Agency report on municipal solid waste generation from 2018.[1]

1.1.1 FOOD WASTE

Food waste is the second largest fraction of municipal solid waste, yet this statistic does not account for commercial scale waste. When considering the entire food chain from farming to

production, distribution, and finally the consumer, the actual statistic is over 100 billion pounds.[3] Food waste occurs for a wide range of reasons including damage, spoilage, and problems during processing.

While food waste should be prevented in the interest of addressing world hunger initiatives, it is also important to address the composition of food. Food is primarily composed of three macromolecular components: carbohydrates, lipids, and proteins. All three contain significant carbon, hydrogen, and oxygen, with protein containing nitrogen in the amino acid backbone. Food is an energy-dense waste product containing 40 – 60% carbon. If left untreated in landfills, food waste has the potential to undergo anaerobic digestion resulting in methane emissions.

1.1.2 LIGNOCELLULOSIC WASTE

Yard clippings and wood waste are considered separate categories of MSW, however, they both fall under the umbrella of lignocellulosic waste, or waste biomass. Lignocellulose is the term describing plant biomass consisting of cellulose, hemicellulose, and lignin. As with food waste, lignocellulose is composed of carbon, hydrogen, and oxygen backbones. Cellulose accounts for 30-55% of lignocellulose, by mass, while lignin constitutes 20 – 30% of the total mass.[4, 5] Cellulose and hemicellulose, which can also be coined holocellulose including the total carbohydrate fraction of biomass, are the primary sugar molecules of plant cell walls. Its glucose backbone is composed of stable β-1,4 glycosidic bonds that allow for hydrogen bonding to create an ordered, crystalline structure.[6, 7] Lignin, on the other hand, is a three-dimensional amorphous polymer composed of aromatic monomers.[5, 8] Depending on the source, the lignin backbone contains guaiacol, syringol, and hydroxyphenol monomers.[8] Lignin is distinctive due to its concentration of aromatic compounds, making it uniquely suited to be a source of fuel and chemical precursors.[9-12]

1.2 BIOMASS CONVERSION TECHNOLOGIES

Researchers have been seeking alternative routes to fuel production for decades due to quickly depleting fossil resources. Biomass is an abundant source of carbonaceous material that can be harnessed through catalytic, enzymatic, or thermochemical processes. First generation biomass conversion technologies focused on raw biomass feedstocks, which increases processing costs and requires large land area for cultivation. Despite the feedstock source, biomass has an inherent water content that increases processing difficulty. Various methods address this issue through the use of drying before processing such as gasification and pyrolysis technologies. Biomass processing technology can be divided into four primary classes: combustion, gasification, pyrolysis, and hydrothermal processes, where further details are included below.

The gasification process converts biomass into a syngas mixture primarily containing CO, CO_2, and H_2.[13, 14] Typical operating conditions exceed 350 °C and the specific conditions have a significant impact on the ratio of gaseous compounds. Gasification technologies obtain higher conversion at higher temperatures, at the detriment of efficiency.[13-15] Combining gasification with a Fischer-Tropsch reactor has been shown to have the largest capital investment, with 28% of expenditure coming from drying and biomass feedstock costs.[15]

Biomass pyrolysis is a well-studied process to convert dry organics into liquid or gaseous products at high (> 450 °C) temperatures in an inert atmosphere. Pyrolysis can be operated in multiple different modes including, fast, slow, catalytic, and non-catalytic which produce varying ratios of solid, liquid, and gaseous products.[ref] Fast pyrolysis is the most well-known, having been commercialized in recent years, and utilizes rapid heating to produce a unstable liquid

biooil.[16, 17] Drawbacks to pyrolysis include extensive energy inputs for drying (~3.6 MJ/kg) as well as costs to stabilize and upgrade the biooil to a usable fuel.[17-19]

1.2.1 HYDROTHERMAL PROCESSES

The last biomass processing technology is liquid processing through hydrothermal methods. These can include hydrothermal carbonization to produce a carbon-rich solid or hydrothermal liquefaction (HTL) to produce biocrude oil – with differing properties than pyrolysis biooil.[20] HTL is an attractive technology for the conversion of municipal solid waste materials due to its ability to handle substantial water content.[21-27] Typical batch processes utilize 10 – 20 wt% solid organic slurries at temperatures between 250 – 400 °C and pressures between 120 – 250 bar.[17] The quality and quantity of the resultant biocrude has been shown to be dependent on the feedstock type, operating temperature, pH, residence time, and solvent used during separation.[14, 28] Feedstock type and reaction temperature have been shown to have the greatest impact on biocrude yield, with the use of homogeneous and heterogeneous catalysts gaining interest and therefore impact.[29]

Despite the prevalent research interest in hydrothermal liquefaction of biomass and waste resources, the majority of these studies have focused on increasing biocrude oil without attempts to understand the process scientifically.[22, 30-32] In order to develop HTL into an economical waste processing method, a fundamental understanding of the effects of catalysts, heteroatoms, and feedstock type and availability on biocrude composition are necessary.

1.3 HYDROTHERMAL LIQUEFACTION PRODUCT PHASES

Hydrothermal liquefaction of all known feedstocks results in four separable product phases: gas, aqueous, biocrude, and solid char. While various solvents can be utilized during HTL product separation, the most commonly used solvents are acetone and dichloromethane (DCM).[22, 25, 27, 33]

Figure 1-2 describes the process to obtain and separate HTL product phases. Biomass and waste products are loaded into the HTL reactor wherein after reaction the product slurry is present.

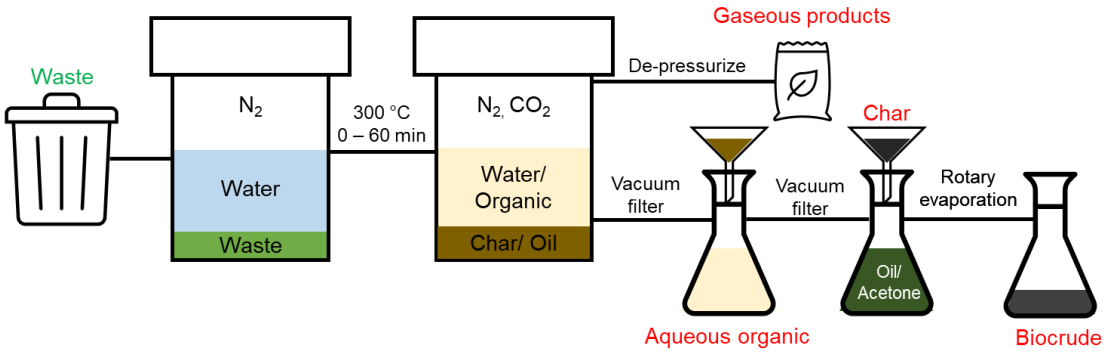

Figure 1-2. Schematic diagram of food waste HTL experimental procedure and characterization methods. Green represents feedstock. Red is representative of HTL product phases and black represents separation processing.

The product slurry is separated by first depressurizing the reactor into a gas bag or other gas storage container for further analysis. This process leaves behind a slurry mixture of water, liquid, and solid-phase organics. To isolate the remaining three phases, a vacuum filter and separatory funnel is used to retain the solid char and sticky biocrude in the filter while separating the aqueous organic phase. After removal of the aqueous phase, the char/oil mixture is washed with acetone or DCM to dissolve the soluble organic biocrude to separate it from the char. Lastly, the solvent is removed via rotary evaporation and the biocrude isolated and measured.

The aqueous phase constitutes the largest mass fraction of the products due to the high initial water loading between 80 – 90 wt%. The solid char typically comprises the second or third largest mass fraction, depending on the feedstock. High-lipid content feedstocks tend to produce 1 – 2 wt% char whereas carbohydrate-based feedstocks such as cellulose can result in up to 10 wt% char.[4, 34] In most cases, the gas is the smallest fraction of the mass, composing 0.5 – 4 wt%, as

typically determined by difference after de-pressurization. Lastly, the biocrude phase mass fraction is highly dependent on the feedstock and HTL conditions. While some conditions can produce only one wt% biocrude, others have been shown to produce nearly 40 wt% biocrude oil.[23, 35, 36]

While understanding mass distributions is important, HTL product yields are conventionally reported on a carbon basis.[37] Carbon is the primary energy carrier in fossil and bio-based fuels, whereas the inherent or added water in the process does not carry sufficient energy. This transformation means that while biocrude composes only ten wt% of the mass, it can account for over 50% of the carbon, and therefore energy, in the reaction.

1.3.1 BIOCRUDE COMPOSITION

In a well optimized system, the biocrude will contain over 50% of the carbon in the system, as previously mentioned. Despite containing a majority of the carbon, the biocrude phase also contains non-negligible amounts of heteroatoms. These heteroatoms are primarily oxygen (lignocellulose, food waste), nitrogen (food waste), and sulfur (lignocellulose, food waste) which serve as biocrude contaminants that require removal before the biocrude can be used as fuel.

It is known that, like yield, biocrude composition is feedstock dependent.[21, 27, 28, 36, 38] High-lipid containing feedstocks are known to contain fatty acids such as hexadecanoic acid as a primary constituent in gas chromatography mass spectrometry (GC-MS) analysis whereas lignocellulosic biomass often results in small oxygenates as the primary GC amenable species. Research by Cheng et al.[23] revealed stark differences in the concentration of fatty acids and fatty acid methyl esters (FAMEs) between high- and low-lipid algal species, further corroborated with Fourier transform infrared spectroscopy (FT-IR) spectra of the biocrudes.[23] Additionally, they found that milder conditions resulted in greater biocrude yields for high-lipid algae whereas for high-protein, low-lipid algae, more severe HTL conditions were preferred.[23]

In addition to the well-characterized light fraction of biocrude that can be analyzed with GC-MS, over half of the biocrude is actually too large to be analyzed in this way. Due to GC-MS's reliance on volatility, only biocrude compounds with a boiling point less than ~325 °C can be identified. To obtain a complete picture of biocrude's chemical composition, further non-volatility based methods are required. In recent years, Fourier transform ion cyclotron resonance mass spectrometry (FT-ICR MS) has emerged as an ionization-based technique to analyze the heavy (> 150 Da) fraction of biocrude.[21, 23, 39] With this technique, unique molecular formula with a resolution of 200 ppb can be identified based on their mass to charge ratio (m/z).[40] HTL research utilizing this technique has identified trends in heteroatom class abundance and its relation to aromaticity and size in biocrude compounds, yet continual research to pair high-resolution mass spectrometry with structural information is required.

There is growing research interest in hydrotreating methods to simultaneously remove the heteroatoms and produce usable drop-in fuels. The majority of these research efforts, however, focus on optimizing the upgrading methods, wherein there remains a significant gap in the fundamental understanding of biocrude composition. To fully optimize upgrading, fundamental chemical knowledge on heteroatomic compounds and their formation is necessary.

1.3.2 AQUEOUS COMPOSITION

Despite the aqueous phase constituting approximately 80% of the mass, it typically contains between 10 – 30% of the carbon, as shown in **Figure 1-3**. Currently, there are no commercially viable technologies to recover this carbon, indicating lost carbon.[41] Furthermore, there are limited analytical techniques suitable for aqueous organic analysis. For this reason, the most common aqueous phase analysis is total organic carbon (TOC), which provides a single analysis of the amount of carbon in parts per million.

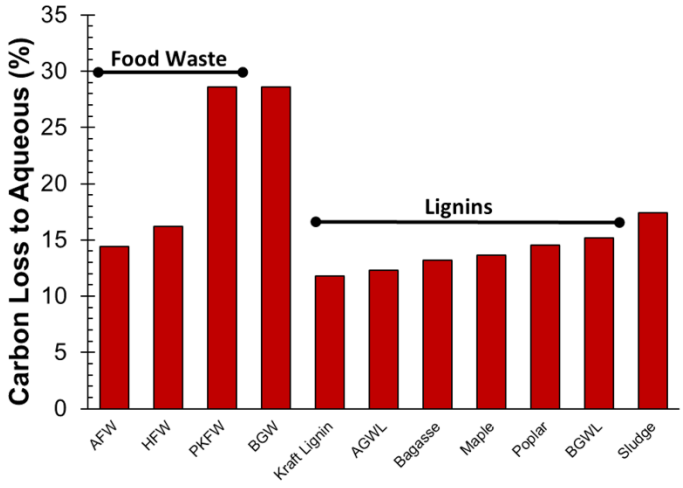

Figure 1-3. Percent of carbon in the aqueous phase as a function of HTL feedstock type. All HTL experiments were performed at 300 °C for 60 minutes in a batch reactor.

Some researchers have adopted a procedure to analyze the aqueous phase on GC-MS through use of an organic extraction process with DCM, however, this does not capture all carbon compounds present in the aqueous phase.[42, 43] To avoid this issue, further characterization can be completed using liquid chromatography MS.[44] Beyond carbon content, it has become commonplace to measure the resultant aqueous pH. It has been shown that lignocellulosic biomass results in a more acidic aqueous phase (pH = 3.5 – 5) than other feedstocks, where algae typically boasts an aqueous pH range between 7.5 – 8.5.[41] Further characterization utilizes inductively coupled plasma spectroscopy or ion chromatography to measure metal and ion concentrations.[41] The concentration of inorganic compounds is highest in the aqueous phase, wherein compounds including ammonia, PO_4^{3-}, K, Na, Mg, Al, Ca, and Fe reside.[41] The ammonia content of the aqueous phase can generally be attributed to protein deamination in manure and food waste feedstocks.[45]

One cannot discuss aqueous phase composition without mention of its inherent toxicity due to the combination of organic and inorganic compounds. Currently, direct disposal poses human and environmental safety and health hazards.[41] Pham et al. and Elliott et al. have both worked to measure the cytotoxicity of HTL aqueous phase, finding that an aqueous phase concentration of only 7.5% resulted in a 50% reduction in cell density, most likely due to the aromatic and nitrogen-containing organics.[46, 47]

While no commercial recommendations exist for HTL aqueous phase treatment, multiple pathways have been proposed including recovery of value-added chemicals before disposal as well as biological conversion.[41] While these separation methods are still a research challenge, researchers have shown the extraction of phenolic compounds via modified resin, or extraction using two-stage nanofiltration.[48, 49] These technologies, however, are limited by material availability and overall process time and cost. Biological conversion and purification, on the other hand, encompasses a wide array of methodology and separation goals that prove promising. The most well-known methodology is anaerobic digestion, wherein organics are converted to methane through the use of bacteria.[50] Anaerobic digestion has been utilized to treat wastewater streams from coal gasification[51, 52] and olive mills[53] with success, however, these streams are pointedly less complex than that from hydrothermal liquefaction. The complexity and toxicity of the aqueous phase introduces hurdles to the use of biological treatment methods due to the high concentrations of nitrogen-containing compounds, aromatics, and heavy metals that can kill or inhibit bacteria. For these reasons, it is imperative that further research is conducted on aqueous phase remediation.

1.4 ANALYTICAL TECHNIQUES

To obtain relevant information from the complex waste-based hydrothermal systems requires a deep understanding of analytical techniques capable of demystifying complex chemistry. Common techniques available for HTL analysis are gas chromatography mass spectrometry (GC-MS), Fourier transform infrared spectroscopy (FTIR), elemental analysis (EA), and total organic carbon (TOC). While each of these techniques provides useful information on the system at hand, they are generally recognized as simple techniques that should be included in every HTL analysis.

GC-MS, as previously discussed, is utilized to analyze the volatile fraction of the biocrude and gas phases. FTIR can be helpful to identify bulk functionality in the solid feed, biocrude, and char phases. Similar to FTIR, elemental analysis can also be used to analyze feedstock, biocrude, and char to determine their carbon, hydrogen, oxygen, nitrogen, and sulfur contents, colloquially referred to as CHONS. Unlike the previous three techniques, TOC is the only one suitable to measure carbon in the aqueous phase. Beyond these common techniques, however, are additional analytics with increased capabilities and complexities.

1.4.1 MICROKINETIC MODELING

Microkinetic modeling is a tool that is used to identify reaction intermediates and rate-determining steps.[54] It can be a beneficial technique to relate computational and experimental observations in order to predict the outcome of complex reaction networks. Kinetic data can be used to optimize reactor design and reaction conditions, as well as predict reaction outcomes.[54] While many microkinetic models of late have focused on catalysts, they also serve as useful tools in understanding subsets of complex reaction networks. It provides a useful framework for reaction mechanism analysis.[54]

The general process for model development begins by identifying a reaction scheme focused on elementary reactions as individual steps. The larger the reaction scheme, the harder it may be to develop the model and understand its results. Afterwards, the thermodynamic properties for the individual species in the network are estimated or calculated. This can be done through computational methods such as density functional theory or estimated using online resources such as the NIST webbook. Microkinetic models, once developed, are used to determine reaction rates and rate-limiting steps imperative to determination of the primary reaction products.

In complex systems, such as those that exist in hydrothermal liquefaction, the key challenge in microkinetic model development lies in identifying and creating an accurate reaction scheme. In addition to the overall complexity of biomass systems, there are few analytical techniques that can provide detailed structural information about multiple feed and product phases. For this reason, microkinetic modeling is typically completed using model compounds. Model reaction networks then should undergo comparisons with experimental data to ensure accuracy, as will be further explored in Chapter 2.

1.4.2 TWO-DIMENSIONAL GAS CHROMATOGRAPHY

Two-dimensional gas chromatography, also called GC×GC, is a technique capable of high resolution separation in complex mixtures.[55] Comprehensive GC×GC utilizes two chromatography columns of different, complementary stationary phases in sequence to enhance separation.[56] Typically, this means that one column will have a polar stationary phase whereas the other will have a nonpolar stationary phase, setup in either direction. This allows for enhanced separation, as few analytes will coelute on both columns.[56]

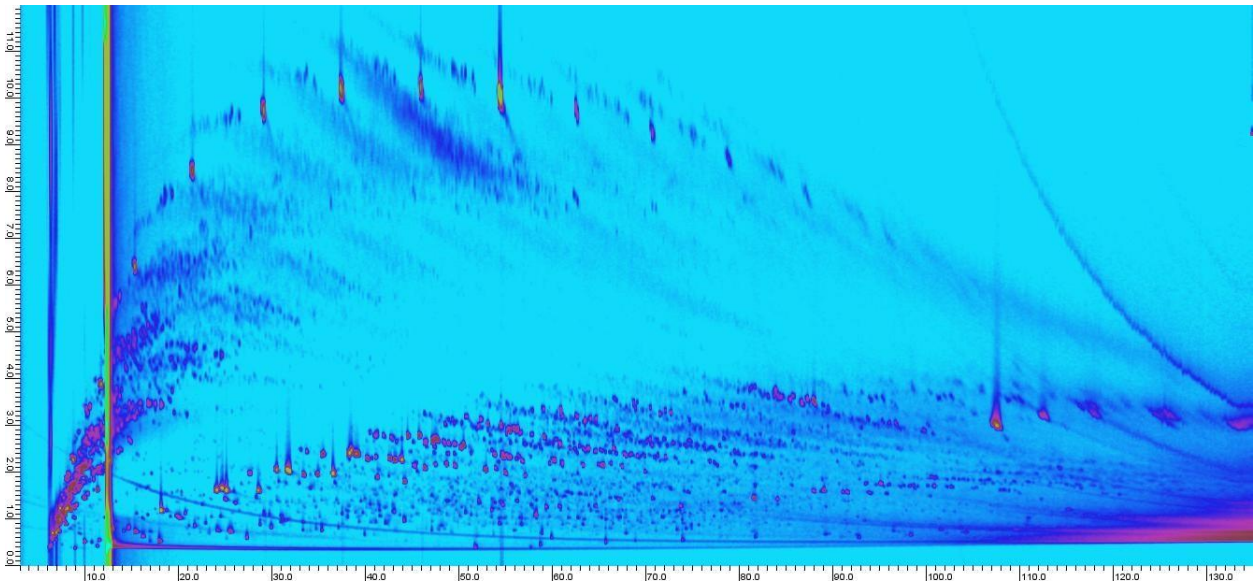

Figure 1-4. Characteristic GC×GC spectrum. The x-axis represents the retention time on the 1st column and the y-axis is the retention time on the 2nd column.

Depending on column orientation and temperature ramp rate, varying chemical classes appear in characteristic locations that can assist in peak assignment. In **Figure 1-4** the sharp, yellow peaks along the top curve represent a series of fatty acids. These components are important to identify in a complex HTL biocrude mixture and can enhance the percentage of amenable compounds from approximately 30% to over 50%.[56, 57]

Analysis of HTL biocrude with GC×GC has revealed fatty acid, amide, ketone, hydrocarbon, alcohol, ester, furfural, and ether group compounds with similarity scores greater than 85%.[58] In addition to enhanced resolution, it provides further detail allowing for enhanced insights into the chemical mechanism and potential reaction pathways to form these compounds. Unfortunately, GC×GC remains a volatility-based technique, which limits analysis to low-boiling point and low-molecular weight compounds. While the overall molecular weight range of biocrude is feedstock dependent, traditionally, this fraction will be no more than 60% of the biocrude.[59] Further analysis of the benefits of GC×GC can be found in Chapter 6.

1.4.3 FOURIER TRANSFORM ION CYCLOTRON RESONANCE MASS SPECTROMETRY

Fourier transform ion cyclotron resonance mass spectrometry (FT-ICR MS) is an advanced analytical technique capable of high resolution and mass accuracy with fast scan times and both positive and negative ion capability.[60] FT-ICR MS has been successfully used for decades in the field of proteomics to study conventional and unconventional crude oils.[61] The basic principles of FT-ICR MS are based on the use of a strong magnetic field to separate and then measure the mass to charge ratio (*m/z*) of ionic species.[60, 61]

The first step in FT-ICR MS analysis is the ionization. There are three commonplace ionization modes that can be operated in negative ion or positive ion mode, based on the sample and desired information. Electrospray ionization (ESI), atmospheric pressure photoionization (APPI), and atmospheric pressure chemical ionization (APCI) are the most common ionization modes, each targeting a specific subset of compounds.

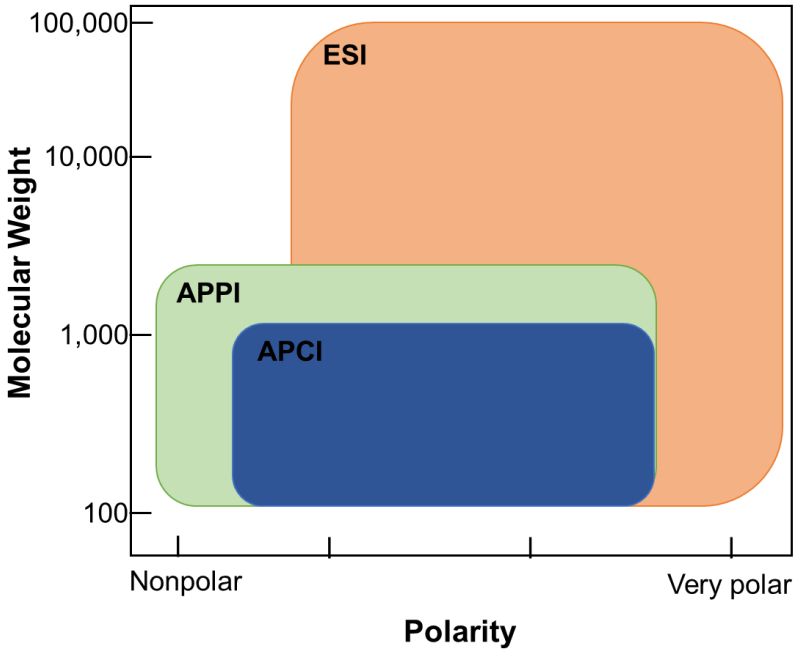

Figure 1-5. Range of polarity and molecular weight that is best suited to be analyzed by ESI, APPI, and APCI ionization techniques. Information taken from the FT-ICR MS short course offered by the EU FT-ICR MS organization, Finland, April 2022.

As depicted in **Figure 1-5** each ionization technique is appropriate for a different subset of compounds. Electrospray ionization is the most common technique, in part due to its broad application across the polarity and molecular weight spectra. However, ESI is not suitable for nonpolar compounds and is primarily employed in the liquid phase.[62] APCI is one of the least common methods due to the difficulty in sample preparation for chemical ionization and is often considered a 'hard' ionization mode due to the inference of chemical changes. It can, however, allow for ionization of less polar compounds than permitted with ESI. The last ionization technique discussed is APPI, which allows for analysis of the most nonpolar compounds of the three. This plays an important role in analysis of crude and biocrude oils due to the presence of hydrocarbons and the high concentration of nonpolar or slightly polar molecules.[62-64] APPI allows for a vaporized

gas stream to flow orthogonally to the mass spectrometer inlet and the krypton vacuum UV lamp, as shown in **Figure 1-6**.[65]

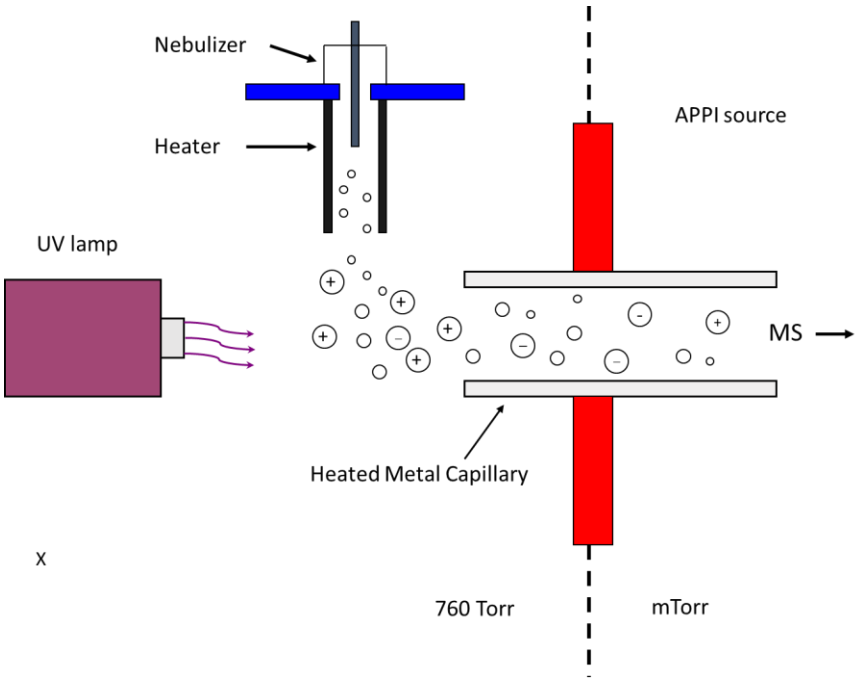

Figure 1-6. Two-dimensional diagram of APPI ionization source for FT-ICR MS. Figure adapted from Purcell et al. *Anal. Chem.* 2006, 78, 5908-5912.

The use and efficiency of FT-ICR MS is dependent on the magnet strength. Currently, the highest magnet strength in use in 21 Tesla, capable of increasing the separation between *m/z* ratio even further than instruments operating at 9.4 T. To obtain a detailed understanding of FT-ICR MS theory, the reader is directed to works by Alan G. Marshall of the National High Magnetic Field Laboratory, however, I will provide the basic introduction herein.

First, it is important to know that ion cyclotron frequency, radius, velocity, and energy are all a function of ion mass, charge and magnetic field strength.[66] This motion is observable by the

application of a uniform electric (or magnetic) field at the same resonant frequency as the ion cyclotron frequency.[66] Therefore, the ICR signal results from the induction of an oscillating charge on two conductive parallel electrodes (assumed to be infinite). Then a frequency domain spectrum can be converted to a mass domain spectrum by Fourier transform of the time-domain ICR signal.[66] Next, ion entrapment via a three-dimensional axial quadrupole shifts the ion cyclotron frequency, but excitation and detection remain linear but reduced proportionality constant. For this reason, FT-ICR MS can be performed with various ion trap geometries. Collisions then broaden the ICR signal and make it possible to cool and compress an ion packet for improved detection.[66] It is also important to note that most ionization techniques work best outside the magnetic field, and that the features mentioned above may be combined to form event sequences.[66]

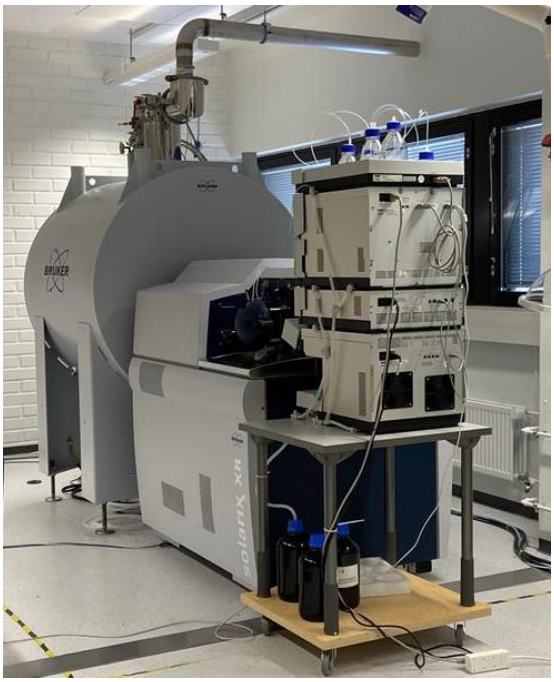

Figure 1-7. Photograph of 12T FT-ICR MS instrument at the University of Eastern Finland. Photograph taken by H.O. LeClerc. April, 2022.

As previously mentioned, FT-ICR MS has been utilized in petroleomics for decades and has become more common to use during the analysis of biocrude oils. The first papers reporting FT-ICR MS analysis for HTL biocrudes appear around 2010 and in the past 20 years have been increasing in frequency. Commonly, it has been used to identify the presence of heteroatom classes with analysis of the relative abundance. Double bond equivalency (DBE) is an important metric in biocrude analysis to understand the degree of aromaticity in a compound, or group of compounds. Research has worked to compare the FT-ICR MS spectra of biocrude samples taken at varying conditions[21, 23, 37, 39], however, it is important to note that abundance values are not equivalent to a concentration and should not be directly compared between samples.

Additionally, FT-ICR MS can distinguish between *m/z* with a resolution of 200 ppb Da, however, it lacks structural information. As the size of compounds increases, the number of potential formula assignments and structural conformers increase proportionally. This is a major drawback in the understanding of HTL biocrude, wherein each compound is unknown and can have a range of structures. Further discussion and explanation of FT-ICR MS use in HTL can be found in Chapters 2, 3, 4, and 6 for an array of feedstocks and purposes.

1.5 FACTORS AFFECTING HTL BIOCRUDE YIELDS

As was previously discussed in Section 1.3.1, biocrude yields are highly dependent on a slew of factors including temperature, residence time, feed composition, particle size, solids loading, heat-up rate, and more. While some of these factors are easier to control than others, it is important to note that the primary factors including feedstock and HTL temperature will vary based on location and feedstock availability. For this reason, this section will focus on additional factors

that can be applied to a variety of waste feedstocks in all locations. Two key parameters will be discussed further here, the presence of a catalyst and the mechanical pretreatment of the feed.

1.5.1 HOMOGENEOUS & HETEROGENEOUS CATALYSIS

The use of a catalyst in HTL has the potential to increase biocrude yield and biomass conversion efficiency for underperforming feedstocks. Catalysts also hold the ability to alter the product phase heteroatom distributions and therefore the energy content or higher heating value (HHV) of the biocrude. Hydrothermal liquefaction research has shown that the effect of catalysts is highly feedstock dependent. For example, the addition of Na_2CO_3 to the HTL reaction mixture of nannochloropsis algae and corn stalk increased biocrude yields by 4 and 14%, respectively.[33] The large difference in catalyst effect based on feedstock is a theme throughout catalytic HTL research and begs the question of why.[27, 33, 34, 37, 42, 67-74] There are two primary catalyst types- homogeneous and heterogeneous, wherein homogeneous catalysts exist in the same state as the reaction mixture, in this case referring to liquid catalysts and heterogeneous catalysts in HTL are solids.

Homogeneous alkali catalysts are one of the most common HTL catalysts, including variants of K, Ca, and Na hydroxides and carbonates.[33] These catalysts have interest due to their low cost as well as their liquid form, which prevents catalyst coking in the harsh hydrothermal environment. Homogeneous catalysts, however, suffer from difficult and energy-intense recovery, oftentimes becoming soluble in the aqueous phase.[33, 67] Another factor to consider is the potential corrosiveness of homogeneous catalysts which can affect the required reactor design and capital costs. Alkali catalysts have been shown to improve biocrude yields primarily through enhanced depolymerization processes and is typically most effective at converting carbohydrate-rich feedstocks.[75, 76] Potassium-based catalysts such as KOH and K_2CO_3 have both been shown to be

effective in enhancing lignocellulose conversion, where K_2CO_3 is preferred due to its breakdown into bicarbonate, forming a secondary catalyst further improving biocrude yields.[33, 77]

Due to the difficult separation and recovery of homogeneous catalysts, researchers have begun transitioning to heterogeneous catalysts. However, the harsh reaction conditions and presence of a majority water phase results in rapid catalyst deactivation, forcing researchers to explore new-age hydrothermally stable catalysts. Based on the success of homogeneous alkali catalysts, researchers began with an exploration of solid base catalysts.[73] These alkali based catalysts include colemanite, magnesium oxides, and hydrotalcites, which all show improved biocrude yields at the detriment to the HHV.[78-80] Additional catalyst categories include transition metals such as nickel and zinc-based catalysts[69], lanthanide oxides, and zeolites.[73]

Zeolites are microporous aluminosilicate framework structures that are known for their large surface area and tunable characteristics. While all zeolites contain tetrahedrally coordinated silicon and aluminum species, the framework is shifted based on the zeolite type. Zeolites have been shown to improve the yield and quality of biocrude, however, they are not known for hydrothermal stability.[14, 73] ZSM-5, a standard zeolite known for its ability to catalyze cracking and cyclization reactions has been utilized in hydrothermal liquefaction reactions and found to reduce char and increase biocrude yields, however, due to the formation of char, catalyst pores were clogged and required additional treatment before subsequent use.[73, 81] Zeolites are not considered hydrothermally stable due to acid and base site degradation in water, indicating the need for further research into the scientific and economical use of zeolites in HTL.[14]

1.5.2 1.5.2 MECHANOCHEMICAL PRE-TREATMENT

One of the advantages of hydrothermal liquefaction over other biomass valorization techniques is its ability to handle wet, mixed waste feeds. Despite this benefit, some feedstocks, particularly

lignocellulosic feeds can still benefit from pretreatment. Mechanochemical treatment is a method of high energy mechanical treatment, defined as having the ability to alter the chemical structure. Mechanochemical pretreatment has emerged as a low-cost method to improve biocrude yields from lignocellulosic biomass. The general purpose of pretreatment is to further breakdown recalcitrant lignin and decrease the crystallinity of the cellulose portion, thus improving contact between the biomass and water to undergo hydrothermal liquefaction.[82] Milling is one standard mechanochemical treatment method which constitutes the use of metal balls (ball-milling) or blades (knife-milling) to rapidly collide with the biomass causing local hot spots and decrease in particle size. Ball-milling pretreatment has been shown to increase HMF yields from lignocellulosic biomass over five times compared to untreated biomass.[82] Further research into the use of ball-milling coupled with NaOH treatment results in double the biocrude yield with a slight increase in energy content.[83] Both of these research works explored the use of ball mills, however, as previously mentioned, there are differing types of mills that can affect energy consumption, particle sphericity, and size in differing ways.[84] The effect of ball milling treatment on HTL biocrude yields and the underlying mechanism will be discussed further in Chapter 5.

1.6 HTL COMMERCIALIZATION

Despite HTL's significant benefits over other conversion methods, commercialization remains a challenge. Current bottlenecks include the development of continuous processes and subsequent continuous separation, in addition to process economics. More specifically, the technical challenges are as follows[85]:

I. Feed processing for solids loading optimization

II. Fouling and pressure drop

III. Optimizing HTL reactor design to reduce solids accumulation

IV. Pressure let-down system design and product separation

V. Potential corrosivity of biocrude

VI. Increased biocrude heteroatom contents (i.e. oxygen and nitrogen)

VII. By-product utilization and disposal, particularly aqueous and solid streams

One of the benefits of hydrothermal liquefaction is feed flexibility, however, each feed experiences differing slurry characteristics and behaviors which require varying feed processing equipment and reactor configurations.[85] In addition, feedstock pre-treatment requirements depend heavily on feedstock type, wherein lignocellulosic biomass may require grinding and particle size adjustments before HTL whereas sewage sludge may require catalysts. Both batch and continuous HTL reactors can operate with solids loadings ranging from 1 – 30%, however, increased solids loading in a continuous reactor drastically increases the clogging potential, as is of concern in challenge III. Further considerations on feedstock type and necessary pre-treatment is the tendency of some feeds to settle in a non-homogenous slurry, which can lead to pump and reactor blockages.[85]

Challenges II – V are all related to overall hydrothermal liquefaction process and reactor design. First-off, in continuous operation, obtaining and maintaining the correct pressures in a potentially compressible slurry is an immense task. Commonly, positive displacement pumps (ex. Piston pump, diaphragm pump) are used to pump the slurry mixture into the reactor and are coupled with a back pressure regulator to control the system pressure. Due to the high temperature operating conditions of HTL, heat exchangers are an integral portion to commercial reactor designs.[85] The thermo-physical properties of the feed slurry play a vital role in the heat exchanger design, including viscosity, density, heat capacity, and fouling factor among others.

In addition to continuous scalability and reactor considerations of the HTL process, further research is required to advance the subsequent hydrotreating of the HTL biocrude to produce a useable fuel in accordance with challenges VI - VII. While the biocrude contains up to 75% of the carbon from the initial feed, it also contains significant weight percent of nitrogen, oxygen, and sometimes sulfur.[86] The heteroatom content of biocrude makes it unusable in its raw form, requiring additional hydrotreating to transform it into drop-in fuels. Research dating back nearly ten years has explored continuous hydrotreating of biocrude, even showing 60% reduction in nitrogen content and 85% reduction of oxygen content in the process.[87] This process, however, should be linked to the hydrothermal liquefaction process to minimize biocrude compositional changes over time and to optimize process economics. The fate and use of byproduct phases, particularly the aqueous phase, will be discussed further in section 1.3.2.

Besides the technical challenges associated with HTL commercialization, process economics and environmental assessments must also be favorable. To this end, researchers at Pacific Northwest National Laboratory (PNNL) have performed extensive technoeconomic assessments (TEA) on the feasibility of the HTL process. These TEAs have been performed with a variety of feedstocks and byproduct disposal methods to obtain a value for minimum fuel selling price (MFSP) in terms of gallon of gasoline equivalency (GGE).[88-91] Recent technoeconomic analyses have begun to determine optimal reactor and upgrading deployment set-ups to maximize the return on investment and minimize the minimum fuel selling price.[92] Process economics remain a challenge to become not only technically accurate, but also favorable to push HTL towards commercialization.

1.7 RESEARCH OBJECTIVES

To begin to solve the knowledge gaps identified above in the previous sections, studies were designed and implemented to address the following objectives:

1. Reveal enhanced knowledge of hydrothermal liquefaction molecular pathways
2. Apply the molecular-level understanding of pathways and sub-mechanisms to real-world feeds and conditions to obtain optimal biocrude yields

To this end, advanced analytical characterization techniques were combined to obtain the most complete picture of biocrude composition and chemistry. Chemical modeling via density functional theory (DFT) and microkinetic modeling are utilized in Chapter 2 to reveal the enhanced knowledge of nitrogen molecular pathways. Modeling techniques were then coupled with experimental results and analysis using GC-MS and FT-ICR MS for determination of biocrude heteroatom distribution and served as model validation, ensuring knowledge of hydrothermal liquefaction molecular pathways.

Through the use of the identified nitrogen molecular pathways, research aimed to continue to enhance the scientific knowledge of biocrude formation pathways through applications to real-world waste feeds and varying process conditions. Throughout this thesis, FT-ICR MS was utilized as a key analytical tool in the determination of heteroatomic and biocrude trends due to changes in feedstock or HTL processing. Chapter 3 introduces a complementary technique, Fourier transform infrared spectroscopy (FTIR), and the introduction of ^{13}C solid-state nuclear magnetic resonance spectroscopy (NMR). Additional tools of GC×GC and thermogravimetric analysis all served as important characterization methods in the determination of biocrude formation pathways.

The identified techniques were then applied to varying real-world problems including feedstock variability and mixing (Chapter 3), local variants in extracted lignin chemistry (Chapter 4), and the addition of catalysts (Chapter 5). Chapter 6 and 7 represent the inclusion of studies designed to optimize biocrude yield by adjusting parameters that were previously found to have a significant impact on biocrude formation pathways. Furthermore, works included in Chapter 7 begin to directly address the remaining challenges that hydrothermal liquefaction faces in commercialization through exploration of biocrude and byproduct phase chemical mechanisms in continuous processing systems.

1.8 REFERENCES

1. Agency, U. S. E. P., National Overview: Facts and Figures on Materials, Wastes and Recycling. epa.gov, 2021.

2. Agency, E. P., Municipal Solid Waste. Agency, E. P., Ed. 2016.

3. Agriculture, U. S. D. o. Food Waste FAQs. https://www.usda.gov/foodwaste/faqs.

4. Climent, M. J.; Corma, A.; Iborra, S., Conversion of biomass platform molecules into fuel additives and liquid hydrocarbon fuels. *Green Chemistry* **2014,** *16* (2), 516-547.

5. Isikgor, F. H.; Becer, C. R., Lignocellulosic biomass: a sustainable platform for the production of bio-based chemicals and polymers. *Polymer Chemistry* **2015,** *6* (25), 4497-4559.

6. O'Sullivan, A. C., Cellulose: the structure slowly unravels. *Cellulose* **1997,** *4* (3), 173-207.

7. Tyufekchiev, M. V. Reaction Engineering Implications of Using Water for the Conversion of Lignocellulosic Biomass. Worcester Polytechnic Institute, 2019.

8. Calvo-Flores, F. G.; Dobado, J. A., Lignin as Renewable Raw Material. *ChemSusChem* **2010,** *3* (11), 1227-1235.

9. Ander, P.; Eriksson, K.-E., Methanol formation during lignin degradation by Phanerochaete chrysosporium. *Applied Microbiology and Biotechnology* **1985,** *21* (1), 96-102.

10. Aro, T.; Fatehi, P., Production and application of lignosulfonates and sulfonated lignin. *ChemSusChem* **2017,** *10* (9), 1861-1877.

11. Beauchet, R.; Monteil-Rivera, F.; Lavoie, J. M., Conversion of lignin to aromatic-based chemicals (L-chems) and biofuels (L-fuels). *Bioresource Technology* **2012,** *121*, 328-334.

12. Becker, J.; Wittmann, C., A field of dreams: Lignin valorization into chemicals, materials, fuels, and health-care products. *Biotechnology Advances* **2019,** *37* (6), 107360.

13. Kumar, M.; Olajire Oyedun, A.; Kumar, A., A review on the current status of various hydrothermal technologies on biomass feedstock. *Renewable and Sustainable Energy Reviews* **2018,** *81*, 1742-1770.

14. Maag, A. R. Converting Biomass Feedstocks through Heterogeneous Catalysis: How Compressed Liquid Water Influences Catalytic Activity and Stability. Worcester Polytechnic Institute, 2019.

15. Anex, R. P.; Aden, A.; Kazi, F. K.; Fortman, J.; Swanson, R. M.; Wright, M. M.; Satrio, J. A.; Brown, R. C.; Daugaard, D. E.; Platon, A.; Kothandaraman, G.; Hsu, D. D.; Dutta, A., Techno-economic comparison of biomass-to-transportation fuels via pyrolysis, gasification, and biochemical pathways. *Fuel* **2010,** *89*, S29-S35.

16. Bridgwater, A. V.; Meier, D.; Radlein, D., An overview of fast pyrolysis of biomass. *Organic Geochemistry* **1999,** *30* (12), 1479-1493.

17. López Barreiro, D.; Prins, W.; Ronsse, F.; Brilman, W., Hydrothermal liquefaction (HTL) of microalgae for biofuel production: State of the art review and future prospects. *Biomass and Bioenergy* **2013,** *53*, 113-127.

18. Renewable Energy Data Book. Laboratory, N. R. E., Ed. 2013.

19. al., M. R. e. *Large-Scale Pyrolysis Oil Production: A Technology Assessment and Economic Analysis.*; National Renewable Energy Laboratory: 2006; pp 1-93.

20. Arun, J.; Gopinath, K. P.; SundarRajan, P.; Malolan, R.; AjaySrinivaasan, P., Hydrothermal liquefaction and pyrolysis of Amphiroa fragilissima biomass: Comparative study on oxygen content and storage stability parameters of bio-oil. *Bioresource Technology Reports* **2020,** *11*, 100465.

21. Bayat, H.; Dehghanizadeh, M.; Jarvis, J. M.; Brewer, C. E.; Jena, U., Hydrothermal Liquefaction of Food Waste: Effect of Process Parameters on Product Yields and Chemistry. *Frontiers in Sustainable Food Systems* **2021,** *5*.

22. Castello, D.; Pedersen, T. H.; Rosendahl, L. A., Continuous Hydrothermal Liquefaction of Biomass: A Critical Review. *Energies* **2018,** *11* (11).

23. Cheng, F.; Cui, Z.; Chen, L.; Jarvis, J.; Paz, N.; Schaub, T.; Nirmalakhandan, N.; Brewer, C. E., Hydrothermal liquefaction of high- and low-lipid algae: Bio-crude oil chemistry. *Applied Energy* **2017,** *206*, 278-292.

24. Déniel, M.; Haarlemmer, G.; Roubaud, A.; Weiss-Hortala, E.; Fages, J., Hydrothermal liquefaction of blackcurrant pomace and model molecules: understanding of reaction mechanisms. *Sustainable Energy & Fuels* **2017,** *1* (3), 555-582.

25. Elliott, D. C.; Biller, P.; Ross, A. B.; Schmidt, A. J.; Jones, S. B., Hydrothermal liquefaction of biomass: Developments from batch to continuous process. *Bioresource Technology* **2015,** *178*, 147-156.

26. Gai, C.; Li, Y.; Peng, N.; Fan, A.; Liu, Z., Co-liquefaction of microalgae and lignocellulosic biomass in subcritical water. *Bioresource Technology* **2015,** *185*, 240-245.

27. Gollakota, A. R. K.; Kishore, N.; Gu, S., A review on hydrothermal liquefaction of biomass. *Renewable and Sustainable Energy Reviews* **2018,** *81*, 1378-1392.

28. Akhtar, J.; Amin, N. A. S., A review on process conditions for optimum bio-oil yield in hydrothermal liquefaction of biomass. *Renewable and Sustainable Energy Reviews* **2011,** *15* (3), 1615-1624.

29. Lababpour, A., Continuous Hydrothermal Liquefaction for Biofuel and Biocrude Production from Microalgal Feedstock. *ChemBioEng Reviews* **2018,** *5* (2), 90-103.

30. Adewuyi, A., Underutilized Lignocellulosic Waste as Sources of Feedstock for Biofuel Production in Developing Countries. *Frontiers in Energy Research* **2022,** *10*.

31. Azadi, P.; Farnood, R., Review of heterogeneous catalysts for sub- and supercritical water gasification of biomass and wastes. *International Journal of Hydrogen Energy* **2011,** *36* (16), 9529-9541.

32. Chakraborty, S.; Aggarwal, V.; Mukherjee, D.; Andras, K., Biomass to biofuel: a review on production technology. *Asia-Pacific Journal of Chemical Engineering* **2012,** *7* (S3), S254-S262.

33. Nagappan, S.; Bhosale, R. R.; Nguyen, D. D.; Chi, N. T. L.; Ponnusamy, V. K.; Woong, C. S.; Kumar, G., Catalytic hydrothermal liquefaction of biomass into bio-oils and other value-added products – A review. *Fuel* **2021,** *285*, 119053.

34. Alonso, D. M.; Bond, J. Q.; Dumesic, J. A., Catalytic conversion of biomass to biofuels. *Green Chemistry* **2010,** *12* (9), 1493-1513.

35. Aierzhati, A.; Stablein, M. J.; Wu, N. E.; Kuo, C.-T.; Si, B.; Kang, X.; Zhang, Y., Experimental and model enhancement of food waste hydrothermal liquefaction with combined effects of biochemical composition and reaction conditions. *Bioresource Technology* **2019,** *284*, 139-147.

36. Biller, P.; Ross, A. B., Potential yields and properties of oil from the hydrothermal liquefaction of microalgae with different biochemical content. *Bioresource Technology* **2011,** *102* (1), 215-225.

37. Cheng, F.; Tompsett, G. A.; Fraga Alvarez, D. V.; Romo, C. I.; McKenna, A. M.; Niles, S. F.; Nelson, R. K.; Reddy, C. M.; Granados-Fócil, S.; Paulsen, A. D.; Zhang, R.; Timko, M. T., Metal oxide supported Ni-impregnated bifunctional catalysts for controlling char formation and maximizing energy recovery during catalytic hydrothermal liquefaction of food waste. *Sustainable Energy & Fuels* **2021,** *5* (4), 941-955.

38. Arturi, K. R.; Strandgaard, M.; Nielsen, R. P.; Søgaard, E. G.; Maschietti, M., Hydrothermal liquefaction of lignin in near-critical water in a new batch reactor: Influence of phenol and temperature. *The Journal of Supercritical Fluids* **2017,** *123*, 28-39.

39. Jarvis, J. M.; Billing, J. M.; Corilo, Y. E.; Schmidt, A. J.; Hallen, R. T.; Schaub, T. M., FT-ICR MS analysis of blended pine-microalgae feedstock HTL biocrudes. *Fuel* **2018,** *216*, 341-348.

40. Savory, J. J.; Kaiser, N. K.; McKenna, A. M.; Xian, F.; Blakney, G. T.; Rodgers, R. P.; Hendrickson, C. L.; Marshall, A. G., Parts-Per-Billion Fourier Transform Ion Cyclotron

Resonance Mass Measurement Accuracy with a “Walking” Calibration Equation. *Analytical Chemistry* **2011,** *83* (5), 1732-1736.

41. Watson, J.; Wang, T.; Si, B.; Chen, W.-T.; Aierzhati, A.; Zhang, Y., Valorization of hydrothermal liquefaction aqueous phase: pathways towards commercial viability. *Progress in Energy and Combustion Science* **2020,** *77*, 100819.

42. Haider, M. S.; Castello, D.; Michalski, K. M.; Pedersen, T. H.; Rosendahl, L. A., Catalytic Hydrotreatment of Microalgae Biocrude from Continuous Hydrothermal Liquefaction: Heteroatom Removal and Their Distribution in Distillation Cuts. *Energies* **2018,** *11* (12).

43. Seehar, T. H.; Toor, S. S.; Shah, A. A.; Nielsen, A. H.; Pedersen, T. H.; Rosendahl, L. A., Catalytic hydrothermal liquefaction of contaminated construction wood waste for biocrude production and investigation of fate of heavy metals. *Fuel Processing Technology* **2021,** *212*, 106621.

44. Panisko, E.; Wietsma, T.; Lemmon, T.; Albrecht, K.; Howe, D., Characterization of the aqueous fractions from hydrotreatment and hydrothermal liquefaction of lignocellulosic feedstocks. *Biomass and Bioenergy* **2015,** *74*, 162-171.

45. Wang, T.; Zhai, Y.; Zhu, Y.; Peng, C.; Xu, B.; Wang, T.; Li, C.; Zeng, G., Influence of temperature on nitrogen fate during hydrothermal carbonization of food waste. *Bioresource Technology* **2018,** *247*, 182-189.

46. Elliott, D. C., Evaluation of Wastewater Treatment Requirements for Thermochemical Biomass Liquefaction. NREL, Ed. 1992.

47. Pham, M.; Schideman, L.; Scott, J.; Rajagopalan, N.; Plewa, M. J., Chemical and Biological Characterization of Wastewater Generated from Hydrothermal Liquefaction of Spirulina. *Environmental Science & Technology* **2013,** *47* (4), 2131-2138.

48. Chen, K.; Lyu, H.; Hao, S.; Luo, G.; Zhang, S.; Chen, J., Separation of phenolic compounds with modified adsorption resin from aqueous phase products of hydrothermal liquefaction of rice straw. *Bioresource Technology* **2015,** *182*, 160-168.

49. Lyu, H.; Chen, K.; Yang, X.; Younas, R.; Zhu, X.; Luo, G.; Zhang, S.; Chen, J., Two-stage nanofiltration process for high-value chemical production from hydrolysates of lignocellulosic biomass through hydrothermal liquefaction. *Separation and Purification Technology* **2015,** *147*, 276-283.

50. Ahring, B. K., Perspectives for Anaerobic Digestion. In *Biomethanation I*, Ahring, B. K.; Angelidaki, I.; de Macario, E. C.; Gavala, H. N.; Hofman-Bang, J.; Macario, A. J. L.; Elferink, S. J. W. H. O.; Raskin, L.; Stams, A. J. M.; Westermann, P.; Zheng, D., Eds. Springer Berlin Heidelberg: Berlin, Heidelberg, 2003; pp 1-30.

51. Ji, Q.; Tabassum, S.; Hena, S.; Silva, C. G.; Yu, G.; Zhang, Z., A review on the coal gasification wastewater treatment technologies: past, present and future outlook. *Journal of Cleaner Production* **2016,** *126*, 38-55.

52. Zhao, Q.; Liu, Y., State of the art of biological processes for coal gasification wastewater treatment. *Biotechnology Advances* **2016,** *34* (5), 1064-1072.

53. Gonçalves, M. R.; Costa Jc Fau - Marques, I. P.; Marques Ip Fau - Alves, M. M.; Alves, M. M., Strategies for lipids and phenolics degradation in the anaerobic treatment of olive mill wastewater. (1879-2448 (Electronic)).

54. Motagamwala, A. H.; Dumesic, J. A., Microkinetic Modeling: A Tool for Rational Catalyst Design. *Chemical Reviews* **2021,** *121* (2), 1049-1076.

55. Grice, K.; Eiserbeck, C., 12.3 - The Analysis and Application of Biomarkers. In *Treatise on Geochemistry (Second Edition)*, Holland, H. D.; Turekian, K. K., Eds. Elsevier: Oxford, 2014; pp 47-78.

56. Humston-Fulmer, E. M.; Alonso, D. E.; Binkley, J. E., Chapter Six - Improving cannabis differentiation by expanding coverage of the chemical profile with GCxGC-TOFMS. In *Comprehensive Analytical Chemistry*, Ferrer, I.; Thurman, E. M., Eds. Elsevier: 2020; Vol. 90, pp 169-196.

57. Jensen, C. U.; Rosendahl, L. A.; Olofsson, G., Impact of nitrogenous alkaline agent on continuous HTL of lignocellulosic biomass and biocrude upgrading. *Fuel Processing Technology* **2017,** *159*, 376-385.

58. Saengsuriwong, R.; Onsree, T.; Phromphithak, S.; Tippayawong, N., Biocrude oil production via hydrothermal liquefaction of food waste in a simplified high-throughput reactor. *Bioresource Technology* **2021,** *341*, 125750.

59. LeClerc, H. O.; Tompsett, G. A.; Paulsen, A. D.; McKenna, A. M.; Niles, S. F.; Reddy, C. M.; Nelson, R. K.; Cheng, F.; Teixeira, A. R.; Timko, M. T., Hydroxyapatite catalyzed hydrothermal liquefaction transforms food waste from an environmental liability to renewable fuel. *iScience* **2022**, 104916.

60. Asamoto, B., *FT-ICR/MS*. New York, NY (United States); VCH Publishers Inc.: United States, 1991.

61. Cho, Y.; Ahmed, A.; Islam, A.; Kim, S., Developments in FT-ICR MS instrumentation, ionization techniques, and data interpretation methods for petroleomics. *Mass Spectrometry Reviews* **2015,** *34* (2), 248-263.

62. Wang, C., The Ionization Technology of LC-MS, Advantages of APPI on Detection of PPCPs and Hormones. *Austin Chromatography* **2015,** *2* (2), 1032.

63. Ciuffi, B.; Loppi, M.; Rizzo, A. M.; Chiaramonti, D.; Rosi, L., Towards a better understanding of the HTL process of lignin-rich feedstock. *Scientific Reports* **2021,** *11* (1), 15504.

64. Robb, D. B.; Blades, M. W., Factors affecting primary ionization in dopant-assisted atmospheric pressure photoionization (DA-APPI) for LC/MS. *Journal of the American Society for Mass Spectrometry* **2006,** *17* (2), 130-138.

65. Purcell, J. M.; Hendrickson, C. L.; Rodgers, R. P.; Marshall, A. G., Atmospheric Pressure Photoionization Fourier Transform Ion Cyclotron Resonance Mass Spectrometry for Complex Mixture Analysis. *Analytical Chemistry* **2006,** *78* (16), 5906-5912.

66. Marshall, A. G.; Hendrickson, C. L.; Jackson, G. S., Fourier transform ion cyclotron resonance mass spectrometry: A primer. *Mass Spectrometry Reviews* **1998,** *17* (1), 1-35.

67. Biswas, B.; Kumar, A.; Fernandes, A. C.; Saini, K.; Negi, S.; Muraleedharan, U. D.; Bhaskar, T., Solid base catalytic hydrothermal liquefaction of macroalgae: Effects of process parameter on product yield and characterization. *Bioresource Technology* **2020,** *307*, 123232.

68. Chen, Y.; Wu, Y.; Ding, R.; Zhang, P.; Liu, J.; Yang, M.; Zhang, P., Catalytic hydrothermal liquefaction of D. tertiolecta for the production of bio-oil over different acid/base catalysts. *AIChE Journal* **2015,** *61* (4), 1118-1128.

69. Cheng, F.; Tompsett, G. A.; Murphy, C. M.; Maag, A. R.; Carabillo, N.; Bailey, M.; Hemingway, J. J.; Romo, C. I.; Paulsen, A. D.; Yelvington, P. E.; Timko, M. T., Synergistic Effects of Inexpensive Mixed Metal Oxides for Catalytic Hydrothermal Liquefaction of Food Wastes. *ACS Sustainable Chemistry & Engineering* **2020,** *8* (17), 6877-6886.

70. Duan, P.; Wang, B.; Xu, Y., Catalytic hydrothermal upgrading of crude bio-oils produced from different thermo-chemical conversion routes of microalgae. *Bioresource Technology* **2015,** *186*, 58-66.

71. Gärtner, C. A.; Serrano-Ruiz, J. C.; Braden, D. J.; Dumesic, J. A., Catalytic Upgrading of Bio-Oils by Ketonization. *ChemSusChem* **2009,** *2* (12), 1121-1124.

72. Maag, A. R.; Paulsen, A. D.; Amundsen, T. J.; Yelvington, P. E.; Tompsett, G. A.; Timko, M. T., Catalytic Hydrothermal Liquefaction of Food Waste Using CeZrOx. *Energies* **2018,** *11* (3).

73. Scarsella, M.; de Caprariis, B.; Damizia, M.; De Filippis, P., Heterogeneous catalysts for hydrothermal liquefaction of lignocellulosic biomass: A review. *Biomass and Bioenergy* **2020,** *140*, 105662.

74. Xu, D.; Lin, G.; Guo, S.; Wang, S.; Guo, Y.; Jing, Z., Catalytic hydrothermal liquefaction of algae and upgrading of biocrude: A critical review. *Renewable and Sustainable Energy Reviews* **2018,** *97*, 103-118.

75. Zhu, Z.; Toor, S. S.; Rosendahl, L.; Yu, D.; Chen, G., Influence of alkali catalyst on product yield and properties via hydrothermal liquefaction of barley straw. *Energy* **2015,** *80*, 284-292.

76. Bi, Z.; Zhang, J.; Peterson, E.; Zhu, Z.; Xia, C.; Liang, Y.; Wiltowski, T., Biocrude from pretreated sorghum bagasse through catalytic hydrothermal liquefaction. *Fuel* **2017,** *188*, 112-120.

77. Toor, S. S.; Rosendahl, L.; Rudolf, A., Hydrothermal liquefaction of biomass: A review of subcritical water technologies. *Energy* **2011,** *36* (5), 2328-2342.

78. Miyata, Y.; Sagata, K.; Yamazaki, Y.; Teramura, H.; Hirano, Y.; Ogino, C.; Kita, Y., Mechanism of the Fe-Assisted Hydrothermal Liquefaction of Lignocellulosic Biomass. *Industrial & Engineering Chemistry Research* **2018,** *57* (44), 14870-14877.

79. Tekin, K.; Karagöz, S.; Bektaş, S., Hydrothermal liquefaction of beech wood using a natural calcium borate mineral. *The Journal of Supercritical Fluids* **2012,** *72*, 134-139.

80. Yim, S. C.; Quitain, A. T.; Yusup, S.; Sasaki, M.; Uemura, Y.; Kida, T., Metal oxide-catalyzed hydrothermal liquefaction of Malaysian oil palm biomass to bio-oil under supercritical condition. *The Journal of Supercritical Fluids* **2017,** *120*, 384-394.

81. Iliopoulou, E. F.; Stefanidis, S. D.; Kalogiannis, K. G.; Delimitis, A.; Lappas, A. A.; Triantafyllidis, K. S., Catalytic upgrading of biomass pyrolysis vapors using transition metal-modified ZSM-5 zeolite. *Applied Catalysis B: Environmental* **2012,** *127*, 281-290.

82. Zhou, Y.; Shao, Y.; Zhou, D.; Meng, Y.; Shen, D.; Long, Y., Effect of mechano-chemical pretreatment on valorizing plant waste for 5-hydroxymethylfurfural under microwave hydrothermal treatment. *Renewable Energy* **2021,** *180*, 536-543.

83. Zhang, L.; Yang, X.; Sheng, Y.; Huang, Q.; Yang, Z.; Shi, Y.; Guo, X.; Ge, S., Influence of typical pretreatment on cotton stalk conversion activity and bio-oil property during low temperature (180–220 ℃) hydrothermal process. *Fuel* **2022,** *328*, 125250.

84. Williams, O.; Newbolt, G.; Eastwick, C.; Kingman, S.; Giddings, D.; Lormor, S.; Lester, E., Influence of mill type on densified biomass comminution. *Applied Energy* **2016,** *182*, 219-231.

85. Ghadge, R.; Nagwani, N.; Saxena, N.; Dasgupta, S.; Sapre, A., Design and scale-up challenges in hydrothermal liquefaction process for biocrude production and its upgradation. *Energy Conversion and Management: X* **2022,** *14*, 100223.

86. Lian, X.; Xue, Y.; Zhao, Z.; Xu, G.; Han, S.; Yu, H., Progress on upgrading methods of bio-oil: A review. *International Journal of Energy Research* **2017,** *41* (13), 1798-1816.

87. Biller, P.; Sharma, B. K.; Kunwar, B.; Ross, A. B., Hydroprocessing of bio-crude from continuous hydrothermal liquefaction of microalgae. *Fuel* **2015,** *159*, 197-205.

88. Lesley Snowden-Swan, J. B., Michael Thorson, Andy Schmidt, Yuan Jiang, et al., Wet Waste Hydrothermal Liquefaction and Biocrude Upgrading to Hydrocarbon Fuels: 2020 State of Technology. Pacific Northwest National Laboratory: 2021.

89. Li, S.; Jiang, Y.; Snowden-Swan, L. J.; Askander, J. A.; Schmidt, A. J.; Billing, J. M., Techno-economic uncertainty analysis of wet waste-to-biocrude via hydrothermal liquefaction. *Applied Energy* **2021,** *283*, 116340.

90. LJ Snowden-Swan, Y. Z., SB Jones, DC Elliot, AJ Schmidt, RT Hallen, JM Billing, TR Hart, SP Fox, GD Maupin, Hydrothermal Liquefaction and Upgrading of Municipal Wastewater Treatment Plant Sludge: A Preliminary Techno-Economic Analysis. Energy, D. o., Ed. 2016.

91. Swan, L. J. S., Wet Waste Hydrothermal Liquefaction and Biocrude Upgrading to Hydrocarbon Fuels: 2019 State of Technology. **2020**.

92. Shahabuddin, M.; Italiani, E.; Teixeira, A. R.; Kazantzis, N.; Timko, M. T., Roadmap for Deployment of Modularized Hydrothermal Liquefaction: Understanding the Impacts of Industry Learning, Optimal Plant Scale, and Delivery Costs on Biofuel Pricing. *ACS Sustainable Chemistry & Engineering* **2023,** *11* (2), 733-743.

CHAPTER 2

ELUCIDATING THE ROLE OF REACTIVE NITROGEN INTERMEDIATES IN HETERO-CYCLIZATION DURING HTL OF FOOD WASTE

2.1 INTRODUCTION

The current world reliance on fossil fuels and the corresponding environmental impacts have created global interest in alternative, sustainable energy sources. Particularly attractive are approaches that leverage renewable, distributed inputs to sustainably produce liquid fuels and chemicals. Hydrothermal liquefaction (HTL) has emerged as a promising candidate for converting water-rich mixed organic streams into biocrudes without extensive energy-intensive pretreatment. Processing water-rich feeds is typically challenging for thermal processes but is ideal for hydrothermal methods.[1] HTL's high level of feedstock flexibility[2, 3] and the ability to directly produce a liquid biocrude has contributed to a recent surge of interest.[3-5] HTL biocrude production has been demonstrated for algal, lignocellulosic, and waste feedstocks (**Table 2-1**) with energy recoveries ranging from 30 – 60%.[6-8] Despite algae providing greater yields and energy recovery than other feeds, the high cultivation cost and ash content limit its effectiveness and have motivated research into HTL processing of biomass waste, sewage sludge, and food waste feeds.[9-11]

Municipal waste streams (sewage sludge, food waste) are widely available, low-cost feeds that are rich in carbon.[6,12, 13,10] Their water content precludes thermal conversion methods, other than hydrothermal ones. Use of waste feedstocks is economically and environmentally friendly due to

low, potentially negative, cost and because the energy content of these feeds would otherwise not be used productively.[12, 14, 15] Unfortunately, the heteroatom content of waste feeds, especially nitrogen, reduces biocrude quality and possibly yields.[12, 14, 15]

Table 2-1. Biochemical composition and proximate analysis of common HTL feedstocks: algae, food waste, and sewage sludge.

	Proximate Analysis (%)									
Feedstock	**Protein**	**Carb.**	**Lipid**	**Ash**	**Moisture**	**C (%)**	**H (%)**	**N (%)**	**O (%)**	**Source**
Algae	7 - 63	9 - 54	13 - 55	4 - 22	65 - 80	50-62	7-10	1-10	17-35	Shakya et al.[16]
Food Waste	4 - 22	40 - 70	6 - 24	0 - 6	61 - 86	40-60	6-10	1-6	25-55	Paritosh et al.[17]
Sewage Sludge	2 - 42	25 - 52	0.1 - 41	2 - 34	70 - 90	35-50	5-9	3-8	33-60	Chen et al.[1]

To obtain a high-quality oil product, substantial efforts must be made to minimize oil-phase heteroatom (N, O, S) content. HTL input streams can contain anywhere between 1 and 10 wt% nitrogen for woody biomass and high-protein algae, and >50 wt% oxygen.[16, 17] Oxygen is typically found in the aqueous and gas phases in near equal amounts, whereas as much as 50% of the nitrogen present in the feed appears in the biocrude as a contaminant that must be removed by subsequent treatments.[18] Nitrogen removal is conventionally more difficult than oxygen removal, and removing nitrogen heterocycles is especially challenging.[19-21] Moreover, nitrogen interferes with catalytic acid sites intended for oxygen and sulfur removal, further complicating upgrading efforts.[22] Minimizing the nitrogen upstream in the feed or in the biocrude formed during hydrothermal processing is preferred over removing it during biocrude upgrading. In the hydrothermal step, it would be particularly advantageous to selectively control the fate of nitrogen—namely to be able to partition it into the gaseous, solid or aqueous phases, leaving the primary biocrude phase nitrogen-free. Our current knowledge of the chemical pathways that result

in these respective fates, however, are substantially lacking with regard to the role of nitrogen in these reactive mixed feeds.

To better understand these pathways, thermodynamic and kinetic simulations are required. *Ab initio* calculations have been used on biopolymeric systems to understand key degradation steps during lignin depolymerization[23, 24] and to reveal primary homolytic cleavage pathways during cellulose pyrolysis.[25] Notably, however, these studies are typically constrained to the primary reactions of single component, well-ordered feeds or surrogates that are not able to capture the more reactive secondary couplings of oligomeric, mixed component solvated environment that is prevalent during hydrothermal waste processing.

Current knowledge regarding HTL mechanisms are limited to lumped kinetic studies which rely on gas chromatography and mass spectrometry (GC-MS) analysis.[8, 26-28] While this approach has proven valuable in providing insight into product phase distributions and general nitrogen pathways, it fails to describe the highly reactive condensed phase environment and particularly, the molecular-level intermediate pathways and barriers for driving nitrogen to each product phase.[8, 29, 30] When considering food waste decomposition, it is typically considered to progress through two consecutive stages (**Figure 2-1**). In the first, the biopolymers (starches, proteins, fats) are hydrolytically decomposed into short-chained oligomers and monomers.[11] These small, solvated molecules are then free to couple in increasing degrees to form the aqueous (light), oil (heavy) and solid (char) products. With this perspective, the focus of the current study is not to understand the first decomposition stage. Instead, it is to better understand how the small degradation products build back up to form the biocrude, and specifically how the nitrogen functionality, primarily from the proteins, becomes incorporated into the biocrude.

The composition of the reactive intermediate mixture is derived from detailed chemical analysis of the product fractions. The biocrude alone may contain thousands of unique compounds,[31-33] causing analytical challenges, particularly with conventional GC-MS which provide molecular-level precision for volatile biocrude components but is not sufficient for the significant portion of the biocrude that is not volatile enough for GC analysis.[34] Fourier-Transform Ion Cyclotron Resonance Mass Spectrometry (FT-ICR MS) can provide molecular formula with isotopic accuracy on a molecular basis across the entire molecular weight regime of the product oil and is a promising technique for biocrude analysis.[32, 33, 35] While FT-ICR MS has been used to advance scientific understanding of molecular pathways in pyrolysis of biomass,[36-39] its application to biocrude analysis – and especially to pathway discovery – is much more limited.[32, 40] A combination of GC-MS and FT-ICR MS along with the known initial feed structures are used in this study to carefully select key functionality to be incorporated into chemical surrogates to be used in DFT studies to evaluate intermediate reaction pathways.

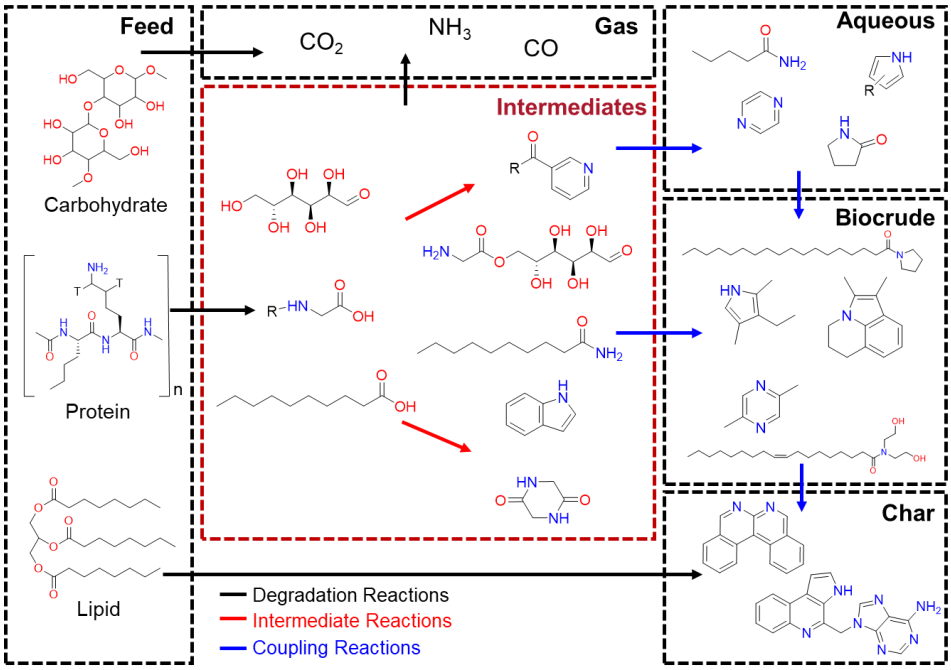

Figure 2-1. Representative nitrogen pathways for hydrothermally depolymerizing macromolecules of food waste and algae to reactive intermediates which form secondary condensation products before ultimately condensing to form biocrudes, and chars. This paper focuses on understanding the condensed phase chemistry in the reactions of intermediates (red dashed box).

This work will examine the role of feedstock composition and temperature on the type and amount of HTL product nitrogen. An analysis of small, volatile molecules found in food waste HTL biocrude will serve to identify important molecular classes which will be used to develop a reaction network for use in thermodynamic and kinetic simulations. The simulation results will then be compared to large biocrude molecules identified via FT-ICR MS to ensure model validity. The results of this work aim to assist in understanding nitrogen heterocycle formation at hydrothermal liquefaction conditions to make recommendations for optimal feedstock-specific operating conditions.

2.2 MATERIALS & METHODS

2.2.1 DEVELOPMENT OF REACTION MECHANISM

Reaction mechanisms were formed capturing the interactions of the three primary components of non-woody biomass, i.e., protein, lipid, and carbohydrates. To maximize computational efficiency, simple model compounds were chosen. Glycine, the smallest amino acid, was chosen as a model protein degradation product; butadiene as the model fatty acid; and various small aldehydes (formaldehyde, glyoxal, furaldehyde, and glyceraldehyde) were used as model carbohydrate decomposition products. Glyceraldehyde was specifically chosen due to its known reactivity during the Maillard reaction.[41, 42] HTL reaction mechanisms were identified from various experimental studies which involved identification of specific compounds resulting from macromolecular interactions.[40, 43-47] Reactions were chosen to represent Maillard, hydrodenitrogenation and Aza Diels Alder (ADA) reactions to ensure representative understanding of the types of nitrogen reactions. These reactions were then divided into schemes based on the type and number of reactants involved.

2.2.2 ELECTRONIC STRUCTURE CALCULATIONS

Quantum chemical calculations were completed with the Gaussian 16 program suite. All chemical species are calculated in their singlet state and gas phase. The composite method CBS-QB3 was used to optimize geometries and evaluate single-point energies. Force constants and vibrational frequencies were calculated with B3LYP/CBSB7. The torsional motion around the single bonds in each molecule were treated as hindered internal rotations where each angle corresponding to an internal rotation was varied in incremental steps of 10° for 36 steps to achieve complete rotation, allowing other coordinates to relax, evaluated with B3LYP/6-31G(d,p). Transition states were also calculated using CBS-QB3, with frequency calculations performed to

verify the existence of only one imaginary frequency per transition state. When necessary, additional optimizations were performed to ensure the result was the lowest energy transition state. All calculations (optimization, frequency, and hindered rotor scans) were repeated using the density functional theory method M06-2X/6-31G+(d,p) for comparison but the results presented here are from CBS-QB3, apart from Scheme 4 reaction 3 because species M_{29} and transition state 4.3 could not be calculated at CBS-QB3 on the available computer hardware.

As water is the solvent and thus in extreme excess, it is taken to be pseudo zeroth order in all kinetic expressions. This is further confirmed by sensitivity analysis (**Figure A2-11**) which shows little sensitivity to changes in water concentration. Solvent effects can have significant impacts on some reaction rates, especially when reactants or products have strong interactions with the solvent, e.g. are hydrophobic or form hydrogen bonds.[48] For example, Bini et al.[49] reported an increase in Diels Alder reaction rate in aqueous media, whereas Baisier et al.[50] reported an increase in Maillard reaction rates in the presence of water with an excess of sugar, representing the two primary reaction types explored in this work. Furthermore, some reactions can be catalyzed by an explicit interaction with a solvent molecule. These effects are necessarily neglected in the current calculations, but the presumption is that to some extent the effects will alter all the competing pathways in a similar manner, and although individual energies and rates will be imprecise, to a first approximation the qualitative trends and relative predictions should be robust.

2.2.3 KINETIC & THERMODYNAMIC PARAMATER ESTIMATION

Enthalpies of formation are evaluated from the CBS-QB3 results using Bond Additivity Correction (BAC) values available in CanTherm Version 2.1.7.[51] To calculate partition functions, the CanTherm software package was utilized with a frequency scale factor of 0.99 for CBS-QB3 and 0.967 for M06-2X/6-31G+(d,p). The results from potential energy scans $V_i(\theta_i)$ are fit to a

Fourier series in CanTherm and the resulting coefficients A_m and B_m in **Equation 2.1** are found using the least squares method.

$$V_i(\theta_i) = \sum_{m=1}^{M} A_{m,i} \cos(m\theta_i) + B_{m,i} \sin(m\theta_i) \quad (2.1)$$

Wherein V_i is potential energy change due to torsion i. $A_{m,i}$ and $B_{m,i}$ are fitting parameters and θ_i is the angle of rotation of the torsion i. The potential values were then used in solving the 1D Schrodinger equation to finally combine the harmonic oscillator (HO) approximation with the hindered rotor contribution. Entropy calculations considered molecular symmetry. Conventional transition state theory was used for calculating rate coefficients for considered pathways, with Eckart tunneling corrections to improve estimated rate coefficients at HTL-relevant temperatures. Rate constants were then fit to the modified Arrhenius equation (**Equation 2.2**) for each of the i^{th} reactions where k_i is the rate constant for each reaction, A_i is the pre-exponential factor, E_i is the activation energy, n is a modification factor to represent the changes more accurately with temperature, and T is the temperature in Kelvin.[52]

$$k_i = A_i T^{n_i} \exp\left(\frac{-E_i}{RT}\right) \quad (2.2)$$

2.2.4 KINETIC MODELING

Thirty-eight reactions consisting of forty-seven molecules were proposed to describe initial intermediate nitrogen reactions in hydrothermal liquefaction. Arrhenius parameters for each reaction were calculated as described above then combined with their respective first and second order rate expressions to form a system of forty-eight ordinary differential equations (**Equation 3**). This system constituted the kinetic model, which was then integrated in MATLAB using ode15s given initial conditions corresponding to the fractional feed composition of the amino acid

(M_1), lipid (M_7), and carbohydrate (M_{12}, M_{18}, M_{26}, or M_{35}). Kinetics calculations were completed as a function of temperature and reaction time. As discussed later, initial compositions covered the ternary compositional space defined in **Table 2.1**. Rates were calculated at 300-1000 K. All simulations were integrated over 30 minutes, unless denoted otherwise, to be consistent with typical experimental HTL timescales. Simulations did not consider secondary reactions to higher molecular weight polymers, chars or phase changes.

$$\frac{dc_j}{dt} = \sum_{i=1}^{N} \nu_{ij} \times r_i$$
$$r_i = k_i(T) \prod_{j=1}^{M} c_j^{-\nu_{ij}} \quad \text{for} \quad \nu_{ij} < 0 \tag{2.3}$$

Where c_j is the concentration of species j of $M = 47$ species; ν_{ij} is the stoichiometric coefficient of species j in reaction r_i of $N = 38$ reactions. Reaction rates were calculated with mass action kinetics based on the proposed mechanism using rate constants described in **Equation 2.2**, as summarized in **Table A2-4**.

2.2.5 EXPERIMENTAL METHODS

Hydrothermal liquefaction experiments were conducted in a 300 mL stainless-steel Parr reactor (Model 4561) fit with a magnetic stirrer consistent with previous studies.[9, 53] For each experiment, 100 g of food waste slurry (15 wt% solids) was loaded into the reactor. The food waste slurry was prepared as previously described[9, 53] and according to Army specifications using a mixture of applesauce, chicken, butter, green beans, rice, instant potatoes, and cheese. After loading, the reactor was sealed and purged three times with nitrogen to remove residual air before pressurization to 65.5 ± 5 bar and heating to 575 ± 5 °C at approximately 279 K/min using an external heating jacket. After heating, the reactor pressure was 200 ± 5 bar, sufficient to maintain

water in its liquid state. The reaction temperature was maintained for 60 minutes, at which point the reaction was quenched by placing the reactor in an ice bath until the measured temperature reached 310 ± 2 °C. Quenching required less than 10 minutes. The biocrude/solid mixture was then separated from the aqueous phase via vacuum filtration before the solids and biocrude were isolated using acetone. The acetone was then evaporated using a rotary evaporator to obtain the final mass of biocrude. Each product phase was carefully massed to ensure closure of the mass balance, as described previously.[9, 53] Deliberate safety precautions were made to handle the high pressure and high temperature reaction mixture. All experiments were conducted in a ventilated fume hood with a properly sized rupture disk (172 bar) vented to the hood. The reactor was pressure tested with nitrogen at ambient temperature to 69 bar prior to each run.

All runs were completed in triplicate, with yield measurements agreeing to within ±10% when experiments were performed under identical conditions. Average values obtained from these experiments are presented here.

HTL biocrude was analyzed via GC-MS, to understand the molecular composition of the volatile fraction. Biocrude and aqueous samples were dissolved in toluene to a final concentration of 125 µg/mL for positive-ion APPI Fourier transform ion cyclotron resonance mass spectrometry (FT-ICR MS). Dissolved samples were analyzed using a custom-built FT-ICR mass spectrometer[54], equipped with a 22 cm room temperature bore 9.4 T superconducting solenoid magnet (Oxford Instruments, Abingdon, U.K.) and a modular ICR data collection station (Predator).[31] Both techniques are described further in **Appendix A**. Further analysis was completed to close the mass balance for carbon, nitrogen, and oxygen. Total organic carbon (TOC) and total nitrogen (TN) analyses were completed on the aqueous phase using a TOC analyzer (Shimadzu Co. Kyoto, Japan). Elemental analysis of the biocrude and char phases was completed

by Midwest Microlabs (Indianapolis, IN). The hydrogen and oxygen composition of the aqueous phase was taken to be the difference between the total feed oxygen content and the sum of the remaining products.

2.3 RESULTS & DISCUSSION

In this work, reaction pathways for the liquefaction of carbohydrate, protein, and lipid monomers are explored through an analysis of thermodynamic reaction equilibrium and kinetics. GC-MS analysis of biocrude from food waste HTL is used to gain an understanding of small biocrude-phase products. A density functional theory (DFT) model is used on proposed reaction schemes involving six primary pathways for the formation of HTL intermediates. Free energy and Arrhenius parameters are calculated and utilized in the development of a kinetic model to evaluate the rates at which these reactions occur. This analysis provides a baseline for understanding the feasibility of the proposed pathways via a discussion of the coupling reactions from the primary model products to the larger molecules seen in HTL biocrude. FT-ICR MS was employed to validate model predictions through comparisons between the carbon number and double bond equivalency of computationally-predicted and experimentally-observed product molecules.

2.3.1 EXPERIMENTAL ANALYSIS OF VOLATILE HTL PRODUCTS

To ascertain the role and molecular contributions of nitrogen during the HTL process, a food waste slurry consisting of 18% protein, 59% carbohydrate, and 22% lipid was heated to 575 K for 60 minutes at 200 bar. This reaction produced, on average, 14% biocrude, 25% solid, and 17% aqueous products on a mass basis. Resultant mass yields were used in conjunction with the elemental composition of each phase to close carbon, nitrogen, hydrogen, and oxygen mass balances within 10%. This analysis shows that the feed contains 3.8% nitrogen, of which, 13.2%

is found in the biocrude. The nitrogen product fractionation for food waste HTL can be seen in **Figure 2-2**, wherein nearly 50% of the nitrogen partitions to the aqueous phase, consistent with previous literature findings.[18, 55] The gas phase was found to contain >98% CO_2, consistent with prior work showing only trace amounts of gas-phase ammonia.[56, 57] Gas-phase nitrogen is below detection limits, leading to it being lumped together with loss, resulting in 95% mass balance closure. Nearly 60% of the nitrogen can be found in the liquid products (biocrude and aqueous), which are assumed to be miscible at reaction conditions, but phase partitioned at ambient temperature. These two phases have the potential to undergo the same reactions before thermodynamic partitioning occurs upon quenching.

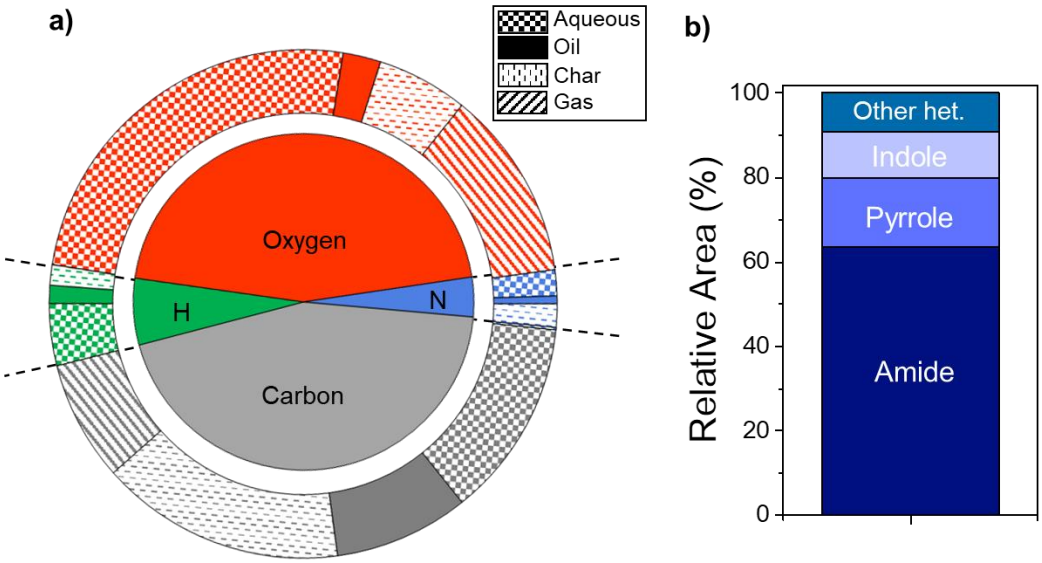

Figure 2-2. a) Elemental analysis tracking the fate of carbon, hydrogen, oxygen, and nitrogen from food waste feedstock (inner circle) to HTL products (outer ring). HTL was performed at 300 °C, 1 h residence time. **b)** GC-MS peak area percentages for the total nitrogen identified in the oil phase, broken into prominent classes. Indoles, pyrroles, and other N heterocycles can be grouped together as the total nitrogen heterocycle content.

Further analysis utilizing GC-MS (**Figure A2-8, Table A2-3**) of the volatile portion of biocrude allows for molecular-level analysis of small molecules where 86% of the total peak area was identified as fatty acids. Fatty acids were confirmed as the most abundant product via GC×GC-HRT, further identifying a suite of fatty acid amides corresponding to the same range of carbon chain lengths (**Figure A2-9**). The second most abundant class is nitrogen-containing compounds, of which 64% have been identified as amides (**Figure 2-2b**). Further analysis of the chromatogram identifies a range of pyrroles, pyrrolidines, and indoles, all classes of nitrogen heterocycles, which accounted for the remaining 36% of the nitrogen compounds identified. Pyrroles account for nearly half of the identified heterocycles and indoles for an additional 30%. These compounds contain nitrogen locked in a ring structure, making them difficult to upgrade and remove. Their presence in HTL biocrude is of express interest in this work.

2.3.2 SIMULATION OF REACTION INTERMEDIATES

Due to the short-lived nature of the reactive small molecules and computational limitations, model species representative of the protein, carbohydrates, and lipid degradation products from food waste were chosen as feedstock molecules. Additional carbon atoms will serve to increase the hydrophobicity at room temperature and can play a role in increased steric hinderance that can affect experimental reaction rates. For this study, glycine was utilized as the model protein, butadiene as the model fatty acid, and four aldehydes (formaldehyde, glyoxal, furaldehyde, and glyceraldehyde) as model carbohydrates. Reaction chemistries commonly identified in literature were evaluated and compared including combination (condensation, cyclization, dehydration) and decomposition (hydrolysis, deamination, decarboxylation) reactions.

At HTL conditions, inorganic and small organic nitrogen molecules readily break down into amines at high temperatures in basic media through various deamination pathways.[58] Heterocycles,

such as pyrroles and indoles, which are present in the side chain of amino acids proline, histidine, and tryptophan, lock their nitrogen in a stable aromatic ring structure which requires severe reaction conditions to break down. The Maillard reaction is a well-known heterocyclic reaction responsible for the browning of foods.[59, 60] Maillard reactions occur between a carbonyl group on a reducing sugar and the amine group of a protein, and have been shown to proceed through pH-dependent pathways.[61, 62] Specifically, retro-aldol reactions are more prominent at basic pH, producing more reactive $C_2 - C_5$ sugar fragments.[61] An additional reaction of importance is the Aza-Diels Alder (ADA) reaction, which has not received as much research attention as the well-known Diels-Alder reaction. ADA represents the cycloaddition of a diene and dienophile without an imine group.[63, 64] This reaction is thought to occur via a single transition state without intermediates. Based on HTL literature and established chemical pathways, the final reaction scheme was reduced to those shown in **Figure 2-3**.[18, 29, 40, 41, 63, 65-73] Studied reactions are divided into six primary pathways denoted by their initial reactants, and all molecules are summarized in **Table A2-3**.

Scheme 1 is the result of glycine decomposition in four potential competitive pathways including decarboxylation (1.5) and deamination (1.3). Schemes 2 – 4 involve the addition of increasingly oxygenated aldehydes (formaldehyde, furaldehyde, glyceraldehyde). Each of the aforementioned schemes include a pathway to the primary amine and a competitive reaction (2.3, 3.3, 4.3) resulting in nitrogen heterocycle formation through the ADA reaction mechanism. The remaining secondary reactions in these schemes do not result in heterocycle formation but include rearrangements, aminations, dehydration, and decomposition reactions. Scheme 5 represents a modified Maillard reaction for the formation of a nitrogen heterocycle. This is an important reaction to consider due to its prevalence in literature and as a dominant heterocycle formation

mechanism. The Maillard reaction contains ten intermediates, making it the longest scheme with multiple kinetic barriers and free energy increases to overcome. The last scheme considered, (6) outlines the pathway for the combination of two glycine molecules through dehydration to form a nitrogen heterocycle.

Transition state theory is used to calculate the temperature-dependent reaction rates while accounting for tunneling effects and fit to a modified Arrhenius equation (**Equation 2.2**) as reported in **Table 2-2**. The Eyring equation is then used to derive the Gibbs energy of activation ($\Delta^{\ddagger}G^{\circ}$) at 600 K, as described in the Supporting Information. This strategy allows for the evaluation of the free energy change for the reaction, indicating the favorability of the reaction, as well the activation free energy, representing the ΔG of the transition state. An exergonic decrease in free energy signifies the system releases energy spontaneously and is favorable in comparison to an endergonic increase in free energy where further energy inputs are required. Likewise, a high activation free energy signifies a slow reaction, and a low activation free energy signifies a faster reaction. Transition state activation free energy and free energy of reactants are shown on the free energy surfaces in **Figure 2-4** and tabulated in **Table A2-4**, all evaluated at 600 K. Reaction schemes are colored based on the reaction step with the largest activation energy, except when the largest step is a rearrangement reaction. The $\Delta^{\ddagger}G^{\circ}$ values at 600 K are also shown in parentheses next to the reaction numbers in **Figure 2-3** and are the activation barriers described in the following discussion.

In Scheme 1, the deamination and decarboxylation of glycine in reactions 1.4 and 1.5 are the most exergonic first-step reactions, however, reaction 1.4 has the highest activation barrier of the reaction network at 109 kcal/mol. The decarboxylation in reaction 1.5 has the lowest barrier of the initial competitive steps in Scheme 1 at 74 kcal/mol. Reaction 1.1 and 1.3 also boast high activation

barriers, both at 107 kcal/mol. Glycine decomposition through the deamination pathway (1.4), despite its activation energy, has been shown to occur at temperatures as low as 559 K, making this pathway the most probable first reaction step in Scheme 1.[74]

In Scheme 2, the formation of a nitrogen heterocycle through ADA is kinetically limited by reaction 2.2 in which the hemiaminal formed in the previous reaction undergoes dehydration to a Schiff base. This reversible reaction becomes increasingly exergonic (and hence spontaneous) as temperatures rise above about 400 K but has the highest barrier in Scheme 2 (57 kcal/mol) and a rate strongly dependent on reaction temperature. The ADA reaction (2.3) occurs with a slightly lower energy barrier (52 kcal/mol) than the competing reaction. Reaction 2.3 also has a lower energy barrier than the competing decarboxylation reaction, indicating heterocycle favorability. The same analysis holds true for Schemes 3 and 4, wherein ADA has a lower activation barrier than the competing reactions studied. The predicted nitrogen heterocycles from ADA are all substituted pyridines, wherein GC-MS analysis does not identify any pyridines but instead has a higher concentration of nitrogenated five-membered rings. This may be due to the presence of tryptophan in real food waste that is not considered in the model.

In Scheme 5, many of the reactions have energy barriers above 50 kcal/mol. Reaction 5.2 of the Maillard reaction has a large activation energy at 61 kcal/mol and reaction 5.5 has the largest energy barrier at 66 kcal/mol. Reaction 5.2, the formation of a Schiff base, is reversible, but at typical HTL conditions the reverse rate is negligible, especially compared to the onward reaction 5.3, and has not been considered. The Strecker Degradation (SD) that occurs in the final stages of the pathway (5.2) as well as the dicarbonyl produced from the Amadori rearrangement (5.4) react with an amino acid (glycine) to produce a hemiaminal (5.7) via a mechanism with an energy barrier of 54 kcal/mol, after the second rate-limiting step at 5.5. This reaction is the dehydration of a

previously formed nitrogen heterocycle (1,2,3,6-tetrahydropyrazin-2-ol) to 2,5-dihydropyrazine. Reaction 5.8 is necessary for nitrogen heterocycle formation, followed by two dehydration rearrangements. Due to the large energy barrier of reaction 5.9, it is most likely that piperazine-2,5-diol (M_{43}) will be the final product of this reaction scheme. Experimentally, only one pyrazine compound was identified with GC-MS constituting 2% of the nitrogen-containing compounds. Contrary to the model predicting alcohol-substituted pyrazine, the observed molecule is methylated, potentially indicating the prevalence of tertiary dehydration reactions at longer residence times. On the other hand, the coupling of two glycine molecules in Scheme 6 via dehydration occurs with an energy barrier of 64 kcal/mol, indicating the enhanced stability of glycylglycine (M_{46}) and the potentially unfavorable dehydration to piperazine-2,5-dione (M_{47}).

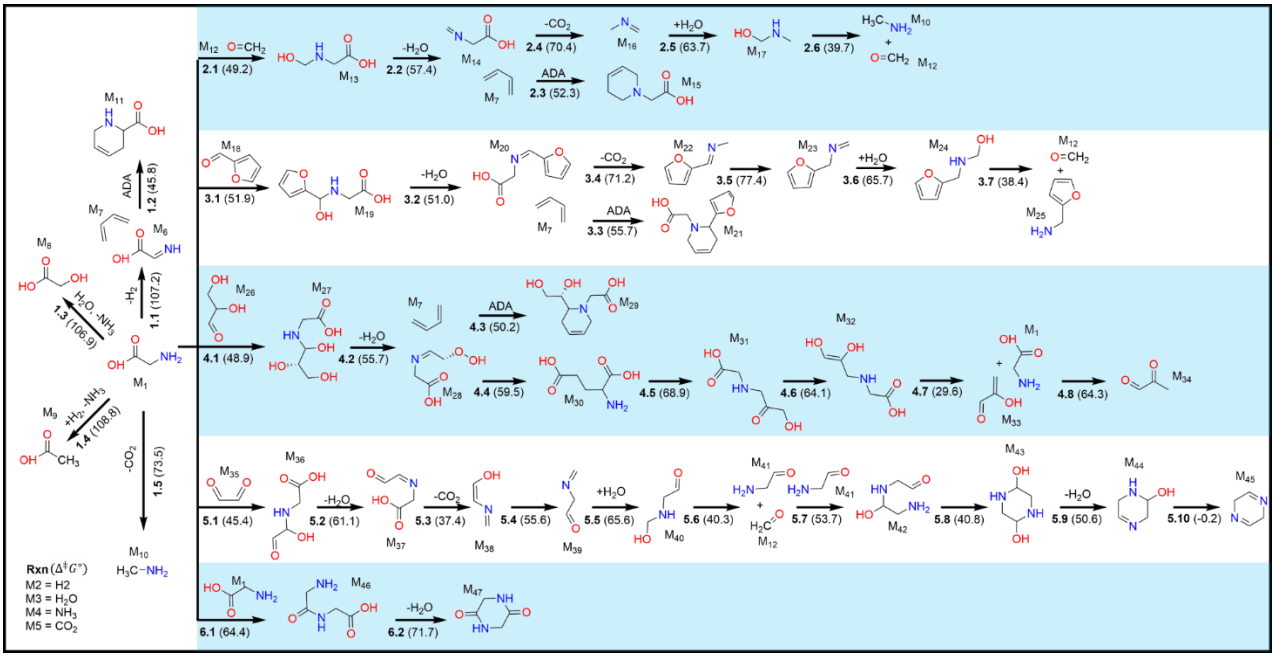

Figure 2-3. Overall reaction network divided into six primary reactions schemes. Scheme 1 shows four decomposition routes for the thermolysis of glycine. Schemes 2, 3, and 4 show the reactions of glycine with four different aldehydes (formaldehyde, glyoxal, furaldehyde, and glyceraldehyde) and showcase the competitive Aza Diels Alder (ADA) reaction to nitrogen heterocycle formation. Scheme 5 is a modified Maillard reaction and Scheme 6 showcases the self-combination route of two glycine molecules. $\Delta^{\ddagger}G^{\circ}$ [=] kcal/mol

Another consideration, across all schemes, is the formation of gaseous byproducts. CO_2 is produced in reactions 1.5, 2.4, 3.4, and 5.3 while NH_3 can be found in reactions 1.3 and 1.4. All CO_2 formation reactions considered are thermodynamically favorable at 600 K, constituting a decrease in free energy, whereas only one of the two ammonia producing reactions is exergonic. Kinetically, all reactions forming CO_2 as a byproduct have lower activation energies than the two NH_3 reactions by at least 33 kcal/mol. This finding is consistent with experimental results, where over 98% of the gaseous products are carbon dioxide, and only trace ammonia is detected.

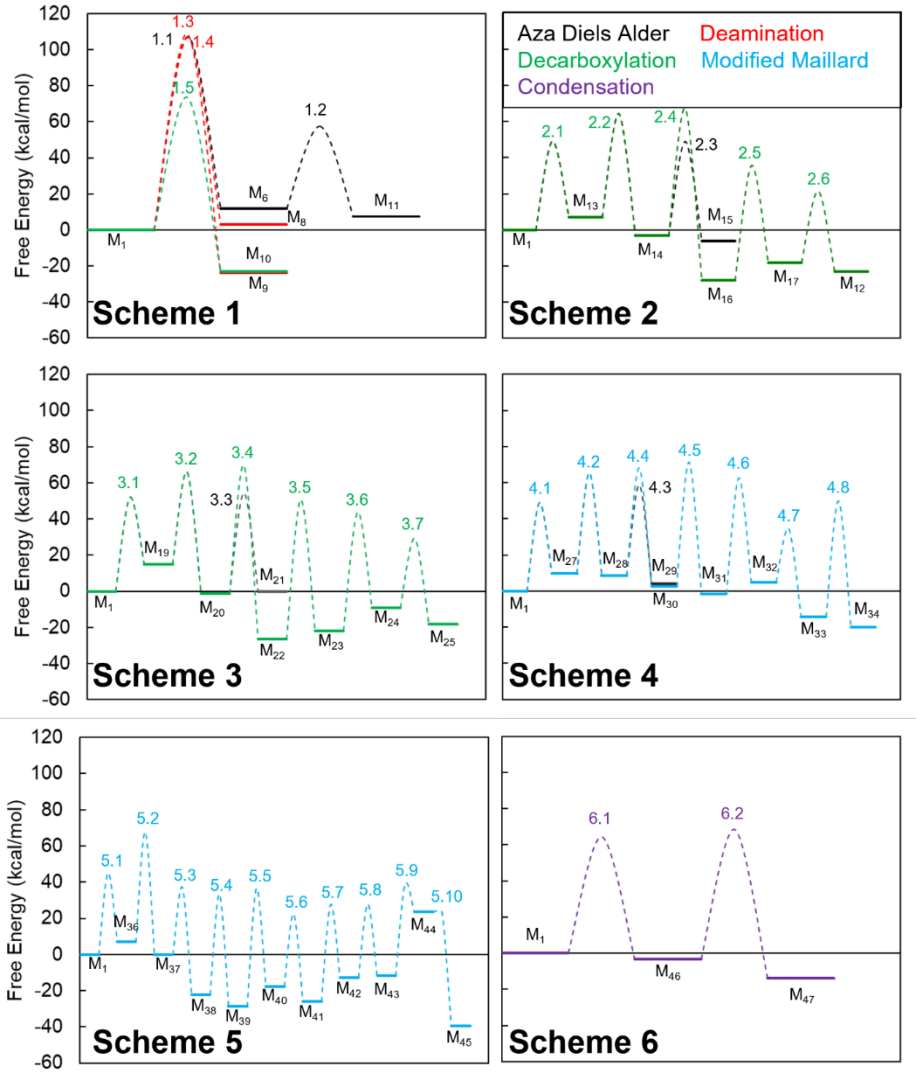

Figure 2-4. Free energy diagram for all reaction pathways at 600 K. Reaction pathways are colored based on the reaction step with the largest activation energy, except when a rearrangement reaction had the highest activation energy.

The kinetic parameters summarized in **Table 2-2** are used to construct a model to perform a reaction flux analysis and identify dominant chemical pathways during hydrothermal operation, particularly with the goal of revealing pathways by which the observed heterocyclic nitrogen molecules are produced. The model does not consider further polymerization reactions, solely predicting the behavior of the intermediates. Cross reactions, wherein products from one scheme can react with reactants or products from another scheme, were also not considered.

Table 2-2. Modified Arrhenius rate parameters (Equation 2.2) calculated using the CBS-QB3 method. Calculated rate constant for all reactions at 600 K.

Reaction	A_i	n	E_i (kcal/mol)	k_i (600 K)	Class[+]
1.1*	2.4 E-79	27.34	64.1	1.0E-26	Degradation
1.2**	1.8 E+04	1.53	20.3	1.3E+01	ADA[+]
1.3**	4.0 E+01	3.04	85.7	6.6E-22	Deamination[+]
1.4**	4.7 E+06	2.07	94.1	1.3E-22	Deamination[+]
1.5*	1.1 E-24	11.07	56.2	2.0E-14	Decarboxylation[+]
2.1**	4.6 E-05	4.29	21.2	7.1E-01	Combination
2.2*	1.0 E-06	5.71	48.6	1.5E-08	Dehydration
2.3**	3.0 E-01	2.69	22.6	5.3E-02	ADA[+]
2.4*	4.6 E-33	13.58	49.3	2.6E-13	Decarboxylation[+]
2.5**	6.2 E+01	3.12	43.6	3.8E-06	H_2O Addition
2.6*	5.9 E+02	2.86	33.2	4.4E-02	Degradation
3.1**	1.3 E-06	4.65	22.4	7.6E-02	Combination
3.2*	3.3 E+18	-1.57	54.0	3.1E-06	Dehydration
3.3**	5.7 E-01	2.32	23.9	3.0E-03	ADA[+]
3.4*	1.3 E-31	13.03	49.9	1.3E-13	Decarboxylation[+]
3.5*	2.9 E-07	5.86	68.3	7.4E-16	Rearrangement
3.6**	3.8 E-01	3.48	42.3	6.9E-07	H_2O Addition
3.7*	4.6 E+12	-0.06	36.8	1.3E-01	Remove CH_2O
4.1**	1.5 E+01	2.21	20.2	9.0E-01	Combination
4.2*	8.0 E+08	0.91	51.2	6.2E-08	Dehydration
4.3**	4.5 E+01	-0.67	25.5	3.3E-01	ADA[+]
4.4*	5.7 E-14	8.42	51.4	2.6E-09	Rearrangement
4.5*	7.6 E-01	3.43	58.9	9.3E-13	Rearrangement
4.6*	3.2 E-30	12.83	45.1	5.3E-11	Rearrangement
4.7*	1.8 E+16	-1.13	29.7	2.0E+02	Degradation
4.8*	5.5 E-47	18.11	39.5	4.6E-11	Rearrangement
5.1**	7.7 E-04	3.75	16.6	1.8E+01	Combination
5.2*	9.3 E+17	-1.31	64.6	6.5E-10	Dehydration
5.3*	1.4 E+12	-0.25	32.9	2.9E-01	Decarboxylation
5.4*	1.4 E-29	12.66	37.0	6.7E-08	H_2O Addition
5.5**	4.0 E-20	9.16	33.4	7.9E-07	Decomposition
5.6*	3.6 E+13	-0.24	39.7	2.7E-02	Addition
5.7**	5.7 E-07	4.44	21.6	1.7E-02	Rearrangement
5.8*	8.3 E+09	-0.15	31.0	1.7E-02	Dehydration
5.9*	2.5 E+15	-0.35	54.2	4.6E-06	Dehydration
5.10*	1.1 E+13	0.44	3.0	1.5E+13	Dehydration
6.1**	2.0 E-01	2.87	35.5	2.2E-06	Coupling
6.2*	1.7 E+06	1.23	62.3	8.9E-14	Condensation[+]

*1st order reaction with units A [=] s^{-1}, k [=] s^{-1}

**2nd order reaction with units A [=] cm^3/mol*s, k [=] cm^3/mol*s

[+] Indicates primary reaction mechanism corresponding to colors in Figure 4.

The molecules considered in this reaction network are distributed into fourteen chemical classes (**Table A2-3**) for ease of reporting the kinetic model. The first three classes denote the primary reactants: amino acid, diene, and aldehyde which together account for six of the forty-seven molecules examined. Additional chemical classes identified are as follows: Amine, Amide, Hemiaminals, Amino-aldehydes, Alkanolamines, Acids, Schiff base, Gases, Nitrogen heterocycles, and Other. These classes will be referenced throughout the remainder of this study.

2.3.3 TEMPERATURE DEPENDENCE

Standard HTL reactions take place between 525 – 675 K, resulting in a range of potential dominant reactions. Reaction temperature has been shown to affect HTL mass yields and composition.[32] One variable often considered is the optimal reaction temperature. Operating below 525 K often results in high solids (char) formation and is traditionally coined hydrothermal carbonization. The model assumes and kinetics confirm that the monomeric species are stable at these reaction temperatures, and will not couple to form oligomers, biocrude-soluble products, or char. This observation is consistent with the understanding that carbonization primarily progresses directly from concerted biopolymer rearrangements, not from the bottom-up approach whereby the biocrude is polymerized to char.[75] Hydrothermal liquefaction reactions, on the other hand, typically occur between 525 – 625 K to ensure complete breakdown of macromolecules and to limit low-temperature char formation. With this analysis, operating conditions can be fine-tuned to limit heterocycle production in the liquid products. **Figure 2-5** plots the effect of reaction temperature at 30 minutes for four real feedstock compositions taken from algae and food waste (**Table A2-5**).[9, 76] Carbohydrate concentration was divided evenly among the four possible reactant aldehydes. All kinetic simulations were assumed to be single phase in this study, and changes to

physical or kinetic properties upon phase transition (oil/aqueous or supercritical) were not considered.

Low protein feeds (< 50%) resulted in hemiaminals as the sole nitrogen intermediate product at HTL conditions (525 – 625K). At these conditions, higher protein feeds also contain a small (< 3%) fraction of amides that increases substantially with increasing temperature. When the majority of the feed is carbohydrates, no amide formation occurs at any of the explored temperatures, potentially due to the low concentration of glycine, inhibiting reaction 6.1 due to its high kinetic barrier compared to parallel steps in the competing schemes. There is no shortage of aldehydes to undergo Maillard and competing combination reactions. The model predicts an overwhelming majority of hemiaminals within traditional HTL temperature range, yet a minor increase in temperature introduces unfavorable heterocycles as well as amide, gaseous, and amine products.

Despite predicting no appreciable formation of nitrogen heterocycles until 650 K, experimental findings from algae and food waste feeds have identified oil-phase heterocycles at 575 K. This is likely caused by a combination of unreactive side chains present in the native proteins and tertiary reactions whereby the intermediate products continue to react as they build up to larger biocrude molecules. Five of the twenty essential amino acids contain heterocyclic side chains and are likely present in food waste. In experiments performed between 550 – 590 K with algae, appreciable amounts of pyrroles, pyridines, indoles, diketopiperazines (DKPs), and imidazoles were identified in the biocrude.[32, 77] Previously mentioned analysis with food waste HTL has also identified the presence of nitrogen heterocyclic compounds, despite reaction temperatures below 650 K.[3] The hemiaminals predicted by the model exhibit similar functionality to some of the observed heterocycles, including DKPs with the presence of nitrogen and double-

bonded oxygen in the same molecule. Both have the potential to form from the interaction between amino acids and monosaccharides, often proceeding through a hemiaminal intermediate before the final cyclization step.[78] The experimentally observed heterocycles are larger ($>C_6$) and likely result from secondary coupling reactions from the intermediate products predicted here. Additionally, the model predicts less than 2% of the products are heterocycles in the typical reaction temperature range. Notably, the vast majority of the nitrogen remains as unreacted glycine due to the initial energy barriers to decomposition. The proposed model serves to understand dominant pathways and molecular functionality that are critical steppingstones towards further combination and cyclization interactions to produce the experimentally identified molecules.

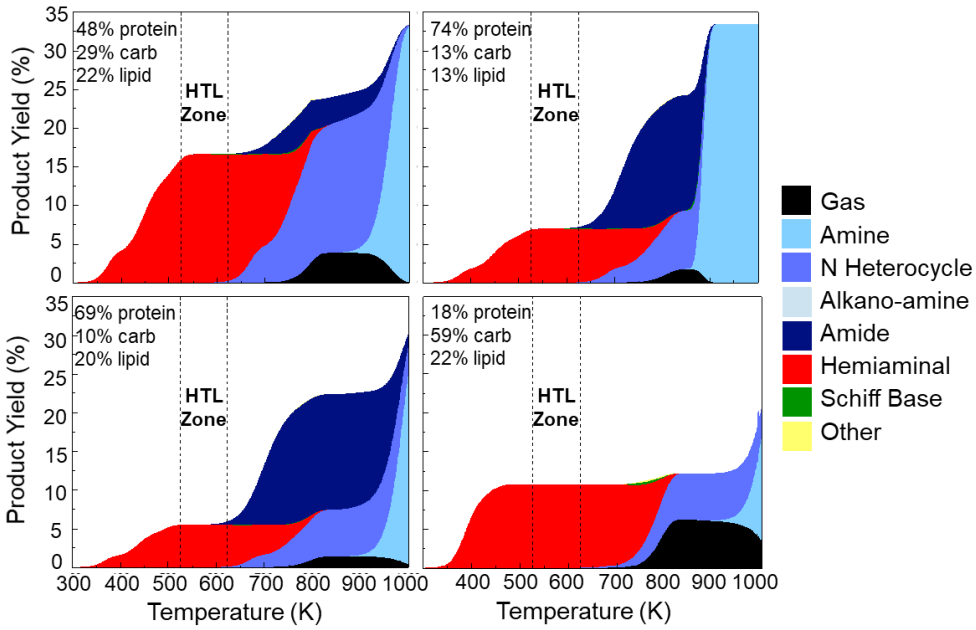

Figure 2-5. The effect of temperature on HTL intermediate product distributions for four surrogate feedstock compositions representative of food waste, and various algae streams. Shades of blue represent nitrogen containing classes identified in the GC-MS. Dashed lines indicate the temperature range for conventional HTL experiments. All models were completed at 30 min residence time for a range of 300 – 1000K discretized to 1200 points.

2.3.4 FEED COMPOSITION EFFECTS

The composition of the feed can vary from 2 – 75% protein (**Table 2-1**), which can have a substantial effect on the prevalence of nitrogen reactions and resultant product distributions. Due to this large variance, **Figure 2-6** examines the effect of feedstock composition on the concentration of four nitrogen-containing product classes (amine, hemiaminal, amide, and nitrogen heterocycles). The kinetic model was run at 600 K for 30 minutes with starting feed compositions evenly distributed between the reactants in 1% discretization. Due to the exclusion of secondary coupling reactions of intermediate products, concentrations do not continue to change (within 1%) after this time for all simulations. Product classes were grouped so as to exclude the

initial concentrations of amino acid, aldehyde, and diene. The resulting data was interpolated and presented as a heat map for the four heteroatom classes.

The amino acid, specifically glycine, is the sole reactant containing nitrogen in the model, leading to its concentration having the greatest effect on product distribution and yield. In the amine and amide classes, this trend is the clearest, where increased amino acid content directly increases resultant product concentration. The hemiaminal and nitrogen heterocycle classes, however, result in a more interesting trend that does not directly correlate with increasing amino acid concentration, indicating these molecules are the result of emergent monomeric interactions between macromolecule decomposition products. The hemiaminals (carbinolamines) are characterized by a hydroxyl and amine group attached to the same carbon, thereby opening additional pathways to formation including from aldehydes. Looking back to the reaction network, hemiaminals are products of the first reaction in Schemes 2, 3, and 4 (reactions 2.1, 3.1, and 4.1), which represents the addition of glycine with each of the starting aldehydes. It is for this reason that the highest concentration of hemiaminals occurs close to a 50:50 mixture of amino acid and aldehyde, continuing to decrease moving further away from the stoichiometric ratio.

While hemiaminal formation is relatively easy to explain, nitrogen heterocycle synthesis is more complicated. In the GC-MS analysis, HTL of food waste resulted in 36% of the volatile nitrogen species in the biocrude as heterocycles. Nitrogen heterocycles are formed in the reaction network in all schemes through a variety of pathways. Scheme 1 uses the Aza Diels Alder reaction to complete a cycloaddition of an imine (M_6), formed from the dehydrogenation of the amino acid, with butadiene (M_7). Schemes 2 – 4, however, react through the previously discussed synthesis of a hemiaminal (M_{13}, M_{19}, M_{27}) which then undergoes dehydration to produce the reactive imine (M_{14}, M_{20}, M_{28}). The Maillard reaction is responsible for nitrogen heterocycle formation in Scheme

5, wherein glycine undergoes an addition reaction with glyoxal (M_{35}, aldehyde) to form a hemiaminal (M_{36}) before dehydration to produce an imine (M_{37}). In Schemes 2 – 4, the same first three steps occur, with the addition of diene to promote nitrogen heterocycle formation. Scheme 5, on the other hand, does not include the addition of butadiene and instead allows for decarboxylation of the imine and subsequent hydrolysis and decomposition reactions leading to the formation of a Strecker aldehyde (M_{12}) and a reductive amination product. In the last stage, condensation of the two amino-carbonyl compounds results in the formation of a nitrogen heterocycle (piperazinediol, M_{43}) that can further dehydrate to pyrazine compounds (M_{44}, M_{45}). Lastly, Scheme 6 produces a nitrogen heterocycle through two subsequent dehydration and inter/intramolecular condensation reactions to form a diketopiperazine (M_{46}).

In the kinetic analysis, Scheme 1 is not predicted to contribute substantially to the observed product distribution or heterocycle formation, likely due to the high activation barrier of reaction steps 1.1, 1.3, and 1.4 coupled with their slow rate constants on the order of 10^{-50} s^{-1} or cm^3/mol*s. The rate constants of schemes 2-6 are comparable, indicating their similar reactivity and likelihood for these reactions to proceed. For this reason, Scheme 5 appears to contribute the most to heterocycle formation due to its sustained low activation barriers, assuming the energy input is suitable to proceed past reaction 5.2 ($\Delta^{\ddagger}G^{\circ}$ = 61.1kcal/mol).

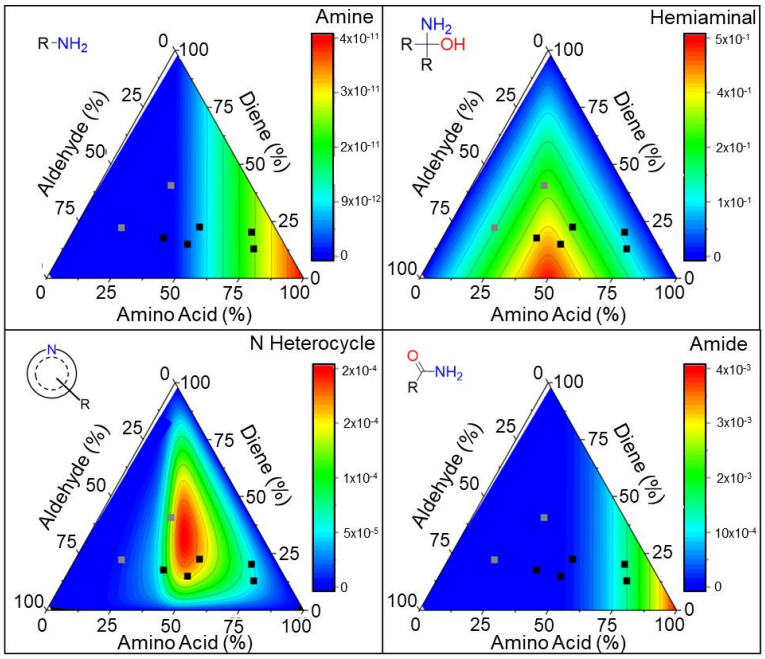

Figure 2-6. Ternary diagrams relating the product composition (color map) of four intermediate compound classes resulting from a particular starting composition defined on the ternary diagram. All data were taken interpolated from the kinetic model simulations at 600 K and 30-minute residence time. Black squares (■) represent known algae feedstock compositions and gray squares (■) are representative of food waste feedstocks where the aldehyde, amino acid and diene fractions are taken as surrogates for the carbohydrate, protein and fats, respectively. Color bar represents product concentration resulting from the kinetic model, [mol/cm^3].

To further understand the effect of feedstock composition on nitrogen heterocycle formation, real feed compositions are referenced. In **Figure 2-6**, the black squares are representative of various algae feedstocks while gray show food waste compositions, all highlighted in **Table 2-1** and **A2-5**. The comparatively low concentration of amines is primarily due to their role in the reaction scheme, wherein it is present as the reactant or as only one of the products of reaction 2.6. The lack of observed amines is indicative of their highly reactive nature in the reaction network and is consistent with GC-MS results which identified no primary amines in the product mixture (**Figure 2-2b**).

Heterocycles are the sole class of the four examined here whose concentration depends on all three primary macromolecule contents. For this reason, the center of the high intensity area appears to occur near a stoichiometric mixture of all three reactants. All five algae compositions are within the bounds of increased heterocycle production. Food waste, on the other hand, often contains low protein and high carbohydrate content, indicative of the typical American diet. Of the two food waste feedstocks explored, one occurs in a region of moderate protein concentration while the other is in an area of low protein concentration. Recall, heterocycles are highly undesired in biocrude, as it requires harsh hydrodenitrogenation (HDN) conditions to remove this nitrogen during upgrading. Elevated aromatic nitrogen has generally been observed in HTL oils from algal feeds, but lower amounts from food waste.[79, 80] This is consistent with our model findings which show that sub-stoichiometric mixtures of protein results in lower heterocycle concentration. Cheng et al. has shown through FT-ICR MS that nitrogen heterocycles are present in both high and low-lipid algae biocrude in similar concentrations.[32] *N. salina,* a high-lipid algae, has shown to produce an oil high in alkyl substituted pyrroles and indoles, whereas *G. sulphuraria* biocrudes show higher degrees of alkylation with larger double-bond equivalency (DBE) range.[32] Low-lipid food waste, on the other hand, results in indoles as the primary heterocycle- still with an overall concentration less than 1%. This is most likely due to the presence of tryptophan as a common amino acid in chicken. Overall, the feed composition can be shown to be an important factor in determining the HTL product distribution.

2.3.5 CLOSING THE GAP BETWEEN SMALL & LARGE MOLECULES

Making the connection back to experimental results, **Figure 2-7** showcases the observed trends between all nitrogen-containing heteroatom classes for both the biocrude and aqueous phases. Positive ion APPI FT-ICR MS was utilized to probe the molecular space, revealing

similarities in the carbon number and DBE relationship for both liquid phases (biocrude and aqueous) across heteroatom classes. DBE provides insight into chemical makeup by capturing the degree of unsaturation resulting from double bonds or rings, as is typically resultant from molecular condensations. All four nitrogen classes contain biocrude molecules with a DBE greater than five, indicating the presence of at least one ring structure. It can also be seen that with increasing nitrogen number, the lower DBE limit increases, indicating further formation of heterocycles, most likely via dimerization pathways. Tryptophan, with an indole side chain, has the potential to undergo the Maillard reaction to produce a molecule with two nitrogen and a DBE > 10, consistent with identified molecules in the N_2O_x heteroatom class. Dimerization of this molecule then results in a compound with DBE > 20, $>C_{30}$ and four nitrogen, also consistent with **Figure 2-7**. Notably, over 70% of all observed nitrogen-containing compounds had $<C_{40}$, suggesting that chain growth may be limited based on the availability of reactive amines and molecules larger than C_{50} begin to partition to solid products.

Further comparisons of this data to macromolecular trends can be found in **Figure A2-10**, wherein the regions of high abundance are consistent with the polymerization of common carbohydrates and fatty acids. A compelling trend emerges from this data, whereby a strong linear relationship is observed across product classes. To better understand this trend, a range of chemistries were analyzed, starting with the Maillard reaction. By considering the chemistry that occurs during the Maillard reaction, it is noted that an amine condenses with a sugar molecule to form an N-substituted glycosylamine which undergoes Amadori rearrangement (5.4) to produce an Amadori rearrangement product (ARP). This is followed by dehydration to produce furfurals and reductones, based on pH. Additionally, sugar fragmentation and Strecker degradation occur nearly simultaneously alongside the dehydration. During Strecker degradation, amino acids are

oxidized in the presence of dicarbonyl compounds to produce CO_2, aldehydes, and amino-ketones. The resultant aldehydes react with each other through aldol condensation in the final stage of the Maillard reaction. Finally, aldehydes react with amines through condensation and cyclization reactions to produce nitrogen heterocycles, including pyrroles, pyridines, and pyrazines. The Maillard reaction nets the loss of a carbon dioxide and three water molecules, with the addition of three R-NH_2 groups, effectively increasing the DBE by one (ring formation) and increasing the net carbon number by two, on average (DBE = 0.5×C). To better approximate this trend, chemistries from literature were examined[32, 47, 81] by quantifying the change in DBE upon completion of the Maillard reaction as $[(DBE)_{products} - (DBE)_{reactants}]/[(C)_{products} - (C)_{reactants}]$; after doing this, the average relationship was updated as DBE = 0.48×C, as plotted in **Figure 2-7** as a black dashed line. Previous work has identified the importance of the Maillard reaction in biocrude formation from model sugars and amino acids, citing the formation of pyrazines as well as increased production of aromatic amines and amides.[47]

A similar analysis was performed using the reaction chemistry examined in this work. Reaction pathways were weighted by product abundance and correlated to DBE to reveal a trend, DBE = 0.51×C, with the corresponding fit plotted in green in **Figure 2-7**. For comparison with experimentally observed products, the relationship is extrapolated to larger carbon numbers as the expectation is that the intermediates will couple to form the larger products in secondary reactions. Notably, this relationship holds true as the dominant trend from all three data sets: the monomeric reactions (kinetic model), the final aqueous, and the final oil products, suggesting that the Maillard reactions are a dominant coupling pathway. Furthermore, the trend underscores that for every two carbons, one DBE is introduced, suggesting that other pathways may also be involved, such as aldol condensation or cycloaddition. As can be seen in **Figure 2-7**, the resultant model products

correlate well with Maillard reaction products, consistent with the high degree of aromaticity observed in GC-MS. The trend also agrees with the identified pathways from the proposed intermediates to the highly aromatic compounds identified, indicative of aqueous phase molecules having a lower carbon number and DBE than oil molecules, with considerable overlap in their ranges. This suggests a common pathway for the formation of biocrude and water-soluble molecules, and is consistent with the understanding that at reaction temperatures, the two phases are miscible and are only phase separated and partitioned upon cooling.[9] The FT-ICR MS findings show that polymerization is scale-independent where the ring structure and intra-chain unsaturation's are maintained across small molecules in the aqueous and larger organics in the oil. Furthermore, the trend suggests a high degree of saturation, as in the monomeric species glycine, tetrahydropyridine, and N-methylmethanimine captured by this kinetic model. This serves as valuable insight into the validity of the model in accurately predicting key HTL intermediate product distributions.

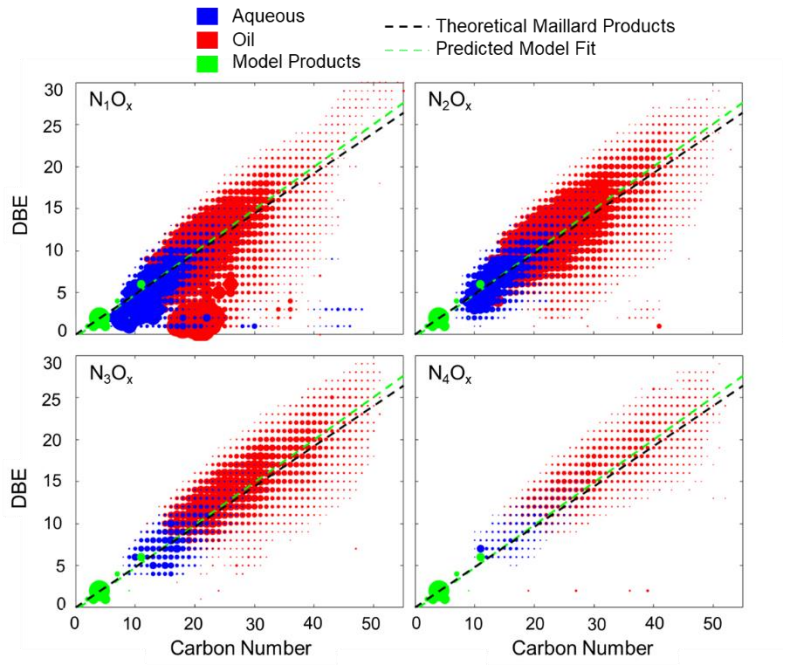

Figure 2-7. Double bond equivalency (DBE) versus carbon number for four nitrogen-containing heteroatom classes in the biocrude oil (red) and aqueous (blue) phases on food waste HTL at 575 K for 30 minutes. The green dots represented the products from the kinetic model (18% glycine, 22% diene, and 59% aldehyde split evenly between the four starting aldehydes). Model feedstock concentration was chosen to match that of the food waste HTL experiments. Experimental data points are sized by relative abundance and model points by relative concentration. The black dashed line represents the average trend for Maillard reaction products where the green line is the weighted average fit observed for products in the kinetic model.

To assess model robustness, a sensitivity analysis was performed to measure the effect of a 1% perturbation in rate constants on individual product yields. **Figure A2-11** reports these results, indicating the overall sensitivity of the competitive reactions 2.1, 3.1, 4.1, and 5.1 on overall product distribution and yields. The analysis highlights the competitiveness of the initial amine-oxygenate reactions and suggests that no single aldehyde functionality is solely responsible for the coupling reactions. Further discussion can be found in Appendix A.

Water also plays an integral role in the hydrothermal processing and chemical transformations examined in this study. In addition to being a reactant or product in 10 of the 38

reaction pathways examined, its ability to solvate the reaction species can play a potentially significant role in the reaction energetics and kinetics. The sensitivity analysis (**Figure A2-11**) confirms that water is in excess in the system and its final amount does not depend on the reaction rates ($\sigma_{ij} = 0$ for all instances of *i*=water). Future work should attempt to resolve the specific role of water as a solvent in these key reaction pathways. In this study, all activity coefficients are assumed to be unity, indicating that non-ideal solvent interactions have been neglected. It has been shown that under supercritical conditions (675 K, 275 bar) the activity coefficient of water decreases to 0.5, thereby reducing the corresponding reaction rates by a factor of two.[82] While typical HTL reaction conditions are nearly 375 K and 75 bar below the explored supercritical conditions, the activity of water at these conditions remains relevant in improving the accuracy of the model.

The model pathways presented in this work are representative of elementary reactions that occur in the condensed phase chemistry during food waste HTL. As revealed by FT-ICR-MS, however, tens of thousands of unique species are detected across a wide molecular weight distributions ranging from light oxygenates to non-volatile hydrochars. Future work should 1) continue to explore elementary pathways with a larger breadth of functionality and sizes, 2) introduce solvent interactions to improve computational energetic calculation accuracy in the hydrothermal environment, and 3) consider the transient environmental changes in reaction environment due to primary (biopolymer degradation) and tertiary (polymerization) reactions.

2.4 CONCLUSIONS

Experimental analysis of food waste HTL products has revealed the presence of organic nitrogen in the form of fatty amides, indoles, and amines. Particularly notable is the prevalence of

nitrogen-containing heterocyclic aromatics, the removal of which by conventional hydrodenitrogenation is difficult but necessary to hit fuel quality standards and avoid NO_x emissions. A detailed kinetic mechanism was proposed using model compounds representative of typical HTL feedstock monomers; subsequent DFT calculations and kinetic models were used to evaluate likely reaction pathways. The analysis revealed the Maillard reaction as a likely source of nitrogen heterocycle formation at HTL reaction conditions. FT-ICR MS characterization and analysis further supported this conclusion, revealing strong correlations between theoretical Maillard reaction products, experimentally measured HTL reaction products, and the model-predicted products.

These analyses serve to illuminate dominant chemistries and kinetic pathways by examining the activity of the highly reactive short chain intermediates that typically react on the order of seconds in HTL reactors. Substantial energetic barriers were shown to exist in deamination and cyclization reactions, whereas condensation and ADA pathways experienced relatively low activation barriers, due to the relative stability of the transition states. This led to nitrogen heterocycles and gaseous nitrogen only being observed at higher temperatures; hemiaminals are the dominant product at lower temperatures. Strong compositional effects were observed in the formation of nitrogen heterocycles, which required stoichiometric amounts of amine, aldehyde, and diene. Sub-stoichiometric amounts of diene promoted production of hemiaminal and amide products, which is consistent with known hydrothermal products resulting from low lipid feedstocks. The predicted model trends correlated well with the experimentally observed product distributions from food waste HTL, with the FT-ICR MS showing final liquid products — dimer- and trimerization of amino acids, carbohydrate hydrolysis products, and fats — consistent with the Maillard reactions observed in the kinetic model. Ultimately, imines and aldehydes have been

shown to be key classes in the proposed model, further showcasing its importance and accuracy in predicting HTL nitrogen intermediates. Future model expansions should consider the secondary reactions between the intermediates toward the formation of larger final products and the inclusion of solvent effects. Based on this work, the thermal barriers to deamination are revealed to be substantial kinetic limitations, so catalytic promotion of those pathways may be necessary to overcome large activation energetics.

2.5 APPENDIX A

2.5.1 $\Delta^{\ddagger}G^{\circ}$ CALCULATION

The free energy barrier of the transition state ($\Delta^{\ddagger}G^{\circ}$) uses the parameters from the modified Arrhenius expression $k = A\left(\frac{T}{1K}\right)^{n} \exp\left(-\frac{Ea}{RT}\right)$ and the Eyring equation for transition state theory $k = \kappa\frac{k_b}{h}T \exp\left(-\frac{\Delta^{\ddagger}G^{\circ}}{RT}\right)c^{1-m}$ where c is the standard concentration, or 1 bar / RT with standard state of 1 bar. From the Eyring equation, a transmission coefficient κ of one is assumed, and the Gibbs Free Energy of activation is derived: $\Delta^{\ddagger}G^{\circ} = -RT\ln\left(k\left(\frac{1\ bar}{RT}\right)^{m-1}\frac{h}{k_bT}\right)$. Afterwards, the rate coefficient was evaluated and $\Delta^{\ddagger}G^{\circ}$ was calculated at the desired temperature (600 K).

2.5.2 GC-MS

Biocrude samples were dissolved in acetone at a ratio of 3 mg/mL for analysis with gas chromatography. The GC-MS consisted of a GC-2010 Plus gas chromatograph coupled with a QP2010 SE mass spectrometer and an AOC-20i autoinjector (Shimadzu Co., Kyoto, Japan). The column used was an SHRXI-5MS (30 m × 0.25 mm ID × 0.5 μm film thickness) (Restek Co., Bellefonte, PA), run with an injection temperature of 290 °C and an ion source temperature of 260

°C. 3 µL of sample was injected into the GC-MS in split mode (25:1) with a constant flow of helium carrier gas (3.0 mL/min).

The temperature program was set to start at 30 °C for 4 minutes followed by heating at 3 °C/min to 290 °C and held for 5 min. The mass spectrometer was operated in ionization energy in m/z 35 – 500 scan range. Chromatogram peaks were then evaluated using the GCsolution station (Shimadzu Co., Kyoto, Japan). Peak identities were compared with the NIST Mass Spectral Database (NIST11) with all peaks having a confidence greater than 85%.

2.5.3 (+) APPI FT-ICR MS AT 9.4 TESLA

Biocrude and aqueous samples were dissolved to a final concentration of 125 µg/mL in toluene for analysis via (+) APPI FT-ICR MS at a flow rate of 50 µL/min. Toluene increases the ionization efficiency for nonpolar aromatic compounds through dopant-assisted APPI[83, 84] through charge exchange,[85, 86] and proton transfer[87] reactions between ionized toluene molecules and neutral analyte molecules as previously reported. An atmospheric pressure photoionization (APPI) source (Thermo-Fisher Scientific, San Jose, CA) was coupled to the first stage of a custom-built FT-ICR mass spectrometer (see below) through a custom-built interface.[88] The tube lens was set to 50 V (to minimize ion fragmentation) and heated metal capillary current was 4.5 A. A Hamilton gastight syringe (5.0 mL) and syringe pump were used to deliver the sample (50 µL/min) to the heated vaporizer region (350 °C) of the APPI source, where N_2 sheath gas (50 psi) facilitates nebulization. After nebulization, gas-phase neutral analyte molecules exit the heated vaporizer region as a confined jet. A krypton vacuum ultraviolet gas discharge lamp (Syagen Technology, Inc., Tustin, CA) produces 10 −10.2 eV photons (120 nm).

All samples were analyzed with a custom-built FT-ICR mass spectrometer[54] equipped with a 22 cm horizontal room temperature bore 9.4 T superconducting solenoid magnet (Oxford

Instruments, Abingdon, U.K.), and a modular ICR data station (Predator)[31] facilitated instrument control, data acquisition, and data analysis. Positive ions generated at atmospheric pressure enter the skimmer region (~2 Torr) through a heated metal capillary, pass through the first radiofrequency (rf)-only octopole, pass through an rf-only quadrupole, and are externally accumulated[89] (25−50 ms) in a second octopole equipped with tilted wire extraction electrodes for improved ion extraction and transmission.[90] Helium gas introduced during accumulation cools ions upon collision prior to transfer through rf-only quadrupoles (total length 127 cm) (into a 7-segment open cylindrical cell with capacitively coupled excitation electrodes based on the Tolmachev configuration.[91, 92] 100 individual transients of 6.8 s duration were signal averaged. The data was collected at the maximum memory depth of the data station hardware (16 million samples), apodized with a single sided Hanning apodization, zero-filled to 16 megasample (16777216 samples or 224). An additional zero fill brings the preFT data packet to 32 megasample, which in turn is processed via absorption-mode FT analysis.[93, 94] Experimentally measured masses were converted from the International Union of Pure and Applied Chemistry (IUPAC) mass scale to the Kendrick mass scale[95] for rapid identification of homologous series for each heteroatom class (i.e., species with the same $C_cH_hN_nO_oS_s$ content, differing only be degree of alkylation)[96]

For each elemental composition, $C_cH_hN_nO_oS_s$, the heteroatom class, type, double bond equivalents, (DBE = number of rings plus double bonds to carbon, DBE = C − h/2 + n/2 + 1),[97] and carbon number, c, were tabulated for subsequent generation of heteroatom class relative abundance distributions and graphical relative-abundance weighted DBE versus carbon number images. Peaks with signal magnitude greater than 6 times the baseline root-mean- square noise at m/z 500 were exported to peak lists, internally calibrated based on the "walking calibration"[98] and molecular formula assignments and data visualization were performed with PetroOrg software[99]

Molecular formula assignments with an error >0.5 ppm were discarded, and only chemical classes with a combined relative abundance of ≥0.15% of the total were considered. For all mass spectra, the achieved spectral resolving power approached the theoretical limit over the entire mass range: for example, average resolving power, $m/\Delta_{m50\%,}$ in which $\Delta m_{50\%}$ is mass spectral peak full width at half-maximum peak height, was ∼1 000 000−1 500 000 at m/z 500.

2.5.4 SENSITIVITY ANALYSIS

Sensitivity calculations were completed in MatLab, using the equations shown below. The change in rate constant (k) was evaluated for a 1% perturbation, which was then fed back into the original kinetic model to solve for the new product distribution and resultant concentrations. Sensitivity was plotted for each individual species and reaction, wherein

$$\Delta k = k_i - k_{i-1}$$

$$\Delta C = C_i - C_{i-1}$$

$$Z_{ij} \cong \frac{\Delta C_i}{\Delta k_j}$$

$$\sigma_{ij} = \frac{k_j}{C_i} Z$$

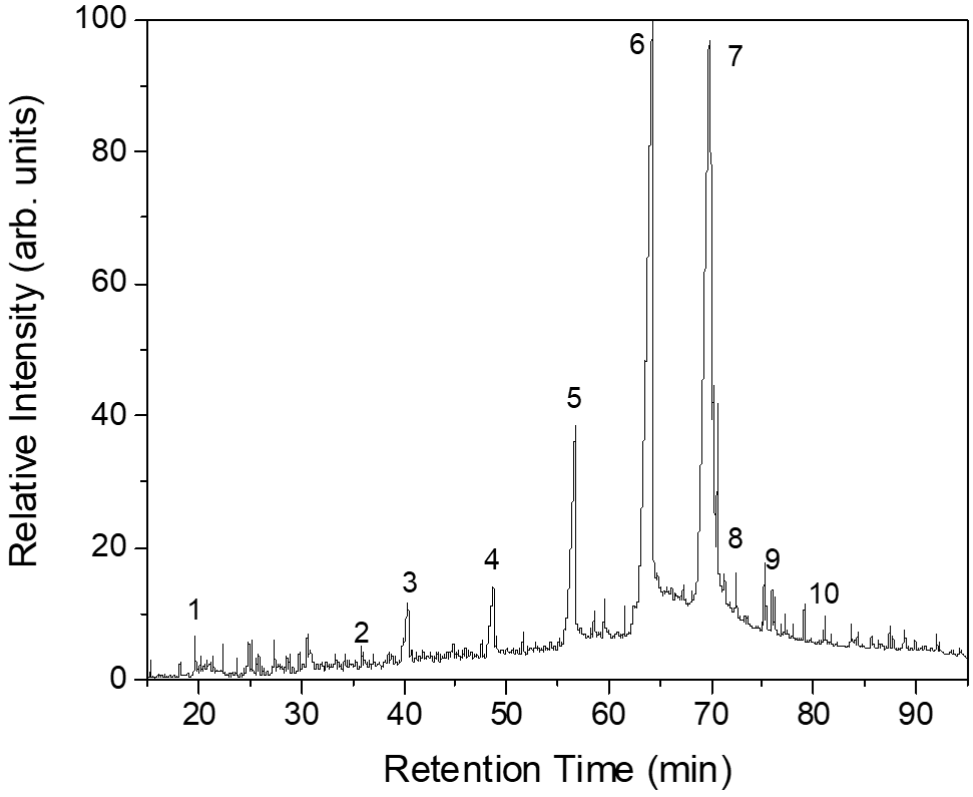

Figure A2-8. GC-MS chromatogram for food waste HTL oil. Hydrothermal liquefaction was performed at 15 w% organics loading at 300 °C for 1 h. Labeled peaks are as follows: (1) 2,3,4-Trimethylpyrrole, (2) Indole, (3) n-Decanoic acid, (4) Dodecanoic acid, (5) Tetradecanoic acid, (6) Hexadecanoic acid, (7) Octadecanoic acid (8) Octadecanamide, (9) N-Methyldodecanamide, (10) 1-(1-ocxooctadecyl) pyrrolidine.

2.5.5 GC×GC-HRT METHOD

GC×GC-HRT chromatographic analysis was performed on a LECO Pegasus GC×GCHRT 4D system consisting of an Agilent 7890B GC configured with a LECO LPAL3 split/splitless auto-injector system and a dual stage cryogenic modulator (LECO, Saint Joseph, Michigan).1 Samples were injected in splitless mode. The cold jet gas was dry N2 chilled with liquid N2. The hot jet temperature offset was 15 °C above the temperature of the main GC oven and the inlet temperature was isothermal at 310 °C. Two capillary GC columns were utilized in this GC×GC experiment. The first-dimension column was an SGE BPX-50, (60-m length, 0.25 mm I.D., 0.25

μm df) and second-dimension separations were performed on an SGE BPX-50 (2-m length, 0.25 mm I.D., 0.25 μm df). The temperature program of the main oven was held isothermal at 80 °C (12.5 min) and was then ramped from 80 to 330 °C at 1.25 °C min^{-1}. The hot jet pulse width was 2 seconds with a modulation period of 8 seconds. The second-dimension oven was held isothermal at 85 °C (12.5 min) and was then ramped from 85 to 335 °C at 1.25 °C min^{-1}. The carrier gas was helium at a flow rate of 1 mL min^{-1}. Mass resolution was +/- 0.0005 amu. HR-TOF data was sampled at an acquisition rate of 200 spectra per second (actual data collection rate was 187.5 spectra per second) in the mass range of 40 to 700 amu. The ionization method was EI with an Electron Energy of -70 Volts and the Extraction Frequency was 1.5 kHz.

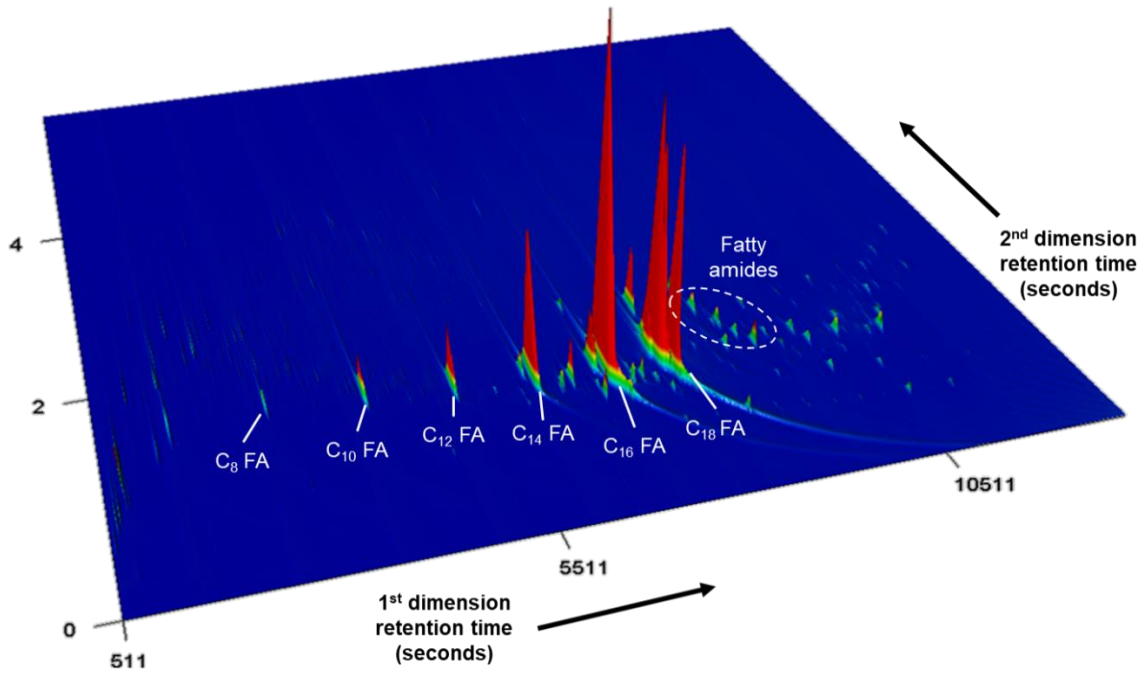

Figure A2-9. GC×GC-HRT selected ion mountain plot chromatogram from food waste HTL. The primary products identified are C_8 – C_{18} fatty acids. A group of fatty amides is also present in moderate abundance.

Table A2-3. Chemical name for all identified reactants and products in the kinetic model studied.

	Chemical Name	Schemes	Species Class
M1	glycine	1, 2, 3, 4, 5, 6	Amino Acid
M2	hydrogen	1	Gas
M3	water	1, 2, 3, 4, 5, 6	Water
M4	ammonia	1	Gas
M5	carbon dioxide	1, 2, 3, 5	Gas
M6	2-iminoacetic acid	1	Imine
M7	buta-1,3-diene	1, 2, 3, 4	Diene
M8	2-hydroacetic acid	1	Hydroxy-acid
M9	acetic acid	1	Carboxylic acid
M10	methanamine	1, 2	Amine
M11	1,2,3,6-tetrahydropyridine-2-carboxylic acid	1	N-heterocycle
M12	formaldehyde	2, 3	Aldehyde
M13	(hydroxymethyl)glycine	2	Hemiaminal
M14	2-(methyleneamino) acetic acid	2	Schiff base
M15	2-(3,6-dihydropyridin-1(2H)-yl) acetic acid	2	N-heterocycle
M16	N- methylmethanimine	2	Schiff base
M17	(methylamino) methanol	2	Alkanolamine
M18	furfural	3	Aldehyde
M19	(furan-2-yl(hydroxy)methyl) glycine	3	Hemiaminal
M20	(Z)-2-((furan-2- ylmethylene)amino)acetic acid	3	Schiff base
M21	2-(2-(furan-2-yl)-3,6- dihydropyridin-1(2H)-yl) acetic acid	3	N-heterocycle
M22	(Z)-1-(furan-2-yl)-Nmethylmethanimine	3	Schiff base
M23	N-(furan-2-ylmethyl)methanimine	3	Schiff base
M24	((furan-2-ylmethyl)amino)methanol	3	Alkanolamine
M25	furan-2-ylmethanamine	3	Amine
M26	(S)-2,3-dihydroxypropanal; glyceraldehyde	4	Aldehyde
M27	((2S)-1,2,3-trihydroxypropyl)glycine	4	Hemiaminal
M28	(R,Z)-2-((2,3- dihydroxypropylidene)amino)acetic acid	4	Schiff base
M29	2-(2-((R)-1,2-dihydroxyethyl)-3,6-dihydropyridin-1(2H)-yl)acetic acid	4	N-heterocycle
M30	(Z)-(2,3-dihydroxyprop-1-en-1- yl)glycine	4	Enamine
M31	(3-hydroxy-2-oxopropyl)glycine	4	Amadori
M32	(Z)-(2,3-dihydroxyallyl)glycine	4	Enediol
M33	2-hydroxyacrylaldehyde	4	Aldehyde
M34	2-oxopropanal; pyruvaldehyde	4	Dicarbonyl
M35	oxalaldehyde; glyoxal	5	Aldehyde
M36	(1-hydroxy-2-oxoethyl)glycine	5	Hemiaminal
M37	(Z)-2-((2-oxoethylidene)amino)acetic acid	5	Schiff base
M38	(Z)-2-(methyleneamino)ethen-1-ol	5	Schiff base
M39	2-(methyleneamino)acetaldehyde	5	Amino-aldehyde

M40	2-((hydroxymethyl)amino)acetaldehyde	5	Amino-aldehyde
M41	2-aminoacetaldehyde	5	Amino-aldehyde
M42	2-((2-amino-1- hydroxyethyl)amino)acetaldehyde	5	Amino-aldehyde
M43	piperazine-2,5-diol	5	N-heterocycle
M44	1,2,3,6-tetrahydropyrazin-2-ol	5	N-heterocycle
M45	2,5-dihydropyrazine	5	N-heterocycle
M46	glycylglycine	6	Amide
M47	piperazine-2,5-dione	6	N-heterocycle

Table A2-4. Summary of all reactions, rate expression (mol/cm^3/s), Gibbs energy of activation at 600 K, and chemical class.

Rxn #	Reaction	r_j	ΔG_{ts} (kcal/mol)	Class*
Scheme 1				
1.1	M_1 --> M_2 + M_6	$k_j[M_1]$	107.24	Degradation
1.2	M_6 + M_7 --> M_{11}	k_j $[M_6][M_7]$	45.80	ADA*
1.3	M_1 + M_3 --> M_4 + M_8	k_j $[M_3][M_1]$	106.93	Deamination*
1.4	M_1 + M_2 --> M_4 + M_9	k_j $[M_1][M_2]$	108.83	Deamination*
1.5	M_1 --> M_5 + M_{10}	k_j $[M_1]$	73.5	Decarboxylation*
Scheme 2				
2.1	M_1 + M_{12} --> M_{13}	$k_j[M_1][M_{12}]$	49.23	Combination
2.2	M_{13} --> M_3 + M_{14}	k_j $[M_{13}]$	57.44	Dehydration
2.3	M_{14} + M_7 --> M_{15}	$k_j[M_{14}][M_7]$	52.32	ADA*
2.4	M_{14} --> M_5 + M_{16}	k_j $[M_{14}]$	70.44	Decarboxylation*
2.5	M_{16} + M_3 --> M_{17}	k_j $[M_{16}][M_3]$	63.70	H20 addition
2.6	M_{17} --> M_{12} + M_{10}	k_j $[M_{17}]$	39.66	Degradation
Scheme 3				
3.1	M_1 + M_{18} --> M_{19}	$k_j[M_1][M_{18}]$	51.90	Combination

3.2	M_{19} --> M_{20} + M_3	$k_j[M_{19}]$	51.04	Dehydration
3.3	M_{20} + M_7 --> M_{21}	$k_j[M_{20}][M_7]$	55.74	ADA*
3.4	M_{20} --> M_5 + M_{22}	$k_j[M_{20}]$	71.24	Decarboxylation*
3.5	M_{22} --> M_{23}	k_j $[M_{22}]$	77.44	Rearrangement
3.6	M_{23} + M_3 --> M_{24}	$k_j[M_{23}][M_3]$	65.73	H2O addition
3.7	M_{24} --> M_{12} + M_{25}	$k_j[M_{24}]$	38.39	remove CH2O
Scheme 4				
4.1	M_1 + M_{26} --> M_{27}	$k_j[M_1][M_{26}]$	48.94	Combination
4.2	M_{27} --> M_3 + M_{28}	$k_j[M_{27}]$	55.71	Dehydration
4.3	M_{28} + M_7 --> M_{29}	$k_j[M_{28}][M_7]$	50.15	ADA*
4.4	M_{28} --> M_{30}	$k_j[M_{28}]$	59.48	Rearrangement
4.5	M_{30} --> M_{31}	$k_j[M_{30}]$	68.95	Rearrangement
4.6	M_{31} --> M_{32}	$k_j[M_{31}]$	64.13	Rearrangement
4.7	M_{32} --> M_1 + M_{33}	$k_j[M_{32}]$	29.60	Degradation
4.8	M_{33} --> M_{34}	$k_j[M_{33}]$	64.30	Rearrangement
Scheme 5				
5.1	M_1 + M_{35} --> M_{36}	$k_j[M_1][M_{35}]$	45.35	Combination
5.2	M_{36} --> M_3 + M_{37}	$k_j[M_{36}]$	61.14	Dehydration
5.3	M_{37} --> M_5 + M_{38}	$k_j[M_{37}]$	37.40	Decarboxylation
5.4	M_{38} --> M_{39}	$k_j[M_{38}]$	55.62	H2O addition
5.5	M_{39} + M_3 --> M_{40}	$k_j[M_{39}][M_3]$	65.57	Decomposition
5.6	M_{40} --> M_{41} + M_{12}	$k_j[M_{40}]$	40.26	Addition
5.7	2M_{41} --> M_{42}	$k_j[M_{41}][M_{41}]$	53.65	Rearrangement
5.8	M_{42} --> M_{43}	$k_j[M_{42}]$	40.79	Dehydration
5.9	M_{43} --> M_{44} + M_3	$k_j[M_{43}]$	50.58	Dehydration
5.10	M_{44} --> M_{45} + M_3	$k_j[M_{44}]$	-0.21	Dehydration
Scheme 6				
6.1	2M_1 --> M_{46}	k_j[M1][M1]	64.35	Coupling
6.2	M_{46} --> M_{47} + M_3	k_j[M46]	71.74	Condensation*

*Indicates primary reaction mechanism corresponding to colors in Figure 4.

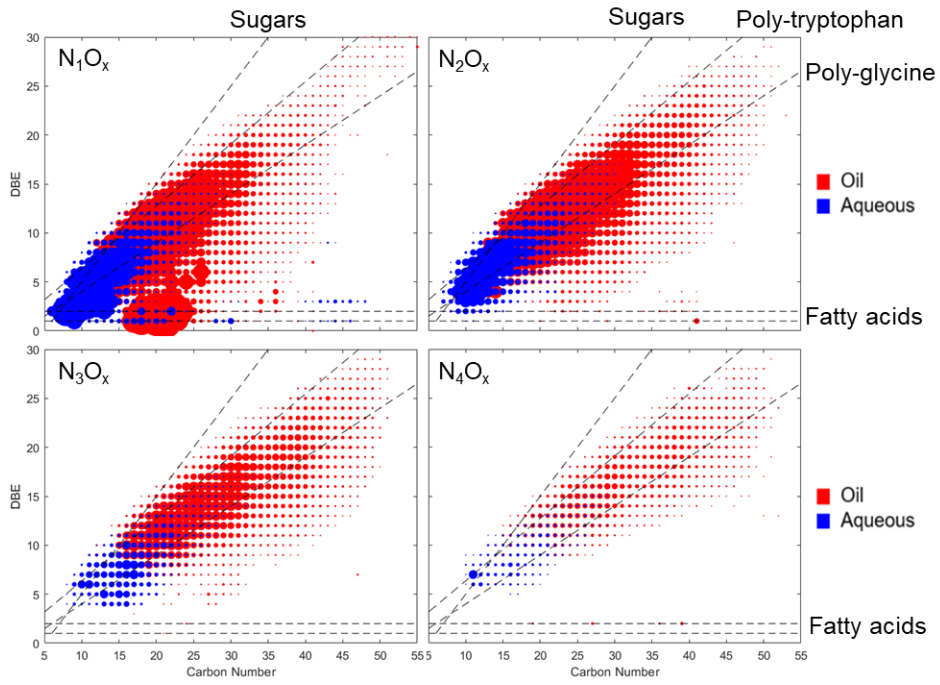

Figure A2-10. Double bond equivalency (DBE) dependance on carbon number for four primary nitrogen classes seen in food waste HTL products including predictive lines representing sugar, fatty acid, and two poly-amino acids. Datapoints sized by relative abundance.

For the biocrude phase, FT-MS reveals the average empirical formula as $C_{29}H_{36}N_2O_3$ and $C_{12}H_{17}NO_2$ for the aqueous phase, a difference solely in carbon number. This is in comparison to elemental analysis which predicts an oil-phase empirical formula of $C_{21}H_{31}NO_4$. The effect can be further observed by comparing the molecular distributions in each phase. FT-MS predicts a CHONS molecular formula and relative abundance for each molecule detected, which allows a DBE to be calculated. ($DBE = C - \frac{H}{2} + \frac{N}{2} + 1$). Utilizing this formula, **Figure A2-10** showcases the linearity that exists between carbon number and DBE for both oil and aqueous phases among heteroatom classes. The relationship demonstrates a continuum across the two product fractions showing how lower carbon number molecules, with a lower DBE, tend to partition to the aqueous phase, while molecules of a larger carbon number and DBE are found in the oil phase.

Additionally, the presence of the dashed lines bound the product distribution by showing the feed ratios from saturated and unsaturated fatty acids, as well as sugar dimers. In the N_1O_x class, the intense region centered around C_{20} at DBE < 5 is representative of a high abundance of fatty acid amides in the oil phase. It can also be seen that a small amount of these molecules were also found in the aqueous phase, potentially indicating incomplete phase separation due to equilibrium, as these compounds typically have a partition coefficient <5. The presence of fatty acid amides arises from the reaction of fatty acids from the hydrolysis of triglycerides with amines from protein degradation.[100]

The size of the points in **Figure A2-10** directly correspond to their relative abundance, indicating a higher overall abundance in the N_1O_x and N_2O_x classes compared to the N_3O_x and N_4O_x classes. A shift can also be seen in the location of the high abundance compounds in each class, wherein the N_1O_x class begins near C_5, DBE = 1 and the N_4O_x class does not show molecules until above C_{10}, DBE = 5 therefore indicating dimerization to high molecular weight nitrogen heterocycles. The apparent linear trend of the response data falls between that of the sugar molecules and the fatty acids. The presence of nitrogen across classes results in a slope of approximately 0.5, indicating that for every one carbon that is added, the DBE increases by 0.5, resulting from the addition of one hydrogen, no nitrogen, and up to two oxygen.

Table A2-5. Protein, lipid, and carbohydrate content for various algae strains and food waste sources references in this study.

	Protein	Lipid	Carbohydrate	Source
Berbesia m.	22	10	27	Neveux et al.
Nannochloropsis	46	15	36	Neveux et al.
Tetraselmas*	74	13	13	Neveux et al.
Pavlova*	48	22	29	Neveux et al.
Nannochloropsis*	69	20	10	Neveux et al.
Food Waste*	18	22	59	Cheng et al.
Food Waste	32	38	30	This work

*indicates conditions used in Figure 2.5

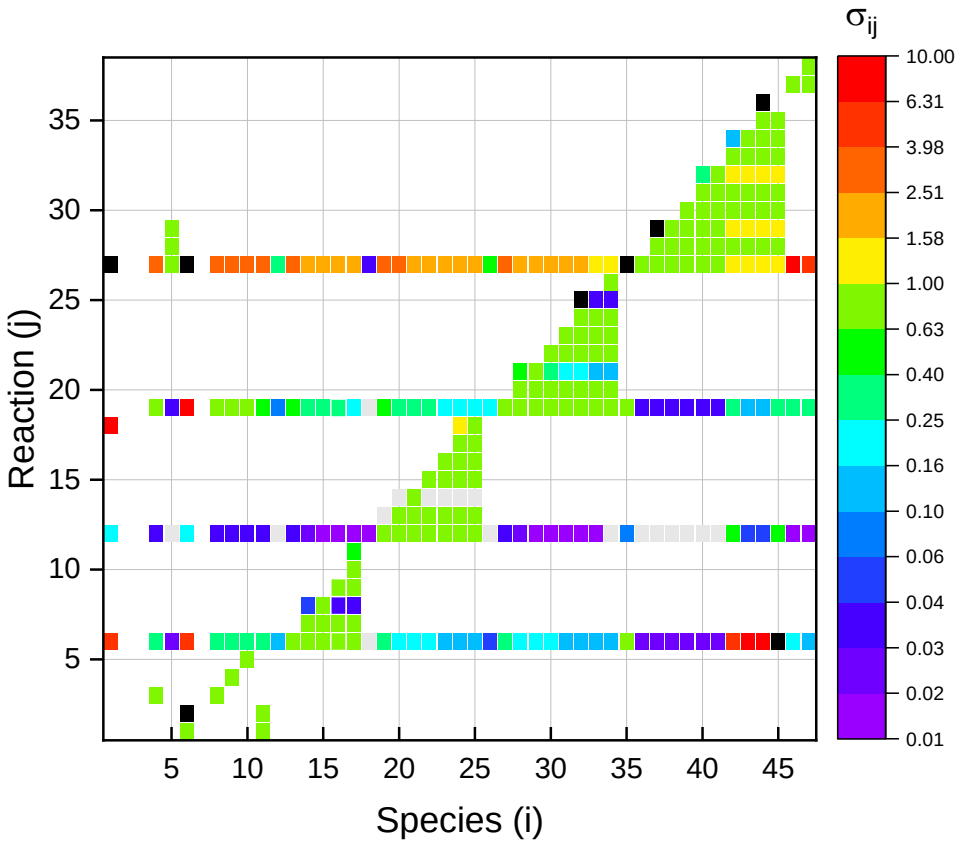

Figure A2-11. Heatmap showing the average sensitivity of each k value for each species identified in the reaction network. Sensitivity is calculated as an average value across the entire 30 minute reaction window range. Sigma is plotted on a log base 10 scale.

Sensitivity allows for identification of potential model limitations. Analysis of Figure A4 reveals four horizontal lines occurring on reactions 2.1, 3.1, 4.1, and 5.1. This artifact is due to the location of these reactions in the network. Each of these reactions has glycine as a primary reactant, meaning that they are in direct competition with one another. A slight change in the rate of one of these four reactions has the potential to alter the entire product distribution by shifting favorability from one scheme to another. Of these key reactions, scheme 5- the Maillard reaction- appears to result in the highest sensitivity across species. A change in reaction 5.1's reaction rate causes the biggest shift in product distribution, causing an even larger fraction of glycine to proceed through the Maillard reaction.

2.6 REFERENCES

1. Chen, W.-T.; Haque, M. A.; Lu, T.; Aierzhati, A.; Reimonn, G., A perspective on hydrothermal processing of sewage sludge. *Current Opinion in Environmental Science & Health* **2020,** *14*, 63-73.

2. Elliott, D. C.; Biller, P.; Ross, A. B.; Schmidt, A. J.; Jones, S. B., Hydrothermal liquefaction of biomass: Developments from batch to continuous process. *Bioresource Technology* **2015,** *178*, 147-156.

3. Gollakota, A. R. K.; Kishore, N.; Gu, S., A review on hydrothermal liquefaction of biomass. *Renewable and Sustainable Energy Reviews* **2018,** *81*, 1378-1392.

4. Guo, Y.; Song, W.; Lu, J.; Ma, Q.; Xu, D.; Wang, S., Hydrothermal liquefaction of Cyanophyta: Evaluation of potential bio-crude oil production and component analysis. *Algal Research* **2015,** *11*, 242-247.

5. Hu, H.-S.; Wu, Y.-L.; Yang, M.-D., Fractionation of bio-oil produced from hydrothermal liquefaction of microalgae by liquid-liquid extraction. *Biomass and Bioenergy* **2018,** *108*, 487-500.

6. Neveux, N.; Yuen, A. K.; Jazrawi, C.; Magnusson, M.; Haynes, B. S.; Masters, A. F.; Montoya, A.; Paul, N. A.; Maschmeyer, T.; de Nys, R., Biocrude yield and productivity from the hydrothermal liquefaction of marine and freshwater green macroalgae. (1873-2976 (Electronic)).

7. Rowbotham, J. S.; Dyer, P. W.; Greenwell, H. C.; Theodorou, M. K., Thermochemical processing of macroalgae: a late bloomer in the development of third-generation biofuels? *Biofuels* **2012,** *3* (4), 441-461.

8. Sheehan, J. D.; Savage, P. E., Modeling the effects of microalga biochemical content on the kinetics and biocrude yields from hydrothermal liquefaction. *Bioresource Technology* **2017,** *239*, 144-150.

9. Cheng, F.; Tompsett, G. A.; Murphy, C. M.; Maag, A. R.; Carabillo, N.; Bailey, M.; Hemingway, J. J.; Romo, C. I.; Paulsen, A. D.; Yelvington, P. E.; Timko, M. T., Synergistic Effects of Inexpensive Mixed Metal Oxides for Catalytic Hydrothermal Liquefaction of Food Wastes. *ACS Sustainable Chemistry & Engineering* **2020,** *8* (17), 6877-6886.

10. LJ Snowden-Swan, Y. Z., SB Jones, DC Elliot, AJ Schmidt, RT Hallen, JM Billing, TR Hart, SP Fox, GD Maupin, Hydrothermal Liquefaction and Upgrading of Municipal Wastewater Treatment Plant Sludge: A Preliminary Techno-Economic Analysis. Energy, D. o., Ed. 2016.

11. Maag, A. R.; Paulsen, A. D.; Amundsen, T. J.; Yelvington, P. E.; Tompsett, G. A.; Timko, M. T., Catalytic Hydrothermal Liquefaction of Food Waste Using CeZrOx. *Energies* **2018,** *11* (3).

12. U.S. Environmental Protection Agency, U.S. Food Waste Statistics.

13. U.S. Environmental Protection Agency, U.S Waste Fact Sheet.

14. U.S. Environmental Protection Agency, Clean Cities Alternative Fuel Price Report.

15. Badgett, A.; Newes, E.; Milbrandt, A., Economic analysis of wet waste-to-energy resources in the United States. *Energy* **2019,** *176*, 224-234.

16. Li, H.; Liu, Z.; Zhang, Y.; Li, B.; Lu, H.; Duan, N.; Liu, M.; Zhu, Z.; Si, B., Conversion efficiency and oil quality of low-lipid high-protein and high-lipid low-protein microalgae via hydrothermal liquefaction. *Bioresource Technology* **2014,** *154*, 322-329.

17. Quinkenstein, A.; Pape, D.; Freese, D.; Schneider, B. U.; Hüttl, R. F., Biomass, Carbon and Nitrogen Distribution in Living Woody Plant Parts of Robinia pseudoacacia L. Growing on Reclamation Sites in the Mining Region of Lower Lusatia (Northeast Germany). *International Journal of Forestry Research* **2012,** *2012*, 891798.

18. Lu, J.; Zhang, J.; Zhu, Z.; Zhang, Y.; Zhao, Y.; Li, R.; Watson, J.; Li, B.; Liu, Z., Simultaneous production of biocrude oil and recovery of nutrients and metals from human feces via hydrothermal liquefaction. *Energy Conversion and Management* **2017,** *134*, 340-346.

19. Li, W.; Zhao, Y.; Yao, C.; Lu, J.; Li, R.; Wu, Y., Migration and transformation of nitrogen during hydrothermal liquefaction of penicillin sludge. *The Journal of Supercritical Fluids* **2020,** *157*, 104714.

20. Wang, F.; Tian, Y.; Zhang, C.-C.; Xu, Y.-P.; Duan, P.-G., Hydrotreatment of bio-oil distillates produced from pyrolysis and hydrothermal liquefaction of duckweed: A comparison study. *Science of The Total Environment* **2018,** *636*, 953-962.

21. Wang, T.; Zhai, Y.; Zhu, Y.; Peng, C.; Xu, B.; Wang, T.; Li, C.; Zeng, G., Influence of temperature on nitrogen fate during hydrothermal carbonization of food waste. *Bioresource Technology* **2018,** *247*, 182-189.

22. Jensen, C. U.; Rosendahl, L. A.; Olofsson, G., Impact of nitrogenous alkaline agent on continuous HTL of lignocellulosic biomass and biocrude upgrading. *Fuel Processing Technology* **2017,** *159*, 376-385.

23. Anderson, E. M.; Stone, M. L.; Katahira, R.; Reed, M.; Muchero, W.; Ramirez, K. J.; Beckham, G. T.; Román-Leshkov, Y., Differences in S/G ratio in natural poplar variants do not predict catalytic depolymerization monomer yields. *Nature Communications* **2019,** *10* (1), 2033.

24. Brandner, D. G.; Kruger, J. S.; Thornburg, N. E.; Facas, G. G.; Kenny, J. K.; Dreiling, R. J.; Morais, A. R. C.; Renders, T.; Cleveland, N. S.; Happs, R. M.; Katahira, R.; Vinzant, T. B.; Wilcox, D. G.; Román-Leshkov, Y.; Beckham, G. T., Flow-through solvolysis enables production of native-like lignin from biomass. *Green Chemistry* **2021,** *23* (15), 5437-5441.

25. Mettler, M. S.; Mushrif, S. H.; Paulsen, A. D.; Javadekar, A. D.; Vlachos, D. G.; Dauenhauer, P. J., Revealing pyrolysis chemistry for biofuels production: Conversion of cellulose to furans and small oxygenates. *Energy & Environmental Science* **2012,** *5* (1), 5414-5424.

26. Duan, P.; Savage, P. E., Hydrothermal Liquefaction of a Microalga with Heterogeneous Catalysts. *Industrial & Engineering Chemistry Research* **2011,** *50* (1), 52-61.

27. Gollakota, A.; Savage, P. E., Fast and Isothermal Hydrothermal Liquefaction of Polysaccharide Feedstocks. *ACS Sustainable Chemistry & Engineering* **2020,** *8* (9), 3762-3772.

28. Leng, L.; Zhou, W., Chemical compositions and wastewater properties of aqueous phase (wastewater) produced from the hydrothermal treatment of wet biomass: A review. *Energy Sources, Part A: Recovery, Utilization, and Environmental Effects* **2018,** *40* (22), 2648-2659.

29. Bareha, Y.; Girault, R.; Guezel, S.; Chaker, J.; Trémier, A., Modeling the fate of organic nitrogen during anaerobic digestion: Development of a bioaccessibility based ADM1. *Water Research* **2019,** *154*, 298-315.

30. Obeid, R.; Lewis, D. M.; Smith, N.; Hall, T.; van Eyk, P., Reaction kinetics and characterisation of species in renewable crude from hydrothermal liquefaction of monomers to represent organic fractions of biomass feedstocks. *Chemical Engineering Journal* **2020,** *389*, 124397.

31. Blakney, G. T.; Hendrickson, C. L.; Marshall, A. G., Predator data station: A fast data acquisition system for advanced FT-ICR MS experiments. *International Journal of Mass Spectrometry* **2011,** *306* (2), 246-252.

32. Cheng, F.; Cui, Z.; Chen, L.; Jarvis, J.; Paz, N.; Schaub, T.; Nirmalakhandan, N.; Brewer, C. E., Hydrothermal liquefaction of high- and low-lipid algae: Bio-crude oil chemistry. *Applied Energy* **2017,** *206*, 278-292.

33. Jarvis, J. M.; Billing, J. M.; Corilo, Y. E.; Schmidt, A. J.; Hallen, R. T.; Schaub, T. M., FT-ICR MS analysis of blended pine-microalgae feedstock HTL biocrudes. *Fuel* **2018,** *216*, 341-348.

34. Torri, C.; López Barreiro, D.; Conti, R.; Fabbri, D.; Brilman, W., Fast Procedure for the Analysis of Hydrothermal Liquefaction Biocrude with Stepwise Py-GC-MS and Data Interpretation Assisted by Means of Non-negative Matrix Factorization. *Energy & Fuels* **2016,** *30* (2), 1135-1144.

35. Jarvis, J. M.; Billing, J. M.; Hallen, R. T.; Schmidt, A. J.; Schaub, T. M., Hydrothermal Liquefaction Biocrude Compositions Compared to Petroleum Crude and Shale Oil. *Energy & Fuels* **2017,** *31* (3), 2896-2906.

36. Fernandez-Lima, F. A.; Becker, C.; McKenna, A. M.; Rodgers, R. P.; Marshall, A. G.; Russell, D. H., Petroleum Crude Oil Characterization by IMS-MS and FTICR MS. *Analytical Chemistry* **2009,** *81* (24), 9941-9947.

37. Kim, S.; Rodgers, R. P.; Blakney, G. T.; Hendrickson, C. L.; Marshall, A. G., Automated electrospray ionization FT-ICR mass spectrometry for petroleum analysis. *Journal of the American Society for Mass Spectrometry* **2009,** *20* (2), 263-268.

38. Li, M.; Cheng, D.; Pan, X.; Dou, L.; Hou, D.; Shi, Q.; Wen, Z.; Tang, Y.; Achal, S.; Milovic, M.; Tremblay, L., Characterization of petroleum acids using combined FT-IR, FT-ICR–MS and GC–MS: Implications for the origin of high acidity oils in the Muglad Basin, Sudan. *Organic Geochemistry* **2010,** *41* (9), 959-965.

39. Du, S.; Valla, J. A.; Bollas, G. M., Characteristics and origin of char and coke from fast and slow, catalytic and thermal pyrolysis of biomass and relevant model compounds. *Green Chemistry* **2013,** *15* (11), 3214-3229.

40. Déniel, M.; Haarlemmer, G.; Roubaud, A.; Weiss-Hortala, E.; Fages, J., Hydrothermal liquefaction of blackcurrant pomace and model molecules: understanding of reaction mechanisms. *Sustainable Energy & Fuels* **2017,** *1* (3), 555-582.

41. Candiano, G.; Ghiggeri, G. M.; Delfino, G.; Quierolo, C.; Cuniberti, C.; Gianazza, E.; Righetti, P. G., Reaction of lysine with aldoses. *Carbohydrate Research* **1985,** *145* (1), 99-112.

42. Hayashi, T.; Namiki, M., Role of Sugar Fragmentation in an Early Stage Browning of Amino-carbonyl Reaction of Sugar with Amino Acid. *Agricultural and Biological Chemistry* **1986,** *50* (8), 1965-1970.

43. Gai, C.; Zhang, Y.; Chen, W.-T.; Zhang, P.; Dong, Y., An investigation of reaction pathways of hydrothermal liquefaction using Chlorella pyrenoidosa and Spirulina platensis. *Energy Conversion and Management* **2015,** *96*, 330-339.

44. López Barreiro, D.; Beck, M.; Hornung, U.; Ronsse, F.; Kruse, A.; Prins, W., Suitability of hydrothermal liquefaction as a conversion route to produce biofuels from macroalgae. *Algal Research* **2015,** *11*, 234-241.

45. Yang, W.; Li, X.; Li, Z.; Tong, C.; Feng, L., Understanding low-lipid algae hydrothermal liquefaction characteristics and pathways through hydrothermal liquefaction of algal major components: Crude polysaccharides, crude proteins and their binary mixtures. *Bioresource Technology* **2015,** *196*, 99-108.

46. Zhang, B.; Lin, Q.; Zhang, Q.; Wu, K.; Pu, W.; Yang, M.; Wu, Y., Catalytic hydrothermal liquefaction of Euglena sp. microalgae over zeolite catalysts for the production of bio-oil. *RSC Advances* **2017,** *7* (15), 8944-8951.

47. Zhang, C.; Tang, X.; Sheng, L.; Yang, X., Enhancing the performance of Co-hydrothermal liquefaction for mixed algae strains by the Maillard reaction. *Green Chemistry* **2016,** *18* (8), 2542-2553.

48. Slakman, B. L.; West, R. H., Kinetic solvent effects in organic reactions. *Journal of Physical Organic Chemistry* **2019,** *32* (3), e3904.

49. Bini, R.; Chiappe, C.; Mestre, V. L.; Pomelli, C. S.; Welton, T., A rationalization of the solvent effect on the Diels–Alder reaction in ionic liquids using multiparameter linear solvation energy relationships. *Organic & Biomolecular Chemistry* **2008,** *6* (14), 2522-2529.

50. Baisier, W. M.; Labuza, T. P., Maillard browning kinetics in a liquid model system. *Journal of Agricultural and Food Chemistry* **1992,** *40* (5), 707-713.

51. Gao, C. W.; Allen, J. W.; Green, W. H.; West, R. H., Reaction Mechanism Generator: Automatic construction of chemical kinetic mechanisms. *Computer Physics Communications* **2016,** *203*, 212-225.

52. Laidler, K. J., The development of the Arrhenius equation. *Journal of Chemical Education* **1984,** *61* (6), 494.

53. Cheng, F.; Tompsett, G. A.; Fraga Alvarez, D. V.; Romo, C. I.; McKenna, A. M.; Niles, S. F.; Nelson, R. K.; Reddy, C. M.; Granados-Fócil, S.; Paulsen, A. D.; Zhang, R.; Timko, M. T., Metal oxide supported Ni-impregnated bifunctional catalysts for controlling char formation and maximizing energy recovery during catalytic hydrothermal liquefaction of food waste. *Sustainable Energy & Fuels* **2021,** *5* (4), 941-955.

54. Kaiser, N. K.; Quinn, J. P.; Blakney, G. T.; Hendrickson, C. L.; Marshall, A. G., A Novel 9.4 Tesla FTICR Mass Spectrometer with Improved Sensitivity, Mass Resolution, and Mass Range. *Journal of the American Society for Mass Spectrometry* **2011,** *22* (8), 1343-1351.

55. Madsen, R. B.; Biller, P.; Jensen, M. M.; Becker, J.; Iversen, B. B.; Glasius, M., Predicting the Chemical Composition of Aqueous Phase from Hydrothermal Liquefaction of Model Compounds and Biomasses. *Energy & Fuels* **2016,** *30* (12), 10470-10483.

56. Madsen, R. B.; Christensen, P. S.; Houlberg, K.; Lappa, E.; Mørup, A. J.; Klemmer, M.; Olsen, E. M.; Jensen, M. M.; Becker, J.; Iversen, B. B.; Glasius, M., Analysis of organic

gas phase compounds formed by hydrothermal liquefaction of Dried Distillers Grains with Solubles. *Bioresource Technology* **2015,** *192*, 826-830.

57. Ellersdorfer, M., Hydrothermal co-liquefaction of chlorella vulgaris with food processing residues, green waste and sewage sludge. *Biomass and Bioenergy* **2020,** *142*, 105796.

58. Dander, J. E.; Garg, N. K., Breaking Amides using Nickel Catalysis. *ACS Catalysis* **2017,** *7* (2), 1413-1423.

59. Hodge, J. E., Dehydrated Foods, Chemistry of Browning Reactions in Model Systems. *Journal of Agricultural and Food Chemistry* **1953,** *1* (15), 928-943.

60. Monnier, V. M.; Sell, D. R.; Wu, X.; Rutter, K., The prospects of health and longevity from the inhibition of the Maillard reaction in vivo. *International Congress Series* **2002,** *1245*, 9-19.

61. Martins, S. I. F. S.; Jongen, W. M. F.; van Boekel, M. A. J. S., A review of Maillard reaction in food and implications to kinetic modelling. *Trends in Food Science & Technology* **2000,** *11* (9), 364-373.

62. Wedzicha, B. L.; Leong, L. P., Modelling of the Maillard Reaction: Rate Constants for Individual Steps in the Reaction. In *The Maillard Reaction in Foods and Medicine*, O'Brien, J.; Nursten, H. E.; Crabbe, M. J. C.; Ames, J. M., Eds. Woodhead Publishing: 2005; pp 141-146.

63. Dewar, M. J. S.; Olivella, S.; Stewart, J. J. P., Mechanism of the Diels-Alder reaction: reactions of butadiene with ethylene and cyanoethylenes. *Journal of the American Chemical Society* **1986,** *108* (19), 5771-5779.

64. Norton, J. A., The Diels-Alder Diene Synthesis. *Chemical Reviews* **1942,** *31* (2), 319-523.

65. Alimoradi, S.; Stohr, H.; Stagg-Williams, S.; Sturm, B., Effect of temperature on toxicity and biodegradability of dissolved organic nitrogen formed during hydrothermal liquefaction of biomass. *Chemosphere* **2020,** *238*, 124573.

66. Arun, J.; Gopinath, K. P.; SundarRajan, P.; Malolan, R.; AjaySrinivaasan, P., Hydrothermal liquefaction and pyrolysis of Amphiroa fragilissima biomass: Comparative study on oxygen content and storage stability parameters of bio-oil. *Bioresource Technology Reports* **2020,** *11*, 100465.

67. Azizi, K.; Keshavarz Moraveji, M.; Abedini Najafabadi, H., A review on bio-fuel production from microalgal biomass by using pyrolysis method. *Renewable and Sustainable Energy Reviews* **2018,** *82*, 3046-3059.

68. Berg, J., Tymoczko, JL, Stryer, L. Biochemistry. 5th Edition. . https://www.ncbi.nlm.nih.gov/books/NBK22547/.

69. Biller, P.; Ross, A. B., Potential yields and properties of oil from the hydrothermal liquefaction of microalgae with different biochemical content. *Bioresource Technology* **2011,** *102* (1), 215-225.

70. Costanzo, W.; Jena, U.; Hilten, R.; Das, K. C.; Kastner, J. R., Low temperature hydrothermal pretreatment of algae to reduce nitrogen heteroatoms and generate nutrient recycle streams. *Algal Research* **2015,** *12*, 377-387.

71. D.J. Zastrow, P. A. J. In *Hydrothermal Liquefaction of Food Waste and Model Food Waste Compounds*, AIChE, San Francisco, CA, San Francisco, CA, 2013.

72. Dodds, W. K.; Whiles, M. R., Chapter 14 - Nitrogen, Sulfur, Phosphorus, and Other Nutrients. In *Freshwater Ecology (Third Edition)*, Dodds, W. K.; Whiles, M. R., Eds. Academic Press: 2020; pp 395-424.

73. Li, Y.; Leow, S.; Fedders, A. C.; Sharma, B. K.; Guest, J. S.; Strathmann, T. J., Quantitative multiphase model for hydrothermal liquefaction of algal biomass. *Green Chemistry* **2017,** *19* (4), 1163-1174.

74. Li, J.; Wang, Z.; Yang, X.; Hu, L.; Liu, Y.; Wang, C., Evaluate the pyrolysis pathway of glycine and glycylglycine by TG–FTIR. *Journal of Analytical and Applied Pyrolysis* **2007,** *80* (1), 247-253.

75. Lucian, M.; Volpe, M.; Gao, L.; Piro, G.; Goldfarb, J. L.; Fiori, L., Impact of hydrothermal carbonization conditions on the formation of hydrochars and secondary chars from the organic fraction of municipal solid waste. *Fuel* **2018,** *233*, 257-268.

76. Shakya, R.; Adhikari, S.; Mahadevan, R.; Shanmugam, S. R.; Nam, H.; Hassan, E. B.; Dempster, T. A., Influence of biochemical composition during hydrothermal liquefaction of algae on product yields and fuel properties. *Bioresource Technology* **2017,** *243*, 1112-1120.

77. Sheng, L.; Wang, X.; Yang, X., Prediction model of biocrude yield and nitrogen heterocyclic compounds analysis by hydrothermal liquefaction of microalgae with model compounds. *Bioresource Technology* **2018,** *247*, 14-20.

78. Regenass, P.; Riché, S.; Péron, F.; Rognan, D.; Hibert, M.; Girard, N.; Bonnet, D., A step-economical multicomponent synthesis of 3D-shaped aza-diketopiperazines and their drug-like chemical space analysis. *Organic & Biomolecular Chemistry* **2016,** *14* (37), 8859-8863.

79. Motavaf, B.; Savage, P. E., Effect of Process Variables on Food Waste Valorization via Hydrothermal Liquefaction. *ACS ES&T Engineering* **2021,** *1* (3), 363-374.

80. Xu, D.; Savage, P. E., Effect of reaction time and algae loading on water-soluble and insoluble biocrude fractions from hydrothermal liquefaction of algae. *Algal Research* **2015,** *12*, 60-67.

81. Valdez, P. J.; Nelson, M. C.; Wang, H. Y.; Lin, X. N.; Savage, P. E., Hydrothermal liquefaction of Nannochloropsis sp.: Systematic study of process variables and analysis of the product fractions. *Biomass and Bioenergy* **2012,** *46*, 317-331.

82. Kida, Y.; Class, C. A.; Concepcion, A. J.; Timko, M. T.; Green, W. H., Combining experiment and theory to elucidate the role of supercritical water in sulfide decomposition. *Physical Chemistry Chemical Physics* **2014,** *16* (20), 9220-9228.

83. Robb, D. B.; Blades, M. W., Factors affecting primary ionization in dopant-assisted atmospheric pressure photoionization (DA-APPI) for LC/MS. *Journal of the American Society for Mass Spectrometry* **2006,** *17* (2), 130-138.

84. Robb, D. B.; Covey, T. R.; Bruins, A. P., Atmospheric Pressure Photoionization: An Ionization Method for Liquid Chromatography−Mass Spectrometry. *Analytical Chemistry* **2000,** *72* (15), 3653-3659.

85. Purcell, J. M.; Rodgers, R. P.; Hendrickson, C. L.; Marshall, A. G., Speciation of nitrogen containing aromatics by atmospheric pressure photoionization or electrospray ionization fourier transform ion cyclotron resonance mass spectrometry. *Journal of the American Society for Mass Spectrometry* **2007,** *18* (7), 1265-1273.

86. Smith, D. R.; Robb, D. B.; Blades, M. W., Comparison of dopants for charge exchange ionization of nonpolar polycyclic aromatic hydrocarbons with reversed-phase LC-APPI-MS. *Journal of the American Society for Mass Spectrometry* **2009,** *20* (1), 73-79.

87. Purcell, J. M.; Hendrickson, C. L.; Rodgers, R. P.; Marshall, A. G., Atmospheric Pressure Photoionization Proton Transfer for Complex Organic Mixtures Investigated by Fourier Transform Ion Cyclotron Resonance Mass Spectrometry. *Journal of the American Society for Mass Spectrometry* **2007,** *18* (9), 1682-1689.

88. Purcell, J. M.; Hendrickson, C. L.; Rodgers, R. P.; Marshall, A. G., Atmospheric Pressure Photoionization Fourier Transform Ion Cyclotron Resonance Mass Spectrometry for Complex Mixture Analysis. *Analytical Chemistry* **2006,** *78* (16), 5906-5912.

89. Senko, M. W.; Hendrickson, C. L.; Emmett, M. R.; Shi, S. D. H.; Marshall, A. G., External accumulation of ions for enhanced electrospray ionization fourier transform ion cyclotron resonance mass spectrometry. *Journal of the American Society for Mass Spectrometry* **1997,** *8* (9), 970-976.

90. Wilcox, B. E.; Hendrickson, C. L.; Marshall, A. G., Improved ion extraction from a linear octopole ion trap: SIMION analysis and experimental demonstration. *Journal of the American Society for Mass Spectrometry* **2002,** *13* (11), 1304-1312.

91. Tolmachev, A. V.; Robinson, E. W.; Wu, S.; Kang, H.; Lourette, N. M.; Paša-Tolić, L.; Smith, R. D., Trapped-ion cell with improved dc potential harmonicity for FT-ICR MS. *Journal of the American Society for Mass Spectrometry* **2008,** *19* (4), 586-597.

92. Kaiser, N. K.; Savory, J. J.; McKenna, A. M.; Quinn, J. P.; Hendrickson, C. L.; Marshall, A. G., Electrically Compensated Fourier Transform Ion Cyclotron Resonance Cell for Complex Mixture Mass Analysis. *Analytical Chemistry* **2011,** *83* (17), 6907-6910.

93. Xian, F.; Corilo, Y. E.; Hendrickson, C. L.; Marshall, A. G., Baseline correction of absorption-mode Fourier transform ion cyclotron resonance mass spectra. *International Journal of Mass Spectrometry* **2012,** *325-327*, 67-72.

94. Xian, F.; Hendrickson, C. L.; Blakney, G. T.; Beu, S. C.; Marshall, A. G., Automated Broadband Phase Correction of Fourier Transform Ion Cyclotron Resonance Mass Spectra. *Analytical Chemistry* **2010,** *82* (21), 8807-8812.

95. Kendrick, E., A mass scale based on CH2 = 14.0000 for high resolution mass spectrometry of organic compounds. *Analytical Chemistry* **1963,** *35*, 2146-2154.

96. Hughey, C. A.; Hendrickson, C. L.; Rodgers, R. P.; Marshall, A. G.; Qian, K., Kendrick Mass Defect Spectrum: A Compact Visual Analysis for Ultrahigh-Resolution Broadband Mass Spectra. *Analytical Chemistry* **2001,** *73* (19), 4676-4681.

97. McLafferty, F. W. T., F., *Interpretation of Mass Spectra, 4th ed.* 4th ed.; University Science Books: 1993.

98. Savory, J. J.; Kaiser, N. K.; McKenna, A. M.; Xian, F.; Blakney, G. T.; Rodgers, R. P.; Hendrickson, C. L.; Marshall, A. G., Parts-Per-Billion Fourier Transform Ion Cyclotron Resonance Mass Measurement Accuracy with a "Walking" Calibration Equation. *Analytical Chemistry* **2011,** *83* (5), 1732-1736.

99. Corilo, Y. E., PetroOrg Software. Florida State University, Omics LLC: 2014.

100. Betancourt-Jimenez, D.; Youngblood, J. P.; Martinez, C. J., Synthesis and Characterization of Fatty Acid Amides from Commercial Vegetable Oils and Primary Alkyl Amines for Phase Change Material Applications. *ACS Sustainable Chemistry & Engineering* **2020,** *8* (36), 13683-13691.

CHAPTER 3

EMERGENT CHEMICAL BEHAVIOR IN MIXED FOOD AND LIGNOCELLULOSIC GREEN WASTE HYDROTHERMAL LIQUEFACTION

3.1 INTRODUCTION

To reduce the reliance on fossil fuels and counteract the effects of climate change, waste streams offer a low-carbon emission, energy-dense source to petroleum fuels. Worldwide, over 1.3 billion tons of waste are thrown away annually[1], ending up in landfills, the oceans, and scattered through the environment. Left untreated, these wastes result in fugitive greenhouse gas emissions, cause toxic run-off, and result in algal blooms that substantially disrupt local ecosystems. By utilizing waste and diverting it from landfills, there is the potential to reduce greenhouse gas emissions by over 2.4% in the United States.[2]

Hydrothermal liquefaction (HTL) is a water-assisted thermochemical conversion process that operates at temperatures from 250 to 400 °C and sufficient pressure to maintain a liquid water phase.[3] The use of HTL has been extensively studied for the conversion of single-source waste feeds into an energy dense biocrude that is a biofuel precursor.[3-7] High-lipid feedstocks have been shown to achieve yields upwards of 40 wt.%[3, 8, 9] in comparison to the typical 10 – 40% yields seen with un-catalyzed lignocellulosic HTL.[10]

HTL biocrude yields are highly dependent on feedstock compostion.[11] Lipid content plays a crucial role in HTL biocrude yields due to the inherent lyophilic nature of the constituent fatty acids.[12] The relationship between lipid content and biocrude yields means that many food wastes,[5,

[13] some sewage sludges,[14, 15] and certain types of algae cultivated on wastewater[12, 16] are especially suitable for HTL. Waste biomass and low-lipid containing sewage sludge and food waste have traditionally been less desirable for use as an HTL feed primarily due to their lipid contents.[3]

Co-feeding multiple streams to HTL can sometimes result in surprising benefits. For example, Yang et al. reported that co-liquefaction of 50% spent coffee grounds with 50% corn stalk resulted in a 20.9% increase in biocrude yield compared to either of the individual feedstocks.[17] In fact, as a rule, measured biocrude yield is rarely equal to the expected performance predicted from physical mixing of the unique feeds and the performance of the corresponding pure streams,[18, 19] with both synergistic and antagonistic effects reported in the literature. Clearly, processes should be designed to take advantage of synergistic effects while mitigating the antagonistic effects. As shown by LeClerc et al.[20], understanding elementary reaction pathways of model compounds permits prediction of feed compositions which maximize biocrude yields. Applying a molecularly detailed pathway analysis strategy to the synergistic and antagonistic effects of co-HTL of realistic feeds is therefore a promising, yet under-developed area to maximize obtainable yields.

A recent study by Jarvis et al. advanced the understanding of co-HTL of algae and lignocellulosic feeds using Fourier transform ion-cyclotron resonance mass spectrometry (FT-ICR MS) operated in positive ion atmospheric pressure photoionization (+ APPI) mode.[18] FT-ICR MS identified at least 6,000 peaks per biocrude sample, with mixed feed biocrudes containing a higher proportion of algal-derived species than pine-derived species.[18] The work also identified > 20% unique elemental formula in biocrude obtained from algae-pine mixtures that were absent from either biocrude obtained from HTL of pure feeds.[18] Synergy was reported for processing a mixture consisting of 50% algae and 50% pine, which coincided with the increase in N_1O_3 and N_2O_3

species range identified by FT-ICR MS.[18] While the study with algae and pine points to a potential molecular interpretation of synergistic effects for mixed feeds, both algae and pine are relatively simple and comparatively expensive feeds compared with municipal wastes,[9] meaning that similar analysis is needed for abundant and inexpensive feeds like food waste and green waste.

Combined, food waste and green waste account for an estimated 1.5 billion tons per year,[2, 21] with real prices that are often negative.[22, 23] Moreover, they are co-produced in similar urban and dense suburban communities, making their mixtures an attractive feed stream for HTL. Molecularly, food and green waste are distinct from one another, and these differences are anticipated to affect their ability to be transformed into biocrude as well as the resultant biocrude composition. Food waste typically contains 40 – 60% carbon, primarily in starch, proteins, and especially lipids, and an ash content < 5%. Green waste is composed primarily of cellulose, hemicellulose, and lignin, and its ash content can be greater than 10%.[20] Heteroatom content and speciation – specifically oxygen and nitrogen – are of utmost importance in determining the fate of biocrude and upgrading potential.[12, 15, 24] Here, food waste typically contains much more nitrogen than green waste, with most of the nitrogen content in organic forms associated with proteins.[20, 25, 26] Oxygen in the dominant heteroatom present in green waste, arising from the glycosidic linkages and hydroxy and acetyl sidechains of cellulose and hemicellulose.[12, 27] The presence of multiple, poorly defined types of chemicals in food waste and green waste opens a wide range of potential pathways for biocrude formation that must be understood for selection of optimized blending ratios in HTL feed streams.

In this work, a cafeteria food waste and a lignocellulosic green waste were mixed in five blending ratios and used as HTL feeds. Yields of biocrude as well as the char, aqueous phase, and gas byproducts were measured, with the objective of identifying synergistic and antagonistic

phenomena, with synergism and antagonism defined based on the performance of the pure feeds. The resulting biocrudes were then analyzed using gas chromatography and FT-ICR MS to identify molecular-level differences that give rise to synergism and antagonism.[18] The results of this study advance current understanding of the molecular-level phenomena that arise from co-HTL of real-world waste streams, a key step toward technological implementation.

3.2 MATERIALS AND METHODS

3.2.1 MATERIALS

Food waste was obtained from a veteran's hospital cafeteria (via Greener Chemistry LLC.). An Ecovim dehydrator was used to pre-grind and dry the food waste, which was then stored in a freezer at −20 °C prior to use. Green waste, consisting of grass, wood chips, and yard clippings, was obtained from BDP Industries Inc., Greenwich, NY. Green waste was placed in air-tight bags and stored in a freezer at −20 °C. Green waste was removed from the freezer, dried, ground, and sieved to < 0.85 mm particle size immediately before use. Both food waste and green waste were dried in an oven at 60 °C overnight prior to weighing so that the slurry feed to the reactor could be fixed at a solids loading of 15 wt.% dry weight.

Other reagents included >99.5% pure acetone (Sigma Aldrich), which was utilized for biocrude recovery and cleaning; deionized water with electrical resistivity greater than 18.0 MΩ, which was used to prepare feedstock slurries; and gases. Nitrogen gas (purity >99.9%, Airgas) was used to purge air from the reactor and to pre-pressurize it to ensure a liquid water phase was present during HTL. Helium (grade 5.0, Airgas) was used as the carrier gas for GC analysis.

3.2.2 HYDROTHERMAL LIQUEFACTION REACTIONS

HTL reactions were conducted in a 300 mL Parr stainless steel batch reactor, as has been previously described.[28, 29]. Reactions were completed at 300 °C and approximately 200 bar to ensure water remained in the liquid phase. Heat-up required approximately 45 min. When the reaction temperature reached 295 °C, the 60 min reaction time was started. After the reaction, the reactor was quenched in an ice bath to < 40 °C. Quenching required approximately 10 min.

After quenching, biocrude and solids were separated from the aqueous phase via vacuum filtration after which the biocrude and solid phases were separated from one another using acetone. Acetone was stripped from the biocrude using rotary evaporation set at 40 °C and 350 mmHg to maximize solvent removal and minimize biocrude losses. Solvent extraction was kept constant for all samples and not optimized based on feedstock type.[30] The mass of the gas phase was determined by difference between the reactor mass before and after venting. The masses of the gas, aqueous phase, solid, and biocrude products were summed and compared with the mass charged to the reactor to close the overall mass balance. In all cases, data reported here correspond to overall mass balance closure > 90%. Losses represent residual material that could not be removed from the reactor, transfer losses, and the precision of the analytical balance used to estimate gas yields (± 0.5 g).

3.2.3 PRODUCT ANALYSIS

Products were analyzed gravimetrically, by elemental composition, and by molecular composition using a combination of methods that have been described previously in the literature for similar applications. Analytical methods are described briefly here, with further details on characterization techniques found in previous papers[20, 29, 31] and the Supporting Information.

Elemental analysis (CHN) was utilized to determine the carbon content of the biocrude and char phases (Midwest Microlabs, Indianapolis, IN). Total organic carbon (TOC) measured the carbon in the aqueous phase, and gas-phase carbon was assumed to be 98% CO_2 based on previous studies.[28, 29] The feedstocks and biocrudes were also sent to Mainstream Engineering (Rockledge, FL) for higher heating value (HHV) analysis using a Parr Instruments semimicro calorimeter. Energy recovery was calculated based on the gravimetric biocrude yield and its measured HHV. Masses of the gas, aqueous phase, char, and biocrude products was converted into carbon terms using the aforementioned elemental analysis methods and compared with the initial carbon charge. In all cases, the carbon balance closed to within 5%.

Gas chromatography mass spectrometry (GC-MS) (Agilent 6890N equipped with a 5973N mass spectrometer) was performed on all biocrude samples to determine chemical composition of products with normal boiling points < 300 °C. Further GC-MS method details have been reported previously.[20, 28] Individual compounds were identified based on similarity with a built-in mass spectral database;[32] only compounds with matches >80% are reported here.

Fourier-transform attenuated total reflectance infrared spectroscopy (FT-ATR-IR) was used to analyze the functional group content of biocrude and char products. A Shimadzu FT-IR spectrometer equipped with a QATR-S single reflection ATR cell and with a resolution of 8 cm^{-1} was used for all measurement. Spectra were compared with known databases[33, 34] to identify bands attributable to specific functional groups.

Biocrude samples were further analyzed using positive-ion atmospheric pressure photoionization 21 Tesla Fourier-transform ion cyclotron resonance mass spectrometry (+APPI FT-ICR MS).[35, 36] Samples were dissolved in a 50/50 (by volume) mixture of toluene and

tetrahydrofuran to a final concentration of 125 µg/mL prior to analysis. Further details on FT-ICR MS methodology can be found in the Supporting Information.

Thermal gravimetric analysis (TGA) was performed on a Shimadzu TGA-50. The heating rate was set to 10 °C/min and samples were heated from 25 to 800 °C under a constant nitrogen flow rate of 25 mL/min.

3.3 RESULTS

This work aims to identify and understand the chemical interactions between lignocellulosic and food-based components that occur during co-HTL. To produce a series of feeds with intermediate compositions, five feedstocks were studied: one consisting of a food waste sourced from a veteran's hospital cafeteria (HFW), one green waste (GW) sourced from a local composter, and three blends corresponding to ratios of 75 wt% food waste (75:25), 50 wt% food waste (50:50), and 25 wt% food waste (25:75). These five feeds were treated under HTL conditions (300 °C and 1 hr. reaction time) selected to be representative of conditions commonly used for HTL.[20, 28, 29] The product mixture was quantified for yields of solvent-soluble biocrude, water-soluble aqueous phase, solid char, and gaseous products. The biocrude was further analyzed using GC-MS, FT-IR, TGA, and FT-ICR MS to capture the molecular composition and as the basis for understanding the chemical interactions.

3.3.1 HTL FEED CHARACTERIZATION

Table 3-1. Food and green waste feedstock properties as determined from proximate, elemental, and biochemical analysis.

	Food Waste	Green Waste
Proximate Analysis (wt.%) [a]		
Moisture [b,e]	0.7 ± 0.1	0.5 ± 0.2
Ash [f]	1.9 ± 0.9	14.1 ± 1.3
Elemental Analysis (wt.%) [a,e]		
Carbon	52.2 ± 0.9	42.2 ± 0.1
Hydrogen	7.5 ± 0.2	5.2 ± 0.2
Nitrogen	4.3 ± 0.1	0.2 ± 0.1
Sulfur	1.0 ± 0.1	0.7 ± 0.2
Oxygen [c]	33.2 ± 2.1	51.7 ± 1.8
Biochemical Analysis (wt.%) [a,e]		
Carbohydrates	29.8	-
Holocellulose	-	69.7
Lignin	-	16.2
Lipids	38.9	-
Protein [d]	26.8 ± 0.6	-
H/C_{eff}	0.55	-0.39
HHV(MJ/kg)	23.6 ± 3.0	13.5 ± 0.6

[a] Dry basis. [b] As received. [c] Oxygen determined by difference. [d] protein = N content * 6.25. [e] standard deviation reported as ± where n = 3, [f] Standard deviation reported as ± where n = 2.

Feedstock compositions provided in **Table 3-1** show that food waste has greater carbon and hydrogen content and higher heating value (HHV) than green waste; differences are attributable to lipid content in the food waste and the combined cellulose and hemicellulose content of the green waste. Similarly, the effective hydrogen to carbon ratio (H/C_{eff}) of food waste is greater than that measured for green waste (**Table 3-1**). H/C_{eff} is calculated as:

$$\frac{H}{C_{eff}} = \left(\frac{H - 2O - 3N - 2S}{C}\right) \tag{3.1}$$

and is a measure to describe the potential of a feed to be economically converted into biocrude with a final $H/C_{eff} > 2$.[37, 38] **Figure 3-1** shows that biocrude yields increase with increasing $H/C_{eff,}$ as H/C_{eff} increases with increasing food waste content. Accordingly, the H/C_{eff} values reported in **Table 3-1** indicate that HTL conversion of HFW should be expected to lead to the greatest biocrude yield and energy recovery (**Figure B3-9**) and green waste the least, with HTL conversion of mixtures producing intermediate biocrude yields weighted by their blending ratios. **Table B3-2** provides further characterization data on the two feeds.

3.3.2 HTL PRODUCT YIELDS

HTL conversion of organic wastes produces biocrude, char, aqueous, and gas products. Gravimetrically determined carbon yields of these four products are shown in **Figure 3-1**. Dashed lines represent the linear weighted average between the two pure feeds (HFW and GW) corresponding to the expected physical mixture of food and green waste in the absence of any synergistic or emergent effects. Data in **Figure 3-1** show that increased food waste content results in increased biocrude yield (carbon wt.%), consistent with the carbon and lipid content of food waste and the H/C_{eff} analysis discussed earlier.

Figure 3-1 reveals the presence of emergent behavior for several feeds. A synergistic effect on the biocrude yield is observed for the 75:25 food waste:green waste mixture, corresponding to a biocrude yield increase of 14.4% relative to the expected weighted average performance. On the other hand, an antagonistic effect is observed for the 25:75 food waste:green waste mixture, which produced 13.8% less biocrude than expected based on the yields observed for the two pure feeds. The effects on biocrude yield are mirrored by decreases in char yields for the 75:25 mixture and corresponding char yields increases for the 25:75 mixture. Notably, HTL of lignocellulosic biomass is known to result in lower oil yields. While the green waste itself is challenging to

breakdown, it is also noted that the substantially large ash content of the green waste shown in **Table 3-1** may contribute to diminished oil yields and HHV, as shown in previous literature studies. [39, 40] Taken collectively, the biocrude and char yield data shown in **Figure 3-1** indicate that synergistic effects between food waste and green waste reactants can shift carbon away from char-producing pathways and into biocrude-producing ones; antagonistic interactions have the opposite effects.

A final trend can be observed in **Figure 3-1** regarding the gas formation. All blends resulted in increased gas levels compared with the individual wastes, with carbon dioxide present as the dominant gas-phase product. Gaseous products are resultant of the deoxygenation and especially decarboxylation reactions, suggesting that emergent chemical pathways are able to promote these pathways. Gas yields observed for the 25:75 food waste:green waste blend, which was 58% greater than predicted based on behavior of the pure feeds, are especially noteworthy. The gas yields observed for mixtures are further corroborated by elemental analysis, which shows blended feedstocks result in biocrudes with decreased oxygen content compared to the levels expected from the pure streams (**Table B3-4**).

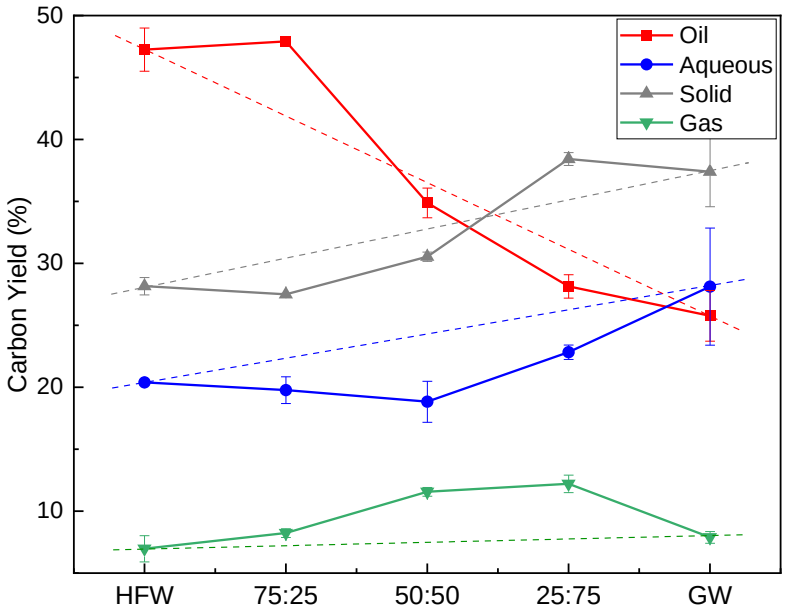

Figure 3-1. Hydrothermal liquefaction product yields, expressed as carbon yield, for mixtures of food and lignocellulosic green waste. Dashed lines represent the expected, theoretical trend if performance was a linear combination of pure food waste and pure green waste. Error bars represent the standard deviation from performing at least two runs and are present yet too small to be seen on the 75:25 experimental runs.

To understand the emergent behavior indicated by carbon yields in more detail, biocrude samples were analyzed using thermogravimetric analysis (TGA). **Figure 3-2a** shows the results, quantified into fractions based on volatility corresponding to gasoline (< 190 °C), jet fuel (190 – 290 °C), diesel (290 – 340 °C), vacuum gas oil (340 – 540 °C), and residue (> 540 °C). TGA indicates that residue is the most abundant of these fractions, followed by vacuum gas oil and jet fuel in the green waste-derived biocrude, consistent with the decomposition of cellulose and lignin into C_6-C_{12} oxygenates. In contrast, jet fuel is most abundant component in the food waste biocrudes, consistent with C_{12}-C_{18} fatty acid content. Further analysis reveals that blending causes a decrease in the percentage of compounds in the residue range in mixtures of 75:25, containing only 10% of compounds, compared to the predicted 16%. Instead, blending at this ratio caused a

corresponding increase in diesel range molecules. On the other hand, 25:75 food waste-green waste mixtures caused a sharp increase in gasoline-range molecules.

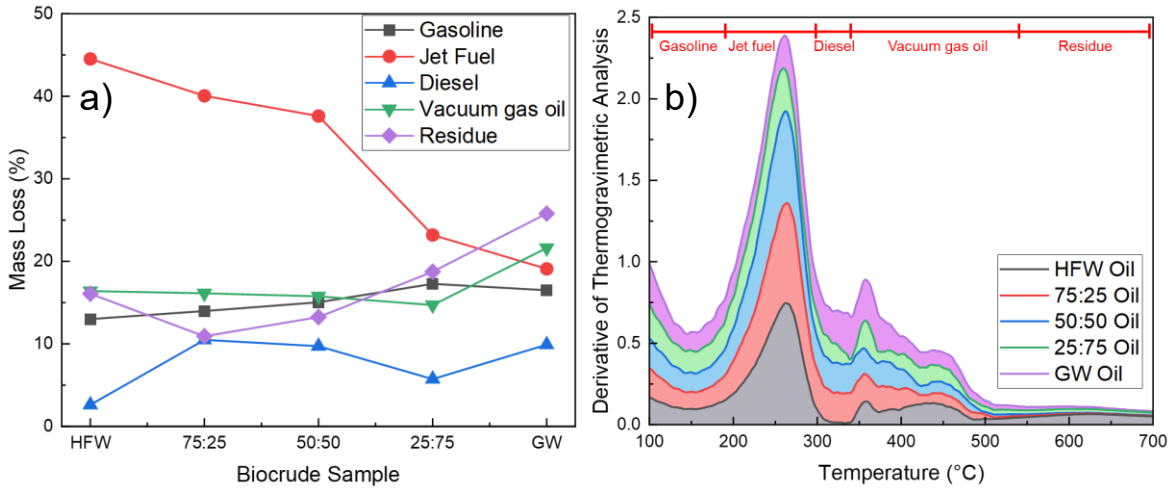

Figure 3-2. **a)** Mass loss as a function of biocrude sample for temperature ranges corresponding to different fuel fractions analyzed from thermogravimetric analysis. **b)** Stacked thermogravimetric analysis (TGA) differential mass loss percent plotted as a function of temperature. Temperature ranges were chosen to match those reported in Haider et al.[41] Gasoline = <190 °C, jet fuel = 190-290 °C, diesel = 290-340 °C, vacuum gas oil = 340-540 °C, residue = >540 °C. Compounds associated with mass loss at T > 540 °C can also be termed asphaltenes.

TGA further indicates that less than 60% of biocrude compounds are analyzable with gas chromatography (T< 325 °C), with food waste biocrude yielding a higher analyzable fraction than green waste. Further TGA and DTG data can be visualized in **Figure B3-10**. Green waste biocrude, however, has a high concentration of residue-range compounds with vaporization temperatures above 500 °C, leading to only 37% of its mass loss occurring at temperatures less than 300 °C. The remaining samples' percentage of GC-amenable compounds are summarized in **Table B3-5**.

3.3.3 BIOCRUDE MOLECULAR CHARACTERIZATION

TGA shows that approximately 60% of the food waste biocrude is amenable to GC analysis whereas only 37% is in green waste biocrude. To analyze the non-volatile biocrude fraction, 21 tesla (+) APPI FT-ICR MS was used to obtain high resolution (50 ppb) mass spectra of ionizable components heavier than approximately 100 Da. Ionization efficiency is determined by the molecular structure of the analyte mixture, and the polydispersity and polyfunctionality of biofuels result in a range of species with different ionization potentials, and APPI is more selective towards aromatic species found in green waste.

FT-ICR-MS of each of the five samples, revealing the presence of thousands of compounds in each of them, are shown in **Figure 3-3**. Molecular species from each mass spectrum range from 9,000-15,000 elemental compositions, with a total of ~60,000 species identified across all samples. **Figure 3-3** shows that only 4,199 species were identified as common across all samples, highlighting the abundance of unique species identified with different feedstock combinations. Specifically, 165 (1.8%) and 2,470 (19.9%) species are unique to food waste and green waste biocrude, respectively, whereas green waste and 25:75 biocrude accounted for over 4,000 unique elemental composition assignments—almost 10% of the total number of species identified.

Molecular identification by FT-ICR MS highlights hundreds of unique compounds from each biocrude and indicates unique chemical interactions between food and green waste components. Food waste biocrude contains only 165 unique species, 15-times fewer than green waste biocrude, which is likely due to differences in aliphatic and aromatic content of these two feeds (see **Table 3-1**). In particular, green waste lignocellulosic content reacts to form highly aromatic oxygenated compounds that are more efficiently ionized by atmospheric pressure photoionization than more aliphatic (e.g., fatty acids and carboxylic acids) compounds found in

food waste. Food waste consists of a significant aliphatic component from fatty acids; aliphatic compounds are less efficiently ionized by atmospheric pressure photoionization, hence the relatively small number of unique species identified in the food waste biocrude may be attributable to the importance of aliphatic molecules in this sample.

Taking this analysis a step further, the black outline encompassing the hash-marked region in **Figure 3-3** denotes the area of elemental compositions found in the pure feedstock and represents physicochemical interactions retained upon mixing. Outside this shaded region are emergent species, which arise from reactive chemistry to produce species not found in either pure feed (8.0% of identified elemental compositions). Venn diagram analysis helps to identify the presence of emergence, it does not: a) provide information on the chemical makeup or heteroatom distribution of the emergent species, or b) quantify differences in non-emergent species to identify pathways enhanced or suppressed by blending food and green waste biomolecules in varying ratios at HTL conditions. Since (+) APPI FT-ICR MS provides elemental composition assignments, qualitative, compositional trends between the samples can be visualized based on heteroatom class and degree of aromaticity.

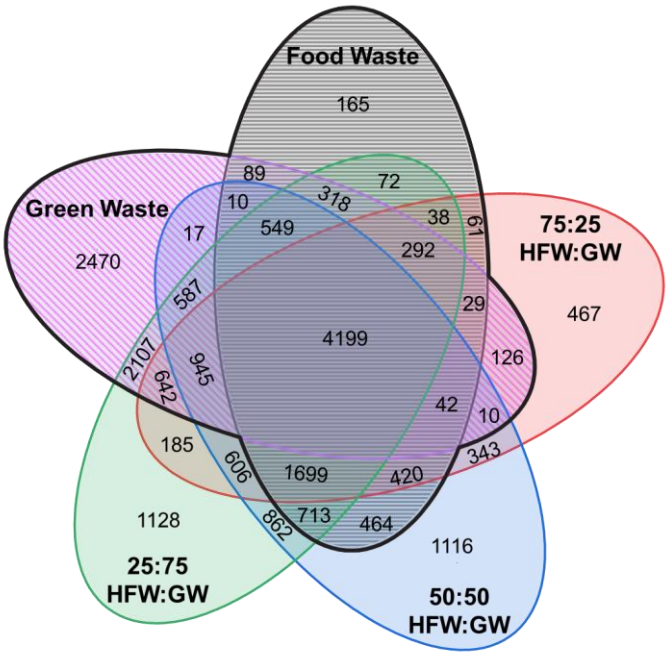

Figure 3-3. Venn diagram depicting the number of elemental compositions derived from (+) APPI FT-ICR MS at 21 tesla shared between the five biocrude samples. The total number of molecular species identified in each sample: HFW: 9,160; 75:25: 10,104; 50:50: 12,582; 25:75: 14,942; GW: 12,432. The outer envelope (not hashed) is the number of unique species not found in any of the other biocrudes.

To understand the compositional differences in greater molecular detail, the biocrude products were analyzed using FT-IR to identify functional groups and GC-MS to identify specific molecules present in the biocrude volatile fraction. **Figure 3-4a** provides FT-IR spectra showing the fingerprint regions of the five biocrude samples comprising this study. In all cases, a band attributable to the carbonyl stretch and a second band attributable to the C-O stretch are present in the spectra. The position of this band does not change between spectra, occurring at ~1700 cm^{-1} in all cases, representative of a carboxylic acid or conjugated acid. The strong C=O stretching band in HFW biocrude is consistent with carboxylic acids from food waste's high lipid content, whereas the same band in GW biocrude is more likely attributable to conjugated sugars.

In addition to these common features, the individual biocrude spectra contain substantive variations from one another. The spectra of green waste and 25:75 HFW:GW biocrudes contain strong evidence of phenolic groups (**Table B3-6**), as indicated by bands at 1516, 1330, 1200, 1114, 1092, and 1030 cm^{-1}.[34] The family of phenolic bands decrease in intensity as the percentage of food waste in the feed increases, disappearing entirely in the spectrum of pure food waste biocrude, indicating the absence of phenolic compounds in food waste biocrude. Similarly, a band located at 1469 cm^{-1} and attributable to the CH_2 stretching mode of alkanes increases in intensity with increasing food waste content, a finding which is consistent with hydrolysis of lipids to produce fatty acids.[33]

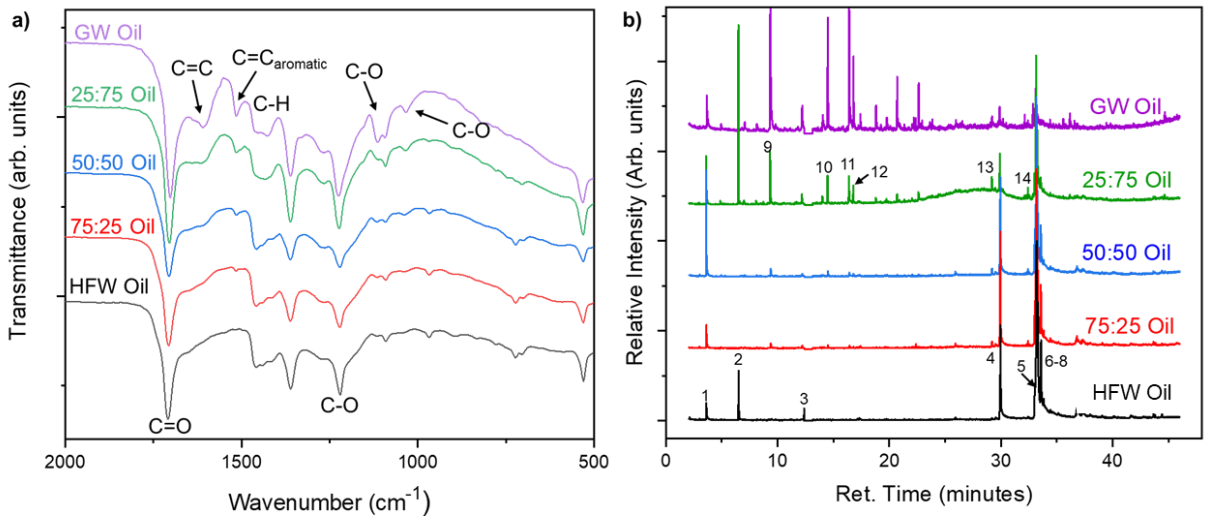

Figure 3-4. **a)** Fourier-transform infrared spectroscopy (FT-IR) spectra of the five biocrudes obtained from mixed-feed HTL. **b)** Gas chromatography (GC-MS) spectra of the five biocrudes. Peaks with identification confidence score greater than 80% are numbered. Number identities can be found in the Supporting Information (Table B3-6).

FT-IR provides some general information about functional groups present in the biocrude, but on its own cannot explain the observed emergent behavior in the FT-ICR MS and arising from synergistic or antagonistic interactions between food waste and green waste compounds. Next,

samples were analyzed using GC-MS for the characterization of the light biocrude compounds, defined here on a volatility basis as compounds with a normal boiling point less than 300 °C. Spectra are shown in **Figure 3-4b** with peaks corresponding to >80% matches on the mass spectra data base search numbered (see the Methods Section for more details). GC-MS spectra of food waste contain C_{16} and C_{18} fatty acids (peak numbers 4-8) as the most prominent peaks, with the intensities of the corresponding peaks decreasing in intensity with increasing green waste content in the feed. The fatty acid content of the food waste biocrude identified is consistent with the FT-IR spectra shown in **Figure 3-4a** and is the expected outcome of lipid hydrolysis to form biocrude-soluble fatty acids.[12] The chromatogram obtained from the green waste biocrude is dominated by highly volatile, low retention time phenolic derivatives such as methoxyphenol (peak number 9) and ethylguaiacol (peak number 10). These peaks are also present in the 25:75 food waste: green waste chromatogram and are the putative breakdown products of lignin present in green waste. The identification of individual phenolic products in the biocrudes derived in whole or in part from green waste is entirely consistent with the FT-IR spectra shown in **Figure 3-4a**, providing a mutually consistent interpretation.

Whereas fatty acid and phenolic biocrude components can be explained entirely by physical mixing effects, several other peaks shed light on emergent behavior that can only be explained by chemical interactions. Specifically, peaks 13 and 14 in **Figure 3-4b** can be attributed to hexadecenoic acid methyl ester and octadecanoic acid methyl ester, respectively. Octadecanoic acid methyl ester is one of a class of compounds called fatty acid methyl esters (FAMEs)[12, 13] that appear in the greatest concentration in the 25:75 biocrude and are present in the 50:50 and 75:25 biocrudes in small quantities but absent from the food waste biocrude. The presence of FAMEs cannot be explained entirely by physical mixing of the two parent biocrudes and must instead be

explained by chemical interactions. In this case, the probable explanation is reaction between methanol, formed as a hydrolysis product of methoxy phenols,[42] and fatty acids. The high temperatures and acids present in the HTL reaction mixture facilitate their reaction.[42]

3.3.4 COMPOSITIONAL COMPARISON: HETEROATOM CLASS DISTRIBUTION BY APPI FT-ICR MS AT 21T

Figure 3-4 helps explain the compounds that commonly occur in the various biocrudes, their physical mixtures, and some of the emergent behavior anticipated from **Figure 3-3**. That stated, the signs of emergent behavior apparent in **Figure 3-4** are admittedly subtle and cannot, on their own, explain the phenomena observed in **Figure 3-3**. The implication is that the emergent products must possess similar functional groups as those present in the pure feeds and further that the emergent products are present primarily in fractions of the biocrude that are insufficiently volatile for GC analysis. Accordingly, the FT-MS data were re-analyzed to mine further molecular-level details for evidence of emergent behavior.

Figure 3-5 shows the heteroatom class distribution derived from 21 T +APPI FT-ICR mass spectra of each biocrude. The most abundant class in the green waste biocrude corresponds to species with six oxygen (O_6), which is typical of cellulosic feedstocks made up of a glucosidic backbone. While this fraction naturally decreases in blends of decreasing fractional green waste in the feed, the decrease is greater than anticipated based simply on mass balance considerations. The dashed lines in **Figure 3-5** represent the weighted average of relative abundances in each class for individual feed distributions. These dashed lines can be considered to be the expected distributions of a physical blend with no emergent behavior. Any deviation from this line represents emergent behavior that either promotes or suppresses the formation of each group upon blending of the feedstocks. The largest variance occurs in classes with five or more oxygen, which are diminished

upon blending with GW. Interestingly, while all blends have decreased oxygenate heteroatom abundance relative to the value expected from physical mixing, the reduction is most exaggerated in the 50:50 and 25:75 blends, where the most deoxygenation was observed in **Figure 3-1** and attributed to emergent or synergistic formation of CO_2. This is further supported by the data shown in **Figure B3-11** which contains the H, N, and O content of the biocrudes, showing a 30% oxygen reduction in the 50:50 biocrude compared to the expected value.

Figure 3-5b shows data obtained from FT-ICR MS analysis corresponding to nitrogen reduction relative to the feed. Increasing GW fraction results in increases in the relative abundance of nitrogen-containing species to values greater than predicted by simple additive mixing, suggesting that emergent behavior partitions more nitrogen into the biocrude diverting from the char or aqueous phases. This is also consistent with the proximate elemental analysis which observed elevated nitrogen in the 50:50 blend (**Table B3-4**). The elemental analysis showed the highest oxygen content in GW biocrude, followed closely by the 25:75, where the remaining three biocrudes have oxygen contents within 1% of each other (**Table B3-5**). FT-ICR MS analysis reveals that there is also a decrease in oxygen class abundance, as observed in **Figure 3-5**. The emergence of nitrogen-oxygen classes in the FT-ICR MS suggests that the decrease in oxygen class abundance is not due to a bulk change in oxygen partitioning from the biocrude, but instead due to chemical interactions between molecular intermediates to create new nitrogen-oxygen compounds. The differences in abundance from the theoretical prediction in the N_xO_y classes and O_y classes in the 50:50 biocrude results in similar HHV for the 50:50 and 75:25 biocrudes at 34.2 MJ/kg, and 34.3 MJ/kg, respectively.

Species that contain six oxygens (O_6) correspond to the average relative abundance in the green waste biocrude. Molecules that contain six oxygen are consistent with cellulose and

potentially lignin precursors. Of these, the glucose backbone of cellulose has the molecular formula $C_6H_{12}O_6$, which would give rise to O_6 heteroatom products. On the other hand, lignin is composed of an array of cross-linked phenol-derivatives as well as furans, each containing one oxygen. Incomplete depolymerization of lignin has the potential to produce large ionizable molecules with six oxygens.[43, 44] However, the molecular weight of glucose (180.16 g mol^{-1}) is on the cusp of potentially identifiable compounds by FT-ICR MS and the low K_{OW} (0.001) of glucose indicates that it would not partition to the biocrude upon separation. Lignin oligomers with six oxygen atoms would be much larger than glucose, owing to differences in oxygen content in lignin and cellulose, and lignin oligomers would have greater biocrude solubility than simple sugars. These considerations strongly suggest lignin as the primary source of these observed O_6 compounds present in GW-derived biocrudes.

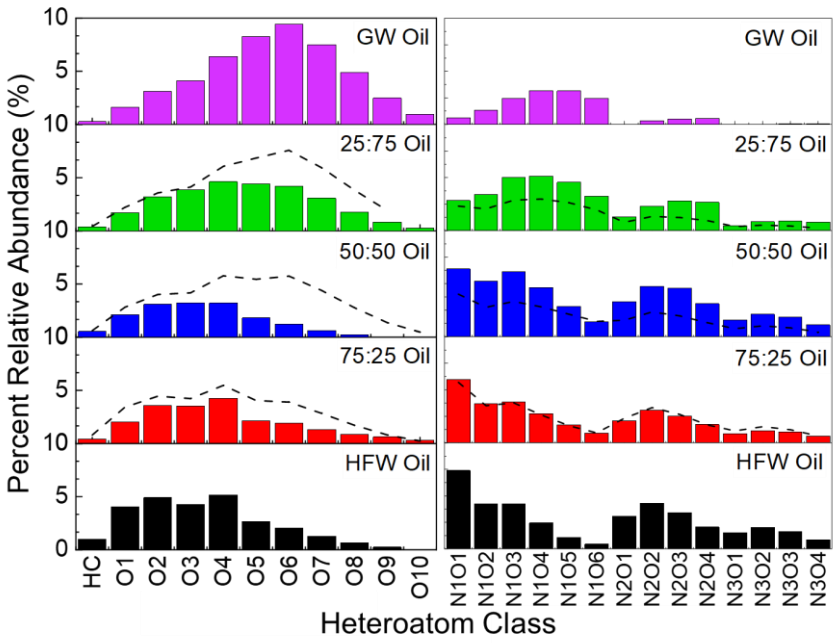

Figure 3-5. **a)** Oxygen heteroatom class distributions derived from 21 tesla (+) APPI FT-ICR MS mass spectra of the five biocrudes. **b)** Nitrogen-oxygen heteroatom class distributions of the five biocrude samples. The dashed lines are a model depicting the predicted weighted average of food and green waste component contributions.

3.3.5 COMPOSITIONAL TRENDS : DBE VERSUS CARBON NUMBER

Because FT-ICR MS provides elemental composition assignment, compositional trends within heteroatom classes can be rapidly visualized by plotting double bond equivalents (DBE, number of rings plus double bonds to carbon, calculated from the elemental composition

$$\text{DBE} = C - H/2 + N/2 + 1)^{45} \qquad (3.2)$$

for each class. **Figure 3-6** plots DBE versus carbon number for only the unique species identified in each biocrude for a suite of nitrogen-oxygen heteroatom classes.

The differences in compositional space coverage seen in **Figure 3-6** provide details on the effects of feedstock mixing. All shades of gray represent species identified in at least two of the

mixed-feed biocrudes whereas red, blue, and green represent those species unique to 75:25, 50:50, and 25:75 biocrudes, respectively. Light blue species are those identified in all five biocrude samples. From this analysis, it can be seen that the majority of the emergent species in the $N_1O_{1\text{-}4}$ classes occur at larger carbon numbers (between 30 – 40) than they appear in food and green waste biocrudes. Unique species in the N_1O_1 class span the full range of double bond equivalents from one to twenty, an indication that emergence is not specific to green waste-derived aromatic compounds nor to aliphatic food waste compounds, but instead represent the condensation of the two species types.

The FT-ICR MS data presented here begins to provide further details on the chemical makeup of the observed emergent behavior. The DBE vs. carbon number plots in **Figure 3-6** provide information on the differing distributions for select heteroatom classes produced by each biocrude and the apparent increase in carbon number range with the addition of green waste. The increased carbon number can be seen clearly in the N_1O_3 and N_1O_4 classes, wherein the region with carbon number greater than 30 and DBE greater than 20 are nearly solely populated by green waste biocrude species—these species no longer appear in the presence of food waste, suggesting that they are a reactive fraction that likely lead to formation of the heavy emergent species observed in N_2O_3 and N_2O_4 classes. Similarly, the N_2O_4 class highlights the emergence of species in this same region in the 25:75 biocrude. With carbon number greater than 35 and the knowledge of the heteroatom class, this can be attributed to polymerization reactions between protein-derivatives and sugar-derivatives, i.e., the Maillard reaction.

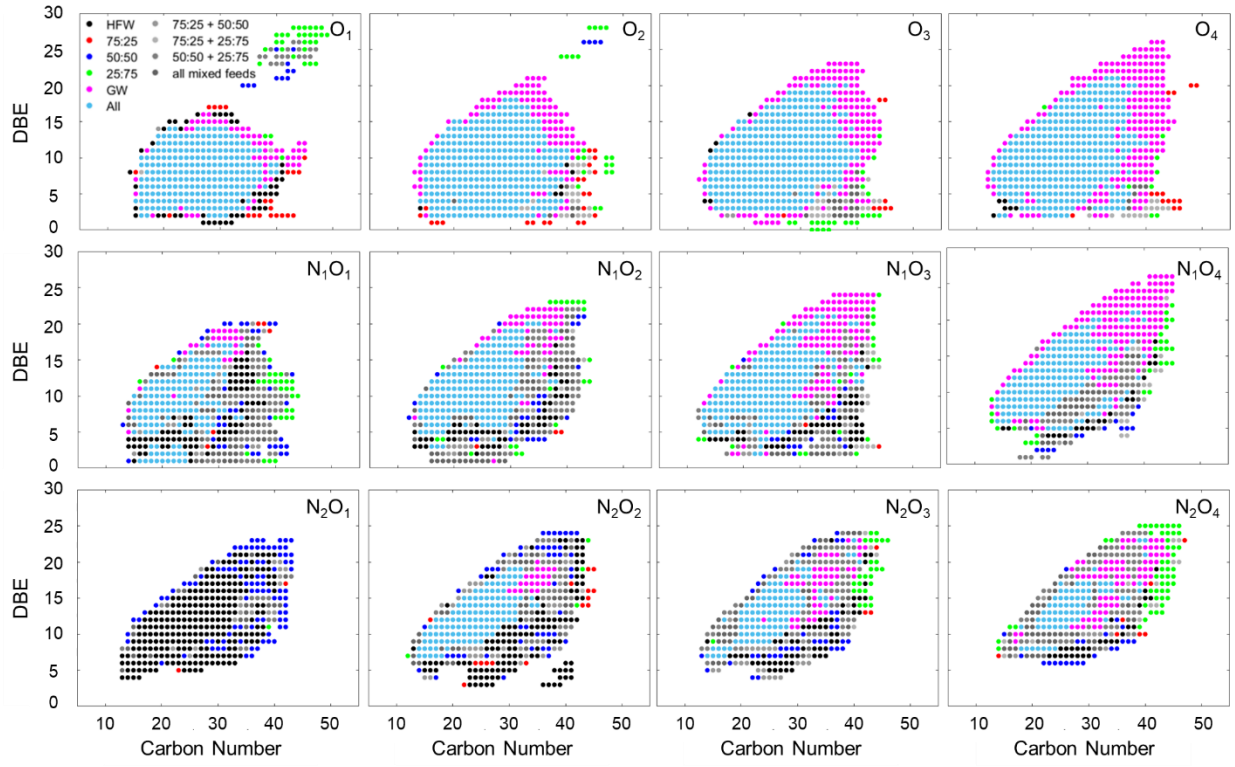

Figure 3-6. Double bond equivalency as a function of carbon number for the $O_{1\text{-}4}$, $N_1O_{1\text{-}4}$, and $N_2O_{1\text{-}4}$ heteroatom classes depicting species derived from the (+) APPI FT-ICR mass spectra of the five biocrude samples.

The most reactive components present in food waste can be determined by identifying which unique species disappear upon blending. In **Figure 3-6,** the N_2O_1 heteroatom class visually stands out from the rest due to the lack of light blue and magenta, and the dominance of black points that represent the fraction of green waste that otherwise reacted in blends. Those reactive points (black) generally represent the low-oxygen containing light compounds. These are likely protein derivatives, such as amino acids and short chain peptides that would otherwise readily react with oxygenates to form the larger emergent molecules upon feedstock blending with green waste. Furthermore, the prevalence of emergent compounds in the 50:50 biocrude (blue) is observed within the N_2O_1 class, primarily occurring at carbon numbers above 35 and DBE greater than 15.

These species are most likely the result of the interaction between green waste-derived oxygenated aromatics with protein-derivatives in Maillard-type reactions, which were previously shown to be dominant at stoichiometric ratios of proteins (food waste) and oxygenates (green waste).[20] This finding supports the previous hypothesis for FAME production, wherein highly aromatic molecules derived from lignin and cellulose react with straight chain molecules from lipids and less aromatic molecules in protein[20] to increase the relative abundance of compounds with intermediate DBE values.

Figure 3-7 represents modified van Krevelen plots of emergent species used to elucidate the effect of nitrogen and oxygen heteroatoms on the biocrude formation. **Figure 3-7** shows an interesting molecular weight periodicity that appears in the 50:50 biocrude as N/C and O/C ratio increase. Increasing heteroatom content, i.e. N_2, N_3, results in a dampening effect wherein H/C ratio spans the entire range in the N_1 range and decreases to 1 – 2. The dampened periodicity with heteroatom content corresponds to the addition of one nitrogen or one oxygen, a potential clue into polymerization reactions. The periodicity in O/C ratio is seen clearly in the emergent molecules (**Figure B3-12**), formed by the interaction between nitrogen-containing protein in the food waste with heavy oxygen-containing lignin molecules. The overall shape of the data is indicative of increased aromaticity in high N/C and O/C ratio compounds, as the maximum H/C value in **Figure 3-7a and b** decreases from nearly 2.5 to 1.5.

Figure B3-13 shows the modified van Krevelen diagrams colored by molecular mass for the biocrudes obtained from food and green waste feedstocks, highlighting that the recurrent trend in molecular weight seen in **Figure 3-7** is emergent and not present as clearly in biocrudes obtained from either of the pure feeds. The areas of high molecular weight (MW > 600) repeat every 0.025 in N/C, corresponding to the approximate addition of 1 nitrogen for 36 carbon. These periodic

repeating distributions are consistent with the expectation that reaction intermediates have molecular distributions similar to their constitutive amino acids; for each monomer containing one nitrogen (N_1), for example, there is a distribution of carbon numbers (glycine N/C = 1/2; phenylalanine N/C = 1/9). Furthermore, for each monomer, there is also a distribution of number of nitrogen atoms (glycine N = 1, arginine N = 4). These two distributions within the feed material result in overlapping yet periodic distributions. The same trend holds true with oxygen-containing intermediates. It is also important to remember that only emergent molecules are shown, indicating that this pattern is based on the interaction between food and green waste components.

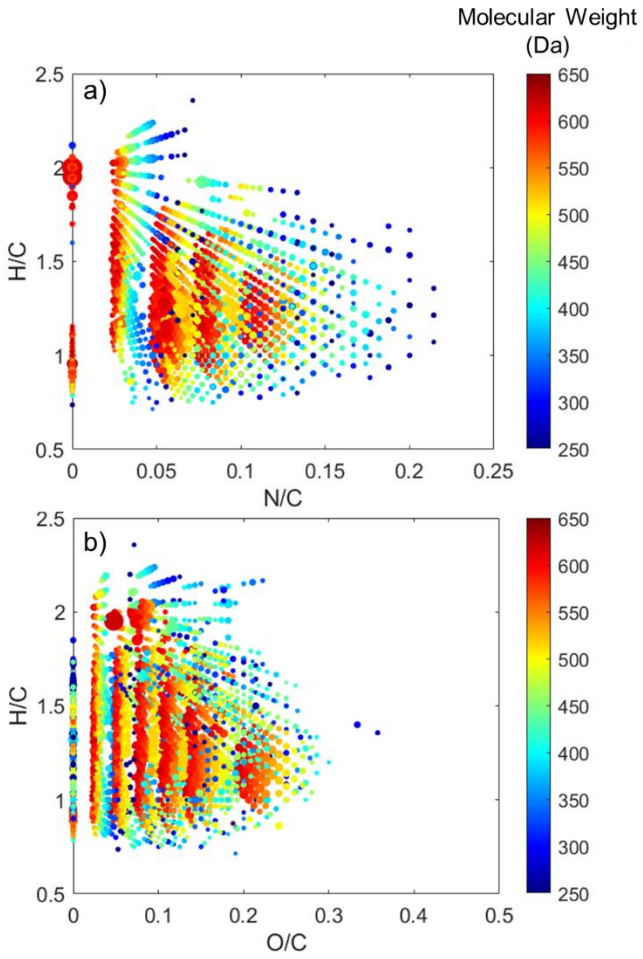

Figure 3-7. (a) Modified van Krevelen plot comparing H/C ratio to N/C ratio for the emergent molecules identified in the 50:50 biocrude colored by molecular mass (determined by m/z ratio). **(b)** Van Krevelen plot comparing H/C ratio to O/C ratio for the emergent molecules identified in the 50:50 biocrude colored by molecular mass.

Repeating units in O/C ratio (**Figure 3-7b**) are similar in magnitude to those for nitrogen (**Figure 3-7a**), occurring with a period of 0.023 O/C. More interestingly, however, is that biocrudes from pure food and green waste do not exhibit the same strong trend in O/C ratio (**Figure B3-13**). At O/C < 0.1, food waste biocrude begins to show the same periodicity but the trend disappears above this ratio, whereas green waste biocrude has a region of high molecular weight compounds spanning from 0.1 – 0.3 O/C and centered around H/C of unity. The presence of emergent

molecules in **Figure 3-7b**, however, are clearly visible across all O/C ratios, further corresponding to an increase in oxygen number as supported by **Figure B3-13**. The appearance of this trend upon mixing food and green waste supports interpretation of a synergistic polymerization wherein oxygen-containing molecules are increasing in size due to coupling with nitrogen-containing molecules or hydrocarbons from food waste, thereby decreasing the O/C ratio and increasing the molecular mass. The way in which the trend holds true for both oxygen and nitrogen classes with near-equal periodicity indicates the phenomenon is a direct result of nitrogen-oxygen coupling reactions, such as the Maillard reaction. These reactions condense a reactive oxygen with a reactive amino group, effectively terminating or capping the two chemistries via the condensation reaction. The maximum molecular mass of approximately 600 Da is due to limitations of the FT-ICR MS analysis technique and may also be indicative of capping reactions due to Maillard reactions.[20, 46]

3.4 DISCUSSION

3.4.1 EMERGENT CHEMICAL PATHWAY ANALYSIS

Figure 3-8 is a schematic representation of the reaction chemistry observed here under hydrothermal conditions, highlighting the emergent chemistries that only become apparent upon blending feeds. Collectively, biocrude yields reported in **Figure 3-1** are consistent with the commonly held model that HTL involves hydrolysis and depolymerization of macromolecules that form short chain reactive species that then condense to form increasingly larger molecules that partition into the aqueous, organic, and solid phases, respectively.[2] Food and green waste feedstocks produce biocrude molecules with different levels of complexity and heteroatoms that promote specific chemical pathways when feedstocks are mixed in varying ratios prior to HTL. With food waste-rich blends, esterification reactions of the fatty acids and other oxygenates result in biocrude containing esters and an overall increase in the oxygen content of the biocrude relative

to that obtained from pure food waste.[3] At equal HFW-GW blending ratios, which possess near-stoichiometric amounts of protein and carbohydrates, sharp decreases in oxygen classes and increased abundance in nitrogen-oxygen heteroatom classes are observed, consistent with reactions such as the Maillard reaction to couple reducing sugars and amino acid derivatives.[20] The 25:75 food waste:green waste blend undergoes more decarboxylation than the other feeds, resulting in a biocrude with relatively increased carbon number and DBE, indicative of polymerization reactions involving nitrogen reacting with cellulose and hemicellulose from green waste. Interestingly, the polymerization reactions terminate while molecules remain in the fuel-range of the biocrude resulting from food waste, rather than forming heavy compounds in the residue range (**Figure 3-2**) or char phase (**Figure 3-1**)—both of which are otherwise prevalent in the products of different feeds, especially for HTL of food waste. While the green waste streams benefit from decarboxylation reactions that lower the oxygen heteroatomic content of the biocrude (**Figure 3-5**), the resulting mixture is more prone to char formation, resulting in insufficient capping to prevent polymerization.[47]

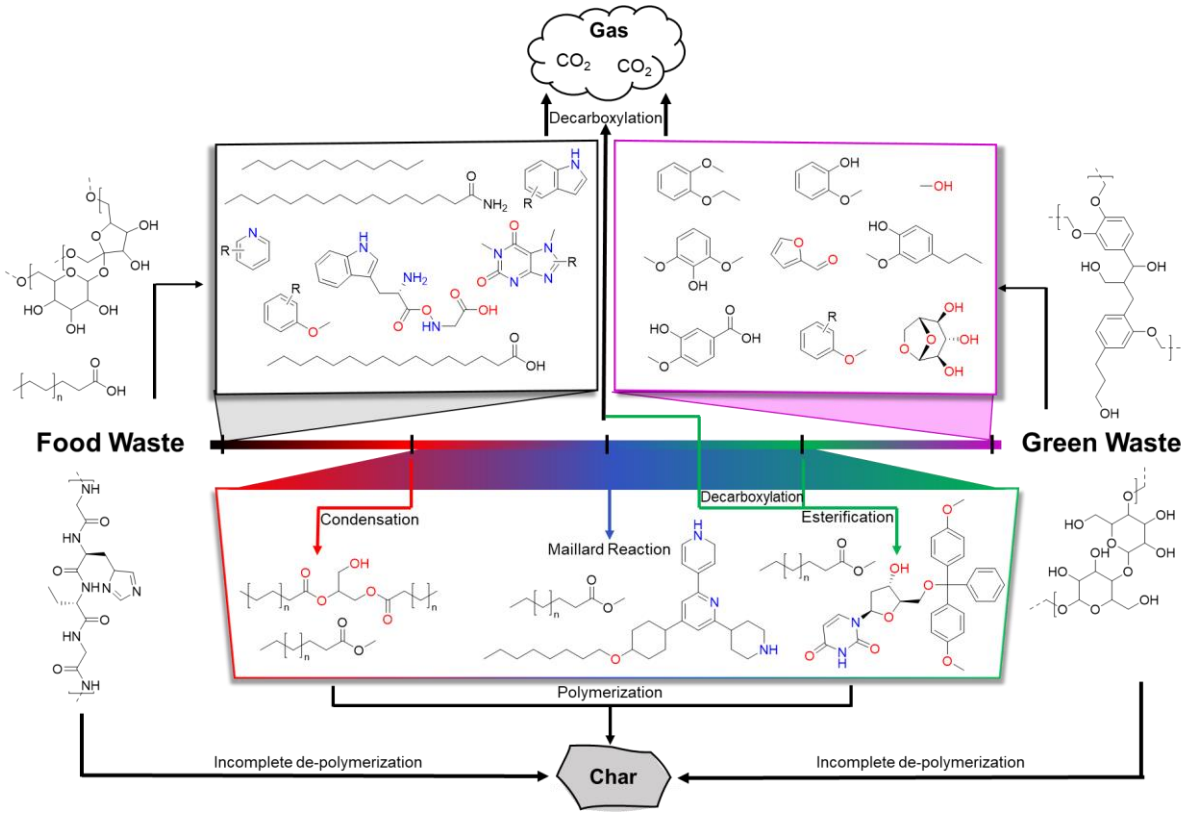

Figure 3-8. Chemical representation of characteristic molecules found in the biocrudes resulting from the interactions between food and lignocellulosic green waste components to produce new biocrude molecules. Compounds in all black are identified with GC-MS or literature.

The combined analytical observations provide a detailed picture of the chemical interactions that form biocrude from mixed food waste and green waste feedstocks. **Figure 3-8** captures the key molecular details governing HTL of pure food waste and green waste feedstocks as well as the transition to feed mixtures. Hydrolysis and thermolysis of proteins, lipids, and carbohydrates is represented by singular arrows from the feedstocks to the reactive intermediates.[48] Consistent with prior literature, food waste HTL results in a suite of fatty acids and nitrogen-containing compounds derived from food waste's protein content as well as the Maillard reaction for the interaction between amino acid and sugar derivatives.[5, 29] Fatty acids and amides are

confirmed primarily through the use of GC-MS, and the presence of substituted fatty amides is corroborated by the FT-ICR MS abundance at high H/C and low N/C values in **Figure 3-7**. The formation of char can progress through hydrothermal carbonization, whereby incomplete feedstock depolymerization is combined with repolymerization reactions to form insoluble products.[6] Additionally, polymerization of small molecules can continue until molecules are too large to remain soluble, thereby forming char.[49]

3.4.2 EMERGENT CHEMISTRY

Emergent behavior arises from several sources, the simplest of which is transesterification of triglycerides from the lipid fraction of food waste and the esterification of their fatty acid derivatives. **Figure 3-8** shows the composition-dependent interactions giving rise to increased biocrude yield in a 75% food waste, 25% green waste feedstock mixture arising from coupling reactions with cellulose and lignin monomers and also resulting in higher-than-expected oxygen content in that biocrude (**Figure B3-11**). HTL of food waste-rich feeds is associated with high biocrude yields, and the chemical composition of the corresponding biocrudes contain substantial fractions of fatty acids and fatty amides that were not fully converted to aliphatic FAMEs.[3, 50] By introducing green waste, the transesterification drastically reduces the fatty acid content, favoring production of FAMEs, as observed by the GC-MS peak areas for fatty acids and FAMEs in the mixed-feed biocrudes, particularly the 25:75 mixture shown in **Figure 3-4b**. Notably, FAMEs are not identified in either of the pure food or green waste biocrudes due to the lack of methanol, resulting in solely hydrolysis. Due to their high abundance in the 25:75 biocrude, it can be interpreted that FAME production in mixed-feed HTL requires high concentrations of cellulose, lignin, or ash. As the carbohydrate content of both food and green waste primarily decompose to glucose and its derivatives,[51] the FAME production is most likely enabled by reaction with lignin

derivatives. Lignin has been shown to produce methanol upon decomposition at elevated temperatures,[52] which allows for the transesterification reaction for FAME synthesis.[53] The transesterification reaction is a well-studied reaction pathway for the synthesis of fatty acid methyl esters for biodiesel from the reaction of fatty acids with methanol.[53]

Coupling reactions primarily impact compounds present in the diesel boiling point range, increasing them to a higher percentage than pure green waste biocrude and causing a corresponding decrease in the jet fuel range, meaning that emergent chemistry will not be captured in volatility-based gas chromatography. The esterification of fatty acids supports the increased fraction of diesel-range compounds in the 75:25 biocrude from thermogravimetric analysis. FT-IR highlights the presence of strong C-O stretching bands indicative of cellulose and lignin-based molecules, as expected, whereas FT-ICR MS identifies the greatest number of molecular formulae without nitrogen, a key factor in increased biocrude quality and upgrading potential.

In addition to FAME production, further evidence of emergent behavior is found in polymerization Maillard-type reactions that react amino acids from the food waste proteins and oxygenates from the lignocellulosic green waste carbohydrates. **Figure 3-5** shows increased $N_{1-2}O_{1-4}$ molecular abundance in the 50:50 biocrude compared to the expected value, coupled with a near-equal decrease in pure oxygenated heteroatom class abundance. This trend is consistent with Maillard-type reactions observed previously in hydrothermal food waste mixtures.[20, 27, 54] Maillard reactions occur between reducing sugars from cellulose decomposition with the food waste decomposition product of organic proteins into amino acids and is most prevalent in stoichiometric ratios.[26] **Figure 3-8** shows the composition-dependent reaction that gives rise to the equivalent N/C and O/C periodicity shown in **Figure 3-7**, consistent with increased relative abundance in the N_xO_y heteroatom classes in the 50:50 biocrude shown in **Figure 3-5**.

Decarboxylation of the heavily oxygenated biocrude formed from green waste and food waste is a final observation that can only be explained by emergent chemical pathways. Without this emergent chemistry, the pure feeds are prone to over-polymerization to chars, as observed with higher char yields (**Figure 3-1)** and heavy residue fractions in the pure feed biocrudes (**Figure 3-2**). When even a small fraction of food waste is blended into green waste, enhanced decarboxylation occurs, resulting in increased gas and char yields in the 25:75 reactions. Decarboxylation is a step in polymerization, removing CO_2 to combine molecules together in the same way that hydrolysis reactions enhance polymerization.[55, 56] Decarboxylation also plays a role in the decreased O_x class abundance seen with FT-ICR MS, and the increased nitrogen abundance from CHON. Borrowing from the hydrothermal carbonization (HTC) literature, lignocellulosic biomass has been shown to undergo extensive decarboxylation to char with increasing reaction severity (i.e. time and temperature), i.e., conditions that are milder yet similar to those used in this study.[57] Dissolved solids from cellulose and hemicellulose degradation polymerize in water via a decarboxylative polymerization to form water insoluble polymers, as evidenced by the increased char fraction of the 25:75 blend, and heavy residue in the respective biocrude, as evidenced by the large residue fraction identified with TGA (**Figure 3-2**).[57, 58]

3.4.3 CO-LIQUEFACTION BENEFITS

Co-liquefaction introduces another layer of complexity to a reactive environment that already produces tens of thousands of unique compounds across three phases through thousands of reaction pathways. The present work shows that feeds can be strategically combined to suppress undesired chemistries present in the pure feedstocks while promoting desirable and new pathways, for example decarboxylation to minimize char formation or Maillard reactions to promote biocrude yields. While adding food waste to green waste does increase the nitrogen of the resulting biocrude,

which will complicate subsequent upgrading efforts,[15, 59] thermogravimetric analysis and FT-ICR MS show that those nitrogen compounds cap the green waste biocrudes to usable molecular weights that would otherwise contain the highest fraction of residue-range compounds, typically regarded as un-usable. Accordingly, adding green waste to food waste does not drastically detract from biocrude quality and has the potential to increase yields while further buffering the supply chain with the addition of plentiful lignocellulosic waste. Co-processing also results in increased energy recovery compared with otherwise low-yielding lignocellulosic wastes, a frequent problem, while also increasing quality by partially deoxygenating prior to downstream refining. Further research should explore the effect of green waste composition on yields and biocrude quality.

3.5 CONCLUSIONS

Co-processing of a green waste and food waste stream was studied under HTL conditions, with subsequent molecular analysis of the biocrude products. Co-processing of a high-lipid food waste with up to 25% cellulose-rich lignocellulosic green waste results in biocrude yields greater than 45% and energy recovery greater than 50%. HTL of blended food and green waste streams resulted in emergent chemical behavior that promotes oil yields at low blend ratios by a combination of esterification, Maillard reactions, and polymerizations. GC-MS revealed the emergence of fatty acid methyl esters in mixed-feed HTL biocrudes that were not present in either individual feedstock. Thermogravimetric analysis confirmed desired molecule size and volatility emergence in the biocrudes before molecular level analysis was performed using (+) APPI FT-ICR MS to reveal deoxygenation and capping trends.

This work begins to unravel the complex reaction networks associated with hydrothermal waste conversion, illuminating both mechanisms and strategies for controlling product

distributions, yields and quality using molecular-level feedstock engineering. Chemistries governing mixed-feed HTL were identified by examining heteroatom trends in biocrude products. An abundance of lignocellulosic material leads to over-polymerization via decarboxylation pathways due to high [OH] functionality pushing molecules from oil-soluble to the solid phase, whereas equal amounts of food and lignocellulosic-based molecules favor Maillard-type reactions that effectively terminate the polymerization at chain lengths that partition into the oil phases. Furthermore, these synergistic reactions result in CO_2 evolution, resulting in substantial deoxygenation and char mitigation. These findings greatly advance the scientific understanding of co-HTL as a practical strategy for biocrude maximization that can also improve supply chain management.

3.6 APPENDIX B

3.6.1 GC-MS METHODOLOGY.

Gas chromatography mass spectrometry was performed using an Agilent 6890N gas chromatogram equipped with an Agilent 5973N mass spectrometer. Samples were diluted 1:100 in acetone before injection of 0.5µL at a 25:1 split ratio with constant flow of helium carrier gas. Inlet temperature was set to 270 °C. The oven was initially heated to 40 °C and utilized a ramp of 10 °C/min to a temperature of 170 °C before reducing the ramp rate to 3 °C until a final temperature of 270 °C was reached. The column utilized was an HP-5.

3.6.2 (+) APPI FT-ICR MS METHODOLOGY.

Biocrude (and aqueous) samples were diluted in (50/50, by volume) toluene/tetrahydrofuran (THF) to a concentration of 125 µg/mL for analysis by positive-ion (+) atmospheric pressure photoionization (APPI) Fourier transform ion cyclotron resonance mass

spectrometry (FT-ICR MS) at 21 tesla. Toluene and THF increased the ionization efficiency of nonpolar aromatic compounds[60, 61] through charge exchange,[62, 63] and proton transfer[64] reactions between ionized toluene molecules and neutral analyte molecules. An atmospheric pressure photoionization (APPI) source (Thermo-Fisher Scientific, San Jose, CA) was coupled to the first stage of a custom-built FT-ICR mass spectrometer (see below) through a custom-built interface.[65] Typical conditions for positive-ion APPI were: S-lens RF level: 45%; sweep gas: 300 °C and heated metal capillary temperature: 350 °C. A Hamilton gastight syringe (2.5 mL) and syringe pump were used to deliver the sample (50 μL/min) to the heated vaporizer region (350 °C) of the APPI source, where N_2 sheath gas facilitates nebulization. After nebulization, gas-phase neutral analyte molecules exit the heated vaporizer region as a confined jet. A krypton vacuum ultraviolet gas discharge lamp (Syagen Technology, Inc., Tustin, CA) produced 10 −10.2 eV photons (120 nm).

All samples were analyzed with a custom-built FT-ICR mass spectrometer[35, 36, 66] equipped with a 22 cm horizontal room temperature bore 21 T superconducting solenoid magnet (Oxford Instruments, Abingdon, U.K.), and a modular ICR data station (Predator)[67] facilitated instrument control, data acquisition, and data analysis. Positive ions generated at atmospheric pressure were accumulated in an external multipole ion guide (1-5 ms) and released *m/z*-independently by decrease of an auxiliary radio frequency potential between the multipole rods and the end-cap electrode.[68] Ions were excited to *m/z*-dependent radius to maximize the dynamic range and number of observed mass spectral peaks (32-64%)[68] and excitation and detection were performed on the same pair of electrodes.[69] The dynamically harmonized ICR cell in the 21 T FT-ICR is operated with 6 V trapping potential.[68, 70] Time-domain transients of 3.1 seconds were conditionally co-added and acquired with the Predator data station that handled excitation and detection only,

initiated by a TTL trigger from the commercial Thermo data station, with 100 time-domain acquisitions averaged for all experiments.[67] Mass spectra were phase-corrected[71] and internally calibrated with 10-15 highly abundant homologous series that span the entire molecular weight distribution based on the "walking" calibration method.[72] Experimentally measured masses were converted from the International Union of Pure and Applied Chemistry (IUPAC) mass scale to the Kendrick mass scale[73] for rapid identification of homologous series for each heteroatom class (i.e., species with the same $C_cH_hN_nO_oS_s$ content, differing only be degree of alkylation)[74]

For each elemental composition, $C_cH_hN_nO_oS_s$, the heteroatom class, type, double bond equivalents, (DBE = number of rings plus double bonds to carbon, DBE = C − h/2 + n/2 + 1),[75] and carbon number, c, were tabulated for subsequent generation of heteroatom class relative abundance distributions and graphical relative-abundance weighted DBE versus carbon number images and van Krevelen diagrams.[76] Peaks with signal magnitude greater than 6 times the baseline root-mean- square noise at m/z 500 were exported to peak lists, internally calibrated based on the "walking calibration"[77] and molecular formula assignments and data visualization were performed with PetroOrg software[78] Molecular formula assignments with an error >0.5 ppm were discarded, and only chemical classes with a combined relative abundance of ≥0.15% of the total were considered.

Table B3-2. Feedstock composition from the mixed food and green waste feeds.

	Food Waste	**75:25 FW:GW**	**50:50 FW:GW**	**25:75 FW:GW**	**Green Waste**
Carbon	52.20	49.70	47.20	44.70	42.20
Hydrogen	7.50	6.92	6.34	5.76	5.18
Nitrogen	4.30	3.28	2.27	1.25	0.23
Sulfur	1.00	0.93	0.87	0.80	0.73
Oxygen	33.20	37.82	42.44	47.05	51.67
H/C_{eff}	0.55	0.35	0.13	0	0

Table B3-3. Experimental product yields (as C%) for all biocrude samples, as well as theoretical product yields for the mixed feeds and percent volatile organics in the biocrude phase as determined from thermogravimetric analysis.

	Carbon Recovery (%)								
	Exp. Biocrude	**Theor. Biocrude**	**Exp. Aqueous**	**Theor. Aqueous**	**Exp. Solid**	**Theor. Solid**	**Exp. Gas**	**Theor. Gas**	**Volatile Compounds (%)**
Hospital FW	47.3	-	20.4	-	28.16	-	6.97	-	59.1
75:25 HFW:GW	47.9	41.9	19.8	22.3	27.50	30.5	8.24	7.2	56.8
50:50 HFW:GW	34.9	36.5	18.8	24.3	30.54	32.8	11.56	7.4	55.3
25:75 HFW:GW	26.8	31.1	22.8	26.2	38.42	35.1	12.21	7.7	41.9
Green Waste	25.8	-	28.1	-	37.40	-	7.89	-	37.4

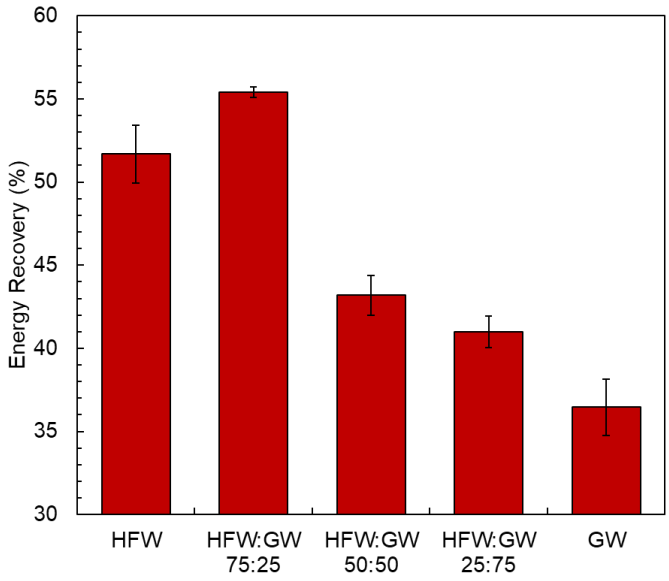

Figure B3-9. Energy recovery (%) for each biocrude taken as a function of the energy density and yield of biocrude as a fraction of the total energy density contained in the feed.

Table B3-4. Carbon, hydrogen and nitrogen content of each biocrude as measured with elemental analysis. Oxygen content was determined by difference. Higher heating value and energy recovery are reported as measured.

	Hosp. FW HTL	75:25 HFW:GW	50:50 HFW:GW	25:75 HFW:GW	GW HTL
C (%)	68.77	69.97	70.36	65.07	64.22
H(%)	9.22	9.38	9.22	9.81	7.43
N (%)	3.64	3.45	3.33	3.49	1.09
O (%)	18.38	17.2	17.09	25.63	27.26
HHV (MJ/kg)	34.01	34.31	34.24	33.98	29.07
Energy Recovery (%)	51.69	58.68	49.46	52.55	55.94

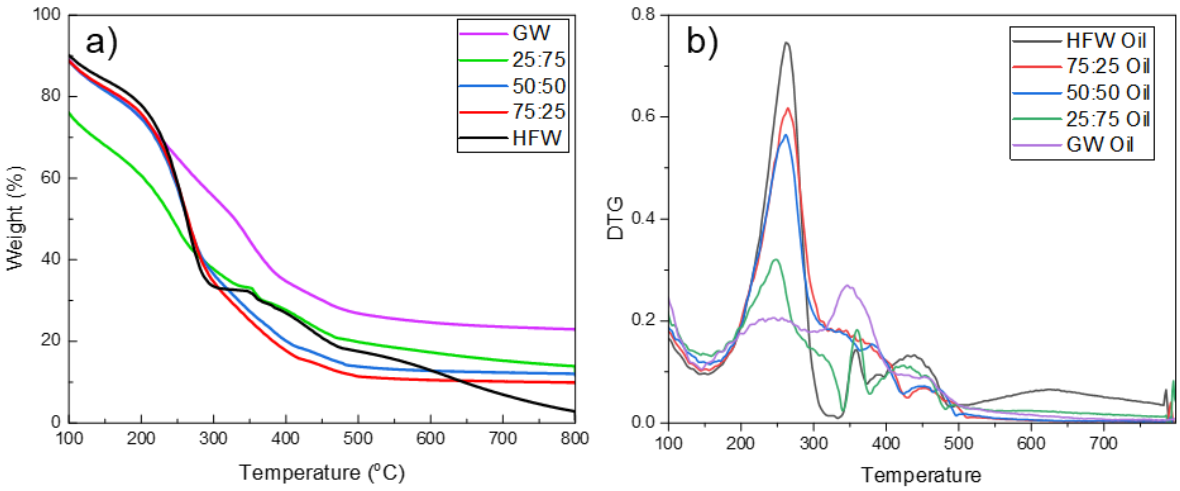

Figure B3-10. Raw data obtained from thermogravimetric analysis of the five biocrude samples. **a)** Raw weight percent from TGA. **b)** derivative of TGA, in units of weight loss per degree C. Gasoline = <190 °C, jet fuel = 190-290 °C, diesel = 290-340 °C, vacuum gas oil = 340-540 °C, residue = >540 °C.

Table B3-5. Numbered GC-MS peak identities and the samples in which they were identified.

Peak Number	Retention Time (min)	Identity	Samples Identified
1	3.62	methyl propyl ketone	HFW, 75:25, 50:50, 25:75
2	6.51	isopropenylbenzene	HFW, 25:75
3	12.38	dodecane	HFW
4	29.97	palmitic acid	HFW, 75:25, 50:50, 25:75
5	33.05	9,12-octadecadienoic acid	HFW, 75:25, 50:50, 25:75
6	33.19	stearic acid	HFW, 75:25, 50:50, 25:75
7	33.29	octadecenoic acid	HFW, 75:25, 50:50, 25:75
8	33.59	stearic acid	HFW, 75:25, 50:50
9	9.33	2-methoxyphenol	25:75, GW
10	14.48	4-ethylguaiacol	25:75, GW
11	16.38	syringol	25:75, GW
12	16.77	2-methoxy-4-propylphenol	25:75, GW
13	29.18	hexadecanoic acid methyl ester	75:25, 50:50, 25:75
14	32.4	octadecanoic acid methyl ester	75:25, 50:50, 25:75
15	18.1	3-hydroxy-4-methoxybenzoic acid	25:75, GW

Table B3-6. Bands identified in Fourier transform infrared spectroscopy in all biocrudes.

Wavenumber (cm^{-1})	Identity
1604	C=C aromatic, alkene
1516	C=C aromatic, (phenolics) or C=N (amino acid, amide)
~1469	CH_2 lipids
~1330	C-O phenolics
~1200	C-O phenolics
1114	C-O alcohols, phenols, acids
1092	C-C-O phenolics
1030	C-O O-CH_3 phenolics

Table B3-7. Gaussian fitting parameters for the distribution of abundances versus oxygen heteroatom class for all biocrude samples.

	μ	St. Dev	Area
HFW Oil	2.66	3.46	8.1
75:25 Oil	3.38	3.59	17.2
50:50 Oil	-	-	-
25:75 Oil	4.57	5.81	41
GW Oil	5.63	4.18	45.4

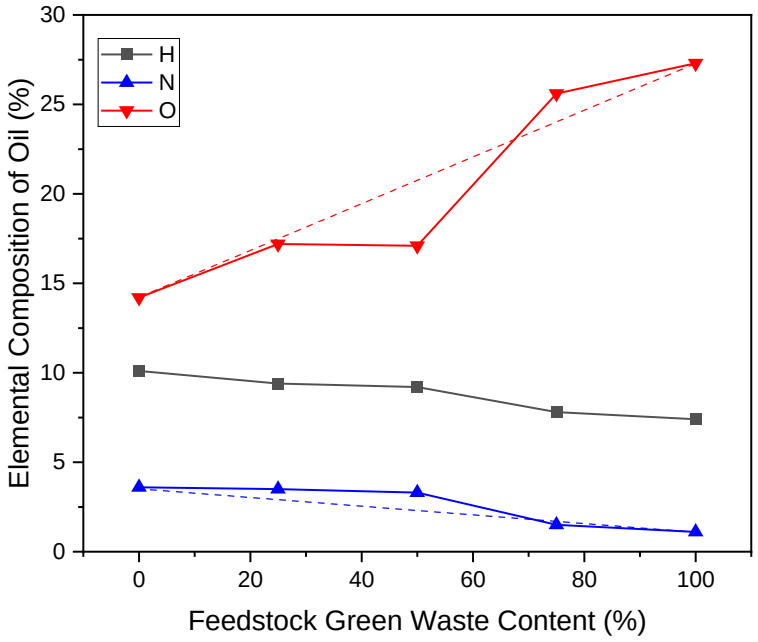

Figure B3-11. Heteroatom composition of the resultant biocrudes obtained through elemental analysis and their expected theoretical trends.

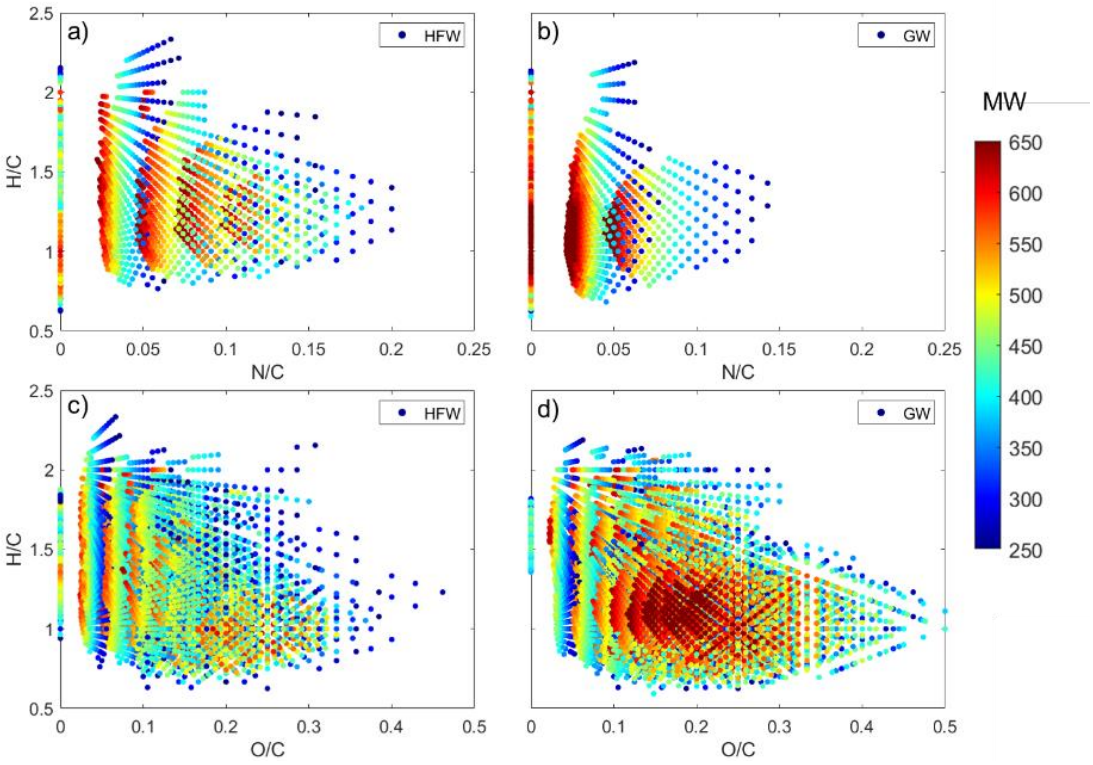

Figure B3-12. Modified van Krevelen plot comparing H/C ratio to N/C and O/C ratio for all molecules identified in food and green waste biocrudes colored by molecular mass as determined from m/z ratio using FT-ICR MS.

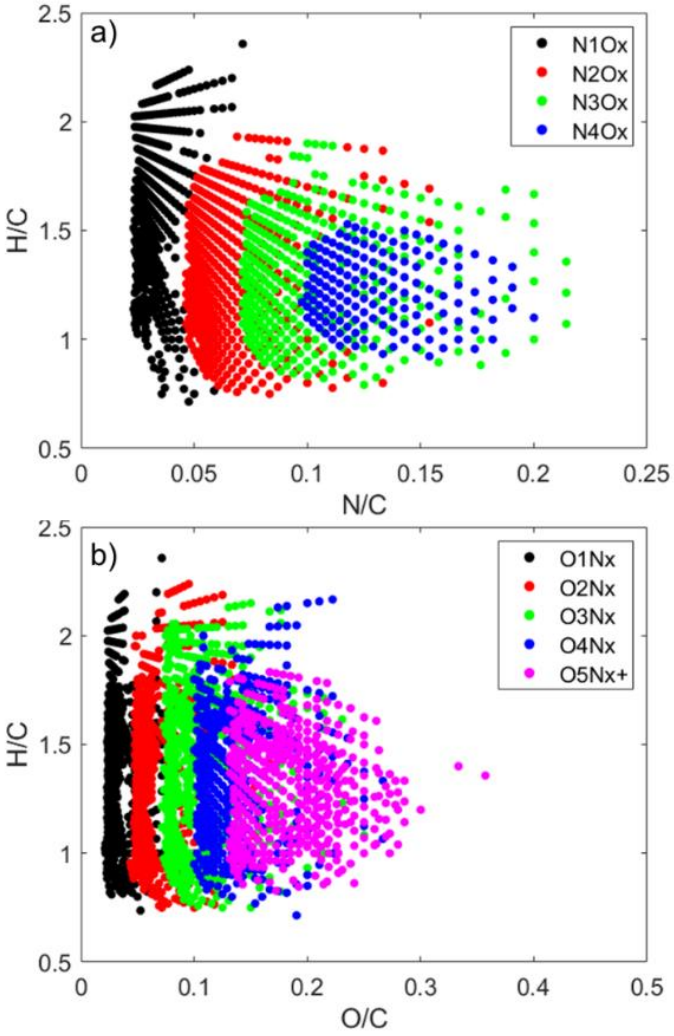

Figure B3-13. (a) Nitrogen van Krevelen plot divided into nitrogen heteroatom classes. (**b**) Oxygen van Krevelen plot divided into oxygen heteroatom classes.

3.7 REFERENCES

1. Schanes, K.; Dobernig, K.; Gözet, B., Food waste matters - A systematic review of household food waste practices and their policy implications. *Journal of Cleaner Production* **2018,** *182*, 978-991.

2. LeClerc, H. O.; Tompsett, G. A.; Paulsen, A. D.; McKenna, A. M.; Niles, S. F.; Reddy, C. M.; Nelson, R. K.; Cheng, F.; Teixeira, A. R.; Timko, M. T., Hydroxyapatite catalyzed hydrothermal liquefaction transforms food waste from an environmental liability to renewable fuel. *iScience* **2022**, 104916.

3. Gollakota, A. R. K.; Kishore, N.; Gu, S., A review on hydrothermal liquefaction of biomass. *Renewable and Sustainable Energy Reviews* **2018,** *81*, 1378-1392.

4. Aierzhati, A.; Stablein, M. J.; Wu, N. E.; Kuo, C.-T.; Si, B.; Kang, X.; Zhang, Y., Experimental and model enhancement of food waste hydrothermal liquefaction with combined effects of biochemical composition and reaction conditions. *Bioresource Technology* **2019,** *284*, 139-147.

5. D.J. Zastrow, P. A. J. In *Hydrothermal Liquefaction of Food Waste and Model Food Waste Compounds*, AIChE, San Francisco, CA, San Francisco, CA, 2013.

6. Katakojwala, R.; Kopperi, H.; Kumar, S.; Venkata Mohan, S., Hydrothermal liquefaction of biogenic municipal solid waste under reduced H2 atmosphere in biorefinery format. *Bioresource Technology* **2020,** *310*, 123369.

7. Minowa, T.; Murakami, M.; Dote, Y.; Ogi, T.; Yokoyama, S.-y., Oil production from garbage by thermochemical liquefaction. *Biomass and Bioenergy* **1995,** *8* (2), 117-120.

8. Elliott, D. C.; Biller, P.; Ross, A. B.; Schmidt, A. J.; Jones, S. B., Hydrothermal liquefaction of biomass: Developments from batch to continuous process. *Bioresource Technology* **2015,** *178*, 147-156.

9. Mishra, R. K.; kumar, V.; Kumar, P.; Mohanty, K., Hydrothermal liquefaction of biomass for bio-crude production: A review on feedstocks, chemical compositions, operating parameters, reaction kinetics, techno-economic study, and life cycle assessment. *Fuel* **2022,** *316*, 123377.

10. Xu, Y.-H.; Li, M.-F., Hydrothermal liquefaction of lignocellulose for value-added products: Mechanism, parameter and production application. *Bioresource Technology* **2021,** *342*, 126035.

11. Cheng, F.; Belden, E. R.; Li, W.; Shahabuddin, M.; Paffenroth, R. C.; Timko, M. T., Accuracy of predictions made by machine learned models for biocrude yields obtained from hydrothermal liquefaction of organic wastes. *Chemical Engineering Journal* **2022,** *442*, 136013.

12. Cheng, F.; Cui, Z.; Chen, L.; Jarvis, J.; Paz, N.; Schaub, T.; Nirmalakhandan, N.; Brewer, C. E., Hydrothermal liquefaction of high- and low-lipid algae: Bio-crude oil chemistry. *Applied Energy* **2017,** *206*, 278-292.

13. Bayat, H.; Dehghanizadeh, M.; Jarvis, J. M.; Brewer, C. E.; Jena, U., Hydrothermal Liquefaction of Food Waste: Effect of Process Parameters on Product Yields and Chemistry. *Frontiers in Sustainable Food Systems* **2021,** *5*.

14. Chen, W.-T.; Haque, M. A.; Lu, T.; Aierzhati, A.; Reimonn, G., A perspective on hydrothermal processing of sewage sludge. *Current Opinion in Environmental Science & Health* **2020,** *14*, 63-73.

15. Leng, L.; Zhang, W.; Peng, H.; Li, H.; Jiang, S.; Huang, H., Nitrogen in bio-oil produced from hydrothermal liquefaction of biomass: A review. *Chemical Engineering Journal* **2020,** *401*, 126030.

16. Li, H.; Liu, Z.; Zhang, Y.; Li, B.; Lu, H.; Duan, N.; Liu, M.; Zhu, Z.; Si, B., Conversion efficiency and oil quality of low-lipid high-protein and high-lipid low-protein microalgae via hydrothermal liquefaction. *Bioresource Technology* **2014,** *154*, 322-329.

17. Yang, L.; He, Q.; Havard, P.; Corscadden, K.; Xu, C.; Wang, X., Co-liquefaction of spent coffee grounds and lignocellulosic feedstocks. *Bioresource Technology* **2017,** *237*, 108-121.

18. Jarvis, J. M.; Billing, J. M.; Corilo, Y. E.; Schmidt, A. J.; Hallen, R. T.; Schaub, T. M., FT-ICR MS analysis of blended pine-microalgae feedstock HTL biocrudes. *Fuel* **2018,** *216*, 341-348.

19. Yang, J.; He, Q.; Yang, L., A review on hydrothermal co-liquefaction of biomass. *Applied Energy* **2019,** *250*, 926-945.

20. LeClerc, H. O.; Atwi, R.; Niles, S. F.; McKenna, A.; Timko, M. T.; West, R. H.; Teixeira, A. R., Elucidating the role of reactive nitrogen intermediates in hetero-cyclization during hydrothermal liquefaction of food waste. *Green Chemistry* **2022**.

21. Adewuyi, A., Underutilized Lignocellulosic Waste as Sources of Feedstock for Biofuel Production in Developing Countries. *Frontiers in Energy Research* **2022,** *10*.

22. Agency, E. P., RIN Trades and Price Information. 2021; Vol. 2021.

23. Debra L. Kantner, B. F. S. *Analysis of MSW Landfill Tipping Fees*; Environmental Research & Education Foundation: April 2019, 2019.

24. Biller, P.; Sharma, B. K.; Kunwar, B.; Ross, A. B., Hydroprocessing of bio-crude from continuous hydrothermal liquefaction of microalgae. *Fuel* **2015,** *159*, 197-205.

25. Lu, J.; Li, H.; Zhang, Y.; Liu, Z., Nitrogen Migration and Transformation during Hydrothermal Liquefaction of Livestock Manures. *ACS Sustainable Chemistry & Engineering* **2018,** *6* (10), 13570-13578.

26. Zhu, Z.; Liu, Z.; Zhang, Y.; Li, B.; Lu, H.; Duan, N.; Si, B.; Shen, R.; Lu, J., Recovery of reducing sugars and volatile fatty acids from cornstalk at different hydrothermal treatment severity. *Bioresource Technology* **2016,** *199*, 220-227.

27. Déniel, M.; Haarlemmer, G.; Roubaud, A.; Weiss-Hortala, E.; Fages, J., Hydrothermal liquefaction of blackcurrant pomace and model molecules: understanding of reaction mechanisms. *Sustainable Energy & Fuels* **2017,** *1* (3), 555-582.

28. Cheng, F.; Tompsett, G. A.; Fraga Alvarez, D. V.; Romo, C. I.; McKenna, A. M.; Niles, S. F.; Nelson, R. K.; Reddy, C. M.; Granados-Fócil, S.; Paulsen, A. D.; Zhang, R.; Timko, M. T., Metal oxide supported Ni-impregnated bifunctional catalysts for controlling char formation and maximizing energy recovery during catalytic hydrothermal liquefaction of food waste. *Sustainable Energy & Fuels* **2021,** *5* (4), 941-955.

29. Cheng, F.; Tompsett, G. A.; Murphy, C. M.; Maag, A. R.; Carabillo, N.; Bailey, M.; Hemingway, J. J.; Romo, C. I.; Paulsen, A. D.; Yelvington, P. E.; Timko, M. T., Synergistic Effects of Inexpensive Mixed Metal Oxides for Catalytic Hydrothermal Liquefaction of Food Wastes. *ACS Sustainable Chemistry & Engineering* **2020,** *8* (17), 6877-6886.

30. Watson, J.; Lu, J.; de Souza, R.; Si, B.; Zhang, Y.; Liu, Z., Effects of the extraction solvents in hydrothermal liquefaction processes: Biocrude oil quality and energy conversion efficiency. *Energy* **2019,** *167*, 189-197.

31. Maag, A. R.; Paulsen, A. D.; Amundsen, T. J.; Yelvington, P. E.; Tompsett, G. A.; Timko, M. T., Catalytic Hydrothermal Liquefaction of Food Waste Using CeZrOx. *Energies* **2018,** *11* (3).

32. Stein, S. E., Estimating probabilities of correct identification from results of mass spectral library searches. *Journal of the American Society for Mass Spectrometry* **1994,** *5* (4), 316-323.

33. Chen, J.; Li, S., Characterization of biofuel production from hydrothermal treatment of hyperaccumulator waste (Pteris vittata L.) in sub- and supercritical water. *RSC Advances* **2020,** *10* (4), 2160-2169.

34. Stankovikj, F.; McDonald, A. G.; Helms, G. L.; Garcia-Perez, M., Quantification of Bio-Oil Functional Groups and Evidences of the Presence of Pyrolytic Humins. *Energy & Fuels* **2016,** *30* (8), 6505-6524.

35. Hendrickson, C. L.; Quinn Jp Fau - Kaiser, N. K.; Kaiser Nk Fau - Smith, D. F.; Smith Df Fau - Blakney, G. T.; Blakney Gt Fau - Chen, T.; Chen T Fau - Marshall, A. G.; Marshall Ag Fau - Weisbrod, C. R.; Weisbrod Cr Fau - Beu, S. C.; Beu, S. C., 21 Tesla Fourier Transform Ion Cyclotron Resonance Mass Spectrometer: A National Resource for Ultrahigh Resolution Mass Analysis. **2015,** (1879-1123 (Electronic)).

36. Smith, D. F.; Podgorski, D. C.; Rodgers, R. P.; Blakney, G. T.; Hendrickson, C. L., 21 Tesla FT-ICR Mass Spectrometer for Ultrahigh-Resolution Analysis of Complex Organic Mixtures. *Analytical Chemistry* **2018,** *90* (3), 2041-2047.

37. Zhang, B.; Zhong, Z.; Min, M.; Ding, K.; Xie, Q.; Ruan, R., Catalytic fast co-pyrolysis of biomass and food waste to produce aromatics: Analytical Py–GC/MS study. *Bioresource Technology* **2015,** *189*, 30-35.

38. Zhang, H.; Cheng, Y.-T.; Vispute, T. P.; Xiao, R.; Huber, G. W., Catalytic conversion of biomass-derived feedstocks into olefins and aromatics with ZSM-5: the hydrogen to carbon effective ratio. *Energy & Environmental Science* **2011,** *4* (6), 2297-2307.

39. Chen, W.-T.; Ma, J.; Zhang, Y.; Gai, C.; Qian, W., Physical pretreatments of wastewater algae to reduce ash content and improve thermal decomposition characteristics. *Bioresource Technology* **2014,** *169*, 816-820.

40. Chen, W.-T.; Qian, W.; Zhang, Y.; Mazur, Z.; Kuo, C.-T.; Scheppe, K.; Schideman, L. C.; Sharma, B. K., Effect of ash on hydrothermal liquefaction of high-ash content algal biomass. *Algal Research* **2017,** *25*, 297-306.

41. Haider, M. S.; Castello, D.; Michalski, K. M.; Pedersen, T. H.; Rosendahl, L. A., Catalytic Hydrotreatment of Microalgae Biocrude from Continuous Hydrothermal Liquefaction: Heteroatom Removal and Their Distribution in Distillation Cuts. *Energies* **2018,** *11* (12).

42. Tan, K. T.; Lee, K. T.; Mohamed, A. R., Production of FAME by palm oil transesterification via supercritical methanol technology. *Biomass and Bioenergy* **2009,** *33* (8), 1096-1099.

43. O'Sullivan, A. C., Cellulose: the structure slowly unravels. *Cellulose* **1997,** *4* (3), 173-207.

44. Ralph, J.; Lapierre, C.; Boerjan, W., Lignin structure and its engineering. *Current Opinion in Biotechnology* **2019,** *56*, 240-249.

45. Rodgers, R. P.; McKenna, A. M., Petroleum Analysis. *Analytical Chemistry* **2011,** *83* (12), 4665-4687.

46. McKenna, A. M.; Nelson, R. K.; Reddy, C. M.; Savory, J. J.; Kaiser, N. K.; Fitzsimmons, J. E.; Marshall, A. G.; Rodgers, R. P., Expansion of the Analytical Window for

Oil Spill Characterization by Ultrahigh Resolution Mass Spectrometry: Beyond Gas Chromatography. *Environmental Science & Technology* **2013,** *47* (13), 7530-7539.

47. Tao, W.; Yang, X.; Li, Y.; Zhu, R.; Si, X.; Pan, B.; Xing, B., Components and Persistent Free Radicals in the Volatiles during Pyrolysis of Lignocellulose Biomass. *Environmental Science & Technology* **2020,** *54* (20), 13274-13281.

48. Motavaf, B.; Savage, P. E., Effect of Process Variables on Food Waste Valorization via Hydrothermal Liquefaction. *ACS ES&T Engineering* **2021,** *1* (3), 363-374.

49. Cantero-Tubilla, B.; Cantero, D. A.; Martinez, C. M.; Tester, J. W.; Walker, L. P.; Posmanik, R., Characterization of the solid products from hydrothermal liquefaction of waste feedstocks from food and agricultural industries. *The Journal of Supercritical Fluids* **2018,** *133*, 665-673.

50. Gärtner, C. A.; Serrano-Ruiz, J. C.; Braden, D. J.; Dumesic, J. A., Catalytic Upgrading of Bio-Oils by Ketonization. *ChemSusChem* **2009,** *2* (12), 1121-1124.

51. Shen, D. K.; Gu, S., The mechanism for thermal decomposition of cellulose and its main products. *Bioresource Technology* **2009,** *100* (24), 6496-6504.

52. Ander, P.; Eriksson, K.-E., Methanol formation during lignin degradation by Phanerochaete chrysosporium. *Applied Microbiology and Biotechnology* **1985,** *21* (1), 96-102.

53. Gerpen, J. V., Biodiesel processing and production. *Fuel Processing Technology* **2005,** *86* (10), 1097-1107.

54. Chen, Y.; Wu, Y.; Ding, R.; Zhang, P.; Liu, J.; Yang, M.; Zhang, P., Catalytic hydrothermal liquefaction of D. tertiolecta for the production of bio-oil over different acid/base catalysts. *AIChE Journal* **2015,** *61* (4), 1118-1128.

55. Gao, H.-Y.; Held, P. A.; Knor, M.; Mück-Lichtenfeld, C.; Neugebauer, J.; Studer, A.; Fuchs, H., Decarboxylative Polymerization of 2,6-Naphthalenedicarboxylic Acid at Surfaces. *Journal of the American Chemical Society* **2014,** *136* (27), 9658-9663.

56. Zhou, H.; Zhang, F.; Wang, R.; Lai, W.-M.; Xie, S.; Ren, W.-M.; Lu, X.-B., Facile Access to Functionalized Poly(thioether)s via Anionic Ring-Opening Decarboxylative Polymerization of COS-Sourced α-Alkylidene Cyclic Thiocarbonates. *Macromolecules* **2021,** *54* (22), 10395-10404.

57. Guo, S.; Dong, X.; Liu, K.; Yu, H.; Zhu, C., Chemical, Energetic, and Structural Characteristics of Hydrothermal Carbonization Solid Products for Lawn Grass. *2015* **2015,** *10* (3), 13.

58. Funke, A.; Ziegler, F., Hydrothermal carbonization of biomass: A summary and discussion of chemical mechanisms for process engineering. *Biofuels, Bioproducts and Biorefining* **2010,** *4* (2), 160-177.

59. Obeid, F.; Chu Van, T.; Brown, R.; Rainey, T., Nitrogen and sulphur in algal biocrude: A review of the HTL process, upgrading, engine performance and emissions. *Energy Conversion and Management* **2019,** *181*, 105-119.

60. Robb, D. B.; Blades, M. W., Factors affecting primary ionization in dopant-assisted atmospheric pressure photoionization (DA-APPI) for LC/MS. *Journal of the American Society for Mass Spectrometry* **2006,** *17* (2), 130-138.

61. Robb, D. B.; Covey, T. R.; Bruins, A. P., Atmospheric Pressure Photoionization: An Ionization Method for Liquid Chromatography−Mass Spectrometry. *Analytical Chemistry* **2000,** *72* (15), 3653-3659.

62. Purcell, J. M.; Rodgers, R. P.; Hendrickson, C. L.; Marshall, A. G., Speciation of nitrogen containing aromatics by atmospheric pressure photoionization or electrospray ionization fourier transform ion cyclotron resonance mass spectrometry. *Journal of the American Society for Mass Spectrometry* **2007,** *18* (7), 1265-1273.

63. Smith, D. R.; Robb, D. B.; Blades, M. W., Comparison of dopants for charge exchange ionization of nonpolar polycyclic aromatic hydrocarbons with reversed-phase LC-APPI-MS. *Journal of the American Society for Mass Spectrometry* **2009,** *20* (1), 73-79.

64. Purcell, J. M.; Hendrickson, C. L.; Rodgers, R. P.; Marshall, A. G., Atmospheric Pressure Photoionization Proton Transfer for Complex Organic Mixtures Investigated by Fourier Transform Ion Cyclotron Resonance Mass Spectrometry. *Journal of the American Society for Mass Spectrometry* **2007,** *18* (9), 1682-1689.

65. Purcell, J. M.; Hendrickson, C. L.; Rodgers, R. P.; Marshall, A. G., Atmospheric Pressure Photoionization Fourier Transform Ion Cyclotron Resonance Mass Spectrometry for Complex Mixture Analysis. *Analytical Chemistry* **2006,** *78* (16), 5906-5912.

66. Kaiser, N. K.; Quinn, J. P.; Blakney, G. T.; Hendrickson, C. L.; Marshall, A. G., A Novel 9.4 Tesla FTICR Mass Spectrometer with Improved Sensitivity, Mass Resolution, and Mass Range. *Journal of the American Society for Mass Spectrometry* **2011,** *22* (8), 1343-1351.

67. Blakney, G. T.; Hendrickson, C. L.; Marshall, A. G., Predator data station: A fast data acquisition system for advanced FT-ICR MS experiments. *International Journal of Mass Spectrometry* **2011,** *306* (2), 246-252.

68. Kaiser, N. K.; McKenna Am Fau - Savory, J. J.; Savory Jj Fau - Hendrickson, C. L.; Hendrickson Cl Fau - Marshall, A. G.; Marshall, A. G., Tailored ion radius distribution for

increased dynamic range in FT-ICR mass analysis of complex mixtures. (1520-6882 (Electronic)).

69. Chen, T.; Beu, S. C.; Kaiser, N. K.; Hendrickson, C. L., Note: Optimized circuit for excitation and detection with one pair of electrodes for improved Fourier transform ion cyclotron resonance mass spectrometry. (1089-7623 (Electronic)).

70. Boldin, I. A.; Nikolaev, E. N., Fourier transform ion cyclotron resonance cell with dynamic harmonization of the electric field in the whole volume by shaping of the excitation and detection electrode assembly. *Rapid Communications in Mass Spectrometry* **2011,** *25* (1), 122-126.

71. Xian, F.; Hendrickson Cl Fau - Blakney, G. T.; Blakney Gt Fau - Beu, S. C.; Beu Sc Fau - Marshall, A. G.; Marshall, A. G., Automated broadband phase correction of Fourier transform ion cyclotron resonance mass spectra. **2010,** (1520-6882 (Electronic)).

72. Savory, J. J.; Kaiser Nk Fau - McKenna, A. M.; McKenna Am Fau - Xian, F.; Xian F Fau - Blakney, G. T.; Blakney Gt Fau - Rodgers, R. P.; Rodgers Rp Fau - Hendrickson, C. L.; Hendrickson Cl Fau - Marshall, A. G.; Marshall, A. G., Parts-per-billion Fourier transform ion cyclotron resonance mass measurement accuracy with a "walking" calibration equation. **2011,** (1520-6882 (Electronic)).

73. Kendrick, E., A mass scale based on CH2 = 14.0000 for high resolution mass spectrometry of organic compounds. *Analytical Chemistry* **1963,** *35*, 2146-2154.

74. Hughey, C. A.; Hendrickson, C. L.; Rodgers, R. P.; Marshall, A. G.; Qian, K., Kendrick Mass Defect Spectrum: A Compact Visual Analysis for Ultrahigh-Resolution Broadband Mass Spectra. *Analytical Chemistry* **2001,** *73* (19), 4676-4681.

75. McLafferty, F. W. T., F., *Interpretation of Mass Spectra, 4th ed.* 4th ed.; University Science Books: 1993.

76. Krevelen, V., Graphical-statistical method for the study of structure and reaction processes of coal. *Fuel* **1950,** *29*, 269-284.

77. Savory, J. J.; Kaiser, N. K.; McKenna, A. M.; Xian, F.; Blakney, G. T.; Rodgers, R. P.; Hendrickson, C. L.; Marshall, A. G., Parts-Per-Billion Fourier Transform Ion Cyclotron Resonance Mass Measurement Accuracy with a "Walking" Calibration Equation. *Analytical Chemistry* **2011,** *83* (5), 1732-1736.

78. Corilo, Y. E., PetroOrg Software. Florida State University, Omics LLC: 2014.

CHAPTER 4

QUANTIFYING STRUCTURAL IMPACTS OF LIGNIN ON ITS HYDROTHERMAL LIQUEFACTION MONOMER YIELDS

4.1 INTRODUCTION

Lignin is the most abundant source of renewable aromatic molecular groups on Earth[1], and therefore provides a unique opportunity to decarbonize chemical and fuel production.[1-3] Lignin is produced as a waste byproduct of paper manufacturing, where it is rejected in the form of "black liquor" as part of the pulping process.[4-8] The black liquor is dried to recover Kraft lignin, which is traditionally burned to provide heat to the papermaking process.[6, 8] Similarly, lignin is a byproduct of many technologies proposed for converting cellulosic feedstocks into biofuels or other bioproducts.[9] Replacing first generation biofuels and bioproducts with second generation versions that are derived from cellulosic feedstocks has energy balance and land use benefits.[10] However, the potential of these new technologies is limited by co-production of a lignin byproduct with no viable market other than combustion.[11, 12] While lignin combustion offsets energy requirements,[13] combustion invariably generates CO_2 emissions, detracting from the environmental benefits of the use of cellulosic feedstocks. New methods that utilize lignin for applications that are otherwise difficult to decarbonize, such as a transportation fuel, chemicals, or materials, are desperately needed.[2, 9, 14, 15]

A big problem with lignin valorization is purity and the presence of contaminants. The problem is covalent linkages between the cellulosic components of biomass and lignin. CELF has recently emerged as a means of producing "pure lignin", that is, lignin with minimal cellulosic

contamination. Like other technologies aiming to convert cellulosic feedstocks into biofuel and biobased chemicals, CELF currently does not valorize the lignin byproduct, which opens up a clear opportunity. CELF lignin may be especially appropriate for aqueous-based conversion technologies, which eliminate drying steps that otherwise detract from an otherwise positive energy balance. Unfortunately, no prior study has evaluated HTL of CELF lignin, meaning that nothing is known about biocrude, biochar, or monomer yields that might be obtained from HTL of CELF lignin.

In addition to this technological motivation, the purity of CELF lignin provides an opportunity to study the relationships between lignin structure and hydrothermal reactivity. Previous studies have shown that compared to untreated, or native, lignin, CELF lignin has a decreased molecular weight, indicative of initial depolymerization. Furthermore, the abundance of free phenolic and carboxylic acid hydroxyl groups are increased in CELF lignin, hinting at its potential as a renewable aromatic material for production of fuels and chemicals.[16, 17] Additionally, ^{13}C NMR spectroscopy has revealed significant reductions in β-O-4 and β-5 linkages in CELF lignin as compared to Kraft lignin samples.[17] Analysis by Meng et al. revealed decreased weight-average (M_w) and number average (M_n) molecular weight and polydispersity index (PDI) of CELF lignin compared to native-like (cellulolytic enzyme) lignin indicating that CELF caused a dramatic depolymerization reaction.[17]

Reports on lignin chemistry often relate lignin structure and source to its reactivity. A report by Anderson et al.[18] explores the impact of syringyl/ guiaicyl ratio (S/G) of natural poplar variants on the monomer yields resulting from reductive catalytic lignin fractionation (RCF). In this report, they find that there is no correlation between lignin S/G ratio and monomer yields,

indicating that factors beyond monomeric composition of lignin play a role in depolymerization chemical pathways.[18]

In this study, we evaluated the use of CELF lignin as an HTL feed to add value to a cellulosic biorefinery that produces a slate of chemicals and fuels. Five different lignin types were studied so that a range of wood types was represented. The feeds were characterized to estimate residual cellulosic content and elucidate lignin structure. HTL product yields were quantified, and the products were characterized at the molecular level using GC-MS, FTIR, and FT-MS. The results of this study establish a baseline for the use of CELF lignin as feeds to the HTL process and provide new insight into the relationship between lignin structure and reactivity.

4.2 MATERIALS & METHODS

4.2.1 BIOMASS MATERIALS

Six types of biomass feedstocks were used in this study: sugarcane bagasse, poplar wood, pine wood, spruce wood, corn stover, and maple wood. Lignin samples were obtained from the wood types mentioned from UC Riverside through the CELF process. Kraft lignin (Sigma Aldrich) derived from spruce wood was used as the standard for comparison to CELF lignin. Acetone (purity>99.5%, Sigma-Aldrich) and ethyl acetate (purity>99.8%, Sigma-Aldrich) were used as the solvent for bio-crude oil extraction and reactor cleaning. All lignin samples were dried at least overnight before use in hydrothermal liquefaction. Deionized water (electrical resistivity>18.0 MΩ·cm) was used to prepare the lignin feedstock for HTL reactions. Helium gas (grade 5.0, Airgas) was used to purge and pressurize the HTL batch reactor prior to each run and also as the carrier gas for gas chromatography.

4.2.2 CELF PRETREATMENT

CELF pretreatment was conducted at the University of California Riverside as described. [27,29,30,43] Biomass was first milled to 2mm particle size, if required, before loading into a 1L Hastelloy Parr autoclave reactor (236HC series, Parr Instruments Co., Moline, IL, USA) equipped with twin pitched-blade Rushton impellers. The reactor was loaded to maintain a solid loading of 7.5 wt.%. The milled biomass was then soaked overnight at 4 °C in a 1:1 (w/w) THF-water solution containing dilute sulfuric acid (0.05 M). Pretreatment occurred at 150 °C and 25 min for agricultural feedstocks, and 160 °C and 15 min for soft and hardwood feedstocks. A lower temperature was used for agricultural feedstocks after finding no solids remained at treatment at 160 °C. All reactions were maintained within ± 1 °C by convective heating using a 4kW fluidized sand bath (Model SBL-2D, Techne, Princeton, NJ, USA). Temperatures were monitored using an internally fixed thermocouple (Omega, K-type). The reaction was quenched in a large room-temperature water bath after the allotted reaction time. The solids were then collected via vacuum filtration and subsequent separation from the pretreatment liquor utilized filter paper. Finally, the dry mass of solids and remaining liquor was recorded.

The collected liquid fraction was poured in a beaker and titrated to pH 7 using ammonium hydroxide. The THF was boiled out of solution at 80 °C utilizing a hot plate with continuous stirring (130 rpm, 4 h) for recovery. The beaker and its contents were then left to cool to room temperature overnight and all liquids were poured into another container. Lignin that had precipitated onto the beaker after THF removal was rinsed with water before drying overnight in a 65 °C oven overnight. The resulting lignin was then washed with diethyl ether and water on glass fiber filter paper to remove soluble impurities before being dried again in the oven overnight to a

moisture content of less than 3%. Finally, the lignin was ground into a fine powder using a mortar and pestle.

4.2.3 HYDROTHERMAL LIQUEFACTION OF LIGNIN

HTL reactions were conducted in a 300-mL stainless-steel bench-top reactor (Model 4841, Parr Instrument Co., Moline, IL, USA) equipped with a magnetic stirring drive. The lignin slurry (100g, 15 wt% solids) was loaded into the reactor before a nitrogen purge to remove residual oxygen before being pressurized to 7.6 MPa. The reactor was heated to 300 °C at a heating rate of ~6 °C min^{-1} using a heating jacket. Once the reaction temperature had been reached, the pressure was 20.7 ± 0.3 MPa, sufficient to maintain >92.3% of the water fed to the batch reactor in its liquid state. Reaction temperature was maintained at 300 ± 2 °C for 1 h, at which point the reaction was quenched by placing the reactor in a water-ice bath. All HTL runs were performed in at least duplicate with the measured product yields consistent to within ±5%. Average values are reported here along with uncertainties estimated from repeated tests. To ensure that the reactor did not leak during testing, the top-down mass balance closure of the reactor and its contents was confirmed to within ±10% by measuring the reactor mass to within ±1.0 g before each experiment, after each experiment, and after venting the gas product formed during the experiment.

The bottom-up carbon mass balance, determined as the sum of the gravimetric yields of oil, gas, aqueous, and char combined with their fractional carbon content, always closed to within 5%, similar to recent reports on HTL mass balance closure.[19, 20] Losses are due to the precision of the top loading analytical balance used to estimate gas yield by difference (±1.0 g out of 16,000 g) and residual material in the reactor fittings, pressure transducer, etc. Of these, under estimation of gas yields will account for >50% of the mass balance closure gap, given the precision of the analytical

balance used for weight measurements. Given the composition of the gas, primarily CO_2, incomplete gas yield estimation has a negligible effect on any conclusion made here.

After quenching and depressurization, the gas yield was determined by gravimetric difference before and after opening the reactor. The reactor was then opened and poured into a vacuum filter to separate the aqueous and char phases. The char was then rinsed with acetone to separate the biocrude from the char phase before being placed in a rotary evaporator to remove the acetone and obtain biocrude yields.

4.2.4 SOLID STATE ^{13}C NMR

Nuclear magnetic resonance spectroscopy (NMR) was performed using a Bruker Avance 400 spectrometer at 100 MHz frequency. The instrument utilized a Bruker double-resonance magic-angle spinning probe head for 4 mm rotors. Samples filled the 9mm long radio-frequency coil from end to end where a cylindrical glass plug of 2mm at the bottom of the roto prevented sample material from being placed outside the coil. To optimize sensitivity, the recycle delays was set to 20s for all lignin samples included in this study. Direct polarization was used for lignin samples with unpaired electrons, particularly the C-Corn Stover sample. For all other samples, the multiple cross polarization (multiCP) was employed.

4.2.5 ELEMENTAL ANALYSIS

Elemental analysis for all lignin samples was performed at Midwest Microlabs (Indianapolis, IN, USA) to obtain carbon, hydrogen, nitrogen, and sulfur contents.

4.2.6 CHARACTERIZATION OF BIOCRUDE OILS

HTL product phases were all analyzed for carbon content to obtain a complete carbon balance of the system. Biocrude and char phases were analyzed using an elemental analyzer from

Midwest Microlabs (Indianapolis, IN, USA). Gaseous products were analyzed by gas chromatography (GC-2014, Shimadzu Co., Kyoto, Japan) equipped with a TCD detector and an 80/100 Hayesep Q packed column (3m x 0.125" x 2.1mm SS). Samples were injected using a 102mL sample loop via an automated valve. The temperature program began with an initial temperature of 30 °C followed by heating to 90 °C at a ramp rate of 5 °C per minute. Once the temperature reached 90 °C it was held for 20 min before continued heating to 130 °C at the same ramp before final heating to 150 °C at a rate of 10 °C per minute. The final temperature was then held for 40 minutes to ensure all products had eluted. Peak areas were integrated and identified using retention time matching to known standards and TCD response was calibrated to standards. The carbon content of the resultant aqueous phase was measured using a Shimadzu total organic carbon (TOC) analyzer. The carbon yields were determined using **Equation 4.1**, which utilizes the measured product mass and resultant carbon weight fraction of each phase and the initial feed. Carbon yields in the product phases were summed to check for overall carbon balance closure, wherein all cases the carbon balance closed to within 5%.

$$Carbon\ yield_{product} = \frac{mass_{product}\ X\ carbon\%_{product}}{mass_{lignin}\ X\ carbon\%_{lignin}}\ X\ 100 \tag{4.1}$$

4.2.7 GAS CHROMATOGRAPHY MS & FID

Biocrude composition was analyzed using a Shimadzu QP 2010 SE gas chromatography mass spectrometry (GC-MS) system. The major monomers identified using MS were then quantified using flame ionization detection (FID), also from Shimadzu. For GC-MS, a SHRZI-5MS column (30m x 0.25mm ID x 0.5µm thickness) was utilized whereas for GC-FID the column was an Rt-Q-BOND (30m x 0.25mm ID x 85µm thickness). Both analyses utilized the same temperature program with an initial temperature of 35 °C followed by heating at 3 °C per minute

to a max temperature of 290 °C which was held for 5 minutes. The injector temperature was set at 300 °C with an injection volume of 3 µL.

4.2.8 FOURIER TRANSFORM ATTENUATED TOTAL REFLECTANT INFRARED SPECTROSCOPY (FT-ATR-IR)

FT-ATR-IR was used to analyze the functional group content of the feedstock, biocrude, and char products from hydrothermal liquefaction. A Shimadzu FTIR spectrometer was equipped with a QATR-S single reflection ATR cell for measurement collection. A resolution of 8 cm^{-1} was used in all measurements and spectra were compared to known databases and literature to identify bands attributable to lignin functional groups.[21-23]

4.2.9 FOURIER TRANSFORM ION CYCLOTRON RESONANCE MASS SPECTROMETRY (FT-ICR MS)

FT-ICR MS was used to analyze biocrude products utilizing positive ion atmospheric pressure photoionization as the ionization mode. The 21 T instrument was custom-built at the National High Magnetic Field Laboratory in Tallahassee, Florida, USA.[24] Samples were prepared by first dissolving them in a 50/50 (volume) mixture of toluene and tetrahydrofuran to a final concentration of 125 µg/mL. Further details on FT-ICR MS analysis can be found in previous literature.[19, 20, 25]

4.3 RESULTS & DISCUSSION

This work aims to understand the effect of wood type on lignin transformation to monomer-rich biocrude through hydrothermal liquefaction. Five lignin samples were studied, including one softwood, two agricultural woods, and two hardwoods. All lignin feeds were obtained through the CELF process and were subsequently analyzed via ^{13}C solid-state NMR. Each lignin sample then

underwent processing via hydrothermal liquefaction at 300 °C for 60 minutes before product yields and carbon distributions determined. To further understand the effect of wood type on biocrude composition, analyses were performed utilizing GC-MS, FTIR, and FT-ICR MS.

4.3.1 LIGNIN CHARACTERIZATION

^{13}C solid-state nuclear magnetic resonance (NMR) spectroscopy is a recognized technique to understand lignin structural motifs.[26-28] **Figure 4-1** contains the ^{13}C-NMR spectra for all lignin feedstocks used in this study. In addition to the five CELF lignins studied, **Figure 4-1** also contains the spectra from softwood Spruce obtained from Kraft fractionation to serve as standard comparison. The spectral range of interest for lignin occurs between 86 – 50 ppm, corresponding to oxygenated and non-oxygenated interunit linkages.[27] The most intense peak in this range belongs to the OCH_3 group present in both syringol and guaiacol monomeric units, appearing at approximately 56 ppm.

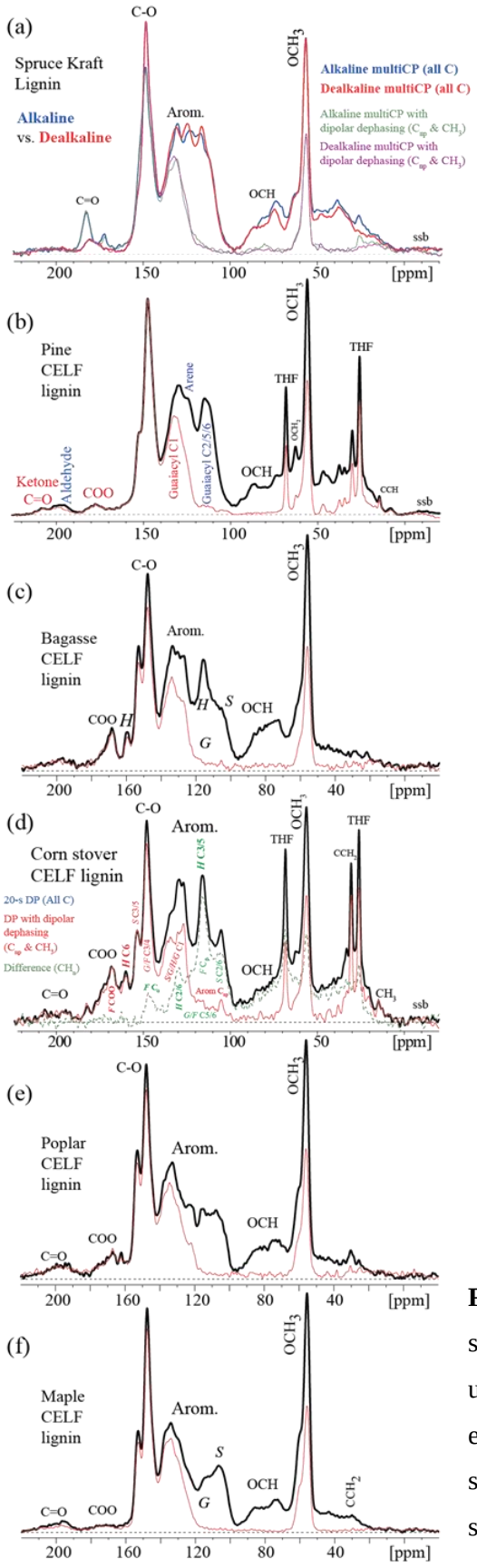

First, comparing the Kraft and CELF softwoods highlights the presence of strong C-O and OCH_3 peaks around 150 and 58 ppm, respectively, in both instances. The pine sample processed through CELF also contains two peaks from residual tetrahydrofuran (THF) contamination, an indication of incomplete washing from the CELF process (about 4% carbon). Barring this impurity in the C-Pine lignin, it contains virtually no other contaminants with less than 2% polysaccharide content, indicated by the absence of carbohydrate peaks between 65 – 95 ppm. The Kraft lignin, on the other hand, is contaminated with carbohydrates due to incomplete hemicellulose removal, as indicated through the peak at ~75 ppm.[29] An additional feature of interest is the presence of alkyl and aromatic groups (~125 ppm) that are not bonded to oxygen, which indicate major modification in lignin structure due to both extraction methods.[26, 27]

Figure 4-1. ^{13}C solid-state NMR spectra of a) Kraft softwood lignin and b-f) CELF lignin samples measured using multiCP with dipolar dephasing. Samples b-f were extracted using the CELF process and are as follows: b) softwood pine, c) agricultural bagasse, d) agricultural corn stover, e) hardwood poplar, and f) hardwood maple.

Next, the five CELF lignins were examined to understand how wood type affects the structural features represented in ^{13}C-NMR. Similar to pine, corn stover also shows peaks corresponding to residual THF. Additionally, all CELF samples have resulted in a pure lignin product with negligible polysaccharide contamination, that is below the detection limit. Compared to ^{13}C-NMR of lignin in literature, the aromatic C-O peak (155 ppm) and COO peak (172 ppm) are both greatly reduced in intensity, indicating that co-solvent enhanced lignin fractionation cleaved the linkages between aromatic rings and the OCH_3 groups.[26-28, 30]

Furthermore, spectral editing of quantitative ^{13}C-NMR allows for calculations of the relative ratios of lignin's fundamental monomeric subunits. In particular, the syringyl (S) and guiaicyl (S) units can be quantified and compared in order to determine the S/G ratio, which is directly correlated to biomass type. **Table 4-1** provides the resultant S/G ratio determined from quantitative NMR as well as information about wood type, CELF processing conditions, and HTL reaction conditions. The S/G analysis shows that softwoods have the lowest, near zero, S/G ratio due to their lack of syringyl units. Hardwoods, on the other hand, typically have S/G ratios greater than one due to their high syringyl content. Further spectral editing also revealed the clear presence of *p*-hydroxyphenol (H) in bagasse and corn stover lignins, as is typical for agricultural woods.

Table 4-1. Wood type, name, and syringol-guaiacol ratios for each lignin samples as determined by ^{13}C-NMR analysis. CELF and HTL processing conditions are also included for comparison.

Wood Type	Wood Name	S/G Ratio	CELF Conditions	HTL Conditions
Softwood	Pine	0.01	160 °C, 15 min, 1:1 THF:H_2O	300 °C, 60 min
Agricultural	Bagasse	0.41	150 °C, 25 min, 1:1 THF:H_2O	300 °C, 60 min
Agricultural	Corn Stover	0.44	150 °C, 25 min, 1:1 THF:H_2O	300 °C, 60 min
Hardwood	Poplar	1.06	160 °C, 15 min, 1:1 THF:H_2O	300 °C, 60 min
Hardwood	Maple	1.35	160 °C, 15 min, 1:1 THF:H_2O	300 °C, 60 min

4.3.2 HYDROTHERMAL LIQUEFACTION PRODUCT YIELDS

Each of the five CELF lignins underwent hydrothermal liquefaction and resulted in four primary product phases- solid char, aqueous organic, biocrude, and gas. The resultant product distribution from these HTL reactions is shown in **Figure 4-2a**. From this, it can be seen that pine resulted in the lowest biocrude yield (45.3%) whereas poplar produced the greatest biocrude percentage at 63.5%. Previous HTL research has indicated that large biomacromolecules undergo depolymerization in the subcritical compressed water before radical-initiated repolymerization into biocrude-soluble molecules.[20, 31, 32] With long reaction times, certain feedstocks are prone to over-polymerization, often resulting in increased char formation. **Figure 4-2a** highlights the increased char yields seen in pine HTL as opposed to the agricultural and hardwood lignins. This finding is consistent with research stating that guaiacyl-based wood structures are more prone to repolymerization due to the extra carbon site on the aromatic ring that can form stable C-C bonds.[33]

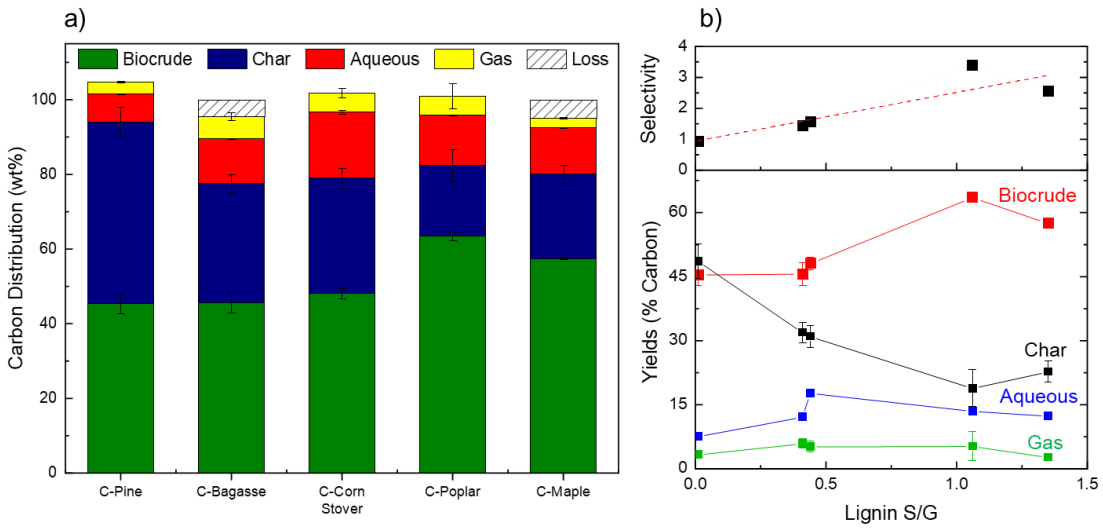

Figure 4-2. **a)** Hydrothermal liquefaction product yields displayed as a function of carbon in the feed for each of the five CELF lignins. All experiments were conducted in at least duplicate and averages and error bars are shown for each sample. All reactions were completed at 300 °C and 60 min reaction time. **b)** Top panel- selectivity to biocrude over char as a function of the S/G ratio of the feed lignin. Bottom panel- Hydrothermal liquefaction product yields as a function of lignin S/G ratio.

Figure 4-2b on the right plots the product distribution as a function of the lignin S/G ratio. Plotting in this way highlights the impact of lignin structure on HTL product distributions. The top panel of **Figure 4-2b** furthers this analysis by looking at selectivity to biocrude over char as a function of S/G ratio. This analysis shows a clear increasing trend in selectivity with increasing S/G, further confirming the idea presented by Kim et al. on softwood susceptibility towards repolymerization.[33] Additional analyses can be made from this figure where aqueous and gas yields are independent of lignin S/G, an important finding, as aqueous phase molecules can be the result of depolymerization reactions to small, water-soluble organics. The relative consistency across aqueous carbon yields indicates that lignin structure does not affect small organic molecules and that polymerization to char occurs solely from larger, traditionally oil-soluble molecules.

4.3.3 BIOCRUDE CHARACTERIZATION

In addition to biocrude yields, biocrude composition and its subsequent quality are of express interest to determine the effect of lignin structure. First off, GC-MS provides qualitative identification of the compounds in the volatile fraction (vaporization temp. < 325 °C) of the biocrude. Following mass spectrometry, GC-FID used in conjunction then allows for quantification of the previously identified compounds. **Figure 4-3** shows the results of the quantitative GC analysis of the biocrudes, whereas the raw MS spectra can be found in the supporting information. Due to the nature of lignin's structure, all biocrudes indicate phenolic and methoxy monomers as the major products. As expected from **Figure 4-1**, the pine biocrude does not contain detectable syringol monomers, whereas both agricultural and hardwoods show appreciable amounts of syringol and guaiacol.

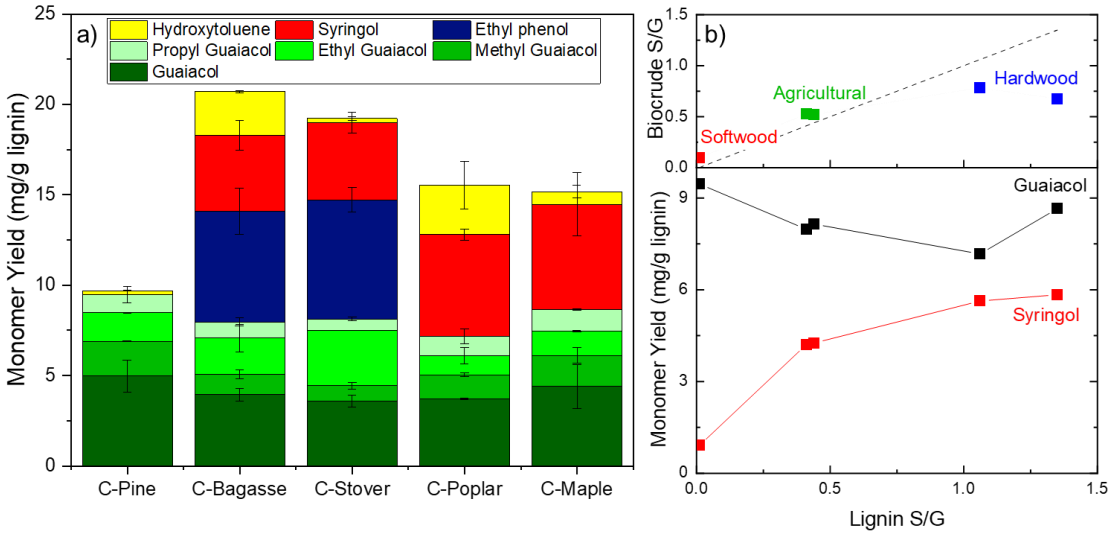

Figure 4-3. **a)** Hydrothermal liquefaction monomer yields in the biocrude phase from each CELF lignin sample as identified through GC-MS and quantified through GC-FID calibration. **b)** Top panel- parity plot of lignin S/G versus calculated biocrude S/G through GC quantification. Bottom panel- syringol and guaiacol monomer yields as a function of lignin S/G ratio.

A closer look at the agricultural woods reveals the greatest monomeric product as ethyl phenol. It is interesting to note that bagasse and corn stover are the only biocrudes to contain this monomer, which may be due to the natural degradation of *p*-hydroxyphenol, the third, less common monomer of lignin, which is confirmed to be present in the agricultural samples through ^{13}C-NMR. In addition to the presence of ethyl phenol, butylated hydroxytoluene (BHT) is also a dominant product in bagasse and poplar biocrudes but appears as a quantifiable product in all biocrude samples. BHT is a phenolic compound that is used widely in foods to slow oxidation.[34] Interestingly, BHT has been shown to reduce degradation reaction rates of G units relative to S, and serves to eliminate free radicals.[34] Consistent with the lignin structure, poplar and maple result in the greatest concentration of syringol monomers of the biocrudes, while guaiacol concentrations remain relatively unchanged across the samples.

Figure 4-3b aims to further understand the effect of lignin structure on biocrude monomer yields by plotting guaiacol and syringol yields as a function of lignin S/G. As would be expected, syringol concentration increases as lignin S/G increases, whereas there is only a slightly negative trend with guaiacol and increasing S/G. The top panel furthers this analysis through use of a parity plot which compares the S/G ratio of the lignin feed to the S/G monomers obtained in the biocrude. The parity plot in **Figure 4-3b** highlights the strong retention of lignin characteristics in the soft and agricultural woods, where the three data points differ from parity by less than 0.1. The hardwoods, on the other hand, experience a stronger negative deviation, indicative of decreased S/G in the biocrude. This is corroborated by the fact that syringol yields never surpass guaiacol, despite S/G ratios greater than 1 in the hardwood lignins. Further characterization on the fate of syringol is required for full pathway analysis.

To better understand the retention of structural motifs from lignin throughout HTL products, FTIR was employed to analyze the feedstock, biocrude, and char phases from each wood type. Pine, bagasse, and poplar were chosen to span the range of lignin S/G ratios. The lignin feeds are similar to one another in their bulk functionality, all containing a characteristic OH stretching band at about 3450 cm^{-1} and CH stretching bands slightly below 3000 cm^{-1}. In the range between 1800 – 1000 cm^{-1} there exists an array of bands related to the monomeric structure and composition of lignin.

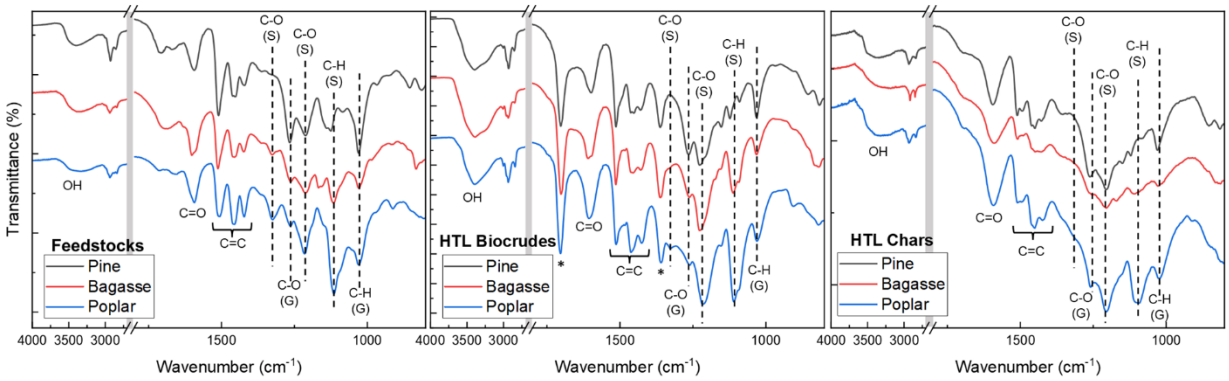

Figure 4-4. Fourier transform infrared spectroscopy (FTIR) spectra for pine, bagasse, and poplar samples from initial feedstock, and resultant biocrude and char phases from hydrothermal liquefaction. Bands labeled with a * in the biocrude samples represent residual acetone adsorbed into the product.

Numerous researchers have explored the differences between softwood and hardwood lignins with FTIR to assist in structure determination.[21, 22] In this way, Kubo et al. has identified the FTIR bands present in both softwood and hardwood lignins, including the unconjugated C=O stretching band which occurs between 1704 – 1682 cm^{-1}. This band can be seen in all three feedstocks in **Figure 4-4** with similar transmittance intensities, as expected.[22] In addition to the bands that are characteristic to both types of lignin structure, there also exists bands specific to the presence (or absence) of guaiacol and syringol monomers. In particular, the C-O stretching band of the syringol

ring is located at 1327 cm^{-1} whereas for the guaiacol ring it occurs at 1269 cm^{-1}.[22] Furthermore, Zhou et al. has identified a syringol band at 1220 cm^{-1}, which should appear in hardwood lignin. The identified guaiacol C-O bands are present in all three lignin spectra, whereas the syringol bands are identified in bagasse and poplar, as predicted. **Table 4-2** highlights the transmittance values at these band locations, where smaller values are indicative of larger bands due to the transmittance-based axis. In this way, it can be seen that the syringol band increases in intensity from softwood to hardwood lignin while the guaiacol band decreases in intensity. Further characterization reveals the presence of C-H deformation bands for syringol and guaiacol located at 1116 and 1151 cm^{-1}, respectively. These additional S and G bands follow the same trend as that identified for C-O vibrations, further confirming the known lignin structure from ^{13}C-NMR.

Table 4-2. FTIR band assignments and transmittance intensities from the bands identified in Figure 4. Estimated S/G ratio from FTIR is included based on the inclusion of absorbance values of the C-O and C-H bands corresponding to syringyl and guaiacyl groups in each phase.

	Band Position (cm^{-1})	Feedstock (%T)	Est. S/G	Biocrude (%T)	Est. S/G	Char (%T)	Est. S/G	Assignment
Pine	1425	90.22	0.73	69.11	0.70	89.16	0.83	CH deformation aromatic
	1327	91.49		73.72		89.61		C-O syringyl
	1269	83.12		54.10		85.58		C-O guaiacyl
	1215	83.89		51.89		84.71		C-C + C-O stretch (S)
	1151	85.56		63.12		86.17		aromatic CH guaiacyl
	1116	85.70		68.70		87.01		aromatic CH syringyl
	1081	86.85		74.03		87.91		C-O aliphatic ether
	1033	81.92		66.12		87.21		aromatic CH (G > S)
Bagasse	1425	90.28	0.97	68.67	0.99	89.26	0.92	CH deformation aromatic
	1327	89.89		69.23		88.66		C-O syringyl
	1269	86.83		60.30		86.56		C-O guaiacyl
	1215	85.10		49.70		85.48		C-C + C-O stretch (S)
	1151	86.06		69.30		86.25		aromatic CH guaiacyl
	1116	83.78		61.22		86.37		aromatic CH syringyl
	1081	86.75		71.30		86.62		C-O aliphatic ether
	1033	85.89		73.56		86.96		aromatic CH (G > S)
Poplar	1425	90.80	1.39	63.70	1.15	87.19	0.95	CH deformation aromatic
	1327	90.29		61.80		86.38		C-O syringyl
	1269	89.73		57.22		83.53		C-O guaiacyl
	1215	85.94		43.05		81.29		C-C + C-O stretch (S)
	1151	89.59		62.94		83.44		aromatic CH guaiacyl
	1116	80.94		46.77		82.25		aromatic CH syringyl
	1081	85.25		55.51		82.04		C-O aliphatic ether
	1033	84.72		64.50		83.48		aromatic CH (G > S)

Next, looking at the biocrude FTIR spectra in **Figure 4-4** reveals that the biocrudes have all maintained the characteristic bands associated with syringol and guaiacol from the parent lignin. In particular, the syringol C-O band continues the increasing trend from soft to hardwood lignin, whereas the guaiacol C-O band is larger for poplar than bagasse, contradictory to the decreased total guaiacol yield determined by GC-MS. An additional area of interest in the biocrude is the increased intensity of the S band at 1220 cm^{-1} in the poplar biocrude in particular.

While upon initial inspection, increased band intensity at 1220 cm^{-1} would indicate increased syringol content in the biocrude, performing a simple estimation of S/G ratio based on band abundance values results in a decrease in poplar S/G ratio compared to that of the feedstock (using FTIR). While the ^{13}C-NMR method for S/G determination is a recognized quantitative method, S/G was estimated from FTIR for all three phases for comparison purposes. This analysis reveals a slight decrease in softwood S/G from feedstock to biocrude, while the hardwood underwent a significant decrease. The differences in the pine and bagasse are both less than 0.05, within the limits of experimental error and follow the lignin-biocrude parity previously shown in **Figure 4-3**. Even more interesting is the decrease from lignin to biocrude S/G in poplar from FTIR is 0.24 whereas from GC-MS it is 0.28, highlighting and providing additional confirmation of the decrease in syringol content from hardwood lignin.

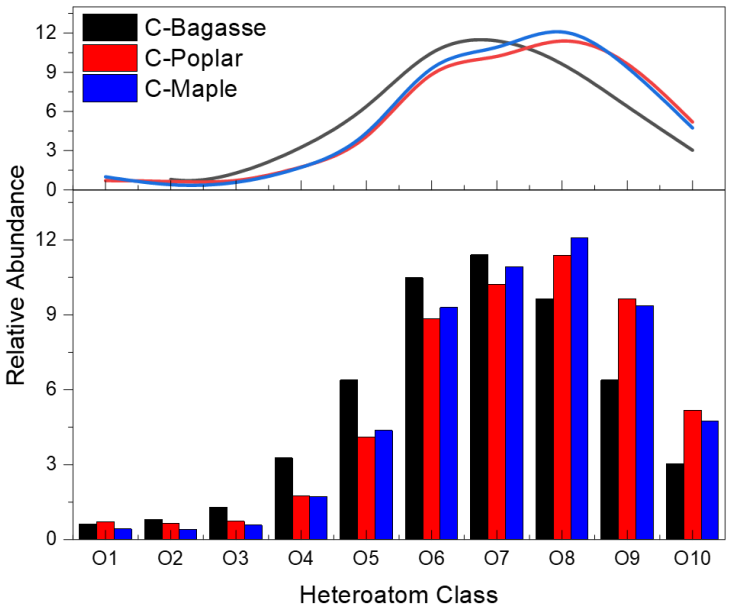

Figure 4-5. Oxygen heteroatom class distribution derived from the analysis of biocrude samples using (+) APPI FT-ICR MS at 21 T. The top panel represents the smoothed trendline described by the bar char.

Moving past the capabilities of GC-MS, FTIR was also used to analyze the resultant char from hydrothermal liquefaction. Compared to the biocrude and lignin phases, the char contains fewer vibrational bands, however, it maintains evidence of the parent syringol and guaiacol. The estimated S/G from bagasse and poplar char both decreased beyond that of the initial lignin, representing a loss of syringol from the char and indicating that syringol may have undergone reactions to transform its characteristic functionality, or is incorporated into the aqueous fraction. On the other hand, the estimated S/G for pine increased 0.1 beyond that of the feedstock. The trends in char S/G follow the previously mentioned idea of softwoods susceptibility towards repolymerization due to the increased proportion of unsubstituted aromatic carbons.[33] Overall, the band identities and intensities work to confirm predicted S/G trends in the hydrothermal liquefaction of lignin.

While GC-MS has the ability to analyze the volatile portion of biocrude and FTIR can provide insights into prominent bulk functionality, the use of FT-ICR MS can provide molecular-level insights into the heavy portion of the biocrude. **Figure 4-5** aims to explore the differences in heteroatom class abundance between a range of S/G ratio lignin biocrude using bagasse, poplar, and maple. The results of this analysis with positive ion atmospheric pressure photoionization and FT-ICR MS at 21 T show apparent Gaussian distributions for oxygen class abundance across all three samples. An interesting trend is seen wherein the maximum abundance is shifted to a higher oxygen number for hardwoods as opposed to bagasse. This shift is representative of an increase in syringol in the lignin framework, which introduces an additional oxygen as opposed to guaiacol. While FT-ICR MS is not a quantitative technique, the transition in oxygenate class abundance represents a paradigm shift in the way S/G affects lignin degradation and repolymerization in hydrothermal liquefaction. Due to the lower limit of detection and ionization method with FT-ICR MS and (+) APPI, these heteroatom class distributions must be the results of oligomers and cross-monomer linkages that can result from incomplete depolymerization or repolymerization under hydrothermal conditions.

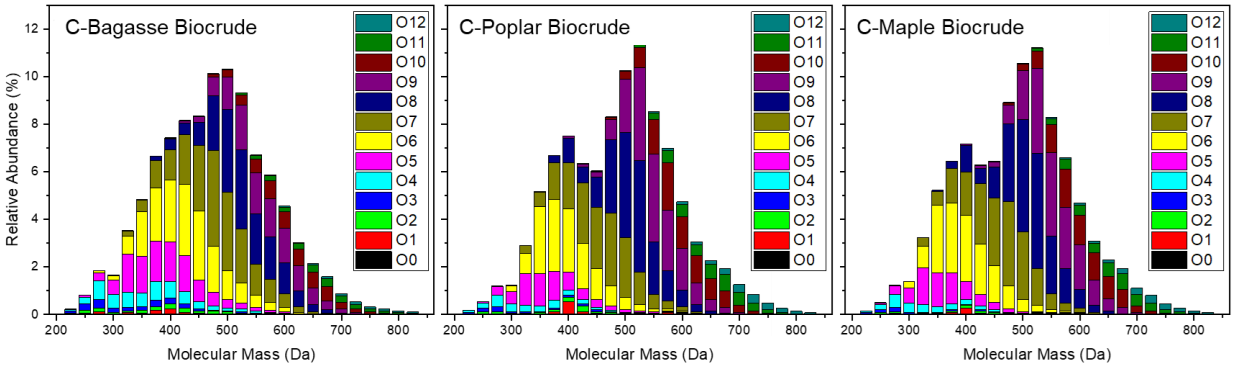

Figure 4-6. Oxygen heteroatom class abundance as a function of molecular weight derived from the analysis of biocrude samples with 21 T (+) APPI FT-ICR MS.

Further investigation into the detailed molecular formula assignments from FT-ICR MS provide insights into molecular mass distributions. In this way, the distribution and therefore understanding of oligomer production can be further explained. The resultant plots in **Figure 4-6** for bagasse, poplar, and maple biocrudes follow a similar shape, wherein all contain a Gaussian-like peak around 500 Da, independent of feedstock S/G. This peak is most likely representative of pentamers and hexamers that form O_8 and O_9 compounds, wherein the hardwood biocrudes begin to show a bimodal distribution wherein a second peak has emerged with an average molecular mass of approximately 375 Da. The emergence of this peak only in poplar and maple biocrude indicates that high S content favors formation of lower molecular weight trimers and tetramers, consistent with the three unsubstituted carbons present in syringol rings.[33] Additionally, it can be seen in **Figure 4-6** that the composition of the peaks shifts to higher-order oxygenate heteroatom classes with increased S/G ratio. In bagasse, the primary heteroatom classes at 500 Da are O_{6-8} classes, wherein the hardwood biocrudes this is shifted to O_{7-9} for the same molecular weight range. This trend follows that seen in **Figure 4-5** for heteroatom class distributions, where the higher the S/G ratio, the higher the dominant oxygen class.

4.4 CONCLUSIONS

Lignin is a complex, aromatic polymer found in the cell walls of plant biomass. CELF pretreatment and extraction represents a new technique to isolate cellulose and hemicellulose for furfural and ethanol production while extracting a useful lignin byproduct. ^{13}C solid-state NMR was used to understand structural changes and calculate S/G ratio in CELF lignin.

This work revealed the conservation of lignin structural components in hydrothermal liquefaction product phases, including the biocrude and char. Hardwood lignin was shown to result

in higher biocrude yields and increased selectivity to biocrude over char, making it preferable as an HTL feedstock. S/G ratio was determined to be a contributing factor in the determination of biocrude and monomer yields, wherein increased S/G ratio was associated with an increase in biocrude yield. The presence of hydroxyphenol monomers in agricultural wood lignins inflated their monomer yields to the highest among the five lignins explored, however, removal of the ethyl phenol monomer reveals that guaiacol and syringol content increases linearly with S/G.

4.5 APPENDIX C

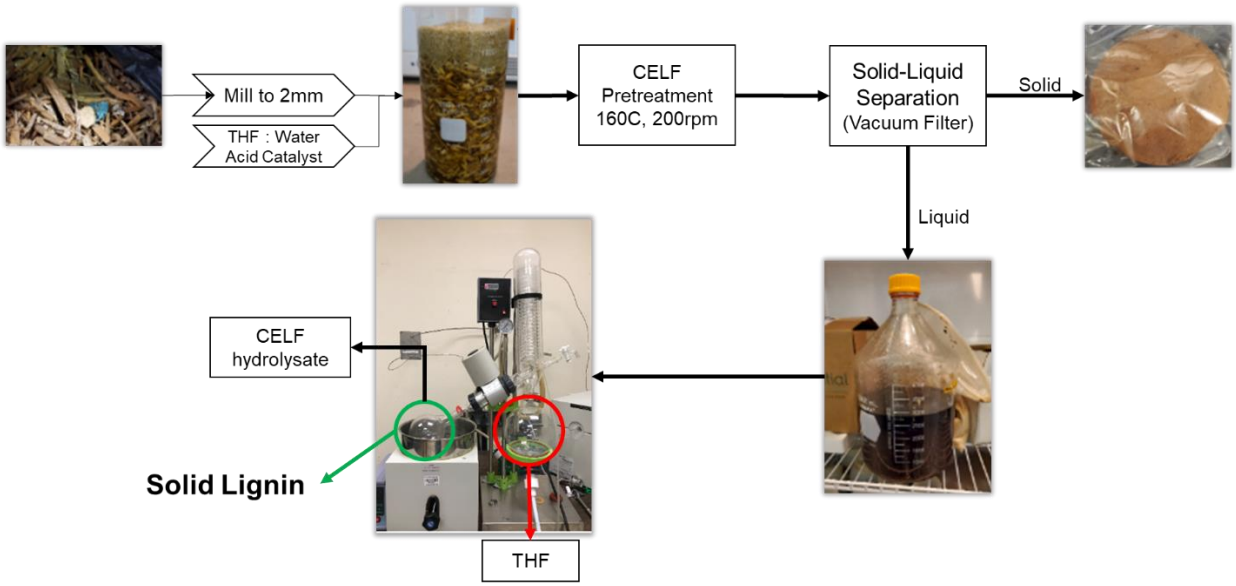

Figure C4-7. Process flow diagram, with images, representing the co-solvent enhanced lignocellulose fractionation process to obtain CELF lignin.

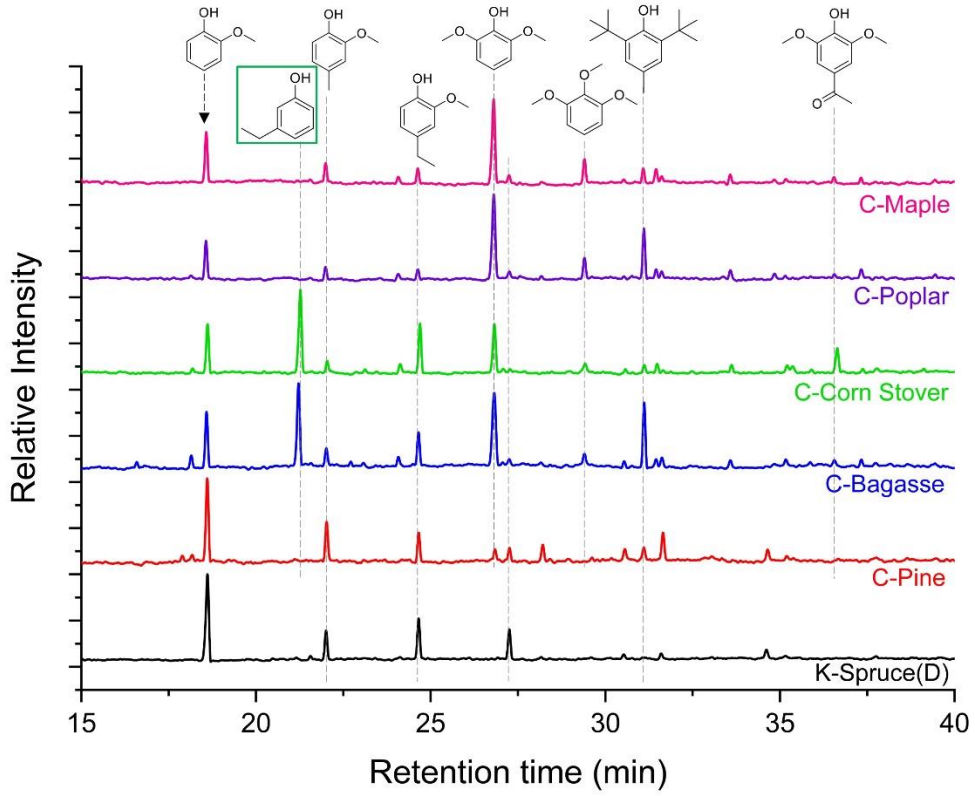

Figure C4-8. Raw GC-MS chromatograms from the analysis of the biocrude phase resulting from hydrothermal liquefaction of CELF lignin at 300 °C for 60 min.

Table C4-3. Quantitative results from the GC-FID analysis of the varying lignin biocrudes to determine their monomer yields and subsequent S/G ratio.

	K-Spruce	C-Pine	C-Bagasse	C-Corn Stover	C-Poplar	C-Maple
Guaiacol	8.84	4.98	3.94	3.58	3.71	4.40
Methyl guaiacol	2.31	1.92	1.13	0.86	1.33	1.71
Ethyl guaiacol	3.23	1.58	2.00	3.05	1.07	1.36
Propyl guaiacol	2.71	0.99	0.90	0.65	1.06	1.17
Ethyl phenol	-	-	6.12	6.58	-	-
Syringol	-	-	4.20	4.26	5.63	5.84
Butylated Hydroxytoluene	-	0.23	2.43	0.25	2.73	0.69
Total	**17.09**	**9.46**	**20.73**	**19.24**	**15.53**	**15.17**
S/G (From FID)	0	0	0.53	0.52	0.78	0.68
S/G (From NMR)	0.01	0.01	0.41	0.44	1.06	1.35

4.6 REFERENCES

1. Graglia, M.; Kanna, N.; Esposito, D., Lignin Refinery: Towards the Preparation of Renewable Aromatic Building Blocks. *ChemBioEng Reviews* **2015,** *2* (6), 377-392.

2. Beauchet, R.; Monteil-Rivera, F.; Lavoie, J. M., Conversion of lignin to aromatic-based chemicals (L-chems) and biofuels (L-fuels). *Bioresource Technology* **2012,** *121*, 328-334.

3. Calvo-Flores, F. G.; Dobado, J. A., Lignin as Renewable Raw Material. *ChemSusChem* **2010,** *3* (11), 1227-1235.

4. Chakar, F. S.; Ragauskas, A. J., Review of current and future softwood kraft lignin process chemistry. *Industrial crops and products* **2004,** *20* (2), 131-141.

5. Gellerstedt, G., Softwood kraft lignin: Raw material for the future. *Industrial Crops and Products* **2015,** *77*, 845-854.

6. Gellerstedt, G.; Lindfors, E.-L., Structural changes in lignin during kraft pulping. **1984**.

7. Gierer, J., Chemical aspects of kraft pulping. *Wood Science and Technology* **1980,** *14* (4), 241-266.

8. Kleppe, P. J., Kraft Pulping. *Tappi* **1970,** *53* (1), 35-47.

9. Becker, J.; Wittmann, C., A field of dreams: Lignin valorization into chemicals, materials, fuels, and health-care products. *Biotechnology Advances* **2019,** *37* (6), 107360.

10. Sivagurunathan, P.; Raj, T.; Mohanta, C. S.; Semwal, S.; Satlewal, A.; Gupta, R. P.; Puri, S. K.; Ramakumar, S. S. V.; Kumar, R., 2G waste lignin to fuel and high value-added chemicals: Approaches, challenges and future outlook for sustainable development. *Chemosphere* **2021,** *268*, 129326.

11. Smith, M. D.; Mostofian, B.; Cheng, X.; Petridis, L.; Cai, C. M.; Wyman, C. E.; Smith, J. C., Cosolvent pretreatment in cellulosic biofuel production: effect of tetrahydrofuran-water on lignin structure and dynamics. *Green Chemistry* **2016,** *18* (5), 1268-1277.

12. Zhao, Z. M.; Meng, X.; Scheidemantle, B.; Pu, Y.; Liu, Z. H.; Li, B. Z.; Wyman, C. E.; Cai, C. M.; Ragauskas, A. J., Cosolvent enhanced lignocellulosic fractionation tailoring lignin chemistry and enhancing lignin bioconversion. (1873-2976 (Electronic)).

13. Gani, A.; Naruse, I., Effect of cellulose and lignin content on pyrolysis and combustion characteristics for several types of biomass. *Renewable Energy* **2007,** *32* (4), 649-661.

14. Adewuyi, A., Underutilized Lignocellulosic Waste as Sources of Feedstock for Biofuel Production in Developing Countries. *Frontiers in Energy Research* **2022,** *10*.

15. Anex, R. P.; Aden, A.; Kazi, F. K.; Fortman, J.; Swanson, R. M.; Wright, M. M.; Satrio, J. A.; Brown, R. C.; Daugaard, D. E.; Platon, A.; Kothandaraman, G.; Hsu, D. D.; Dutta, A., Techno-economic comparison of biomass-to-transportation fuels via pyrolysis, gasification, and biochemical pathways. *Fuel* **2010,** *89*, S29-S35.

16. Cai, C. M.; Zhang, T.; Kumar, R.; Wyman, C. E., THF co-solvent enhances hydrocarbon fuel precursor yields from lignocellulosic biomass. *Green Chemistry* **2013,** *15* (11), 3140-3145.

17. Meng, X.; Parikh, A.; Seemala, B.; Kumar, R.; Pu, Y.; Christopher, P.; Wyman, C. E.; Cai, C. M.; Ragauskas, A. J., Chemical Transformations of Poplar Lignin during Cosolvent Enhanced Lignocellulosic Fractionation Process. *ACS Sustainable Chemistry & Engineering* **2018,** *6* (7), 8711-8718.

18. Anderson, E. M.; Stone, M. L.; Katahira, R.; Reed, M.; Muchero, W.; Ramirez, K. J.; Beckham, G. T.; Román-Leshkov, Y., Differences in S/G ratio in natural poplar variants do not predict catalytic depolymerization monomer yields. *Nature Communications* **2019,** *10* (1), 2033.

19. LeClerc, H. O.; Atwi, R.; Niles, S. F.; McKenna, A.; Timko, M. T.; West, R. H.; Teixeira, A. R., Elucidating the role of reactive nitrogen intermediates in hetero-cyclization during hydrothermal liquefaction of food waste. *Green Chemistry* **2022**.

20. LeClerc, H. O.; Tompsett, G. A.; Paulsen, A. D.; McKenna, A. M.; Niles, S. F.; Reddy, C. M.; Nelson, R. K.; Cheng, F.; Teixeira, A. R.; Timko, M. T., Hydroxyapatite catalyzed hydrothermal liquefaction transforms food waste from an environmental liability to renewable fuel. *iScience* **2022**, 104916.

21. Zhao, J.; Xiuwen, W.; Hu, J.; Liu, Q.; Shen, D.; Xiao, R., Thermal degradation of softwood lignin and hardwood lignin by TG-FTIR and Py-GC/MS. *Polymer Degradation and Stability* **2014,** *108*, 133-138.

22. Kubo, S.; Kadla, J. F., Hydrogen Bonding in Lignin: A Fourier Transform Infrared Model Compound Study. *Biomacromolecules* **2005,** *6* (5), 2815-2821.

23. Stankovikj, F.; McDonald, A. G.; Helms, G. L.; Garcia-Perez, M., Quantification of Bio-Oil Functional Groups and Evidences of the Presence of Pyrolytic Humins. *Energy & Fuels* **2016,** *30* (8), 6505-6524.

24. Hendrickson, C. L.; Quinn Jp Fau - Kaiser, N. K.; Kaiser Nk Fau - Smith, D. F.; Smith Df Fau - Blakney, G. T.; Blakney Gt Fau - Chen, T.; Chen T Fau - Marshall, A. G.; Marshall Ag Fau - Weisbrod, C. R.; Weisbrod Cr Fau - Beu, S. C.; Beu, S. C., 21 Tesla Fourier Transform Ion Cyclotron Resonance Mass Spectrometer: A National Resource for Ultrahigh Resolution Mass Analysis. **2015,** (1879-1123 (Electronic)).

25. LeClerc, H. O.; Page, J. R.; Tompsett, G. A.; Niles, S. F.; McKenna, A. M.; Valla, J. A.; Timko, M. T.; Teixeira, A. R., Emergent Chemical Behavior in Mixed Food and Lignocellulosic Green Waste Hydrothermal Liquefaction. *ACS Sustainable Chemistry & Engineering* **2022**.

26. Chen, C.-L.; Robert, D., Characterization of lignin by 1H and 13C NMR spectroscopy. In *Methods in Enzymology*, Academic Press: 1988; Vol. 161, pp 137-174.

27. Holtman, K. M.; Chang, H. m.; Jameel, H.; Kadla, J. F., Quantitative 13C NMR Characterization of Milled Wood Lignins Isolated by Different Milling Techniques. *Journal of Wood Chemistry and Technology* **2006,** *26* (1), 21-34.

28. Xia, Z.; Akim, L. G.; Argyropoulos, D. S., Quantitative 13C NMR Analysis of Lignins with Internal Standards. *Journal of Agricultural and Food Chemistry* **2001,** *49* (8), 3573-3578.

29. Duchesne, I.; Hult, E.; Molin, U.; Daniel, G.; Iversen, T.; Lennholm, H., The influence of hemicellulose on fibril aggregation of kraft pulp fibres as revealed by FE-SEM and CP/MAS 13C-NMR. *Cellulose* **2001,** *8* (2), 103-111.

30. Wang, Y.-Y.; Sengupta, P.; Scheidemantle, B.; Pu, Y.; Wyman, C. E.; Cai, C. M.; Ragauskas, A. J., Effects of CELF Pretreatment Severity on Lignin Structure and the Lignin-Based Polyurethane Properties. *Frontiers in Energy Research* **2020,** *8*.

31. Katakojwala, R.; Kopperi, H.; Kumar, S.; Venkata Mohan, S., Hydrothermal liquefaction of biogenic municipal solid waste under reduced H2 atmosphere in biorefinery format. *Bioresource Technology* **2020,** *310*, 123369.

32. Mishra, R. K.; kumar, V.; Kumar, P.; Mohanty, K., Hydrothermal liquefaction of biomass for bio-crude production: A review on feedstocks, chemical compositions, operating

parameters, reaction kinetics, techno-economic study, and life cycle assessment. *Fuel* **2022,** *316*, 123377.

33. Kim, K. H.; Kim, C. S., Recent Efforts to Prevent Undesirable Reactions From Fractionation to Depolymerization of Lignin: Toward Maximizing the Value From Lignin. *Frontiers in Energy Research* **2018,** *6*.

34. Schmatz, A. A.; Brienzo, M., Butylated Hydroxytoluene Improves Lignin Removal by Organosolv Pretreatment of Sugarcane Bagasse. *BioEnergy Research* **2022,** *15* (1), 166-174.

CHAPTER 5

HYDROXYAPATITE CATALYZED HYDROTHERMAL LIQUEFACTION TRANSFORMS FOOD WASTE FROM AN ENVIRONMENTAL LIABILITY TO RENEWABLE FUEL

5.1 INTRODUCTION

Over 1.3 billion tons of food is wasted worldwide every year. [1] In the United States, over 63 million tons of food is discarded annually, including manufacturing, residential, and commercial waste.[2] Food waste is energy dense and has potential for production of fuels and chemicals.[3] Multi-step conversion to usable energy has shown promise as a more sustainable approach to food waste management than current practices.[4] Unfortunately, most food waste is discarded in landfills with non-substantive energy recovery occurring with 6.3% of disposal going towards incineration with energy recovery.[5] However, if 100% of the world's annual supply of wasted food was converted to usable energy, it could power the United States for two years based on the 2020 energy consumption rate.[6, 7]

Hydrothermal processes have recently gained attention for conversion of biomass, algal, and organic wets wastes into fuels, chemicals, and materials.[8, 9] Unlike dry thermal conversion technologies (e.g., pyrolysis and gasification), hydrothermal processes are compatible with wet feeds.[8, 9] Compared with anaerobic digestion (days), hydrothermal processes are rapid (minutes), making them appropriate for modular, distributed deployment.[10]

Hydrothermal liquefaction has been extensively studied for use with algal and sludge feedstocks,[9, 11-13] primarily to maximize biocrude yield. Maximizing the lipid content of algae

benefits HTL biocrude yields. However, the National Renewable Energy Laboratory (NREL) has estimated the minimum algae feedstock costs to be $430/ton ash free dry weight (AFDW),[14] and experimental values are above $1,000/ton,[15] which makes conversion of algae into liquid fuels economically infeasible.

Utilizing food waste as a feedstock for HTL can replace the high cost of algae cultivation with feedstocks that have negative costs.[16] Unfortunately, biocrude yields obtained from HTL processing of food waste are much less than those obtained from algae, a feed that is rich in biocrude forming lipids.[17-19] Importantly, additional research is needed to make efficient use of abundant, inexpensive organic wet waste streams, (e.g., food waste) while matching biocrude yields that can be obtained from expensive high-lipid algae.

One approach to improving biocrude yields obtained from HTL processing of low-cost feeds is to use a catalyst.[20] While catalytic HTL has been reported previously in the literature, its impact has been limited by catalyst costs, especially when considering the harsh conditions that prevail during HTL.[21-23] Inexpensive, abundant, stable, and yet effective catalysts are required to make catalytic HTL of wet waste streams economically competitive.[19]

Hydroxyapatite (HAP), a naturally occurring mineral consisting of calcium and phosphorous oxides found in bone with the molecular formula $Ca_{10}(PO_4)_6(OH)_2$, meets all of these criteria.[24] HAP is thermally stable in air at temperatures <700 °C.[25, 26] Hydrothermal stability of HAP has not been examined in detail; however, Roberts et al. reported formation of HAP from calcium and phosphorous precursors naturally present in microalgae during HTL, implying that HAP is stable at HTL conditions.[25] The acid and base properties of HAP can be tuned by altering the pH between 7 and 11 during synthesis to manipulate the coordination of oxygen around the central calcium atom and result in a range of base to acid site ratios.[24, 27] HAP's use in biomass conversion and for

promoting HTL reactions is relatively unexplored, however, others have catalyzed carbon-carbon cross-coupling, condensation, and oxidation reactions.[24, 28-30] Understanding these pathways at the molecular level therefore is a further requirement for HTL to be impactful.[23]

The objective of this work was to evaluate the use of HAP for improving biocrude yields obtained from HTL of organic wet waste and to characterize biocrude compositions as a basis for chemically-resolved biocrude formation models. HTL product distributions, including biocrude yields, were measured for HTL of a model food waste stream using a series of HAP materials with varying acid-base properties. Recovered catalyst was studied after initial use, after prolonged exposure to hydrothermal conditions, and as part of a new method for converting carbon lost to the HTL aqueous phase into biocrude to further understand the role of the catalyst in condensation reactions. Biocrude and aqueous phase products were analyzed using molecular level methods to develop a basis for chemically-resolved biocrude formation models that can guide process development. Lastly, experimental data were input into economic and environmental models to predict potential outcomes. The results and analysis presented here establish a new technological and scientific baseline for the use of catalytic HTL as a method to transform environmental liabilities into renewable fuels.

5.2 MATERIALS AND METHODS

5.2.1 FOOD WASTE HYDROTHERMAL LIQUEFACTION

HTL experiments were conducted in a 300 mL stainless-steel Parr reactor (Model 4561), fit with a magnetic stirrer. For each experiment, 100 g of food waste slurry (15 wt.% solids) was loaded into the reactor. All catalytic experiments were performed with 5 wt.% catalyst, unless otherwise noted. After loading, the reactor was sealed and purged three times with nitrogen to remove residual air before pressurization to 65.5 ± 5 bar and heating to 300 ± 5 °C at approximately

6 °C/min using an external heating jacket. After heating, the reactor pressure was 200 ± 5 bar, sufficient to maintain water in its liquid state. The reaction temperature was maintained within ±5 °C of 300 °C with an immersed Type K thermocouple and PID controller. After 60 minutes at 300 °C, the reaction was quenched by placing the reactor in an ice bath until the measured temperature reached 38 ± 2 °C. Quenching required less than 10 minutes.

All runs were completed in at least duplicate, with yield measurements agreeing to within ±10% when experiments were performed under identical conditions. Average values obtained from these experiments are presented here. Error was calculated as the standard deviation between replicates of the same experimental conditions. For safety, the reactor setup was equipped with a pressure-relief valve and located in a fume-hood.

5.2.2 HTL PRODUCT ANALYSIS

Upon reaction quenching, HTL products partition into four phases (i.e., gas, aqueous, oil, and char) that can each be quantified, as reported previously.[18, 19] The overall mass balance was determined by summing the individual product yields and was found to close within 10% for all experiments. Mass yields were derived from the organic concentration loaded into the reactor. Reactor losses represent residual material that could not be removed from the reactor, transfer losses, and the precision of the analytical balance used to estimate gas yields (± 0.5 g).

Solid and liquid products were separated via vacuum filtration (Whatman no. 1 filter paper, 11µm). Oil products remained with the solid char on the filter while aqueous products were collected in the vacuum flask. Solid and oil products were then weighed and rinsed with approximately 1 L of acetone to separate and collect oil before using a rotary evaporator at 50 ± 5 °C and under vacuum (350 mmHg). Remaining solids contained spent catalyst and char were dried overnight and weighed before additional analysis. Char yield was calculated by subtracting the

known mass of added catalyst from the total mass of solid product. For catalyst reuse experiments, the filtered solids were placed in a COORS USA ceramic boat and calcined in a quartz tube clam shell furnace at 550 °C under continuous air flow (50 cm^3/min) for 6 h to combust char and recover catalyst.

Elemental analysis (CHON) was performed on the food waste feedstock, oil, and char phases at Midwest Microlabs (Indianapolis, IN). The oil and feedstock were also sent to Mainstream Engineering for higher heating value (HHV) analysis using a semimicro calorimeter (25720, Parr, Moline, IL) calibrated with benzoic acid. Total organic carbon (TOC) content of the aqueous phase was measured using a TOC analyzer (Shimadzu, Kyoto, Japan). The samples were diluted and acidified with 1 µL of 6 M HCl per 1 mL of sample and conducted in duplicate. Product mass yields were then utilized in conjunction with elemental analysis, TOC, and gas-phase GC TCD to determine the resultant carbon mass balance (**Equation 5.1**).

$$Carbon\ Yield_{product} = \frac{C_{product} \times Mass_{product}\ (g)}{C_{feed} \times Mass_{feed}\ (g)} \tag{5.1}$$

Carbon mass balance was evaluated by summing the carbon present in the biocrude, char, aqueous, and gas phases. In all cases, the carbon mass balance closed to within 10%. Energy recovery was calculated to determine the amount of energy recovered as desired product as a function of the feedstock energy.

$$Energy\ Recovery = \frac{HHV_{oil} \times Mass_{oil}\ (g)}{HHV_{feed} \times Mass_{feed}} \tag{5.2}$$

Comprehensive two-dimensional gas chromatography was performed on the biocrudes as described in the SI. Fourier-transform attenuated total reflection infrared spectroscopy (FT-ATR-IR) with a resolution of 8 cm^{-1} was used with eight scans taken and averaged for each sample for all biocrude oils to understand biocrude functional groups.

5.2.3 CATALYST CHARACTERIZATION

The different types of HAP were characterized to quantify their surface area via N_2 sorption, acid and base site densities via CO_2 and NH_3 temperature programmed desorption (TPD), crystallinity through X-ray powder diffraction (XRD), elemental composition of the surface via X-ray photoelectron spectroscopy, and morphology via scanning electron microscopy (SEM). Hydroxyapatite catalyst was washed with deionized water (> 18 MΩ•cm) utilizing centrifugation, until the pH of the resultant water phase remained constant, occurring at pH = 7. Approximately 5g of HAP-1.86 was loaded into a centrifuge tube along with 40 mL of DI water. The mixture was shaken for 1 min before being placed in a centrifuge to separate the solid and liquid phases. The pH of the resultant liquid phase was measured before being discarded in a waste container. 40 mL of fresh DI water was then added to the remaining HAP, mixed again for 1 min and placed in the centrifuge. This process was repeated until the liquid pH remained unchanged for 2 cycles, which took, on average 6 total cycles to achieve.

The catalyst crystallinity was determined by X-ray diffraction (XRD) before and after use in hydrothermal liquefaction. An X-ray powder diffractometer (Geigerflex, Rigaku Co., Tokyo, Japan) equipped with the Bragg-Bretano theta-theta configuration was used with CuKα radiation at 27.5 kV and 25 mA. Spectra were obtained in the range of 6 to 80° 2θ with a step size of 0.02°.

The morphology of fresh and spent catalysts were characterized using scanning electron microscopy (SEM). Ca/P ratios were determined through use of a PHI5600 x-ray photoelectron spectroscopy system equipped with a third-party data acquisition system (RBD Instruments, Bend, Oregon). Base chamber pressures remained below 5×10^{-9} torr during all data acquisition. The photoelectrons were collected with a hemispherical energy analyzed positioned at 90° with respect to the incoming mono-chromated Al Kα X-radiation.

5.2.4 LIFE CYCLE ASSESSMENT & TECHNOECONOMIC ANALYSIS

The LCA was performed using the GREET software developed at Argonne National Laboratory. The diesel upgrading step was taken as pre-set in the software for HTL biocrude upgrading to renewable diesel II. A TEA was provided by Pacific Northwest National Laboratory as developed for their 2016 report on sewage sludge.[31] Cost, yield, and quality data were altered as shown in **Table D5-8** to be representative of food waste and food waste experiments. The base PNNL model was modified to include a catalyst by adding the cost to the 'Simple Costs' tab on a per pound basis, and the lifetime included in HTL flows. Hydroxyapatite cost data was taken from Alibaba, where a price of $28.00/ kg was utilized.[32] Food waste feedstock cost was assumed to have a tipping fee of -$66.53/ wet ton, consistent with data published by the Environmental Research & Education Foundation.[16]

5.2.5 CO_2 AND NH_3 TEMPERATURE PROGRAMMED DESORPTION

Nitrogen sorption was utilized to investigate the surface area distribution in all HAP samples examined. Nitrogen sorption is a bulk technique that takes into consideration the porosity of the entire sample. Below P/P_0 of 10^{-3} the isotherm can be associated with gas-catalyst interactions within micropores whereas for $P/P_0 > 0.1$, the isotherm is associated with mesopore gas-gas interactions. Acid and base site densities of the oxide catalysts were determined using NH3- and CO2- temperature programmed desorption (TPD) analysis, respectively. A Quantachrome Autosorb iQ adsorption/chemisorption system equipped with a thermal conductivity detector (TCD), was used for the TPD analysis. The TPD methods used were similar to those reported by Rodrigues et al.,1 and Käßner et al.2. Samples were degassed under continuous flow of helium (20 cm3 min–1) at 550C for 3 hours, followed by cooling to 30 °C. After degassing, samples were then saturated under CO2 gas flow for 10 minutes at 30 °C, after

which the sample cell was purged with helium for 30 minutes at 30 °C to remove excess CO2. The CO2-adsorbed sample was then heated from 30 to 800 °C at a heating rate of 10 °C min–1 under helium, and the CO2 off-gas was quantified using a TCD detector. A similar method was used for NH3-TPD analysis to quantify acid sites.3 Samples were degassed under continuous helium flow for 120 minutes, cooled to 100 °C, and the sample saturated under continuous NH3 flow for 10 min. Degassing temperatures were set based on the thermal stability of the material. After NH3 saturation, the sample cell was purged under continuous helium flow for 30 min, heated to 800 °C at a rate of 2 °C min-1, and finally flushed with helium for 30 minutes. The off-gas was continuously monitored by a TCD detector. TPD calibration curves were generated using a range of measured volumes of NH3 and CO2. The areas under the standard TPD curves were calculated using Magicplot software. The base and acid site densities were calculated as μmol g–1 using TCD response factors.

Surface properties were evaluated using N_2 adsorption at −196.15 °C using a Quantachrome Autosorb iQ TPX instrument (Anton Paar Co., Graz, Austria). Before N_2 dosing, 500–1000 mg catalyst was degassed at 120 °C for up to 3 h under vacuum. Total surface area was estimated by fitting measured isotherms using the using the Brunauer–Emmett–Teller (BET) method. Mesopore diameters were estimated using Barrett, Joyner, and Halenda (BJH) method and the micropore volume and surface area using the Dubinin–Radushkevitch (DR) method.

5.2.6 TWO-DIMENSIONAL GAS CHROMATOGRAPHY

GC×GC-FID chromatography methods were adapted from Cheng et al.[23] as follows. Analyses were performed on a LECO GC×GC instrument equipped with an Agilent 7890A GC configured with a 7683B series split/splitless auto-injector. Biocrude samples dissolved in toluene were injected in splitless mode with a hydrogen carrier gas at 1 mL min^{-1}. The cold jet utilized

liquid nitrogen and the hot jet offset was 15 °C above the temperature of the primary GC oven (inlet T = 310 °C). The first dimension column was a Restek Rxi-1ms (60m, 0.25 mm ID, 0.25 µm df) whereas the second column was a 50% phenyl polysilphenylene-siloxane column (SGE BPX50, 1.2m, 0.10 mm ID, 0.1 µm df). The main oven was held at 65 °C for 12.5 min before ramping from 50 to 340 °C at a rate of 1.25 °C min^{-1}. The second-dimension oven temperature program was held at 70 °C (12.5 min) before ramping to 345 °C at 1.25 °C min^{-1}. The hot jet pulse width was 1.0 sec with a modulation period of 6.5 seconds with a 2.5 second cooling period. FID data was obtained with an acquisition rate of 100 data points per second.

GC×GC-HRT analysis was performed on a LECO Pegasus GC×GC-HRT 4D system equipped with an Agilent 7890A GC and configured with a LECO LPAL3 auto-injector and a LECO dual stage cryogenic modulator. Samples were injected in splitless mode with a helium carrier gas at 1mL min^{-1}. The cold jet utilized liquid nitrogen and the hot jet offset was 15 °C above the temperature of the primary GC oven (inlet T = 310 °C). The first dimension column was a SGE BPX-50 (60m, 0.25mm ID, 0.25µm df) with a SGE BPX-50 (2m, 0.25mm ID, 0.25µm df) second dimension column. The main oven was held at 80 °C for 12.5 min before ramping from 80 to 330 °C at a rate of 1.25 °C min^{-1}. The hot jet pulse width was set at 2.0 seconds with an 8 second modulation period. The second-dimension oven temperature program was held at 85 °C (12.5 min) before ramping to 335 °C at 1.25 °C min^{-1}. Mass resolution was +/- 0.0005 amu and sampled with an acquisition rate of 200 spectra per second in the mass range of 40 to 700 amu. The ionization method was EI with an electron energy of -70 Volts and an extraction frequency of 1.5 kHz.

5.2.7 POSITIVE ION APPI FT-ICR MS AT 9.4 T

Samples dissolved in toluene to a final concentration of 125 μg/mL for (+) atmospheric pressure photoionization Fourier transform ion cyclotron resonance mass spectrometry (APPI FT-ICR MS) at a flow rate of 50 μL/min.[33] An atmospheric pressure photoionization (APPI) source (Thermo-Fisher Scientific, San Jose, CA) was coupled to the first stage of a custom-built FT-ICR mass spectrometer (see below) through a custom-built interface.[33] The tube lens was set to 50 V (to minimize ion fragmentation) and heated metal capillary current was 4.5 A. A Hamilton gastight syringe (5.0 mL) and syringe pump were used to deliver the sample (50 μL/min) to the heated vaporizer region (350 °C) of the APPI source, where N_2 sheath gas (50 psi) facilitates nebulization. The auxiliary port remained plugged. After nebulization, gas-phase neutral analyte molecules exit the heated vaporizer region as a confined jet. A krypton vacuum ultraviolet gas discharge lamp (Syagen Technology, Inc., Tustin, CA) produces 10−10.2 eV photons (120 nm). Toluene increases the ionization efficiency for nonpolar aromatic compounds through dopant-assisted APPI[34, 35] through charge exchange,[36, 37] and proton transfer[38] reactions between ionized toluene molecules and neutral analyte molecules as previously reported.

All samples were analyzed with a custom-built FT-ICR mass spectrometer[39] equipped with a 22 cm horizontal room temperature bore 9.4 T superconducting solenoid magnet (Oxford Instruments, Abingdon, U.K.), and a modular ICR data station (Predator)[40] facilitated instrument control, data acquisition, and data analysis. Positive ions generated at atmospheric pressure enter the skimmer region (∼2 Torr) through a heated metal capillary, pass through the first radiofrequency (rf)-only octopole, pass through an rf-only quadrupole, and are externally accumulated[41] (25−50 ms) in a second octopole equipped with tilted wire extraction electrodes for improved ion extraction and transmission.[42] Helium gas introduced during accumulation

collisionally cools ions prior to transfer through rf-only quadrupoles (total length 127 cm) (into a 7-segment open cylindrical cell with capacitively coupled excitation electrodes based on the Tolmachev configuration.[43, 44] 100 individual transients of 6.8 s duration were signal averaged. The data was collected at the maximum memory depth of the data station hardware (16 million samples), apodized with a single sided Hanning apodization, zero-filled to 16 megasample (16777216 samples or 224). An additional zero fill brings the preFT data packet to 32 megasample, which in turn is processed via absorption-mode FT analysis.[45, 46] Experimentally measured masses were converted from the International Union of Pure and Applied Chemistry (IUPAC) mass scale to the Kendrick mass scale[47] for rapid identification of homologous series for each heteroatom class (i.e., species with the same $C_cH_hN_nO_oS_s$ content, differing only be degree of alkylation)[48]

For each elemental composition, $C_cH_hN_nO_oS_s$, the heteroatom class, type (double bond equivalents, DBE = number of rings plus double bonds to carbon, DBE = C − h/2 + n/2 + 1),[49] and carbon number, c, were tabulated for subsequent generation of heteroatom class relative abundance distributions and graphical relative-abundance weighted DBE versus carbon number images. Peaks with signal magnitude greater than 6 times the baseline root-mean- square noise at m/z 500 were exported to peak lists, internally calibrated based on the "walking calibration"[50] and molecular formula assignments and data visualization were performed with PetroOrg software[51] Molecular formula assignments with an error >0.5 ppm were discarded, and only chemical classes with a combined relative abundance of ≥0.15% of the total were considered. For all mass spectra, the achieved spectral resolving power approached the theoretical limit over the entire mass range: for example, average resolving power, $m/\Delta_{m50\%,}$ in which $\Delta m_{50\%}$ is mass spectral peak full width at half-maximum peak height, was ∼1 000 000−1 500 000 at m/z 500.

5.3 RESULTS AND DISCUSSION

5.3.1 CATALYST CHARACTERIZATION AND PERFORMANCE EVALUATION

Each of the six hydroxyapatite catalysts were tested to establish effectiveness at promoting biocrude formation in the hydrothermal conversion of a model food-waste mixture. The HAP catalysts were selected to represent a range of calcium-to-phosphorus ratios, since this property correlates with catalytic performance in many important reactions.[52] Accordingly, catalysts are named "HAP" for hydroxyapatite with a suffix that denotes the calcium-to-phosphorous ratio of the material. Experiments were performed in the absence of catalyst as a control.

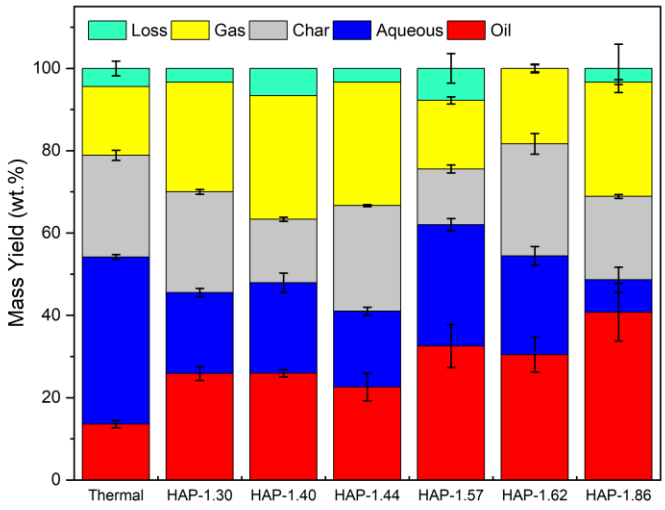

Figure 5-1. Product yields for all phases of HAP catalyzed hydrothermal liquefaction. Product yields reported in mass percent of organic feed. Oil is equivalent to biocrude. All reactions utilized 5% wt % catalyst completed at 300 °C, 1 h residence time, and 15% solids loading.

Figure 5-1 provides the product yields observed for these experiments, reported in terms of mass yield as a percent of the organic loading. Mass balance closure was always greater than 90% and error – ascertained by comparison of multiple runs – was less than 8%.

Addition of HAP increased biocrude mass yield (**Figure 5-1**) from a value of 13.6% in the absence of catalyst to 40.7% for HAP-1.86. The average biocrude yield in the presence of HAP was 29.7%, indicating the importance of specific HAP properties. Biocrude yield was weakly dependent on calcium-to-phosphorus ratio, with the three materials with Ca/P >1.5 resulting in greater biocrude yields than the three materials with Ca/P <1.5. **Figure D5-7** re-plots product fractions on a carbon basis, wherein HAP-1.86 shows increased oil-phase carbon compared to the thermal case.

Table 5-1. Elemental analysis (CHN) percentages for the resultant biocrude phase from HTL of food waste with a variety of hydroxyapatite catalysts. Oxygen weight percent determined by difference. Higher heating value and energy recovery also included for all biocrude runs.

Conditions	C (wt.%)	H (wt.%)	N (wt.%)	O (wt.%)*	Oil Yield (%)	HHV (MJ/kg)	Energy Recovery (%)
Food Waste	47.2	6.7	4.6	41.5	N/A	24.6	N/A
Thermal	69.9	8.4	3.8	17.9	14 ± 1	32.1	18 ± 2
HAP-1.30	68.1	8.5	2.8	20.6	26 ± 3	33.5	35 ± 3
HAP-1.40	60.3	8.4	3.5	27.8	26 ± 5	32.2	34 ± 5
HAP-1.44	67.3	8.8	2.9	21.0	23 ± 7	33.5	31 ± 7
HAP-1.57	68.0	9.2	3.1	19.1	33 ± 5	35.4	47 ± 4
HAP-1.62	67.7	8.3	3.2	20.8	31 ± 4	31.0	38 ± 4
HAP-1.86	70.3	9.0	3.7	17.0	41 ± 5	38.3	63 ± 5

*Oxygen weight percent is determined by difference.

Table 5-1 provides additional detail on the various biocrudes obtained using HAP and in the control run. Biocrude elemental composition is within the range 60-70 wt% carbon, 8-9 wt% hydrogen, 17-27 wt% oxygen, and 3-4 wt% nitrogen. The higher heating values (HHV's) of the biocrude samples were measured independently from composition and found to vary from 31 to 38 MJ kg^{-1} (measurement uncertainty =±1 MJ kg^{-1}). The biocrude obtained from use of HAP-1.86 contains the most carbon, only slightly higher than that from thermal HTL, yet its energy recovery is 3.5 times greater. This finding indicates the need for further analytical characterization for more accurate analysis compared to the bulk.

Table 5-1 shows that the energy recovery obtained using HAP-1.86 was substantially (~25%) greater than any other catalyst. Accordingly, HAP-1.86 was evaluated in more detail and its superior performance was found to arise from the presence of labile base sites on its surface as indicated by surface titration before and after rinsing (**Table D5-4, 5**). **Figure D5-8** provides biocrude yields obtained from tests on a rinsed version of HAP-1.86 and the corresponding supernatant liquid, showing that both of these increased biocrude yield relative to that observed under non-catalytic conditions. The energy recovery observed for HAP-1.86 after rinsing is comparable within the limits of uncertainty to those observed for HAP-1.57 and HAP-1.62. Interestingly, the individual improvements of the supernatant and the washed HAP appear to be additive, causing the same improvement observed using HAP-1.86 in its original state (within the limits of experimental uncertainty). Subsequent experiments with rinsed HAP-1.86 and homogeneous base (**Figure D5-8**) show that the combination of heterogeneous and homogeneous catalysts greatly increases biocrude yields obtained by HTL relative to either one used on its own.

The various HAP-based catalysts were characterized in greater detail for textural, composition, and surface properties. **Figures D5-9** to **D5-15** contain XRD, SEM, and nitrogen sorption curves. Catalyst properties were studied after use and after 200-h endurance tests in liquid water at 300 °C. In summary, the key characteristics required for boosting energy recovery are surface area greater than 20 m^2g^{-1}, balanced presentation of acid and base sites,[27, 52] stability after use and after long-term liquid water exposure (200 h), and most importantly, a calcium-to-phosphorous ratio greater than 1.50.

One problem revealed by catalyst characterization after use was accumulation of char on the surface that will lead to its de-activation over time,[53] a consequence of direct contact between the biopolymers contained in the feed with the catalyst during what can be termed *in situ* catalytic

HTL. Removing the catalyst from the HTL reactor, and instead using it in a secondary reactor to recover oil that would otherwise be lost to the aqueous phase has potential to limit char accumulation by removing it from direct contact with biopolymer present in the feed.[54] Following terminology usage in pyrolysis,[55] using the catalyst in a separate reactor than used for HTL can be termed *ex situ* catalytic HTL.

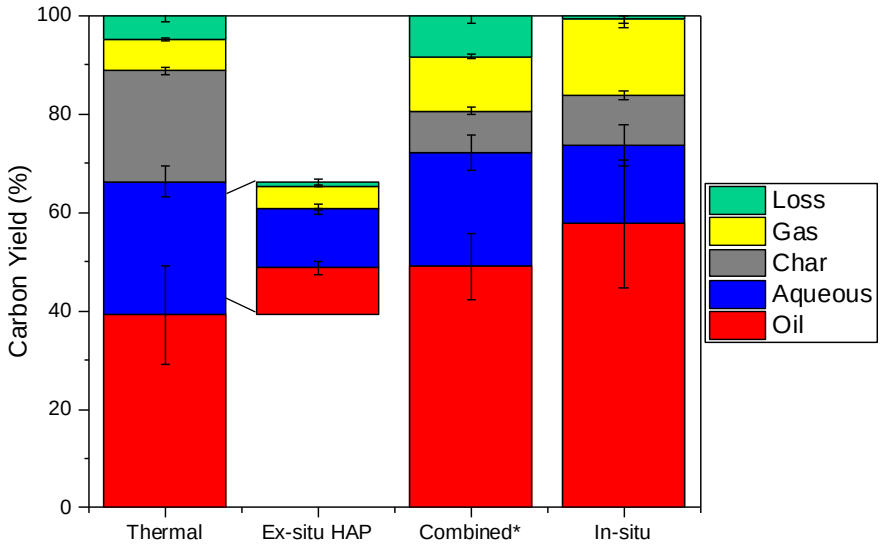

Figure 5-2. Ex-situ carbon yields for oil, aqueous, solid, and gas phases. Ex-situ experiments utilized thermal aqueous phase as the HTL feedstock with 5 wt% HAP-1.86 catalyst. The bar corresponding to ex-situ HAP is sized equally to the thermal aqueous phase to show the percentage of aqueous feed converted to biocrude. *Denotes mathematical combination of thermal and *ex situ* runs. All runs depict the average thermal yield without catalyst addition. Conditions: 300 °C, 1 hr., 200 bar.

The biocrude yields obtained from *in situ* and *ex situ* catalytic HTL experiments are shown in **Figure 5-2**, using HAP-1.86 as a model catalyst. **Figure 5-2** indicates that nearly 36% of the carbon remaining in the aqueous phase can be converted to biocrude by use of *ex situ* catalysis. Summing the biocrude obtained from thermal processing and *ex situ* carbon recovery corresponded to a biocrude carbon yield of 49%, which is the same as that obtained under *in situ* conditions

using the same catalyst within estimated limits of experimental uncertainty. Unlike for *in situ* catalyst use, which accumulated 5-15 wt% carbon on the surface as char, the carbon content of the catalyst used under *ex situ* conditions was less than 1 wt%. **Figure D5-15** contains photographs of the various catalysts. These results indicate that *ex situ* use of the HTL catalyst retains all of the benefits of using a catalyst, without the problems associated with carbon accumulation on the surface.

5.3.2 MOLECULAR-LEVEL ANALYSIS

Table 5-1 presents bulk properties of the HTL biocrudes. However, it lacks the molecular-level detail required for science-based reactor design and upgrading. The next step was molecular characterization of the biocrude product to understand its formation pathways to guide rational design of the HTL process.

Biocrude formation consists of a complicated sequence of biopolymer depolymerization and rearrangement into oil-soluble products. The lipid content of food waste is insufficient to explain the biocrude yields obtained here (**Table 5-1**). In addition to lipids, food waste contains starch, proteins, and simple carbohydrates that must contribute to biocrude formation to explain the observed yields. Understanding how the presence of catalyst promotes participation of the carbohydrates and proteins in biocrude formation is therefore key to utilization of low-lipid feeds for HTL. Reaction pathways of particular interest therefore are ones that convert water-soluble molecules, such as simple carbohydrates and amino acids, into oil-soluble ones that contribute to biocrude formation.

As a complex, multi-component mixture, partitioning of a single molecule into biocrude is not well defined. The octanol-water partition coefficient (K_{ow}) offers a convenient and quantitative proxy to understand biocrude-water partitioning.[56] Unlike biocrude-water partition coefficients,

octanol-water partition coefficients have been measured for many compounds of interest,[57] and empirical methods are available for predicting octanol-water partition coefficients for compounds that have not been studied previously.[58, 59] Moreover, octanol-water partition coefficients have proven to be linearly related to partition coefficients of many poorly defined thermodynamic systems,[60, 61] recommending their use for quantitative description of biocrude partitioning. Accordingly, K_{ow} is used here to guide understanding of what compounds should contribute to biocrude formation.

The various HTL products were analyzed at the molecular level using GC×GC, FT-ICR MS, and FT-IR spectroscopy. Each instrument served a specific purpose, with GC×GC analysis used to obtain precise molecular structure information for volatile products; (+) APPI FT-ICR MS was used to obtain isotopically accurate elemental formulas of ionizable species with molecular weights >150 Da; and FT-IR spectroscopy used to identify functional groups regardless of molecular weight. Data from these methods – especially GC×GC and FT-ICR MS – were then used to reconstruct biocrude and aqueous phase composition and thereby develop a framework for biocrude formation.

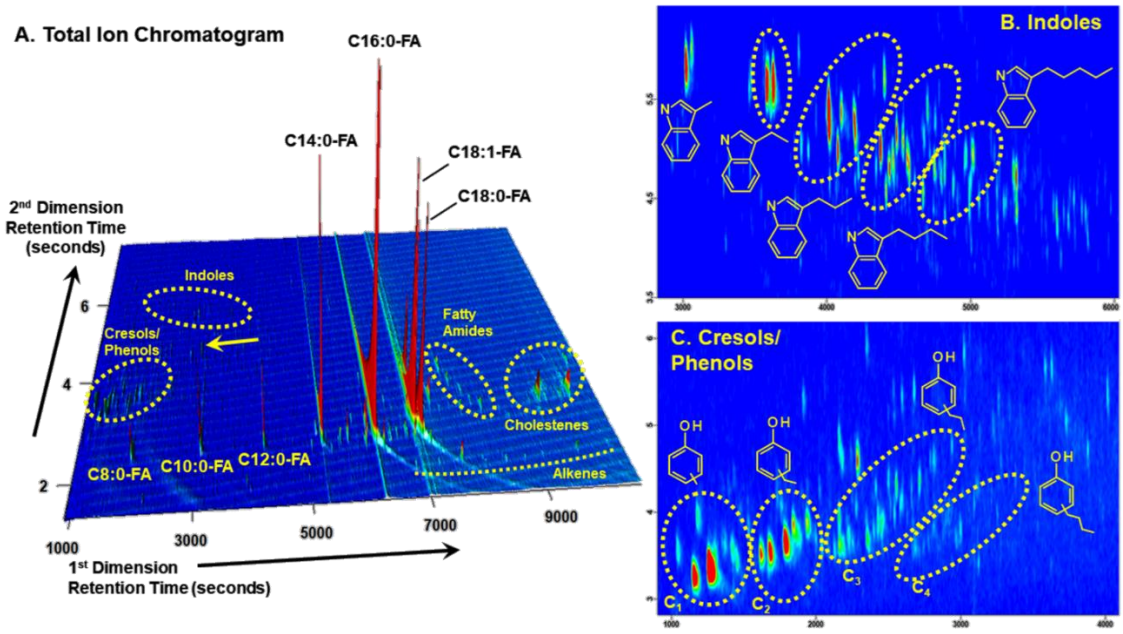

Figure 5-3. **a)** GC×GC-FID total ion mountain plot chromatograms of biocrude obtained from non-catalytic food waste HTL. **b)** GC×GC chromatogram depicting the area showing a range of substituted indoles. **c)** GC×GC chromatogram depicting the range of substituted phenols and cresols.

Figure 5-3 contains GC×GC-FID chromatograms corresponding to the biocrude obtained under non-catalytic conditions. **Figure D5-16** contains chromatograms with identical first and second dimension retention times obtained from analysis of biocrudes obtained in the presence of *in situ* catalysts. Qualitatively, the chromatograms obtained in the presence and absence of catalyst are similar to one another. Two-dimensional GC analysis shown in **Figure 5-3a** leads to multiple groupings of chemical classes, indentifying C_8 – C_{20} fatty acids as the major biocrude products. Fatty acids arise from hydrolysis of triglycerides and possess K_{ow} >> 10, consistent with partitioning into the biocrude phase.[62]

Secondarily, **Figure 5-3a** indicates the presence of n-alkenes, the products of fatty acid decarboxylation, and fatty amides, represented by a cluster of peaks that elute at retention times greater than the corresponding fatty acids. Fatty amides are the putative products formed by

reaction of fatty acids with amino acids and especially their breakdown products, including amines (90%) and methyl amines (10%).[17, 63] As with the fatty acids, the log(K_{ow}) of fatty amides with more than ten carbon atoms is predicted to be greater than 10. Moreover, the abundance of fatty amides establishes the importance of C-N formation reactions as a biocrude formation pathway, as the amino acid reactants on their own are predicted to partition into the aqueous phase (log(K_{ow}) < 2).

Aside from the abundant fatty acids and amides, **Figure 5-3a** indicates the presence of numerous trace-level peaks eluting earlier in the first dimension than the fatty acids. As identified by their corresponding mass spectra, these compounds belong to several classes, including cresols and indoles, highlighted in **Figure 5-3. Figure 5-3c** shows a zoomed in portion of the GC×GC chromatogram showing a series of alkyl phenols (cresols), with between one and four carbons present as side chains, shown in **Figure 5-3b**. The cresols and indoles form from reactions of carbohydrates with one another[64] or with amino acids.[65, 66] Unlike the parent compounds, which are expected to be water soluble, these molecules possess log(K_{ow}) values > 10, consistent with biocrude forming molecules. Detailed mass spectra are provided in Appendix D as **Figure D5-16** and FT-IR in **Figure D5-17**.

Despite GC analysis providing molecularly detailed information, thermal analysis indicates that less than 45% of the biocrude is volatile enough for GC analysis. Accordingly, (+) APPI FT-ICR MS was used to determine isotopically accurate molecular formulae of the ionizable heavy fraction of the biocrude (>150 Da). (+) APPI FT-ICR MS is especially sensitive to aromatic compounds and is capable of ionizing molecules across a broad range of polarities, especially relevant because of biocrude complexity.[34, 38, 67]

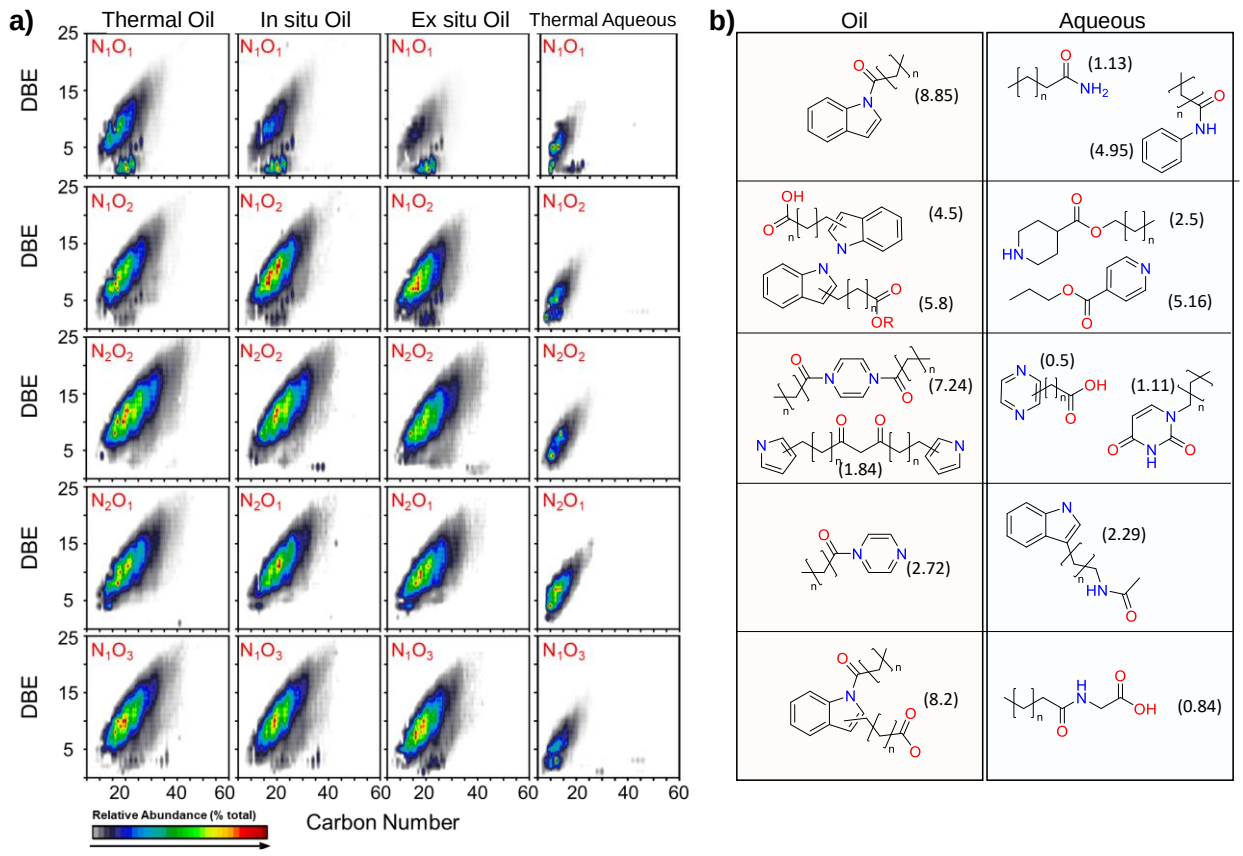

Figure 5-4. a) Double-bond equivalency (DBE) as a function of carbon number for the five most abundant classes identified in (+)APPI FT-ICR MS for the three biocrude phases and the non-catalytic aqueous phase. **b)** Proposed molecular structures and classes consistent with regions of high abundance identified in part a for each heteroatom class. Numbers in parentheses indicate K_{OW} for that particular molecule at that carbon number.

Figure 5-4 contains double-bond equivalency (DBE) data as a function of the number of carbon atoms for the six most abundant heteroatom classes identified in **Figure D5-19**. As more nitrogen and oxygen are incorporated into the molecule, the average carbon number and DBE also increases, as required to maintain K_{ow} values that favor biocrude formation.

In theory, a vast number of molecules can give rise to the FT-ICR MS patterns shown in **Figure 5-4**. In practice, the molecular structures indicated by FT-ICR MS must be consistent both with the components known to be present in the volatile biocrude fraction and known chemical

pathways. The conistency requirement makes tractable the assignment of probable molecular classes to the FT-ICR MS data. The results are provided as part of **Figure 5-4**, which shows that combinations of indoles and fatty acids, compounds that can be termed fatty indoles, are predicted to be especially prevalent in the biocrude. Interestingly, to remain consistent with the predicted DBE and GC×GC, fatty acids are proposed to form bonds with the indole both through the nitrogen atom, the result of an amidation reaction, as well as through formation of C-C bonds, indicating multiple probable mechanisms for fatty indole formation. Similarly, **Figure 5-4** provides K_{ow} values for represenative molecules of these different classes, showing that these products are predicted to partition into the biocrude phase. Analysis of the biocrude formed by *ex situ* catalysis points toward a process involving coupling of water-soluble products into oil soluble ones, thereby resulting in carbon transfer from the aqueous phase to the biocrude. Interestingly, *ex situ* catalysis seems to especially favor amidation reactions, as indicated by the C-N stretch that is much more intense in the *ex situ* biocrude sample compared with the others and as shown in **Figure D5-18** [68].

Figure 5-5 extends this analysis to explore the relationship of molecular weight and heteroatom class, containing a plot of abundance of different heteroatom classes as functions of molecular weight. The number of heteroatoms present in the biocrude molecules generally decreases with decreasing molecular weight, thereby maintaining favorable K_{ow} values across the entire molecular weight spectrum. More information is provided in **Figure D5-20**, showing re-plots of the data shown in **Figure 5-5** as relative abundance that shows compositional dependence in more detail.

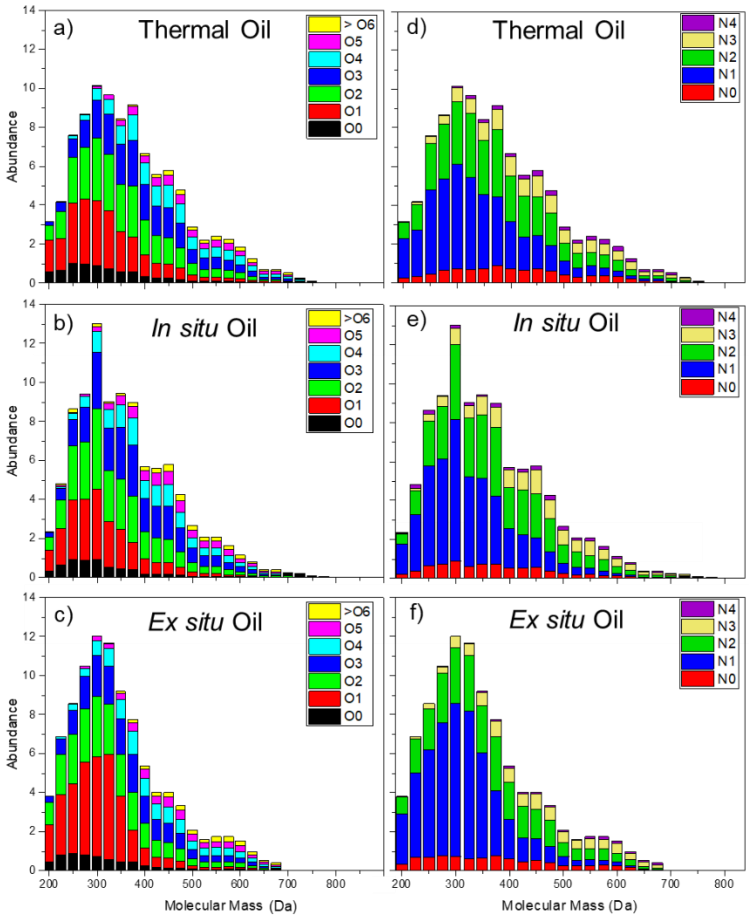

Figure 5-5. Relative abundance of different heteroatom classes as a function of molecular weight as determined by FT-ICR MS operating in (+) APPI mode. a), b), and c) show data for oxygen bearing molecules and d), e), and f) show the same data for nitrogen bearing molecules.

The molecular weight distribution consists of several broad maxima, centered at 300, 450 and 600 Da. The first of these features is consistent with the fatty indoles identified from the analysis shown in **Figure 5-4**. The others, therefore, arise from further condensation reactions, including indoles with multiple fatty acid consistuents and fatty acids cross-linked between indole groups. These molecular weight distributions are only weakly dependent on the presence or absence of catalyst, indicating that biocrude composition depends most strongly on the composition of the feed and secondarily on differences in formation conditions. Similarly, **Figure 5-5** supports the conclusion that the main impact of catalysts is to produce greater amounts of biocrude forming molecules, without introducing entirely new molecules and hence without introducing new pathways and instead amplifying existing ones.

In addition to biocrude analysis, **Figure 5-4** provides data obtained from analysis of the HTL aqueous phase. As expected from all previous discussion, for a given heteroatom class the aqueous phase product consists of lower carbon number and DBE than the same heteroatom class in the biocrude. The final column of **Figure 5-4b** provides molecular structures consistent with the aqueous phase FT-ICR MS data and previous reports of aqueous phase consistuents.[69-72] As compared with the biocrude phase, the aqueous phase consists of similar structural motifs, but with shorter fatty acid side chains that result in K_{ow} values favoring aqueous phase partitioning rather than biocrude formation.

Combining GC×GC and FT-ICR MS provides a detailed picture of the biocrude formed during hydrothermal liquefaction of food waste. **Figure 5-6** is a schematic that captures the most important molecular details. Hydrolysis and thermolysis of the proteins, lipids, and starch present in food waste gives rise to amino acids, fatty acids, and simple carbohydrates. The K_{ow} values of the fatty acids are sufficient for biocrude formation yet the amino acids and carbohydrates must

undergo further dehydration and coupling reactions for biocrude formation. A critical step is formation of C-N and C-C bonds between the indole and phenol products of amino acid and carbohydrate degradation reactions to form fatty indoles that greatly increase the biocrude yield. These coupling reactions are responsible for biocrude yields that far exceed those predicted from the lipid content of the feed. The role of the acid-base catalyst is to boost these C-N and C-C forming reactions, thereby increasing the yields of these specific compounds while only secondarily impacting their structures.

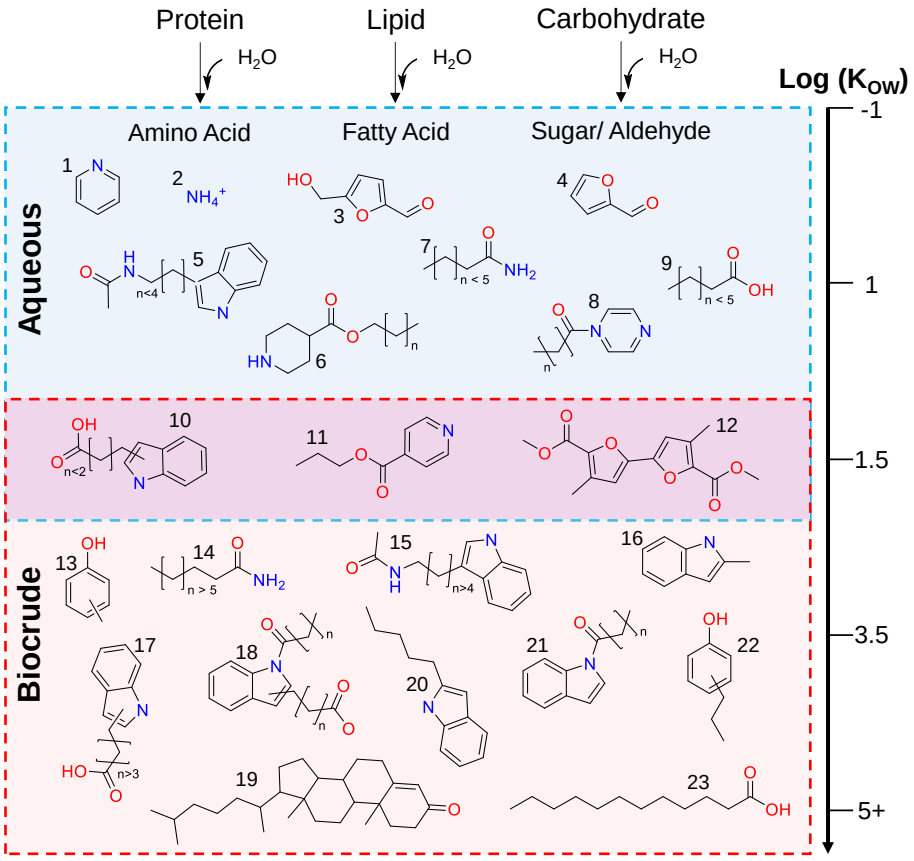

Figure 5-6. Schematic representation of the molecules present in HTL liquid-phase products (biocrude and aqueous). Biocrude formation is the result of biopolymer hydrolysis and thermolysis followed by recombination. For food waste, formation of fatty indoles and alkyl phenols is especially important. K_{ow} values are provided for the various compounds, showing that $\log(K_{ow}) > 2$ is required for biocrude formation.

Figure 5-6 provides K_{ow} values for the various compounds identified in the biocrude. Based on appearance of compounds in the aqueous phase and biocrude phase, a value of $\log(K_{ow}) > 10$ is required for biocrude formation. This observation suggests a correlation between K_{ow} and the corresponding biocrude-water partition coefficient (K_{bw}): $\log K_{bw} = \log K_{ow} + 1$. This correlation will be somewhat sensitive to the feedstock and to the reaction mixture pH, since many of the molecules present in the biocrude are ionizable acids, amines, or amides.

5.3.3 POTENTIAL COMMERCIAL IMPACTS

Economic and environmental analyses were performed to evaluate the potential impacts of the new catalytic HTL technology for converting food waste into fuels. Environmental analysis included greenhouse gas (GHG) emissions reduction, which is provided in the main text, and impacts of secondary products (**Figure D5-23**). Economic analysis used a previous report by PNNL as a starting point that included detailed analysis of both capital and operating expenses.[31]

Full analysis of GHG reduction included three main components: CO_2 offsets due to replacing petroleum fuels with a renewable option, CO_2 emissions associated with refining food waste to diesel relative to those expected for converting petroleum to diesel, and reduction of GHG emissions due to re-directing food waste from landfills to use as a fuel.

Hydrotreating experiments, summarized in the Supporting Information (**Figure D5-22**), suggest hydrotreated biocrude obtained from food waste is suitable for use as a diesel blend stock or replacement and literature reports carbon recovery of nearly 70%.[8, 73, 74] Based on annual food waste production solely in the U.S. (63 million tons) with an organic content of 25 wt%,[2, 75] food waste HTL has the potential to replace 4.5 million tons of diesel per year (28% of U.S. diesel market).[76] Given that combustion of the food waste-derived diesel does not introduce new carbon into the atmosphere (i.e., CO_2 released by combustion will be taken up on rapid time scales to

generate new food) and that combustion of petroleum diesel results in transfer of 3,082 kg of CO_2/ton of diesel from geological reserves to the atmosphere means that converting food waste to diesel has the potential to offset up to 15.3 million tons of CO_2 per year.

Table 5-2. Life cycle assessment emissions and resources calculations from GREET model of hydrothermal liquefaction. The life cycle of the catalyst is not specifically included in calculations due to the ability to use calcium and phosphorus as a soil amendment.

	Conventional Diesel	**Diesel from Algae HTL[14, 77]**	**Diesel from food HTL (base case)**	**Diesel from food HTL (+ HAP-1.87)**
Emissions (per MBTU)				
Total CO_2 [kg]	13.1	21.0	30.6	13.4
CO [g]	13.2	13.2	50.2	13.5
NO_x [g]	23.5	24.9	63.8	23.3
PM_{10} [g]	1.5	3.1	2.9	1.0
SO_x [g]	7.5	86.8	29.5	10.8
CH_4 [g]	100	83.4	210	78.1
Resources				
Energy [MJ]	1249	1506	1703	625

Converting food waste to diesel requires energy inputs. A well-to-pump life cycle analysis (**Table 5-2**) was performed using GREET software[78] to quantify the CO_2 emissions and energy input required for catalytic and non-catalytic HTL of food waste compared with petroleum-based diesel. LCA inputs (**Figure D5-23, Table D5-8**) are consistent with the flow rates and product usage identified in the TEA. [68, 79-82] Interestingly, producing diesel from food waste without a catalyst results in co-production of 2.3-times more CO_2 (30.6 tons) than producing diesel from petroleum (13.1 tons), a consequence of the low biocrude yield. Catalytic HTL of food waste results in CO_2 production values that are roughly equal to those for diesel production from petroleum (13.4 vs. 13.1 tons). These values are comparable to those reported previously by Fortier et al.[83, 84] and Nie et al.[85] for algae and biomass feedstocks, respectively, and indicate that GHG emissions from converting food waste to diesel roughly offset the emissions expected for

converting petroleum to diesel. Accordingly, the GHG term due to HTL diesel production was neglected in further analysis of total GHG reduction. Similarly, the Energy Return on Investment (EROI) estimated for production of diesel from food waste is only 0.81 in the absence of catalysts and increases to 2.42 for catalytic HTL, indicating twice the energy is produced than is consumed in the process.

The well-to-pump analysis summarized in **Table 5-2** does not account for greenhouse gas reductions associated with re-directing food waste from landfills. For landfills lacking methane capture, food waste decomposes to produce greenhouse gases, particularly methane, which is 50 times more climate forcing than CO_2.[86] The U.S. produced 63 million tons of food waste in 2018, and the EPA estimates the methane potential of anaerobic digestion of food waste is equivalent to an estimated 2.49 tons of CO_2 per ton of waste.[87] The result is that landfilling food waste results in annual emission of 156.8 million tons of GHG per year, which is equivalent to 2.4% of annual GHG emissions in the U.S.[88] Diverting food waste from landfills to production of renewable fuel avoids these emissions entirely.

The landfill gas and petroleum diesel replacement analyses can be summed to arrive at a final value for GHG reductions that can be expected from complete conversion of all U.S. food waste into renewable diesel. The maximum possible reduction is 171 million tons/yr. This value is 2.6% of annual U.S. GHG emissions.[89] While the assumptions of 100% of food waste collection and conversion to diesel is optimistic, this analysis provides a very reasonable first assessment of the magnitude of the CO_2 reduction that is possible using the food waste to diesel strategy. Further LCA considerations as they pertain to HTL byproducts are discussed in **Appendix D**.

The LCA indicates the potential for positive environmental benefits of the new technology and clearly establishes the improvements that use of a catalyst can achieve. The next step was to

analyze potential economic impacts by performing a TEA. **Table D5-8** provides values of the inputs to this model.[31] A summary of the non-catalytic and catalytic TEA results can be found in **Table D5-9 and 10.** To reflect current practice, a food waste tipping fee was included in the TEA and an aggregate average was calculated for tipping fees across the northeastern states of the USA (-$66.67)[16] plus a fixed cost of $55/ton for transportation of the food waste to the HTL processing center.

Table 5-3. Predicted MFSP ($/GGE) for biocrude production from different feeds and HTL technologies.

Feed	Feed Cost ($/dry ton)	Catalyst[b]	Catalyst Lifetime[c] (hrs)	Biocrude Yield (wt.%)	MFSP[d] ($/GGE)	Source
Algae				40.9	11.35	Jiang et al.[15]
Algae	1171	None	N/A	38.1	12.03	
Algae				42.4	11.03	
Food Waste	–45[a]	None	N/A	13.6	8.24	This work
		HAP-1.57	100	32.1	8.54	
		HAP-1.86	200	31.8	6.11	
		HAP-1.86 alkali[e]	200	40.7	4.78	

[a]Feed cost includes transportation as $55/ton.[90]

[b]HAP catalysts were used with a catalyst cost of $11.34/ lb. as found on Alibaba[32]

[c]Catalyst lifetime as determined experimentally

[d]Minimum fuel selling price for biocrude without upgrading

[e]Alkali costs taken as $330/ metric ton = $0.01/ lb. as found as Alibaba[91]

Table 5-3 provides estimated values of the minimum fuel selling price (MFSP) of biocrude produced from food waste conversion using the catalytic HTL technology compared with similar values reported for an algae feedstock.[15, 31] Producing biocrude from algae results in an estimated MFSP >$10 per gallon of gasoline equivalent (GGE).[15] The uncompetitive MFSP calculated for algae ($11.03) is a direct consequence of the high feedstock cost (>$1,000/ton) despite the high biocrude yield (40%) achievable with HTL processing of algae.

In the absence of catalyst, HTL conversion of food waste decreases MFSP ($8.24) by 28% relative to the average value predicted for algae. This reduction is a consequence of the tipping fee

that can be claimed by processing food waste, in spite of the differences in biocrude yields obtained by the two processes (i.e., 13.6% compared with as much as 42.4%). Use of a catalyst to increase biocrude yield further decreases the estimated MFSP, with combined use of the heterogeneous-homogeneous catalyst described here resulting in a 57% reduction in MFSP ($4.78) relative to that estimated for algae without a catalyst. The added cost of the catalyst was more than offset by the biocrude yield improvements.

Sensitivity analysis indicated that tipping fees, catalyst cost and lifetime, and biocrude yields are the most important for determining MFSP, as summarized in **Figure D5-24** and **D5-25**. Optimization of these parameters can realistically reduce the predicted MFSP of food waste biocrude. In particular, a tipping fee of −$45/ton, assuming a 50% moisture content, including transportation costs, is a conservative estimate.[90] Tipping fees are generally increasing across the USA, and tipping fees in Alaska already exceed $150/ton,[16] a value which corresponds to a predicted biocrude MFSP of $2.17/GGE for HAP-1.86 with alkali addition, even after including a reasonable estimate for transportation costs at $55/ton.[90]

Aside from deploying the technology in areas that maximize tipping fees, technological improvements can similarly reduce projected MFSP. The most easily validated area for reducing costs is extending the catalyst lifetime parameter input to the model. A 200 h catalyst lifetime used is a conservative estimate, since the 200 h endurance test was the longest test performed in this study. Varying the catalyst lifetime input to the model from 200 to 500 h results in a predicted MFSP of $3.56; a lifetime of 1,000 h results in an MFSP of $3.16. Further improvements in biocrude yield and/or decreased catalyst cost can have similar effects as extending the catalyst lifetime.[18, 23]

Table 5-3 reflects only the MFSP projected for production of biocrude. However, refining the biocrude to a transportation fuel can earn renewable fuel incentives[92] for economically competitive production of HTL diesel. Previous analysis suggests that upgrading algae and sludge-derived HTL biocrude to diesel costs approximately $1.10/GGE.[31, 90] Upgrading experiments performed on the food waste HTL biocrude show similar conversion of biocrude to diesel with 70% yield is possible using inexpensive molybdenum-based catalysts. The Supporting Information provides more detail on the upgrading experiments. Combining the most generous tipping fee currently reported in the USA ($150/ wet ton) with modest extension of catalyst lifetime from 200 to 500 h, and the historical value of the renewable fuel credit appropriate for upgraded HTL diesel ($1.00/GGE)[92, 93] results in an estimated MFSP of $0.96/GGE for the HAP-1.86 + alkali biocrude (without incentives) and $1.06/GGE for the upgraded HTL diesel (including incentives).[92, 93] The projected values of the HTL diesel MFSP show that combining tipping fees, technological improvements, and renewable fuel credits provides a clear pathway for catalytic HTL conversion of food waste from a greenhouse gas emitting liability to an economically competitive renewable fuel.

5.4 LIMITATIONS OF STUDY/ CONCLUSIONS

The economic analysis is based on the n^{th} generation plant assumption and does not capture costs for an initial deployment. Environmental analysis through a life cycle assessment (LCA) utilizes assumptions about the efficiency of certain portions of the fuel production process, including those for obtaining the necessary electricity. Additionally, upgrading costs are currently based on experimental and model predictions from Pacific Northwest National Laboratory, and have the potential to change, both positively and negatively, depending on biocrude composition

and catalyst choice. A single feedstock was used for all experiments and the current approach should be applied to a wider range of feeds to generalize the results observed here.

5.5 APPENDIX D

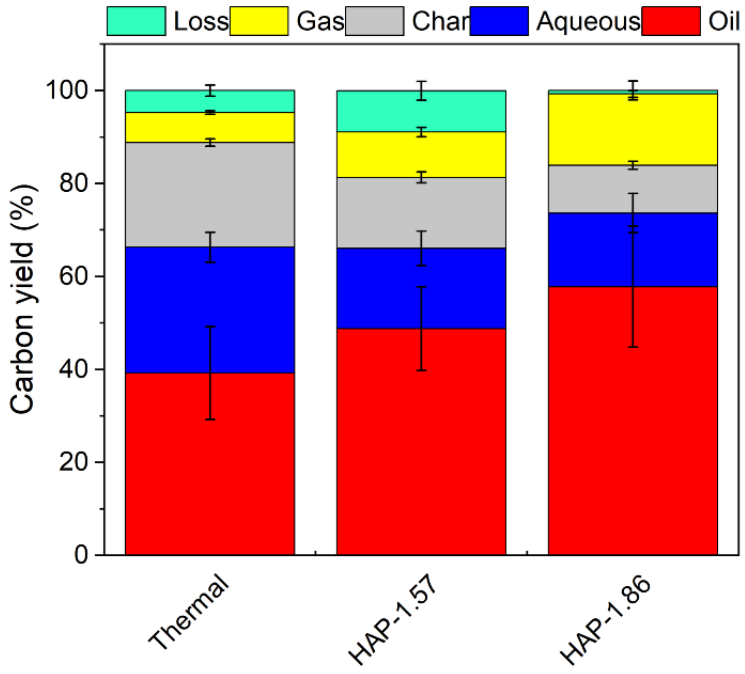

Figure D5-7. **HAP-catalyzed hydrothermal liquefaction carbon balance yields.** Product yields, on a carbon basis, for products for thermal, HAP-1.57, and HAP-1.86 HTL experiments. All reactions were completed at 300 °C, 1 h residence time, 15% solids loading, and catalytic runs utilized 5 wt.% catalyst, related to Figure 5-1.

Table D5-4. **Hydroxyapatite (HAP-1.86) catalyst properties before and after use in HTL and hot liquid water.** Acid and base site densities for HAP after use and endurance testing completed with chemisorption, related to Catalyst Characterization and Performance Evaluation, Table 1 and Figure 5-2.

Catalyst Conditions	Base site density (μmol/g)	Acid site density (μmol/g)	Measured Ca/P Ratio
HAP-1.86	11.3 ± 4.5	0.13 ± 0.05	1.86
After use HAP-1.86	1.14 ± 0.5	0.11 ± 0.04	1.47
Washed HAP-1.86	1.50 ± 0.6	0.13 ± 0.05	
200h HLW HAP-1.86	1.64 ± 0.6	0.12 ± 0.05	

Table D5-5. **Varying hydroxyapatite catalyst properties.** Summary of HAP characteristics indicating a primary difference in base to acid site ratio and calcium to phosphorus ratio, related to Catalyst Characterization and Performance Evaluation, Table 5-1 and Figure 5-2.

Catalyst	Surface Ca/P Ratio	N_2 BET surface area ($m^2\ g^{-1}$)	Total site density (μmol g^{-1})		Base: Acid Site Ratio
			Base	Acid	
HAP-1.30	1.30	58	15.2	0.33	46
HAP-1.40	1.40	50	13.1	0.33	40
HAP-1.44	1.44	35	8.7	0.79	11
HAP-1.57*	1.57	106	8.3	0.36	23
HAP-1.62	1.62	51	21.8	0.33	66
HAP-1.86*	1.86	22	11.3	0.13	87

*Indicates catalysts purchased from Sigma Aldrich.

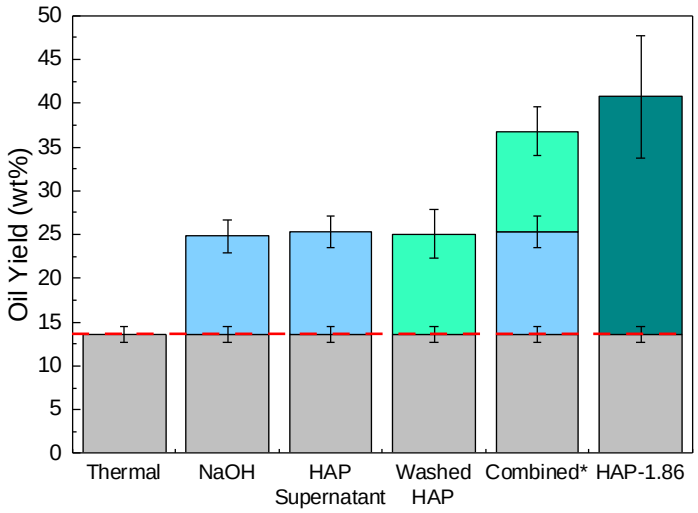

Figure D5-8. **Biocrude mass yields revealing the mixed homogenous and heterogeneous contributions from hydroxyapatite.** Biocrude yields obtained under thermal conditions, using HAP-1.86 in its original state, supernatant recovered from HAP washing, the washed solid HAP, and homogeneous base (NaOH) at identical pH to the supernatant. (pH = 12) related to performance evaluation, Figure 5-2.

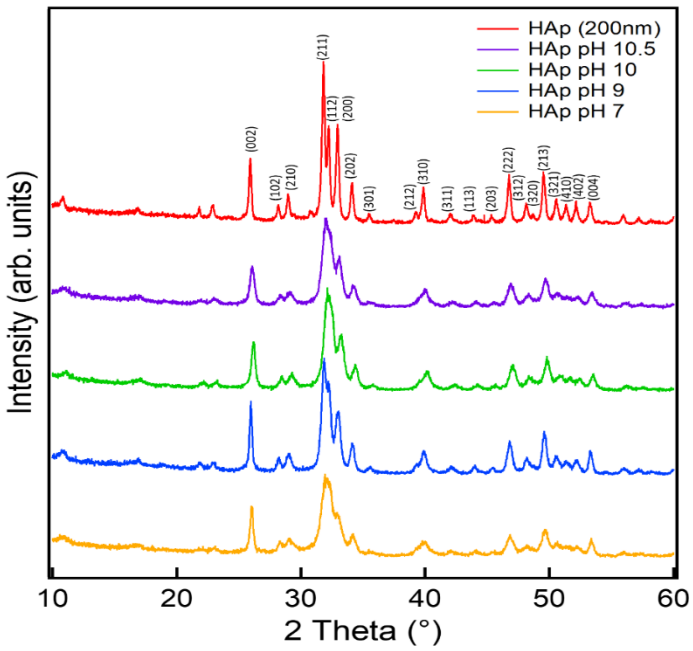

Figure D5-9. **Hydroxyapatite variants XRD diffraction patterns.** X-ray powder diffraction spectra of the synthesized HAP variants compared to the top performing commercial HAP-1.86, related to catalyst characterization, Table 1 and Figure 2.

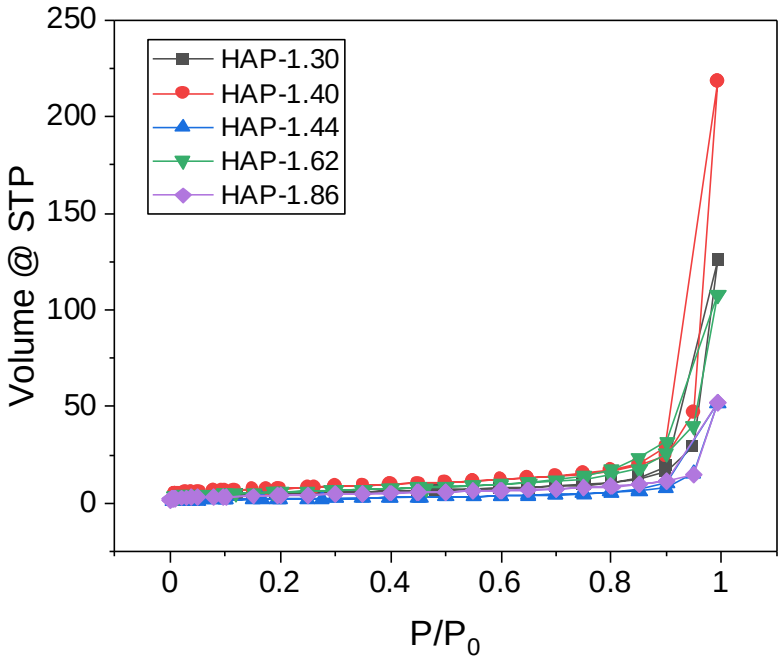

Figure D5-10. **Catalyst sorption curves for HAP surface area estimation.** N_2 sorption curves for estimating surface area for all HAP variants, related to catalyst characterization, Table 5-1 and Figure 5-2. The shape of the nitrogen sorption curve indicates the significance of external surface area. Nitrogen sorption isotherms can be divided into two primary regions, wherein $P/P_0 < 10^{-3}$ is associated with micropore interactions. $P/P_0 > 0.1$, on the other hand, is associated with interactions within mesopores. More specifically, the curvature of the sorption isotherm above $P/P_0 > 0.1$ is attributed to mesoporosity. Figure D5-10 indicates that the majority of the adsorption occurs well above $P/P_0 = 0.1$, occurring closer to 1.0, indicating the high external surface area.

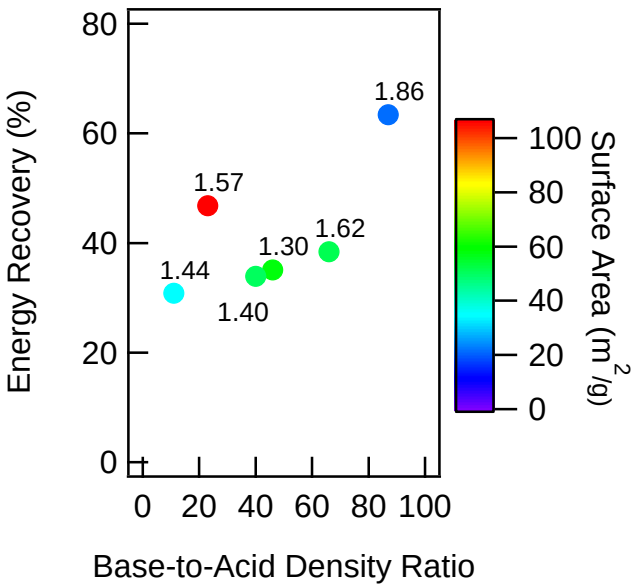

Figure D5-11. Effect of catalyst base to acid site density and surface area on energy recovery. Relationship between base to acid site density ratio and energy recovery in HTL of food waste. Markers are colored based on measured catalyst surface area, related to catalyst characterization, Table 5-1 and Figure 5-2.

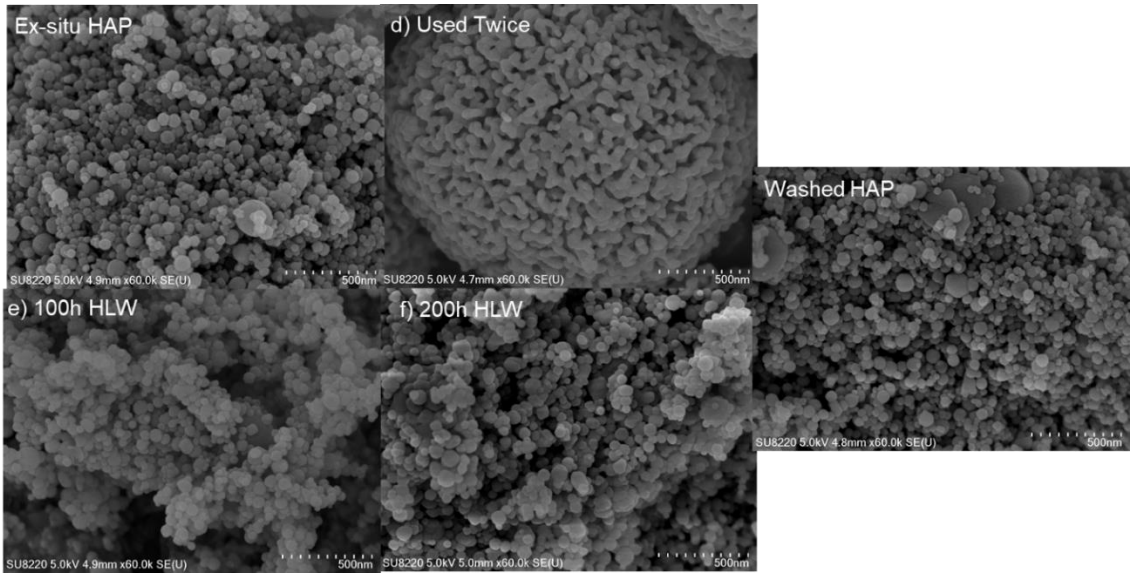

Figure D5-12. **Scanning electron microscopy images of various HAP catalysts.** Representative SEM image of fresh HAP-1.86. Primary particle diameter between 50 – 100 nm, related to catalyst characterization, Table 5-1 and Figure 5-2.

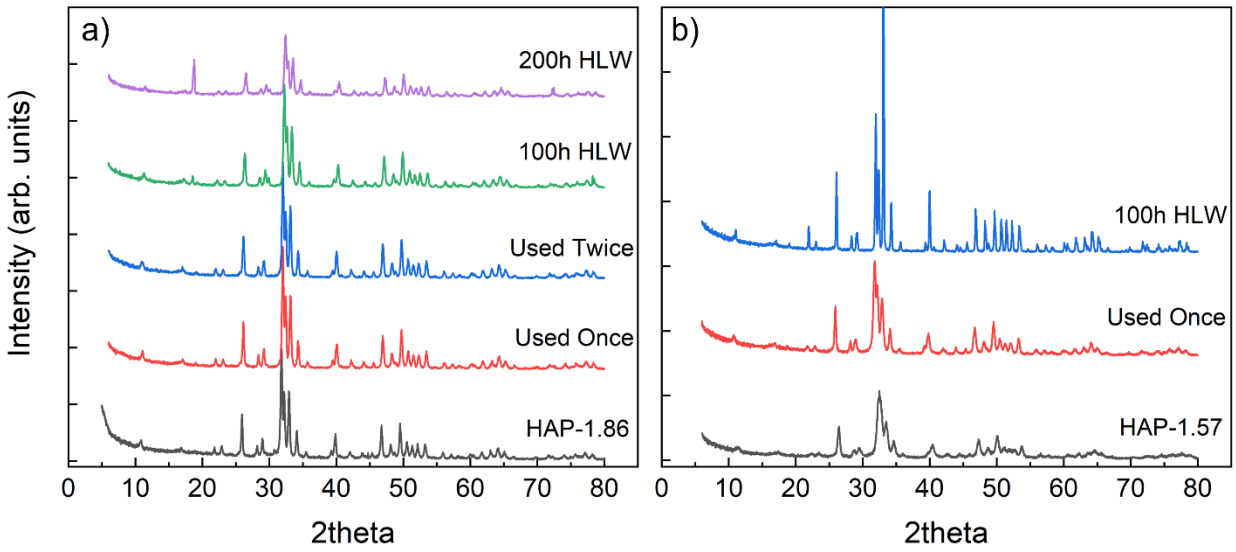

Figure D5-13. **XRD spectra comparing use of HAP-1.86 and HAP-1.57.** Comparison of the X-ray powder diffraction spectra of HAP-1.86 and 1.57, related to catalyst characterization, Table 5-1 and Figure 5-2.

Table D5-6. **Effect of catalyst conditions on aqueous phase pH.** pH of the resultant aqueous phase from HTL of food waste with no catalyst and variations of HAP-1.86, related to catalyst characterization, Table 5-1 and Figure 5-2.

Catalyst Conditions	pH HTL Aqueous
Thermal	5.1
HAP-1.86	4.3
After use HAP-1.86	5.3
Washed HAP-1.86	5.3
200h HAP-1.86	5.0

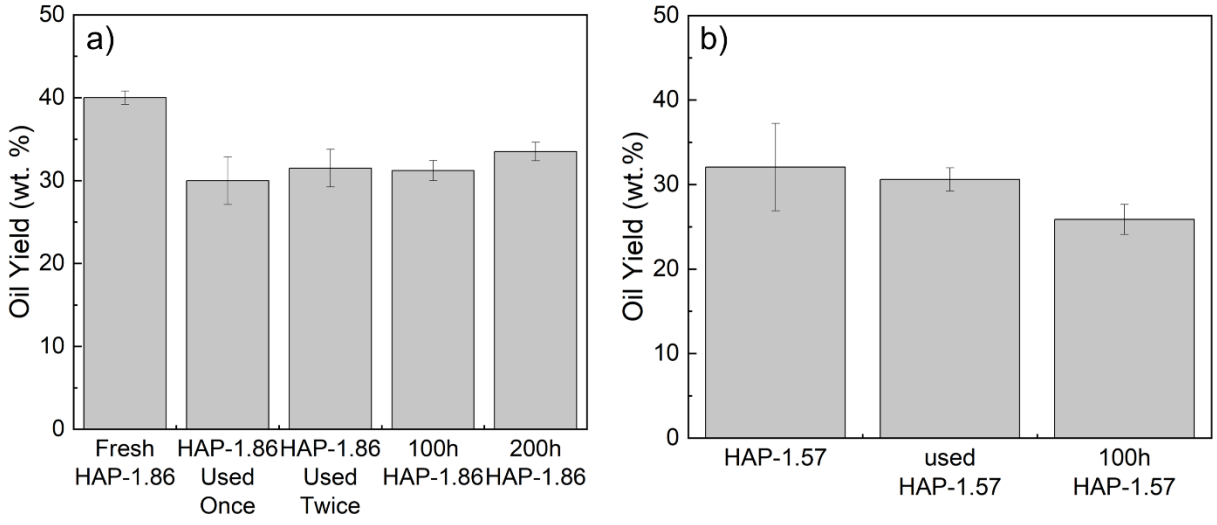

Figure D5-14. **The effect of catalyst re-use on HAP-1.86 and HAP-1.57 oil yields. a)** Oil yield (wt.%) for multiple uses of HAP-1.86 in food waste HTL. HAP-1.86 was used once and twice in food waste HTL runs with 1 hour residence times and calcined in a tube furnace between uses to remove char build-up. Hot liquid water (HLW) experiments contained no food waste and reacted catalyst and water at 300 °C and 200 bar for over 100 hours. **b)** Oil yield (wt.%) for multiple uses of HAP-1.57 in food waste HTL, related to catalyst characterization, Table 5-1 and Figure 5-2.

Figure D5-15. **Photographs highlighting the difference in catalyst color from re-use.** Photographs comparing the initial fresh HAP catalyst, the catalyst after *in situ* hydrothermal liquefaction and after *ex situ* hydrothermal liquefaction, related to catalyst characterization, Table 5-1 and Figure 5-2.

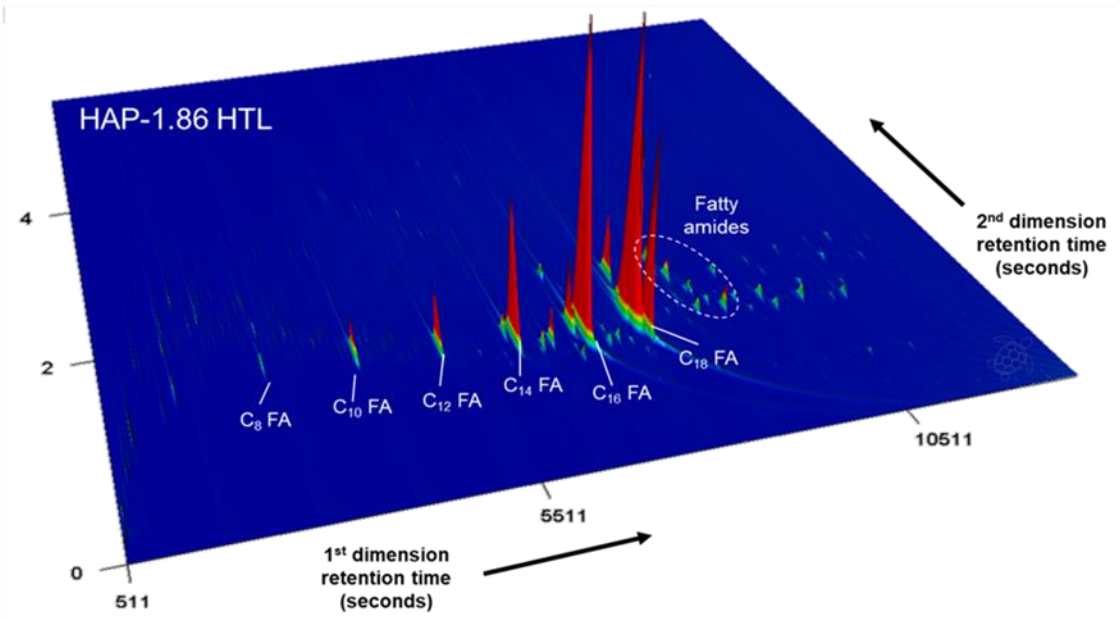

Figure D5-16. **Representative GC×GC chromatogram showing oil compound distribution including HAP-1.86.** Total ion mountain plot GCxGC-FID chromatogram resulting from the hydrothermal liquefaction of food waste in the presence of *in situ* HAP, related to molecular level analysis and Figure 5-3.

a)

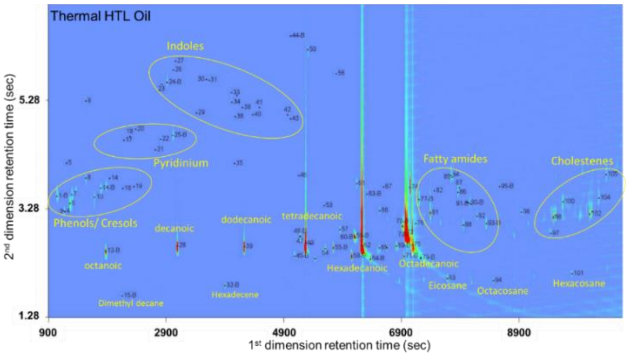
Thermal HTL Oil
Indoles
Pyridinium
Phenols/ Cresols
decanoic
dodecanoic
tetradecanoic
Fatty amides
Cholestenes
octanoic
Hexadecanoic
Octadecanoic
Eicosane
Octacosane
Hexacosane
Hexadecene
Dimethyl decane
2nd dimension retention time (sec)
1st dimension retention time (sec)
5.28
3.28
1.28
900
2900
4900
6900
8900

b)

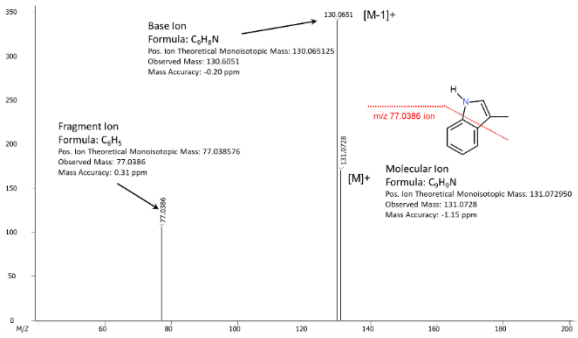
Base Ion
Formula: C8H9N
Pos. Ion Theoretical Monoisotopic Mass: 130.065125
Observed Mass: 130.6051
Mass Accuracy: -0.20 ppm
130.0651
[M-1]+
Fragment Ion
Formula: C6H5
Pos. Ion Theoretical Monoisotopic Mass: 77.038576
Observed Mass: 77.0386
Mass Accuracy: 0.31 ppm
77.0386
131.0728
[M]+
m/z 77.0386 ion
Molecular Ion
Formula: C9H9N
Pos. Ion Theoretical Monoisotopic Mass: 131.072950
Observed Mass: 131.0728
Mass Accuracy: -1.15 ppm
M/Z

c)

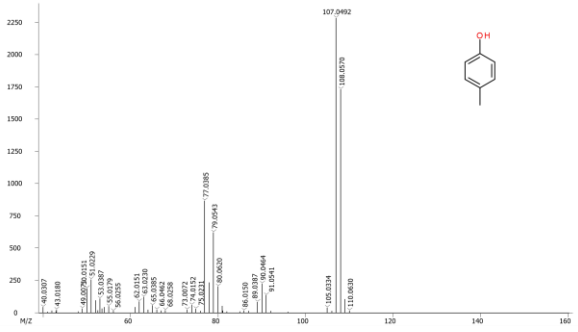
107.0492
77.0385
79.0543
108.0579
OH
M/Z

Figure D5-17. **Representative GC×GC chromatogram and MS results showing oil compound distribution including HAP-1.86. a)** Total ion GCxGC chromatogram labeled with identified molecular classes. **b/c)** Mass spectra resulting from the GCxGC analysis of food waste hydrothermal liquefaction in the absence of catalyst for a representative identified indole and cresol, related to molecular level analysis and Figure 5-3.

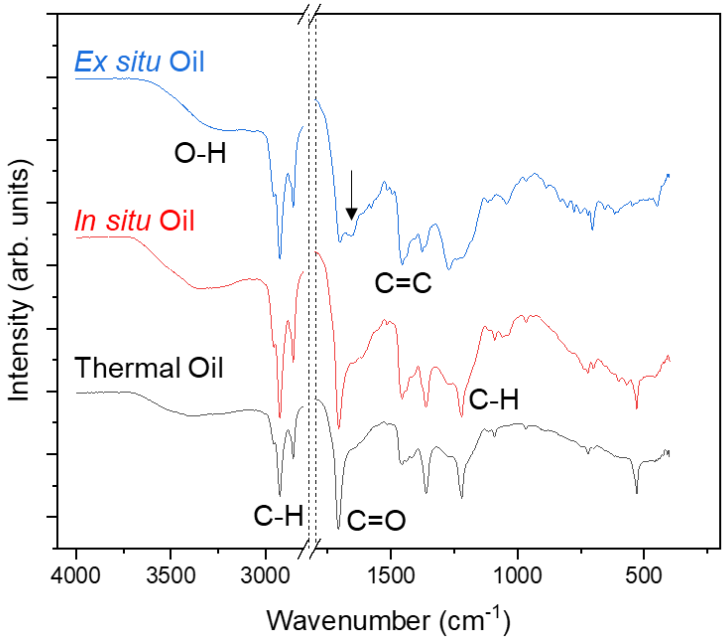

Figure D5-18. **FT-IR spectra comparing non-catalytic and catalytic biocrudes.** Fourier transform infrared spectroscopy (FT-IR) spectra for HTL oils comparing non-catalytic, HAP-catalyzed, and homogeneous-base catalyzed HTL reactions, related to molecular level analysis, Figure 5-3 through 5-5. In all cases, a weak and broad band is present at approximately 3400 cm^{-1}, consistent with the O-H stretching band of alcohol, carboxylic acid, or residual water content. This band can also be associated to the N-H stretch of amine containing molecules in some cases. [68] Partial assignment of the O-H stretch to carboxylic acid group is consistent with the C=O feature that appears in all of the biocrude spectra. Prominent C-H stretch features in the range from 2800-3000 cm^{-1} are consistent with conversion of lipids into biocrude molecules; this assignment is supported by the C-H bending mode that appears at approximately 1250 cm^{-1}. A band at approximately 1500 cm^{-1} can be attributed to furans produced by depolymerization of starch to produce glucose followed by dehydration to produce furanic molecules.

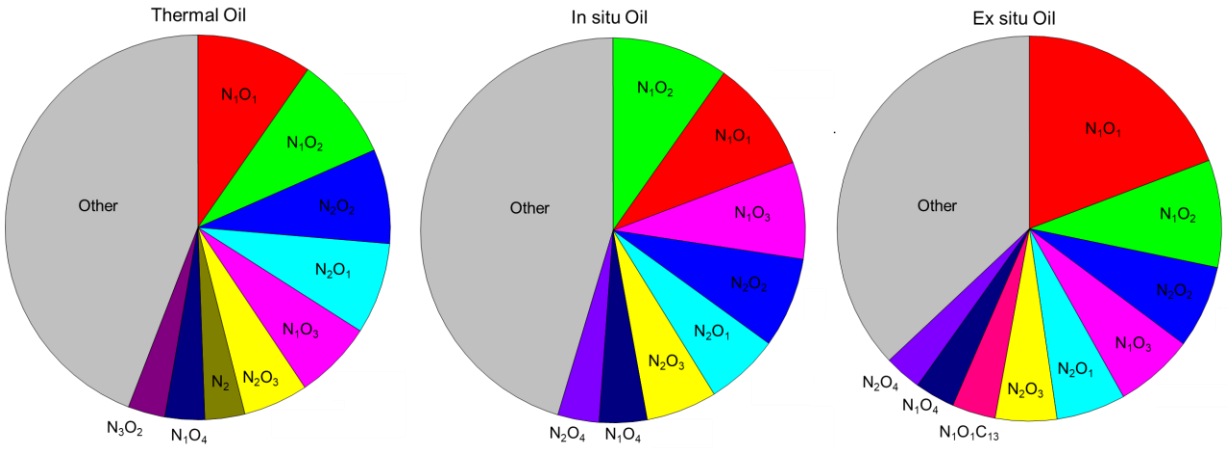

Figure D5-19. **Heteroatom class distribution resulting from (+) APPI FT-ICR MS.** Heteroatom class abundance obtained from positive-ion FT-ICR MS analysis of biocrude obtained in the absence of catalyst, in the presence of catalyst in the HTL reactor, and after ex situ upgrading of the aqueous phase, related to molecular level analysis and Figure 5-4.

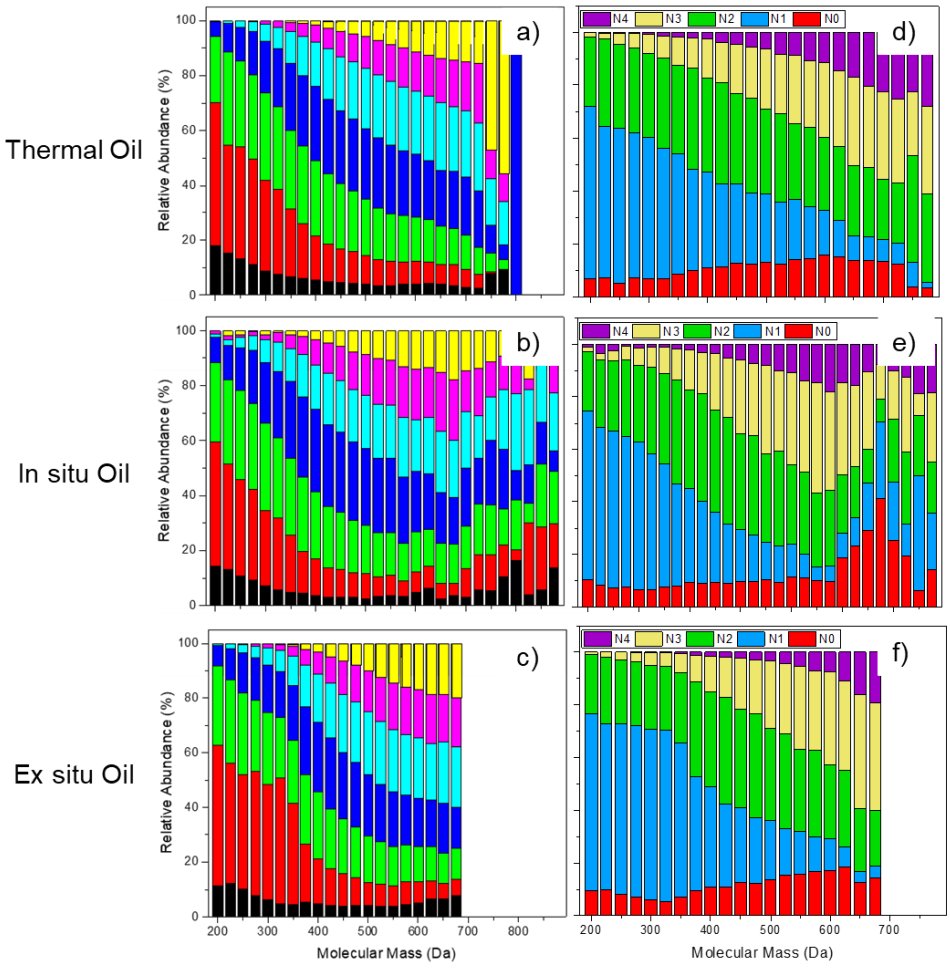

Figure D5-20. **Distribution of nitrogen heteroatom classes in biocrude and aqueous phases from (+) APPI FT-ICR MS.** Relative abundance of the molecular mass classes for oxygenates scaled to the total abundance in that molecular weight range to calculate a percent contribution by each oxygen number. The O_0 class contains all heteroatom classes without oxygen, including $N_1 – N_x$, HC, etc. The $O_1 – O_6$ classes contain all classes with the designated number of oxygen (e.g., N_xO_1), related to molecular level analysis and Figure 5-4.

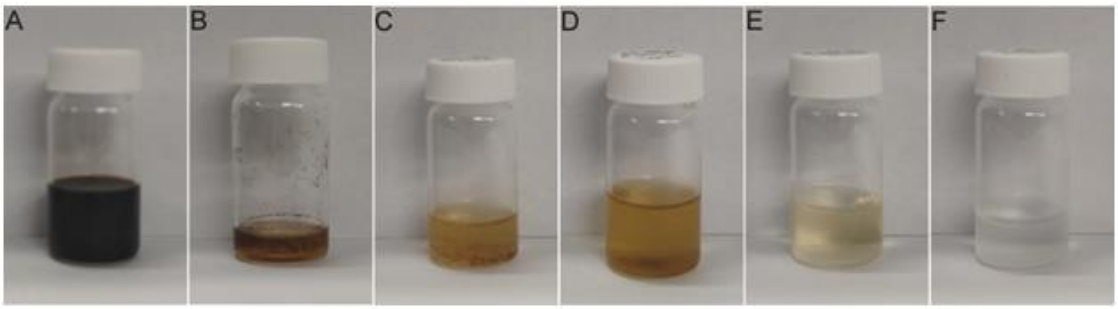

Figure D5-21. Aqueous phase pictures to visualize color differences in carbon percentage. HTG water before and after HTG with different catalysts. A) Organic contaminated water before undergoing HTG. B) Uncatalyzed HTL water, C) Pt/Silica catalyzed HTG water, D) Ni/alumina catalyzed HTL water, E) Ni/Carbon catalyzed HTG water, and F) Ru/Carbon catalyzed HTG water, related to potential commercial impacts. Related to LCA and TEA (Table 5-2 and 5-3). To assist in determining HTL feasibility, it is important to understand the fate of byproducts, including aqueous and char phases. In preliminary work that demonstrates feasibility, HTG experiments were performed to treat HTL water, and identified two catalysts, Ru/Carbon and Ni/Carbon, which effectively convert water-soluble organics to permanent gases. Figure D5-21 contains photographs of organic-contaminated water produced from HTL before and after undergoing HTG at 400 °C. From visual inspection, gasification clearly reduced the concentration of aqueous organics. HTL water (Figure a) contains 28,200 ppm TOC and is a black, opaque liquid. HTG with Ni/Carbon (Figure e) reduced organic contamination to 1,880 ppm (93% conversion) and produced light yellow, transparent water. Ru/Carbon (panel D) reduced organic contamination from 28,200 ppm to 555 ppm (98% conversion) and produced clear, colorless water. Operating at 500 °C and using Ru/Carbon reduced TOC even further to 264 ppm.

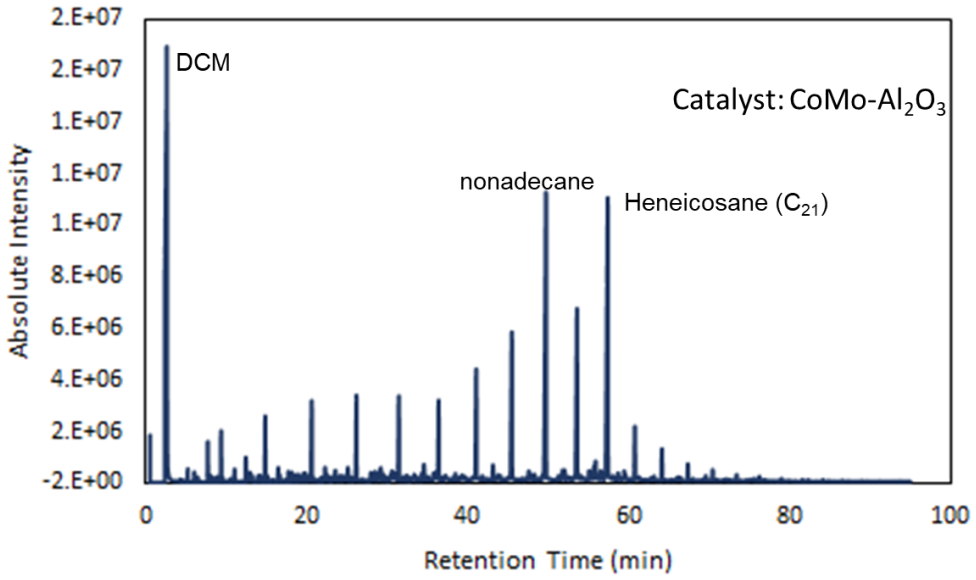

Figure D5-22. **GC-MS chromatogram showing upgraded biocrude.** GC-MS chromatogram for the upgraded biocrude oil after hydrotreatment from food waste. Reaction was completed in a Parr batch reactor at 400 °C for 2 hours with 50 wt% CoMo-Al_2O_3 catalyst. GC-MS highlights the presence of long-chain alkanes in the oil, related to potential commercial impacts. Related to LCA and TEA (Table 5-2 and 5-3). Hydrothermal liquefaction upgrading experiments were performed on food waste biocrude using commercial Cobalt-Molybdenum catalyst supported on alumina. Experiments were performed at 400 °C, using a 50 wt.% catalyst loading. 70 bar of H_2 gas was pre-loaded into the reactor before heating to the desired set-point within 45 minutes. The reaction time was 2 h, before the reactor was quenched with an ice bath to below 40 °C in under 10 minutes. Reaction products were separated utilizing a vacuum filtration set up to remove remaining catalyst and char. The solids were washed with DCM, which was collected and placed in a separatory funnel to remove residual water. The DCM phase was then placed in a rotary evaporator to evaporate the solvent at 35 °C to obtain the final oil product. In addition to CO_2 emissions, a comprehensive LCA must consider potential environmental impacts of byproducts.[83] For catalytic HTL, the chief byproduct is spent catalyst; land application as a soil amendment is an obvious use for it. The catalyst used here, hydroxyapatite, is a natural material composed of P and Ca, both of which are essential to plant growth.[74] Accordingly, utilizing a char-hydroxyapatite composite as a soil amendment has potential as an environmentally benign use of the solid product from catalytic HTL. The aqueous phase can be treated by a combination of hydrothermal gasification to reduce its carbon content and subsequent wastewater treatment.[31, 73] Specific attention must be paid to the presence of emerging contaminants that are not removed in conventional wastewater treatment processes.[94] Treatment with a suitable adsorbent should be sufficient to remove emerging contaminants.

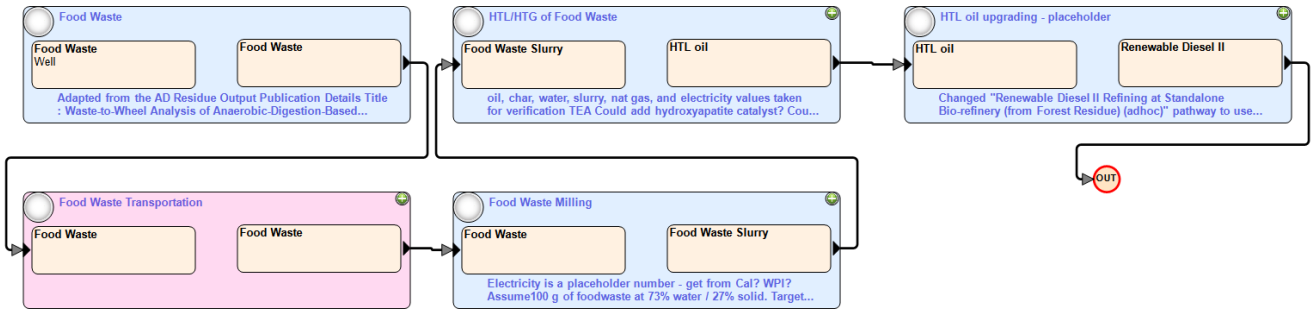
Food Waste
Food Waste
Well
Food Waste
Adapted from the AD Residue Output Publication Details Title : Waste-to-Wheel Analysis of Anaerobic-Digestion-Based...
HTL/HTG of Food Waste
Food Waste Slurry
HTL oil
oil, char, water, slurry, nat gas, and electricity values taken for verification TEA Could add hydroxyapatite catalyst? Cou...
HTL oil upgrading - placeholder
HTL oil
Renewable Diesel II
Changed "Renewable Diesel II Refining at Standalone Bio-refinery (from Forest Residue) (adhoc)" pathway to use...
OUT
Food Waste Transportation
Food Waste
Food Waste
Food Waste Milling
Food Waste
Food Waste Slurry
Electricity is a placeholder number - get from Cal? WPI? Assume100 g of foodwaste at 73% water / 27% solid. Target...

Figure D5-23. **Process flow diagram from GREET 2020® LCA software.** LCA for the production of renewable diesel from food waste HTL, related to potential commercial inputs and Table 5-2. Well-to-pump LCA was utilized in the GREET software for production of renewable diesel II, as pre-loaded. A comparison was made to the pre-set 'Algae Hydrothermal liquefaction (HTL) for Renewable Diesel III' without changes.[77] Most numbers in the LCA were used as-is in the software, where the only things changed were the product yields. The food waste to HTL oil portion was constructed using the PNNL sludge model LCA as a basis, utilizing flows and electricity rates consistent with the TEA in the following section. Food waste numbers were set to 1000 kg to begin, and were adapted from the Waste-to-Wheel Analysis of Anaerobic Digestion-Based Renewable Natural Gas Pathways with the GREET Model.[95] Food waste transportation utilized the source as groceries and kitchen wastes being transported with a medium heavy-duty truck a distance of 48.3km to an HTL plant. HTL product yields were consistent with those reported in the TEA and in this work, taking 13.6% yield for the non-catalytic case and 40.7% yield for the catalytic case. It was assumed that the food waste was 73% moisture and 27% solid with a target HTL feedstock of 15% solid, requiring the addition of added water. HTL upgrading to renewable diesel utilizes numbers and process descriptions from Cai et al[96]., Paulo-Rivera et al. [97], and Lampert et al. [98] Total energy calculations were completed by assuming 63 million tons of food waste is all diverted to energy production with a moisture content of 75%.

$$63\ million\ tons\ food\ waste * 0.25 = 15.7\ million\ tons\ organic\ matter$$

$$15.7\ million\ tons\ organic\ matter * 0.407\ (biocrude\ yield) = 6.4\ million\ tons\ biocrude$$

$$63\ million\ tons\ food\ waste * \left(23\frac{MJ}{kg} * \frac{907MJ}{ton}\right) = 1.3\ trillion\ MJ$$

$$6.4\ million\ tons\ biocrude * \left(\frac{36MJ}{kg} * \frac{907MJ}{ton}\right) = 209\ billion\ MJ$$

Table D5-7. Process parameters for the base case food waste HTL GREET model broken down by section. All inputs and outputs used in the GREET software are included. The HTL oil output is consistent with the value used in the TEA, related to potential commercial impacts and Table 5-2.

		Resource	Value	Units
Food Waste				
		Quantity	1000	kg
Food Waste Transportation				
		Distance	48.28	km
		Share	100	%
		Urban Share	0	%
		Fuel Share	default	
Food Waste Milling				
	Inputs	Food Waste	38070	lb
		Water	31331.5	lb
		Electricity	86	Wh
	Outputs	Food Waste Slurry	69401.5	lb
HTL/HTG of Food Waste				
	Inputs	Food Waste Slurry	78515.5	lb
		Natural Gas	29100.97	MJ
		Electricity	1781.8	MJ
	Outputs	HTL Oil	25350.95	MJ
		HTL Char	586	lb
		Water	81301	lb
HTL Upgrading				
	Inputs	Water	0	gal
		Hydrogen	897.71	Btu
		HTL Oil	1	mmBtu
		Group Amount	70057.06	Btu
		Natural Gas Share	95.01	%
		Electricity Share	4.99	%
	Outputs	Renewable Diesel	1	mmBtu
		CO2	3954.47	g

Table D5-8. **Change log for TEA highlighting changes from the PNNL version.** Detailed change log for the technoeconomic analysis adapted from PNNL[31] to account for food waste feedstock, related to potential commercial impacts and Table 5-3.

Change	Description
1	Changed HHV of feed from 9589 btu/lb to 10576 (24.6 MJ/kg) to reflect change from sludge to food waste
2	Changed original solids of feed from 30% to 27% to reflect change from sludge to food waste
3	Changed ash content in solids from 7.57% to 0.3/(100-73) = 1.1% to reflect change from sludge to food waste
4	Changed feed solids content from 11.2% to 15% to reflect change from sludge to food waste
5	Changed feed frate 7702 lb/hr to xxxx lb/hr from to reflect change from sludge to food waste (maintain total flow rate to reactor = 69401 lb/hr)
6	Changed the HHV and LHV of the oil from 14594 to 13413 btu/lb
7	Fixed equation for COD
8	Added carbonate, at 5%
9	Added carbonate to simple cost
10	Changed COD in HTL flows of HTL water and CW blowdown (12 ppm rather than "same as HTL water", value stayed the same)
11	Changed sludge credit to $50 to match report, also changed sludge excel file
12	Added reactor scale ratio to Equip tab
13	Added volumetric scale ratio and changed equations on HTL flows tab so mass balances work out with changes to solids loading (holding total wet flow constant)
14	Added heterogeneous catalysts cost to HTL flows and Simple Cost
15	Updated DCFROR to reflect changes to Simple Costs
16	Changed "oil yield ratio" to 0.7938 to match the 32.23 mass% oil yield from verification
17	Changed the HHV and LHV of the oil from 13413 to 14485.8 btu/lb
18	Changed catalyst used from CeZrOx to Hydroxyapatite
19	Changed catalyst cost to $12.72/lb
20	Changed the energy recovery calculation to match that of literature- HHV*yield/HHV of feed
21	Changed energy recovery calculation back to original but added mine in another cell. Determined the difference in energy recoveries was based on the scale up
22	Set catalyst lifetime to 100h or 200h where needed

Table 5-9. **Summary of base case TEA results.** Base case, non-catalytic summary economics and performance for food waste HTL plant, related to potential commercial impacts and Table 5-3. The food waste tipping fee calculation takes the average northeast US tipping fee ($-66.67/ wet ton)[16] and the average transportation cost used by PNNL ($50/ tonne).[94] Tonne was converted to ton ($50 * 1.1 = $55/ton) and was added to the tipping fee, ($-67 + $55 = $-12). Then, assuming food waste is 75% moisture gives us a tipping fee with transportation costs of $-45/ dry ton.

Biocrude from Food Waste Hydrothermal Liquefaction and Catalytic Hydrothermal Gasification

Institutional Food Waste

Sludge Credit/Cost:	**-$45**	**$/U.S. ton food waste (dry, ash free basis)**
Minimum Selling Price - Gasoline Gallon Equivalent	**$8.24**	**$/gge**
Minimum Selling Price	$8.03	$/gallon
Bio-oil	1	million gge/yr
	163,847	million Btu/yr
	34.67	gge/US ton AFDW food waste
	4	million Btu/US ton AFDW food waste
Internal Rate of Return (After-Tax)	10%	
Equity Percent of Total Investment	40%	
Cost Year	2016	

CAPITAL COSTS

HTL Oil Production	$18,500,000	63%
CHG Water Treatment	$9,000,000	30%
Steam Cycle	$800,000	3%
Balance of Plant	$1,300,000	4%
Total Installed Capital Cost	$29,600,000	100%
Building, site development, add'l piping	$4,200,000	
Indirect Costs	$18,600,000	
Working Capital	$2,600,000	
Land (plant located at WWTP)	$0	
Total Capital Investment (TCI)	$55,000,000	
Installed Capital per Annual GGE Bio-oil	$21	
TCI per Annual GGE Bio-oil	$39	
Loan Rate	8.0%	
Term (years)	10	
Capital Charge Factor (computed)	0.138	

MANUFACTURING COSTS

Plant Hours per year	7920	
Avg feed rate, dry ash-free food wa	123	TPD to HTL reactor
	$/gge	$/year
Food waste feedstock cost	-1.38	-$1,900,000
Natural Gas	0.85	$1,200,000
Catalysts & Chemicals	0.72	$1,000,000
Waste Disposal	0.13	$200,000
Electricity and other utilities	0.21	$300,000
Fixed Costs	2.34	$3,300,000
Capital Depreciation	1.20	$1,700,000
Average Income Tax	0.71	$1,000,000
Average Return on Investment	3.46	$4,900,000
	8.24	

PERFORMANCE

Total Electricity Usage (KW)	495
Electricity Produced Onsite (KW)	626
Electricity Purchased from Grid (KW)	131
Electricity Sold to Grid (KW)	0
Net Electricity Use (KWh/gge product)	2.8

Table D5-10. **Summary of HAP-1.86 catalyzed HTL economic analysis.** Summary of catalytic (HAP-1.86 + alkali) economics and performance for food waste HTL, related to potential commercial impacts and Table 5-3.

Biocrude from Food Waste Hydrothermal Liquefaction and Catalytic Hydrothermal Gasification

Institutional Food Waste

Sludge Credit/Cost: -$45 $/U.S. ton food waste (dry, ash free basis)

Minimum Selling Price - Gasoline Gallon Equivalent	**$4.78**	**$/gge**
Minimum Selling Price	$4.66	$/gallon
Bio-oil	4	million gge/yr
	490,337	million Btu/yr
	103.77	gge/US ton AFDW food waste
	12	million Btu/US ton AFDW food waste
Internal Rate of Return (After-Tax)	10%	
Equity Percent of Total Investment	40%	
Cost Year	2016	

CAPITAL COSTS

HTL Oil Production	$18,500,000	63%
CHG Water Treatment	$9,000,000	30%
Steam Cycle	$800,000	3%
Balance of Plant	$1,300,000	4%
Total Installed Capital Cost	$29,600,000	100%
Building, site development, add'l piping	$4,200,000	
Indirect Costs	$18,600,000	
Working Capital	$2,600,000	
Land (plant located at WWTP)	$0	
Total Capital Investment (TCI)	$55,000,000	
Installed Capital per Annual GGE Bio-oil	$7	
TCI per Annual GGE Bio-oil	$13	
Loan Rate	8.0%	
Term (years)	10	
Capital Charge Factor (computed)	0.140	

MANUFACTURING COSTS

Plant Hours per year	7920	
Avg feed rate, dry ash-free food wa	123	TPD to HTL reactor
	$/gge	$/year
Food waste feedstock cost	-0.46	-$1,900,000
Natural Gas	0.28	$1,200,000
Catalysts & Chemicals	2.23	$9,400,000
Waste Disposal	0.04	$200,000
Electricity and other utilities	0.07	$300,000
Fixed Costs	0.78	$3,300,000
Capital Depreciation	0.40	$1,700,000
Average Income Tax	0.24	$1,000,000
Average Return on Investment	1.18	$5,000,000
	4.78	

PERFORMANCE

Total Electricity Usage (KW)	495
Electricity Produced Onsite (KW)	626
Electricity Purchased from Grid (KW)	131
Electricity Sold to Grid (KW)	0
Net Electricity Use (KWh/gge product)	0.9

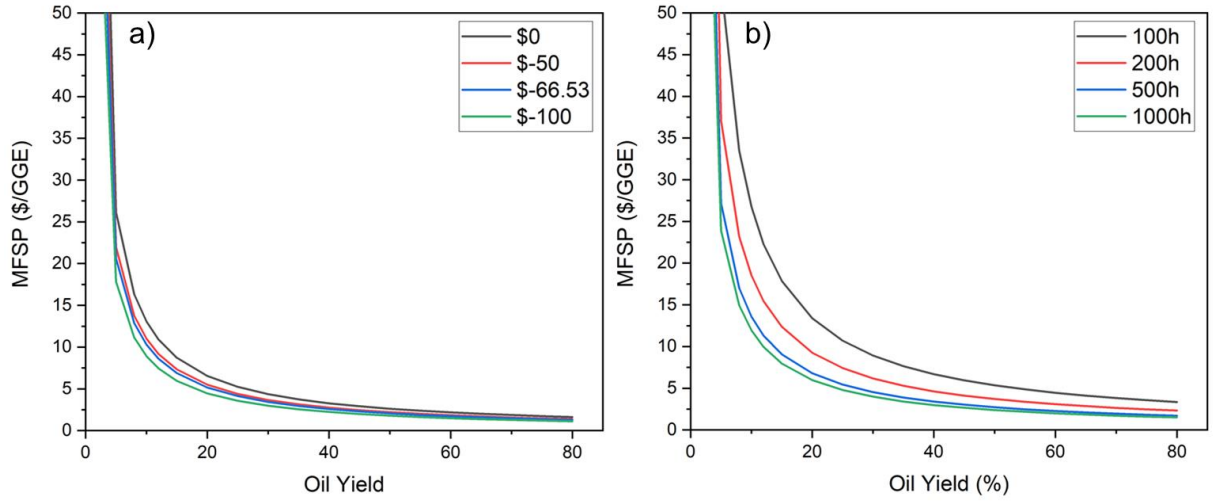

Figure D5-24. **Sensitivity of MFSP to changes in catalyst lifetime and waste tipping fee.** Oil yield versus predicted MFSP for a) change in feedstock cost and b) change in catalyst lifetime, related to potential commercial impacts and Table 5-3.

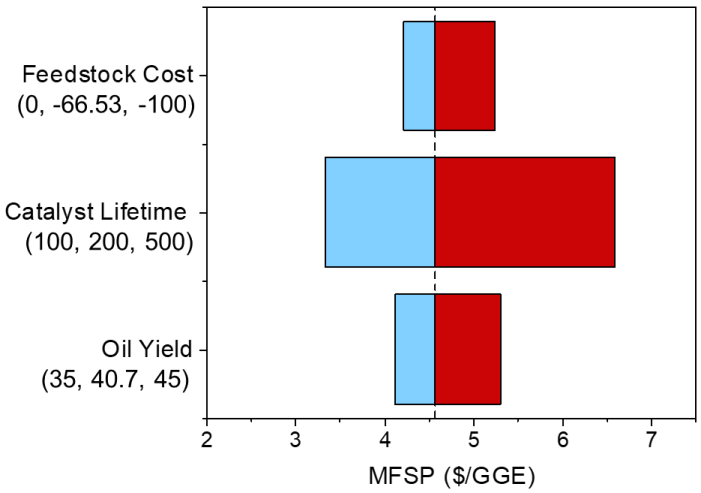

Figure D5-25. **Sensitivity analysis for the primary variables mentioned above.** Sensitivity analysis for three primary variables, showing the oil yield and oil quality to be the most sensitive to a change of plus or minus 50% the initial value, related to potential commercial impacts and Table 5-3.

5.6 REFERENCES

1. Schanes, K.; Dobernig, K.; Gözet, B., Food waste matters - A systematic review of household food waste practices and their policy implications. *Journal of Cleaner Production* **2018,** *182*, 978-991.

2. U.S. Environmental Protection Agency, *Food: Material-Specific Data*; 2021.

3. Pfaltzgraff, L. A.; De bruyn, M.; Cooper, E. C.; Budarin, V.; Clark, J. H., Food waste biomass: a resource for high-value chemicals. *Green Chemistry* **2013,** *15* (2), 307-314.

4. Paritosh, K.; Kushwaha, S. K.; Yadav, M.; Pareek, N.; Chawade, A.; Vivekanand, V., Food Waste to Energy: An Overview of Sustainable Approaches for Food Waste Management and Nutrient Recycling. *BioMed Research International* **2017,** *2017*, 2370927.

5. U.S. Environmental Protection Agency, U.S. Food Waste Statistics.

6. U.S. Energy Information Administration, Electricity Explained: Use of electricity. (accessed January 27).

7. Ouadi, M.; Bashir, M. A.; Speranza, L. G.; Jahangiri, H.; Hornung, A., Food and Market Waste–A Pathway to Sustainable Fuels and Waste Valorization. *Energy & Fuels* **2019,** *33* (10), 9843-9850.

8. Castello, D.; Pedersen, T. H.; Rosendahl, L. A., Continuous Hydrothermal Liquefaction of Biomass: A Critical Review. *Energies* **2018,** *11* (11).

9. Gollakota, A. R. K.; Kishore, N.; Gu, S., A review on hydrothermal liquefaction of biomass. *Renewable and Sustainable Energy Reviews* **2018,** *81*, 1378-1392.

10. Bielenberg, J.; Palou-Rivera, I., The RAPID Manufacturing Institute – Reenergizing US efforts in process intensification and modular chemical processing. *Chemical Engineering and Processing - Process Intensification* **2019,** *138*, 49-54.

11. Gollakota, A.; Savage, P. E., Fast and Isothermal Hydrothermal Liquefaction of Polysaccharide Feedstocks. *ACS Sustainable Chemistry & Engineering* **2020,** *8* (9), 3762-3772.

12. Du, S.; Valla, J. A.; Bollas, G. M., Characteristics and origin of char and coke from fast and slow, catalytic and thermal pyrolysis of biomass and relevant model compounds. *Green Chemistry* **2013,** *15* (11), 3214-3229.

13. Peterson, A. A.; Vogel, F.; Lachance, R. P.; Fröling, M.; Antal, J. M. J.; Tester, J. W., Thermochemical biofuel production in hydrothermal media: A review of sub- and supercritical water technologies. *Energy & Environmental Science* **2008,** *1* (1), 32-65.

14. Ryan Davis, J. M., Christopher Kinchin, Nicholas Grundl, Eric C.D. Tan, Process Design and Economics for the Production of Algal Biomass: Algal Biomass Production in Open Pond Systems and Processing Through Dewatering for Downstream Conversion. Energy, U. S. D. o., Ed. 2016.

15. Jiang, Y.; Jones, S. B.; Zhu, Y.; Snowden-Swan, L.; Schmidt, A. J.; Billing, J. M.; Anderson, D., Techno-economic uncertainty quantification of algal-derived biocrude via hydrothermal liquefaction. *Algal Research* **2019,** *39*, 101450.

16. Debra L. Kantner, B. F. S. *Analysis of MSW Landfill Tipping Fees*; Environmental Research & Education Foundation: April 2019, 2019.

17. Cheng, F.; Cui, Z.; Chen, L.; Jarvis, J.; Paz, N.; Schaub, T.; Nirmalakhandan, N.; Brewer, C. E., Hydrothermal liquefaction of high- and low-lipid algae: Bio-crude oil chemistry. *Applied Energy* **2017,** *206*, 278-292.

18. Cheng, F.; Tompsett, G. A.; Murphy, C. M.; Maag, A. R.; Carabillo, N.; Bailey, M.; Hemingway, J. J.; Romo, C. I.; Paulsen, A. D.; Yelvington, P. E.; Timko, M. T., Synergistic

Effects of Inexpensive Mixed Metal Oxides for Catalytic Hydrothermal Liquefaction of Food Wastes. *ACS Sustainable Chemistry & Engineering* **2020,** *8* (17), 6877-6886.

19. Maag, A. R.; Paulsen, A. D.; Amundsen, T. J.; Yelvington, P. E.; Tompsett, G. A.; Timko, M. T., Catalytic Hydrothermal Liquefaction of Food Waste Using CeZrOx. *Energies* **2018,** *11* (3).

20. Nagappan, S.; Bhosale, R. R.; Nguyen, D. D.; Chi, N. T. L.; Ponnusamy, V. K.; Woong, C. S.; Kumar, G., Catalytic hydrothermal liquefaction of biomass into bio-oils and other value-added products – A review. *Fuel* **2021,** *285*, 119053.

21. Azadi, P.; Farnood, R., Review of heterogeneous catalysts for sub- and supercritical water gasification of biomass and wastes. *International Journal of Hydrogen Energy* **2011,** *36* (16), 9529-9541.

22. Besson, M.; Gallezot, P.; Pinel, C., Conversion of Biomass into Chemicals over Metal Catalysts. *Chemical Reviews* **2014,** *114* (3), 1827-1870.

23. Cheng, F.; Tompsett, G. A.; Fraga Alvarez, D. V.; Romo, C. I.; McKenna, A. M.; Niles, S. F.; Nelson, R. K.; Reddy, C. M.; Granados-Fócil, S.; Paulsen, A. D.; Zhang, R.; Timko, M. T., Metal oxide supported Ni-impregnated bifunctional catalysts for controlling char formation and maximizing energy recovery during catalytic hydrothermal liquefaction of food waste. *Sustainable Energy & Fuels* **2021,** *5* (4), 941-955.

24. Fihri, A.; Len, C.; Varma, R. S.; Solhy, A., Hydroxyapatite: A review of syntheses, structure and applications in heterogeneous catalysis. *Coordination Chemistry Reviews* **2017,** *347*, 48-76.

25. Roberts, G. W.; Sturm, B. S. M.; Hamdeh, U.; Stanton, G. E.; Rocha, A.; Kinsella, T. L.; Fortier, M.-O. P.; Sazdar, S.; Detamore, M. S.; Stagg-Williams, S. M., Promoting catalysis

and high-value product streams by in situ hydroxyapatite crystallization during hydrothermal liquefaction of microalgae cultivated with reclaimed nutrients. *Green Chemistry* **2015,** *17* (4), 2560-2569.

26. Mostafa, N. Y., Characterization, thermal stability and sintering of hydroxyapatite powders prepared by different routes. *Materials Chemistry and Physics* **2005,** *94* (2), 333-341.

27. Tsuchida, T.; Sakuma, S.; Takeguchi, T.; Ueda, W., Direct Synthesis of n-Butanol from Ethanol over Nonstoichiometric Hydroxyapatite. *Industrial & Engineering Chemistry Research* **2006,** *45* (25), 8634-8642.

28. Kaneda, K.; Mori, K.; Hara, T.; Mizugaki, T.; Ebitani, K., Design of hydroxyapatite-bound transition metal catalysts for environmentally-benign organic syntheses. *Catalysis Surveys from Asia* **2004,** *8* (4), 231-239.

29. Tsuchida, T.; Yoshioka, T.; Sakuma, S.; Takeguchi, T.; Ueda, W., Synthesis of Biogasoline from Ethanol over Hydroxyapatite Catalyst. *Industrial & Engineering Chemistry Research* **2008,** *47* (5), 1443-1452.

30. Kiani, D.; Baltrusaitis, J., Surface chemistry of hydroxyapatite for sustainable n-butanol production from bio-ethanol. *Chem Catalysis* **2021**.

31. LJ Snowden-Swan, Y. Z., SB Jones, DC Elliot, AJ Schmidt, RT Hallen, JM Billing, TR Hart, SP Fox, GD Maupin, Hydrothermal Liquefaction and Upgrading of Municipal Wastewater Treatment Plant Sludge: A Preliminary Techno-Economic Analysis. Energy, D. o., Ed. 2016.

32. Hydroxyapatite. https://www.alibaba.com/product-detail/Natural-Price-CAS-1306-06-5_1600266231907.html?spm=a2700.galleryofferlist.normal_offer.d_title.2af14268bySzdI.

33. Purcell, J. M.; Hendrickson, C. L.; Rodgers, R. P.; Marshall, A. G., Atmospheric Pressure Photoionization Fourier Transform Ion Cyclotron Resonance Mass Spectrometry for Complex Mixture Analysis. *Analytical Chemistry* **2006,** *78* (16), 5906-5912.

34. Robb, D. B.; Blades, M. W., Factors affecting primary ionization in dopant-assisted atmospheric pressure photoionization (DA-APPI) for LC/MS. *Journal of the American Society for Mass Spectrometry* **2006,** *17* (2), 130-138.

35. Robb, D. B.; Covey, T. R.; Bruins, A. P., Atmospheric Pressure Photoionization: An Ionization Method for Liquid Chromatography−Mass Spectrometry. *Analytical Chemistry* **2000,** *72* (15), 3653-3659.

36. Purcell, J. M.; Rodgers, R. P.; Hendrickson, C. L.; Marshall, A. G., Speciation of nitrogen containing aromatics by atmospheric pressure photoionization or electrospray ionization fourier transform ion cyclotron resonance mass spectrometry. *Journal of the American Society for Mass Spectrometry* **2007,** *18* (7), 1265-1273.

37. Smith, D. R.; Robb, D. B.; Blades, M. W., Comparison of dopants for charge exchange ionization of nonpolar polycyclic aromatic hydrocarbons with reversed-phase LC-APPI-MS. *Journal of the American Society for Mass Spectrometry* **2009,** *20* (1), 73-79.

38. Purcell, J. M.; Hendrickson, C. L.; Rodgers, R. P.; Marshall, A. G., Atmospheric Pressure Photoionization Proton Transfer for Complex Organic Mixtures Investigated by Fourier Transform Ion Cyclotron Resonance Mass Spectrometry. *Journal of the American Society for Mass Spectrometry* **2007,** *18* (9), 1682-1689.

39. Kaiser, N. K.; Quinn, J. P.; Blakney, G. T.; Hendrickson, C. L.; Marshall, A. G., A Novel 9.4 Tesla FTICR Mass Spectrometer with Improved Sensitivity, Mass Resolution, and Mass Range. *Journal of the American Society for Mass Spectrometry* **2011,** *22* (8), 1343-1351.

40. Blakney, G. T.; Hendrickson, C. L.; Marshall, A. G., Predator data station: A fast data acquisition system for advanced FT-ICR MS experiments. *International Journal of Mass Spectrometry* **2011,** *306* (2), 246-252.

41. Senko, M. W.; Hendrickson, C. L.; Emmett, M. R.; Shi, S. D. H.; Marshall, A. G., External accumulation of ions for enhanced electrospray ionization fourier transform ion cyclotron resonance mass spectrometry. *Journal of the American Society for Mass Spectrometry* **1997,** *8* (9), 970-976.

42. Wilcox, B. E.; Hendrickson, C. L.; Marshall, A. G., Improved ion extraction from a linear octopole ion trap: SIMION analysis and experimental demonstration. *Journal of the American Society for Mass Spectrometry* **2002,** *13* (11), 1304-1312.

43. Tolmachev, A. V.; Robinson, E. W.; Wu, S.; Kang, H.; Lourette, N. M.; Paša-Tolić, L.; Smith, R. D., Trapped-ion cell with improved dc potential harmonicity for FT-ICR MS. *Journal of the American Society for Mass Spectrometry* **2008,** *19* (4), 586-597.

44. Kaiser, N. K.; Savory, J. J.; McKenna, A. M.; Quinn, J. P.; Hendrickson, C. L.; Marshall, A. G., Electrically Compensated Fourier Transform Ion Cyclotron Resonance Cell for Complex Mixture Mass Analysis. *Analytical Chemistry* **2011,** *83* (17), 6907-6910.

45. Xian, F.; Corilo, Y. E.; Hendrickson, C. L.; Marshall, A. G., Baseline correction of absorption-mode Fourier transform ion cyclotron resonance mass spectra. *International Journal of Mass Spectrometry* **2012,** *325-327*, 67-72.

46. Xian, F.; Hendrickson, C. L.; Blakney, G. T.; Beu, S. C.; Marshall, A. G., Automated Broadband Phase Correction of Fourier Transform Ion Cyclotron Resonance Mass Spectra. *Analytical Chemistry* **2010,** *82* (21), 8807-8812.

47. Kendrick, E., A mass scale based on CH2 = 14.0000 for high resolution mass spectrometry of organic compounds. *Analytical Chemistry* **1963,** *35*, 2146-2154.

48. Hughey, C. A.; Hendrickson, C. L.; Rodgers, R. P.; Marshall, A. G.; Qian, K., Kendrick Mass Defect Spectrum: A Compact Visual Analysis for Ultrahigh-Resolution Broadband Mass Spectra. *Analytical Chemistry* **2001,** *73* (19), 4676-4681.

49. McLafferty, F. W. T., F., *Interpretation of Mass Spectra, 4th ed.* 4th ed.; University Science Books: 1993.

50. Savory, J. J.; Kaiser, N. K.; McKenna, A. M.; Xian, F.; Blakney, G. T.; Rodgers, R. P.; Hendrickson, C. L.; Marshall, A. G., Parts-Per-Billion Fourier Transform Ion Cyclotron Resonance Mass Measurement Accuracy with a "Walking" Calibration Equation. *Analytical Chemistry* **2011,** *83* (5), 1732-1736.

51. Corilo, Y. E., PetroOrg Software. Florida State University, Omics LLC: 2014.

52. Tsuchida, T.; Kubo, J.; Yoshioka, T.; Sakuma, S.; Takeguchi, T.; Ueda, W., Reaction of ethanol over hydroxyapatite affected by Ca/P ratio of catalyst. *Journal of Catalysis* **2008,** *259* (2), 183-189.

53. Stummann, M. Z.; Høj, M.; Davidsen, B.; Hansen, L. P.; Beato, P.; Gabrielsen, J.; Jensen, P. A.; Jensen, A. D., Deactivation of a CoMo Catalyst during Catalytic Hydropyrolysis of Biomass. Part 2. Characterization of the Spent Catalysts and Char. *Energy & Fuels* **2019,** *33* (12), 12387-12402.

54. Lucian, M.; Volpe, M.; Gao, L.; Piro, G.; Goldfarb, J. L.; Fiori, L., Impact of hydrothermal carbonization conditions on the formation of hydrochars and secondary chars from the organic fraction of municipal solid waste. *Fuel* **2018,** *233*, 257-268.

55. Wan, S.; Wang, Y., A review on ex situ catalytic fast pyrolysis of biomass. *Frontiers of Chemical Science and Engineering* **2014,** *8* (3), 280-294.

56. Kumar, S.; Lange, J.-P.; Van Rossum, G.; Kersten, S. R. A., Bio-oil fractionation by temperature-swing extraction: Principle and application. *Biomass and Bioenergy* **2015,** *83*, 96-104.

57. Sangster, J., Octanol-Water Partition Coefficients of Simple Organic Compounds. *Journal of Physical and Chemical Reference Data* **1989,** *18*.

58. Meylan, W. M.; Howard, P. H.; Boethling, R. S., Improved method for estimating water solubility from octanol/water partition coefficient. *Environmental Toxicology and Chemistry* **1996,** *15* (2), 100-106.

59. Zissimos, A.; Abraham, M.; Barker, M.; Box, K.; Tam, K., Calculation of Abraham descriptors from solvent-water partition coeffcients in four different systems; evaluation of different methods of calculation. *Journal of The Chemical Society-perkin Transactions 2 - J CHEM SOC PERKIN TRANS 2* **2002,** *2*, 470-477.

60. Hu, H.-S.; Wu, Y.-L.; Yang, M.-D., Fractionation of bio-oil produced from hydrothermal liquefaction of microalgae by liquid-liquid extraction. *Biomass and Bioenergy* **2018,** *108*, 487-500.

61. Budhwani, N., Removal of Polycyclic Aromatic Hydrocarbons Present in Tyre Pyrolytic Oil Using Low Cost Natural Adsorbents. *International Journal of Biological, Biomolecular, Agricultural, Food and Biotechnological Engineering* **2015,** *9* (2), 186-190.

62. Simpson Rb Fau - Ashbrook, J. D.; Ashbrook Jd Fau - Santos, E. C.; Santos Ec Fau - Spector, A. A.; Spector, A. A., Partition of fatty acids. (0022-2275 (Print)).

63. Betancourt-Jimenez, D.; Youngblood, J. P.; Martinez, C. J., Synthesis and Characterization of Fatty Acid Amides from Commercial Vegetable Oils and Primary Alkyl Amines for Phase Change Material Applications. *ACS Sustainable Chemistry & Engineering* **2020,** *8* (36), 13683-13691.

64. Sad, M. E.; Padró, C. L.; Apesteguía, C. R., Selective synthesis of p-cresol by methylation of phenol. *Applied Catalysis A: General* **2008,** *342* (1), 40-48.

65. Lamping, M.; Enck, S.; Geyer, A., Inverse γ-Turn-Inspired Peptide: Synthesis and Analysis of Segetalin A Indole Hemi-aminal. *European Journal of Organic Chemistry* **2015,** *2015* (34), 7443-7448.

66. Meshram, H. M.; Thakur, P. B.; Bejjam, M. B., An efficient synthesis of hemiaminal of indoles by using tetrabutylammonium fluoride (TBAF) in water as a reusable reaction media. *Green Chemistry Letters and Reviews* **2013,** *6* (1), 95-100.

67. He, C.; Fang, Z.; Li, Y.; Jiang, C.; Zhao, S.; Xu, C.; Zhang, Y.; Shi, Q., Ionization selectivity of electrospray and atmospheric pressure photoionization FT-ICR MS for petroleum refinery wastewater dissolved organic matter. *Environmental Science: Processes & Impacts* **2021**.

68. Lu, J.; Li, H.; Zhang, Y.; Liu, Z., Nitrogen Migration and Transformation during Hydrothermal Liquefaction of Livestock Manures. *ACS Sustainable Chemistry & Engineering* **2018,** *6* (10), 13570-13578.

69. Chang, H.; Motagamwala, A. H.; Huber, G. W.; Dumesic, J. A., Synthesis of biomass-derived feedstocks for the polymers and fuels industries from 5-(hydroxymethyl)furfural (HMF) and acetone. *Green Chemistry* **2019,** *21* (20), 5532-5540.

70. Mettler, M. S.; Mushrif, S. H.; Paulsen, A. D.; Javadekar, A. D.; Vlachos, D. G.; Dauenhauer, P. J., Revealing pyrolysis chemistry for biofuels production: Conversion of cellulose to furans and small oxygenates. *Energy & Environmental Science* **2012,** *5* (1), 5414-5424.

71. Mettler, M. S.; Vlachos, D. G.; Dauenhauer, P. J., Top ten fundamental challenges of biomass pyrolysis for biofuels. *Energy & Environmental Science* **2012,** *5* (7), 7797-7809.

72. Obeid, R.; Lewis, D. M.; Smith, N.; Hall, T.; van Eyk, P., Reaction kinetics and characterisation of species in renewable crude from hydrothermal liquefaction of monomers to represent organic fractions of biomass feedstocks. *Chemical Engineering Journal* **2020,** *389*, 124397.

73. Cordova, L. T.; Lad, B. C.; Ali, S. A.; Schmidt, A. J.; Billing, J. M.; Pomraning, K.; Hofstad, B.; Swita, M. S.; Collett, J. R.; Alper, H. S., Valorizing a hydrothermal liquefaction aqueous phase through co-production of chemicals and lipids using the oleaginous yeast Yarrowia lipolytica. *Bioresource Technology* **2020,** *313*, 123639.

74. Glaser, B.; Lehr, V.-I., Biochar effects on phosphorus availability in agricultural soils: A meta-analysis. *Scientific Reports* **2019,** *9* (1), 9338.

75. Zhang, R.; El-Mashad, H. M.; Hartman, K.; Wang, F.; Liu, G.; Choate, C.; Gamble, P., Characterization of food waste as feedstock for anaerobic digestion. *Bioresource Technology* **2007,** *98* (4), 929-935.

76. U.S. Energy Information Administration, Monthly Energy Review: August 2021.

77. Ryan Davis, A. C., Mark Wigmosta, Jennifer Markham, Christopher Kinchin, Yunhua Zhu, Susanne Jones, Jeongwoo Han, Christina Canter, Qianfeng Li *2017 Algae Harmonization Study: Evaluating the Potential for Future Algal Biofuel Costs, Sustainability, and Resource*

Assessment from Harmonized Modeling; ANL-18/12; NREL/TP-5100-70715; Argonne National Laboratory, National Renewable Energy Laboratory, Pacific Northwest National Laboratory: 2018.

78. E.D. Frank, J. H., I. Palou-Rivera, A. Elgowainy, M.Q. Wang *Life-Cycle Analysis of Algal Lipid Fuels with the GREET Model*; ANL/ESD/11-5; 2011.

79. Hao Cai, J. H., Grant Forman, Vince Divita, Amgas Elgowainy, Michael Wang *Analysis of Petroleum Refining Energy Efficiency of U.S. Refineries*; Argonne National Lab Database, 2013.

80. J. Han, M. M., M.Q. Wang *Waste-to-Wheel Analysis of Anaerobic-Digestion-Based Renewable Natural Gas Pathways with the GREET Model*; Argonne National Laboratory: 2011.

81. Lampert, D. J.; Cai, H.; Wang, Z.; Keisman, J.; Wu, M.; Han, J.; Dunn, J.; Sullivan, J. L.; Elgowainy, A.; Wang, M.; Keisman, J. *Development of a Life Cycle Inventory of Water Consumption Associated with the Production of Transportation Fuels*; United States, 2015-10-01, 2015.

82. Palou-Rivera, I.; Wang, M. Q. *Updated estimation of energy efficiencies of U.S. petroleum refineries*; United States, 2010-12-08, 2010.

83. Fortier, M.-O. P.; Roberts, G. W.; Stagg-Williams, S. M.; Sturm, B. S. M., Life cycle assessment of bio-jet fuel from hydrothermal liquefaction of microalgae. *Applied Energy* **2014,** *122*, 73-82.

84. Fortier, M.-O. P.; Roberts, G. W.; Stagg-Williams, S. M.; Sturm, B. S. M., Determination of the life cycle climate change impacts of land use and albedo change in algal biofuel production. *Algal Research* **2017,** *28*, 270-281.

85. Nie, Y.; Bi, X., Life-cycle assessment of transportation biofuels from hydrothermal liquefaction of forest residues in British Columbia. *Biotechnology for Biofuels* **2018,** *11* (1), 23.

86. Agency, E. P., Municipal Solid Waste. Agency, E. P., Ed. 2016.

87. Agency, E. P., Understanding Global Warming Potentials. EPA.gov, 2020.

88. Administration, U. S. E. I. Diesel Fuel Explained. https://www.eia.gov/energyexplained/diesel-fuel/

89. Mausami Desai, V. C., Inventory of U.S. Greenhouse Gas Emissions and Sinks. Agency, U. S. E. P., Ed. 2021.

90. Lesley Snowden-Swan, J. B., Michael Thorson, Andy Schmidt, Yuan Jiang, et al., Wet Waste Hydrothermal Liquefaction and Biocrude Upgrading to Hydrocarbon Fuels: 2020 State of Technology. Pacific Northwest National Laboratory: 2021.

91. Sodium Hydroxide Flakes. https://www.alibaba.com/trade/search?fsb=y&IndexArea=product_en&CatId=80202&SearchText=sodium+hydroxide+50%25&viewtype=&tab=.

92. Greene, P. 101 for RINs.

93. Agency, E. P., RIN Trades and Price Information. 2021; Vol. 2021.

94. Swan, L. J. S., Wet Waste Hydrothermal Liquefaction and Biocrude Upgrading to Hydrocarbon Fuels: 2019 State of Technology. **2020**.

95. J. Han, M. M., M.Q Wang, Waste-to-Wheel Analysis of Anaerobic-Digestion-Based Renewable Natural Gas Pathways with the GREET Model. 2011.

96. Hao Cai, J. H., Grant Forman, Vince Divita, Amgad Elgowainy, Michael Wang, Analysis of Petroleum Refining Energy Efficiency of U.S. Refineries. Laboratory, A. N., Ed. 2013.

97. Paulou-Rivera, I., Han, J., Wang, M, Updated Estimation of Energy Efficiencies of U.S. Petroleum Refineries. Laboratory, A. N., Ed. 2011.

98. D. Lampert, H. C., Z. Wang, J. Keisman, M. Wu, J. Han, J. Dunn, E. Frank, J. Sullivan, A. Elgowainy, M. Wang, Development of a Life Cycle Inventory of Water Consumption Associated with the Production of Transportation Fuels. Laboratory, A. N., Ed. 2015.

CHAPTER 6

EFFECTS OF FEEDSTOCK PARAMETERS ON HTL BIOCRUDE YIELDS

6.1 INTRODUCTION

As climate change continues to progress, alternative sources of fuel are required to reduce carbon dioxide emissions. To reduce the reliance on fossil fuels and counteract the effects of climate change, waste streams offer a low-carbon emission and energy-dense source to replace petroleum fuels. Billions of tons of waste materials including food, wood waste, and agricultural waste are disposed of annually.[1-3] By utilizing this waste and diverting it from landfills, CO_2 emissions can be reduced by over 2% in the United States.[4, 5]

One promising waste conversion method is hydrothermal liquefaction (HTL), which benefits from its feedstock flexibility and ability to utilize wet-waste feeds without intensive drying steps. Despite HTL's inherent feedstock flexibility, the properties of the chosen feedstock will affect the amount and quality of the resultant biocrude.[6, 7] Research has indicated that some of the most important factors in determining biocrude yield are feed composition, in terms of protein, carbohydrate, lipid, and lignin content, as well as inherent particle size, and even the acidity of the feed.[6, 8-13] Of these parameters, lipid content is thought to play a crucial role in HTL biocrude yields due to the inherent lyophilic nature, making food waste lipid content an important factor for producing a high biocrude yield.[14] Additionally, the overall acidity, or pH, of the feedstock can alter the chemical processes and reaction kinetics, wherein researchers often believe that HTL

occurs through an acid-catalyzed decomposition followed by a base-catalyzed polymerization through aldol condensation.[15]

Feedstock composition has been shown to play a key role in biocrude production and process efficiency, however, real waste results in significant variability in feed composition. For food waste sources, seasonal variability occurs with the prevalence of fruits and vegetables in summer versus winter, the high uptick in carbohydrate and fat-rich desserts around the winter holiday season, and overall seasonal changes in food availability. While feedstock composition has been shown to affect biocrude yields, it is important to have significant understanding of the way in which slight variations affect biocrude properties to ensure that demand can be met in all seasons.

In addition to food waste, the factors affecting lignocellulose HTL are an important, yet less explored, research area. Lignocellulose is primarily composed of three macromolecules: lignin, cellulose, and hemicellulose.[16, 17] While biomass type is the most important factor in determining chemical composition of lignocellulose, variability is also known to occur based on sample location within a single tree or plant.[18] Furthermore, waste biomass changes in composition seasonally, as spring and summer contain high amounts of grasses, whereas autumn shifts to leaves, and the lignocellulosic waste content decreases drastically in winter months, particularly in regions with a cold climate.[19-22] The same trends have been shown in physicochemical and microbial properties of dairy waste, highlighting the changes in nutrient values and seasonal composition and their effects on climate change.[22]

Due to the importance of feedstock composition and the natural variations in waste throughout the year, this work aims to explore the effect that lipid content, pH, and mechanochemical pretreatment have on the resultant biocrude yield from hydrothermal

liquefaction. In this study, a series of food waste feedstocks were synthesized and evaluated to determine the effect of lipid and pH parametric changes in feedstock composition on the resultant hydrothermal liquefaction product distribution. Lignocellulosic waste was obtained and utilized to explore the effects of mechanochemical pretreatment, wherein the results from these experiments suggest new methods for determination and prediction of seasonal biocrude changes based on feedstock availability.

6.2 MATERIALS & METHODS

6.2.1 MATERIALS.

Food waste was synthesized to represent U.S. Army rations and to be generally representative of institutional food waste. Seven individual food items were obtained and mixed in specific ratios to achieve the desired product composition. American cheese, canned chicken, instant potatoes, green beans, white rice, applesauce, and butter were all mixed accordingly and used in all experiments denoted in sections 3.1 and 3.2.

Lignocellulosic waste (green waste) was obtained from BDP Industries Inc. Greenwich, NY and placed in air-tight bags and stored in a freezer at -20 °C. Before use, it was removed from the freezer, dried overnight, and ground in a coffee grinder before sieving to < 0.85 mm.

Additional reagents for HTL experiments included >99.5% pure acetone obtained from Sigma-Aldrich utilized for biocrude recovery and cleaning; deionized water with an electrical resistivity greater than 18.0 MΩ, used to prepare the feedstock mixtures; and nitrogen gas with >99.9% purity from Airgas, which was used to purge air from the reactors for experiments.

6.2.2 HYDROTHERMAL LIQUEFACTION REACTIONS

All HTL reactions were performed in a 300 mL stainless steel bench-top reactor from Parr Instruments Co. (model 4841) equipped with a magnetic stirring drive. For experiments conducted with food waste, 15 wt% solids and 85 wt% water loadings were used, but for lignocellulose, 10 wt% solids were used in all HTL experiments. The reactor was sealed, purged with nitrogen to remove residual oxygen, and then pressurized with nitrogen to approximately 1000 psi. Afterwards, the reactor was heated to 300 °C at a rate of approximately 5 °C/min using an external heating jacket. Once the internal reactor temperature reached 300 °C, it was maintained for 60 minutes before the reactor was quenched in an ice bath to 40 °C within 10 minutes.

To determine the carbon mass balance, first, all product yields were obtained through gravimetric analysis before and after reaction and separation. Carbon content of the biocrude and char phases were determined through elemental analysis completed at Midwest Microlabs. Aqueous phase carbon was analyzed via a total organic carbon analyzer. The acetone used in product separation was recovered via rotary evaporation at 40 °C under vacuum.

6.3 RESULTS & DISCUSSION

In this work, parameters effecting biocrude yield for the liquefaction of food and lignocellulosic wastes are explored through an analysis of carbon yields and product-phase analytics. Product yields are obtained for the biocrude, aqueous, char, and gas phases before further characterization with elemental analysis, total organic carbon (TOC), and GC-TCD to determine the carbon content of each phase. HTL is used as a thermochemical waste-to-energy technique to reveal how important feedstock qualities affect the resultant biocrude. This analysis provides a baseline for understanding the feasibility of converting varying waste types to usable biofuels.

Here, varying properties of food and lignocellulosic wastes are explored and analyzed to determine their effects on the hydrothermal liquefaction process.

6.3.1 INCREASED LIPID CONTENT INCREASES BIOCRUDE YIELD

The primary macromolecules in food are proteins, carbohydrates, and lipids. Proteins are known for their amino acid backbone containing nitrogen and oxygen heteroatoms, whereas carbohydrates are oxygenated-sugars. Lipids, on the other hand, are typically long-chain hydrocarbons with a terminal carboxylic acid (COOH) group. In this study, the effect of long-chain lipids is explored, wherein the fat, protein, and carbohydrate contents of the feeds can be found in **Table 6-1.**

Table 6-1. Feedstock composition for the five varying lipid ratio feedstocks. Feeds were composed of a mixture of grocery store items combined together manually to achieve the desired fat content.

	No Butter	**10% Lipid**	**20% Lipid**	**30% Lipid**	**40% Lipid**
Fat Content (%)	4.66	9.59	20.27	30.46	40.43
Carb Content (%)	76.97	72.96	64.26	55.96	47.85
Protein Content (%)	18.37	17.45	15.47	13.58	11.73
Oil Yield (%)	22.22 ± 3.42	28.87 ± 0.93	32.33 ± 3.30	45.33 ± 3.46	43.78 ± 4.82

The compositions in **Table 6-1** represent changes in the mass of butter added to a mixture of simulated food waste. This waste contained a mixture of American cheese, canned chicken, instant potatoes, green beans, white rice, applesauce, butter, and water. Additional information regarding amounts of each ingredient in the feedstock can be found in **Appendix E**. It can be seen that the percentages of carbohydrates and protein in the feed decrease with increasing lipid content, however, it is important to note that the ratio between carbohydrate and protein remains constant at approximately 4.2 times the carbohydrate content to the protein content. This ensures that the

resultant changes in HTL product yield distributions are due to changes in lipid content and not subsequent changes in other interactions.

The hydrothermal liquefaction experiments were conducted at 300 °C for 60 minute reaction time in all cases. The resultant product distribution from these experiments is shown in **Figure 6-1** wherein it can be seen that biocrude yield increases with increased lipid content in the feed. Without the addition of butter to the food waste feed, biocrude yields achieved average 26% whereas for a feed of 40% lipid, biocrude yield exceeds 60% on a carbon basis. This represents a 142% increase in total biocrude yield with the addition of approximately 35% more lipid.

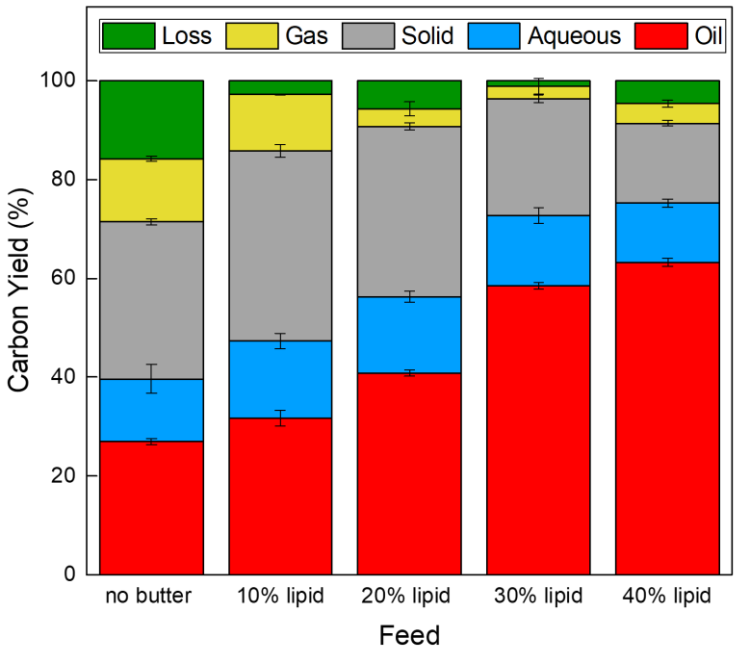

Figure 6-1. Carbon distribution for all four product phases and loss for the varying lipid content feedstocks explored. Operating conditions were 300 °C, 60 min, with N_2 gas headspace to ensure reactants remained in the liquid phase. Error bars represent the standard deviation of two or three repeat tests.

An additional point of interest in **Figure 6-1** is the subsequent decrease in char yield with an increase in lipid content. This indicates that the addition of lipid to the feedstock alters the

selectivity to biocrude over char. Changes in selectivity can be due to a plethora of reasons, one of which may be a decrease in repolymerization reactions due to the inherent stability and nature of the extracted lipids. Furthermore, the increase in lipid content of the feed is coupled to decreases in protein and carbohydrate fractions, which often can result in high char yields due to the initial size of proteins and ability of carbohydrates to form a high number of bonds. In addition to the trend in char yields, there is no change in aqueous phase yields with respect to lipid content. The constant aqueous yield is a sign that the lipids never undergo sufficient depolymerization to water-soluble molecules, but instead are merely extracted to the biocrude, thereby having little effect on the aqueous product.

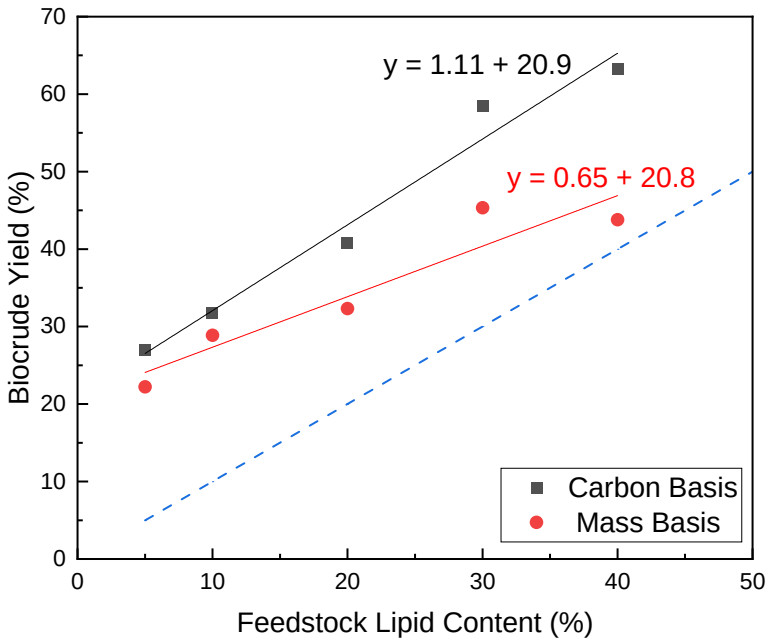

Figure 6-2. Parity plot comparing the lipid content of the feedstock to the resultant biocrude yield on both a carbon and a mass basis. The blue dashed line represents parity of equal lipid content to equal biocrude yield.

While it was determined in **Figure 6-1** that lipid content has the greatest impact on biocrude and char yields, it is also important to understand how lipid content impacts the biocrude quality.

Figure 6-2 attempts to understand the impact of lipid on the resultant biocrude through the use of a parity plot. For a data point to exist on the parity line, it would be assumed that 100% of the lipid at that particular lipid content was converted to biocrude-soluble products and that 0% of the non-lipid fraction of the feed contributed to the biocrude yield. From this analysis, it can be seen that all data points for both mass and carbon yields fall above the parity line, indicating that additional reactions are occurring to cause some of the carbohydrate and protein fractions to partition to the biocrude.

Furthermore, **Figure 6-2** contains linear fits to the two data sets. First-off, it is interesting to note that both fits result in the same y-intercept, which can indicate that biocrude yield and carbon yield have similar accuracy at low lipid-contents. As the lipid content increases, however, the two data sets begin to deviate, wherein the mass yield results in a slope of < 1 and carbon yield has a slope > 1. The slope of 0.65 for changes in mass yield as a function of lipid content indicates that the percent of additional carbohydrate and protein that reacts to form biocrude decreases as the lipid content increases. This trend follows what intuition would say, as an increase in lipid content decreases the amount of available protein and carbohydrate compounds available to react. Following this same trend, one would then expect the biocrude yield to reach a limit as lipid content increases. If the assumption holds true that 100% of the lipid can be converted to biocrude, then the apparent maximum would also be 100%.

The trend in **Figure 6-2** in regard to biocrude carbon-based yield, on the other hand, results in a slope of 1.11. This slope of greater than 1 indicates that as lipid content increases, the biocrude carbon content is going to increase at a rate faster than that of the added lipid. As previously mentioned, lipids are long-chain hydrocarbons with a carboxylic acid group whereas proteins and carbohydrates contain a higher percentage of oxygen and nitrogen heteroatoms per molecule. If

viewed as an oxygen-carbon ratio (O/C), carbohydrates would have the greatest O/C ratio, near or potentially greater than one, whereas lipids would occur in the range of 0.01 – 0.3, on average. The same trend can be seen with nitrogen-carbon ratios and proteins, where lipids typically result in a N/C ratio of zero. While the overall mass of the resultant biocrude represents the increase in biocrude-soluble lipid molecules and a reduction in carbohydrate and protein content, the overall carbon content of the biocrude increases due to inclusion of less heteroatoms than if the biocrude contained carbohydrates and proteins. Furthermore, this trend is corroborated by the increase in biocrude higher heating value (HHV) or energy content that is seen with increased lipid content (**Appendix E**).

6.3.2 PH DEPENDENCE OF BIOCRUDE YIELD

While the overall process for the conversion of waste to biofuels through hydrothermal liquefaction is largely shrouded in mystery, researchers have proposed that initial degradation of waste occurs through an acid-catalyzed depolymerization followed by base-catalyzed aldol condensation.[15] The idea of this acid-base type mechanism indicates that feedstock pH may be of importance in the production of biocrude from HTL. To attempt to uncover the pH dependence of biocrude yield, the varying lipid content feedstocks from the previous section were adjusted from pH 4.9 with the addition of NaOH to reach pH values of 6, 8, 10, and 12 before undergoing hydrothermal liquefaction reactions.

Figure 6-3 highlights the extremes, showing the resultant biocrude yields from HTL of food waste at four different lipid contents at pH 4.9 and pH 12. It is important to note that despite the lipid content, all initial feedstocks had a pH of 4.9. In this figure it can be seen that the addition of homogeneous base to increase pH resulted in a decrease in the overall biocrude yield. For feedstocks with no butter (5% lipid), 20% lipid, and 40% lipid, the decrease was beyond the limit

of uncertainty and was therefore a statistically significant change. In the 10% lipid feedstock, however, the decrease was only 1.6%, well within the limits of uncertainty represented by the error bars.

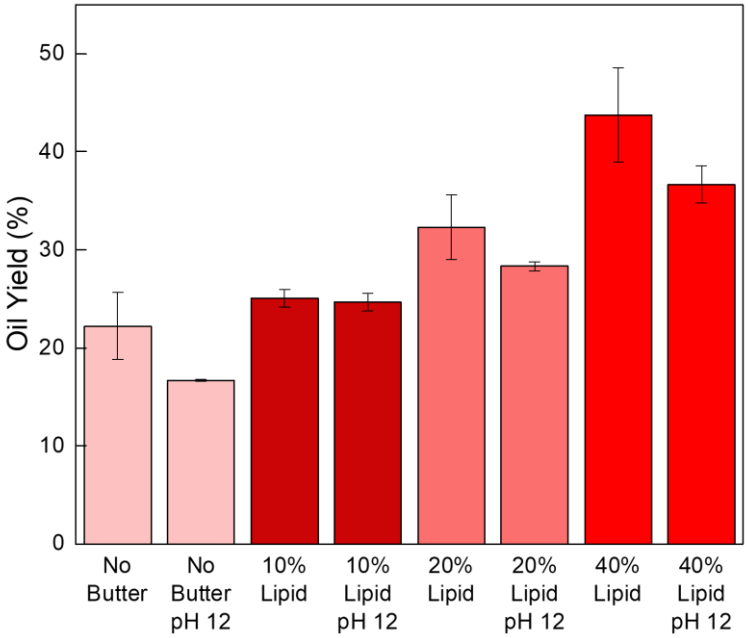

Figure 6-3. Biocrude oil mass yields as a function of lipid content and added homogeneous base in the form of NaOH. Bars of the same color indicate the same lipid content. All HTL reactions were performed at 300 °C for 60 minutes with a N_2 gas headspace to maintain liquid pressure.

Relating back to research hypotheses, a decrease in biocrude yield at high pH could be due to a decrease in initial depolymerization, which can cause increased char and even aqueous phase yields. Looking at the overall product distribution plot in **Appendix E** shows that the increase is actually occurring in the aqueous phase, which may represent a shift in reaction kinetic rates to slow initial depolymerization towards aqueous-soluble molecules, without the time or sufficient reaction conditions to rebuild into biocrude. If the primary increase in product yields occurred in the char phase, then it would be feasible to hypothesize that the increase in initial feedstock pH

caused incomplete depolymerization and further polymerization through the formation of base-catalyzed aldol condensation products that have molecular weights and K_{OW} values that are too high to fraction into a biocrude and instead result as a solid product.

Continuing this trend, feedstocks with no butter, 20% lipid, and 40% lipid are explored to determine the effect of a range of initial pH values on their resultant biocrude yields. **Figure 6-4** showcases the results of this analysis, indicating overall negative trends for all three lipid content feedstocks. An interesting trend is seen however, in that the point farthest from the trend occurs at a pH of 8. Similar to the trends seen in **Figure 6-3**, the slope of the trend increases with increasing lipid content, indicating that increases in pH have a larger effect on high-lipid feeds than low-lipid feeds.

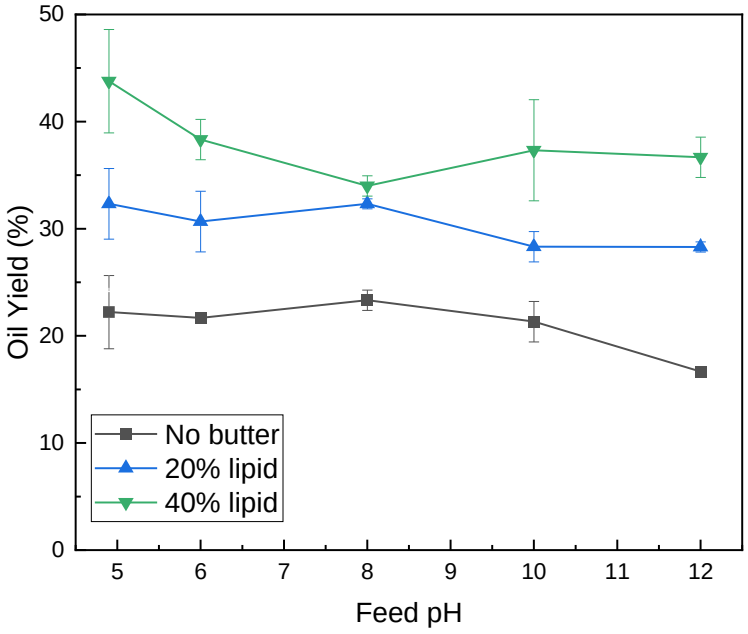

Figure 6-4. Relationship between the biocrude yield and initial feedstock pH for three different lipid content feedstocks. All HTL experiments were conducted at 300 °C, 60 min.

While some research has indicated that the addition of homogeneous base to the feedstock can improve biocrude yields, the work completed here refutes that idea, indicating that increasing pH of the feedstock results in decreased oil yield. While pH is traditionally considered for aqueous solutions and not feedstocks, the inherent 80 – 90% water content of the feedstock allows pH to be an inherent metric. The result of this, however, is that the aqueous phase can change in pH based on these changes. **Figure 6-5** highlights the changes in aqueous pH as a function of both feedstock lipid content and feedstock pH.

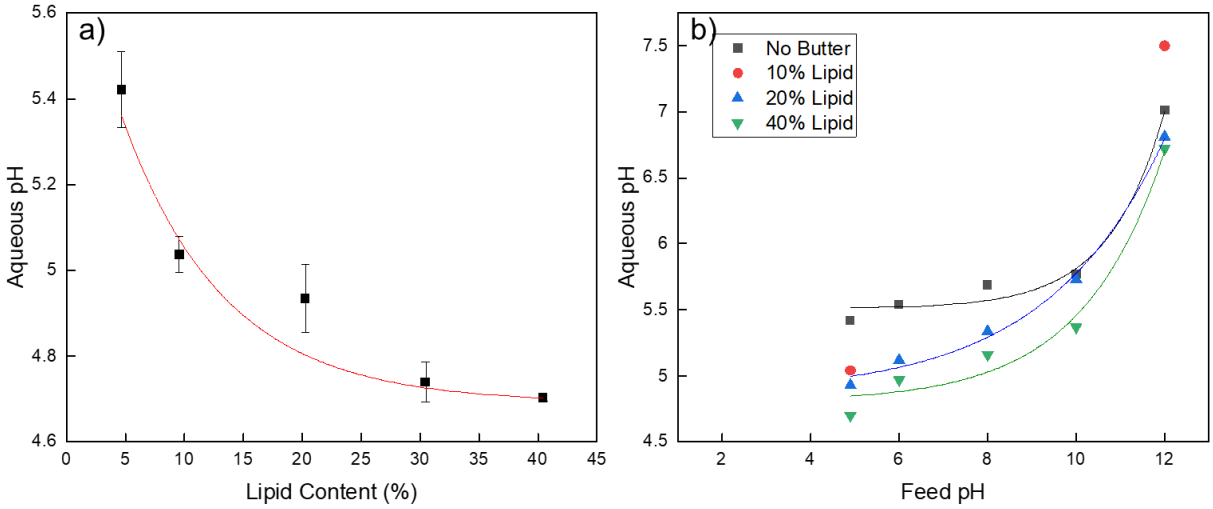

Figure 6-5. **a)** The effect of lipid content on aqueous pH. **b)** the Effect of feed pH on the resultant aqueous pH from hydrothermal liquefaction.

The trends seen in **Figure 6-5** provide an interesting perspective on the relationship between aqueous phase composition and feedstock parameters. In part a, it can be seen that aqueous pH follows an exponential decay trend with increasing feedstock lipid content. This trend can be explained by the chemical structure of the macromolecules contained within the feedstock, wherein carbohydrates contain evidence of acids, ketones, alcohols, and sugars. While lipid content increases, the carbohydrate content decreases, thereby removing some of the acidity

associated with acid groups, but also removing some basicity associated with the alcohol groups. Proteins are more complicated in that their acidity is based on their specific isoelectric point (pI). At pH values below their isoelectric point, they are positively charged molecules and are negatively charged at values above.[23] For this reason, proteins are not directly correlated to the resultant aqueous pH. Lastly, lipids contain a carboxylic acid group, indicating an increase in acidity with increasing lipid content. For the lipids to have an effect on the aqueous phase pH, however, some lipid must be dissolved or broken down into water-soluble acids, which refutes the constant aqueous yields identified in **Figure 6-1.**

Furthering this analysis through a comparison of feed pH and aqueous pH reveals that as feed pH increases, the aqueous pH increases. This increase, however, is not proportional to the increase in feed pH, with a significant jump between feed pH of 10 and 12. The jump that occurs spans a full pH unit, which may be related to a pK_a value for one, or multiple, components of the aqueous phase.

6.3.3 MECHANOCHEMICAL PRETREATMENT EFFECTS ON LIGNOCELLULOSIC WASTE

Sections 3.1 and 3.2 discuss composition-dependent parameters of the feedstock that are related to chemical structure and identity, however, there exists additional parameters related to the mechanical properties of the feedstock. In particular, lignocellulosic feeds are known for having additional mechanical property effects such as the presence of cellulose fibers, crystallinity, and even particle size. In this section, the effect of mechanochemical pretreatment of lignocellulosic biomass on biocrude yields is explored through an understanding of the affected parameters.

Table 6-2 serves as a basis for understanding the effects of ball-milling as a mechanochemical pretreatment method on the feedstock carbon, moisture, and ash content. The lignocellulosic (green) waste has similar bulk properties to the ball-milled waste, with only slight differences in all elemental, proximate, and biochemical compositional values indicative of method and experimental error.

Table 6-2. Biochemical, elemental, and proximate analysis for untreated and ball-milled green waste.

	Green Waste	**BM-Green Waste**
Elemental Analysis (wt %)		
Carbon	42.20	45.56
Hydrogen	5.18	5.67
Nitrogen	0.23	0.93
Oxygen	52.40	47.84
Proximate Analysis (wt %)		
Moisture	0.50	0.50
Ash	7.56	6.07
Biochemical Analysis (wt %)		
Holocellulose	69.70	69.70
Lignin	16.20	16.20

Ball-milling was completed in small batches for a period of 45 minutes before hydrothermal liquefaction experiments were completed. Due to the availability of the ball-milling equipment, all green waste HTL runs were completed at 10 wt.% solids loading and 90 wt% moisture. The results from these HTL runs are summarized in **Figure 6-6**, wherein it can be seen that ball-milling of lignocellulosic waste increases biocrude yield by a factor of nearly two. In addition, the right axis represents biocrude/char selectivity that begins at a value of 0.75 for green waste and increases to 2.30 for ball-milled green waste, indicating a stark shift in product distribution from char to biocrude.

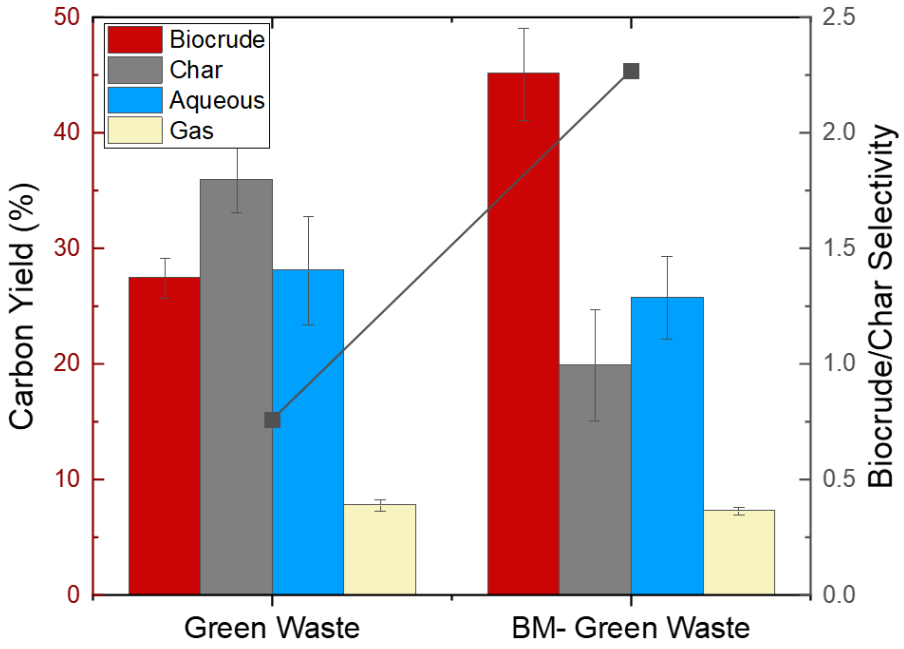

Figure 6-6. Hydrothermal liquefaction product distribution for untreated and ball-milled green waste feedstocks. The right axis shows the change in selectivity to biocrude over char for the two pretreatment scenarios.

Similar to the effect of lipid content, the overall aqueous and gas yields remain unchanged by the addition of mechanochemical pretreatment to the waste. The reduction in char formation and alteration in selectivity showcases the impact on degradation of crystalline green waste and may be affected by changes in particle size or biomass crystallinity. To attempt to address this question, green waste and BM-green waste were sieved into particle size fractions, before additional characterization and experiments were performed. **Figure 6-7** highlights the changes in biomass crystallinity, attributed to cellulose crystallization and de-crystallization as a function of the particle size fraction.

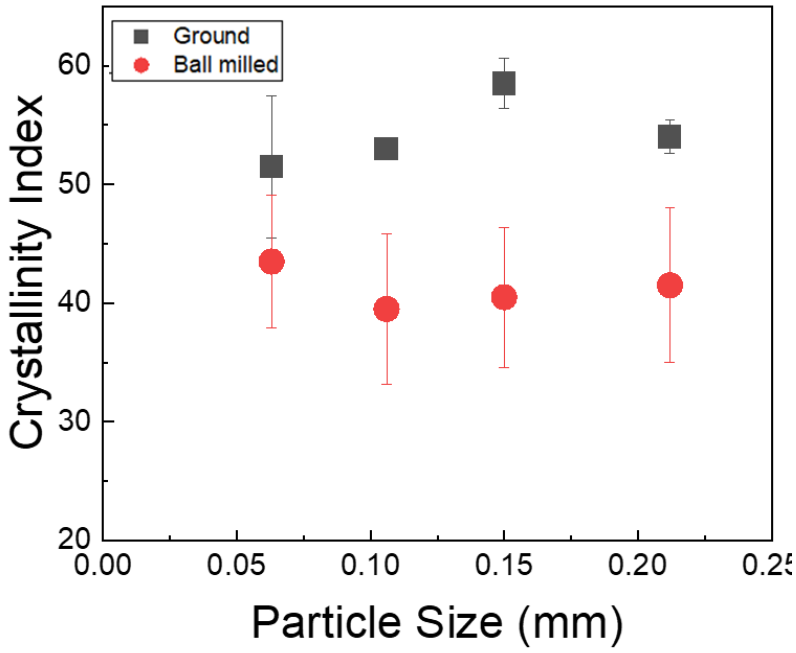

Figure 6-7. The relationship between crystallinity index and particle size for untreated and ball-milled green waste. Crystallinity index was determined through powder X-ray diffraction analysis.

In all particle size fractions, the relative crystallinity index is lower for ball-milled waste than untreated waste. Despite ball-milled waste having larger error bars than the untreated portion, four of the five fractions have statistically significant differences in crystallinity. As cellulose represents the crystalline fraction of biomass[24, 25], the calculated crystallinity index is representative of a decrease in the cellulose crystallinity specifically.

To continue to address the question of how ball-milling affects the resultant product distribution and its potential mechanism, the sieved particle size fractions were used as individual feedstocks in hydrothermal liquefaction experiments. The results of these experiments are shown in **Figure 6-8**. Here, it can be seen that the greatest increase in biocrude yield between untreated and ball-milled green waste occurs in the lower particle size fractions. In the fraction < 0.063 mm, ball-milling increased biocrude yield by 49.4% whereas in the fraction 0.106 – 0.15 mm

experienced only a 4.2% increase. Even more surprisingly, the biocrude yield decreased nearly 8% in the largest particle size range of 0.15 – 0.212 mm.

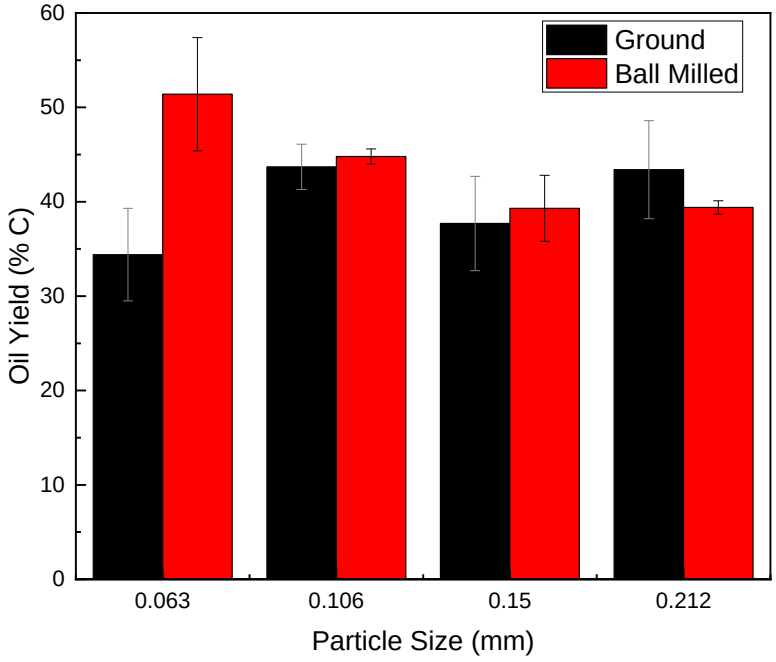

Figure 6-8. Biocrude oil yield represented on a carbon basis as a function of particle size for ground and ball-milled green waste. All HTL experiments were completed at 300 °C, 60 min and were conducted in at least duplicate.

The results presented in **Figure 6-8** can additionally be analyzed by comparing the trends in particle size differences within the untreated and ball-milled samples separately. As expected, based on simple mass and heat transfer knowledge, biocrude yield decreases as particle size increases in the milled green waste. The untreated green waste, on the other hand, exhibits no clear trend with particle size, and is instead, constant, within the experimental error.

The change in biocrude effect based on particle size is most likely due to the introduction (and removal) of intrinsic barriers and limitations within the system. As the particle size of the feed decreases, inherent rate-limiting diffusional barriers are removed, allowing for enhanced heat

and mass transfer and causing more efficient breakdown of the biomass particles and therefore, increased production into biocrude. On the flip side, the increased particle size introduces more diffusional limitations and results in slower heat and mass transfer, causing decreases in biocrude yield.

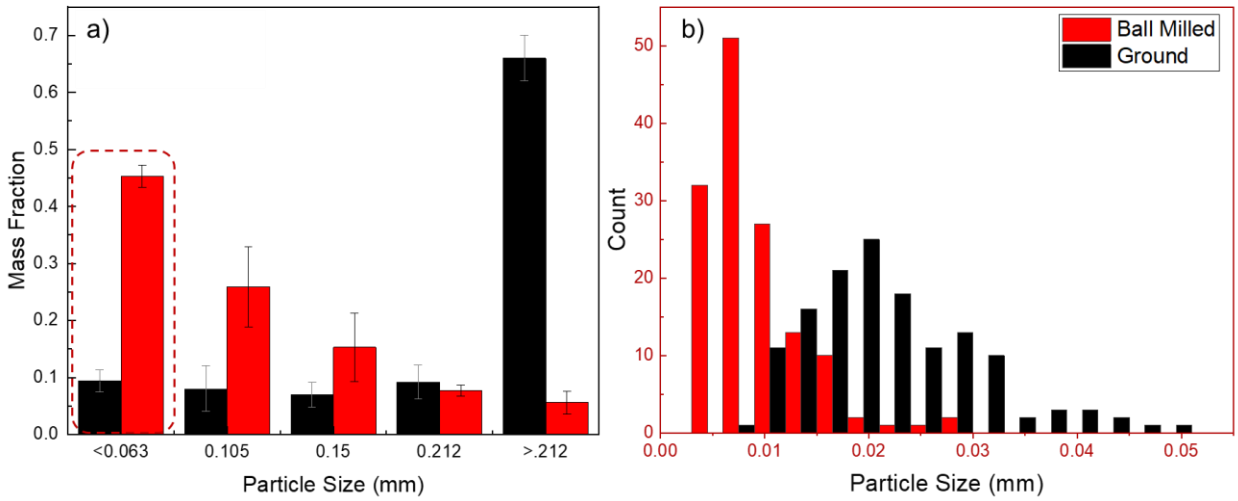

Figure 6-9. **a)** The fraction of ground and ball-milled biomass in each particle size range as determined by obtaining and weighing the sieve-separated fractions. **b)** Histogram of particle size distribution within the < 0.063 mm fraction for ground and ball-milled samples.

The effect of particle size distribution identified above results in questions relating back to the overall yield improvement from **Figure 6-6**. The < 0.063 mm particle size range resulted in a biocrude yield increase closest to that observed with no particle size fractionation. To further explore this trend, it was imperative that the number of particles in each fraction was determined. In **Figure 6-9a**, the mass fraction was determined for each particle size range, highlighting the drastic change in overall mass distribution between the untreated and ball-milled waste. In the ball-milled sample, nearly 50% of the mass has a particle size less than 0.063 mm whereas the untreated sample contains over 65% of its mass in particle sizes greater than 0.212 mm. It is important to note that both green waste samples were capped at a maximum particle size of 0.85 mm with a

sieve before any HTL experiments were conducted, indicating that the 65% of mass in the untreated sample occurs between .212 and 0.85 mm.

While the two samples have opposite compositional trends in regard to particle size distribution, the large percentage of mass in the smallest fraction of the ball-milled sample does not have a bottom size limit. For this reason, **Figure 6-9b** digs deeper into this fraction, showing a histogram of particle size distribution within the < 0.063 mm fraction. This analysis highlights further the disparity in particle size between the two green waste samples, wherein over 70% of the particles in the ball-milled sample are actually less than 0.01 mm compared to about 1% of the untreated green waste. On the other hand, the ground waste particle size distribution exhibits a pseudo gaussian distribution centered around 0.02 mm, double that of some of the largest ball-milled particles.

The results presented here in regard to the effect of mechanochemical pretreatment on lignocellulose biocrude yield indicate that the primary performance metric is particle size reduction. Data presented in **Figure 6-7** through **6-9** indicate that decreased cellulose crystallinity plays a minor role in improving depolymerization kinetics and therefore increasing biocrude yield, however, ball-milling effectively reduced the particle size distribution from > 0.2 mm to < 0.05 mm. Based on mass and heat transfer equations, the reduction in particle size constitutes a significant increase in reaction rate due to the removal of rate-limiting mass transfer steps. Additionally, the decreased initial particle size means that complete depolymerization can occur, allowing for biocrude formation reactions to dominate.

6.4 CONCLUSIONS

The studies performed here reveal that feedstock engineering and preconditioning are key metrics towards understanding hydrothermal conversion to biocrudes. Specifically, mechanochemical pretreatment was shown to increase biocrude yield from lignocellulosic waste by 63%, whereas increasing lipid content from 5% to 40% resulted in a 110% increase in biocrude yield from simulated food waste. Furthermore, the addition of NaOH as a homogeneous base to increase feedstock pH resulted in decreases in biocrude yield due to incomplete feed depolymerization and premature aldol condensation.

The work presented here focuses on the impacts of feedstock engineering parameters on biocrude yields, whereas additional studies should be completed to determine the effects of feed composition and mechanochemical pretreatment on chemical pathways towards biocrude formation. Enhanced understanding of biocrude formation pathways will allow for enhanced feedstock engineering capable of maintaining constant biocrude yields and properties despite seasonal variability in waste composition.

This study begins to unravel and determine the effects of feedstock parameters on the complex reaction networks associated with hydrothermal waste conversion, illuminating strategies for increasing biocrude yield. These findings greatly advance the scientific understanding of HTL feedstock effects and propose practical strategies for maximizing biocrude yields that can have positive effects on improving supply chain management through the diversion of waste from landfills.

6.5 APPENDIX E

Table E6-3. Simulated Army food waste composition for each a representative 10% lipid content feedstock.

Use for Food Waste Calculation Below

Step 1) Input green beans	green bean weight:	115.44	g
Step 2) copy and paste the "value" of I1 into J1	0.277840903	0.277840903	
Step 3) values for food waste will be in the wet basis column below (in yellow)			
The water content should be 85% when you copy and paste I1 into J1			

Food Item	Wet Basis (g)	Water Content (g)	Fat Content	Carb Content	Protein Content
American Cheese	6.43		1.542291	0.610490107	1.22098
Canned Chicken	21.31	13.83	0.42624	0	4.68864
Instant Potatoes	5.32		0	4.204148154	0.28205
Green Beans	115.44	107.96	0	2.886	0.92352
White Rice	9.59		0	7.671290158	0.642471
Apple Sauce	95.20	84.01	0	17.13622287	0
Butter	9.60		8.16	0	0.0672
Water	235.00	235.00	0	0	0
Total:	497.89	440.80	10.12853	32.50815129	7.824861
Total without water	57.09		0.2007	0.6442	0.1551
	Water content	88.53%			

Table E6-4. HTL biocrude and char elemental analysis results, including yields, biocrude higher heating values and overall energy recovery in the biocrude phase.

Lipid Content (Feed)	Oil Elemental Analysis				Char Elemental Analysis				Oil Yield (g)	Char Yield (g)	HHV (MJ kg^{-1}) (estimated)	Energy Recovery (%)
	C	H	O	N	C	H	O	N				
no butter	61.4	9	3.37	26	68.3	5.8	5.18	21	3.30	3.50	28.84	26.05
10%	63.4	8.4	25.1	3.1	68	5.2	21.9	5	3.80	4.30	28.94	29.80
20%	69	8.9	19.8	2.4	65.5	4.9	24.8	4.8	4.50	4.00	32.33	39.42
30%	68.4	9.5	20.2	1.8	66.8	5	23.3	4.9	6.50	2.70	33.10	58.31
40%	73.2	12	1.86	13	64.8	5.7	4.67	25	6.60	1.90	38.70	68.95

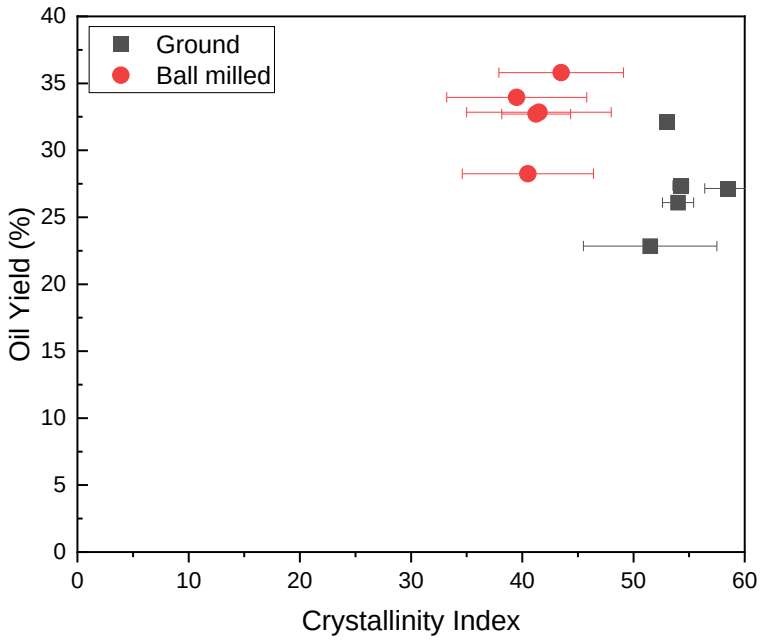

Figure E6-10. Dependence of biocrude yield from hydrothermal liquefaction of lignocellulosic waste untreated (i.e. ground) and ball-milled as a function of crystallinity index as determined by powder X-ray diffraction analysis.

6.6 REFERENCES

1. U.S. Environmental Protection Agency, Municipal Solid Waste. Agency, E. P., Ed. 2016.

2. U.S. Environmental Protection Agency, *Food: Material-Specific Data*; 2021.

3. U.S. Environmental Protection Agency, National Overview: Facts and Figures on Materials, Wastes and Recycling. epa.gov, 2021.

4. U.S. Environmental Protection Agency, Understanding Global Warming Potentials. EPA.gov, 2020.

5. LeClerc, H. O.; Page, J. R.; Tompsett, G. A.; Niles, S. F.; McKenna, A. M.; Valla, J. A.; Timko, M. T.; Teixeira, A. R., Emergent Chemical Behavior in Mixed Food and Lignocellulosic Green Waste Hydrothermal Liquefaction. *ACS Sustainable Chemistry & Engineering* **2022**.

6. Aierzhati, A.; Stablein, M. J.; Wu, N. E.; Kuo, C.-T.; Si, B.; Kang, X.; Zhang, Y., Experimental and model enhancement of food waste hydrothermal liquefaction with combined effects of biochemical composition and reaction conditions. *Bioresource Technology* **2019,** *284*, 139-147.

7. Bi, Z.; Zhang, J.; Peterson, E.; Zhu, Z.; Xia, C.; Liang, Y.; Wiltowski, T., Biocrude from pretreated sorghum bagasse through catalytic hydrothermal liquefaction. *Fuel* **2017,** *188*, 112-120.

8. Alimoradi, S.; Stohr, H.; Stagg-Williams, S.; Sturm, B., Effect of temperature on toxicity and biodegradability of dissolved organic nitrogen formed during hydrothermal liquefaction of biomass. *Chemosphere* **2020,** *238*, 124573.

9. Bayat, H.; Dehghanizadeh, M.; Jarvis, J. M.; Brewer, C. E.; Jena, U., Hydrothermal Liquefaction of Food Waste: Effect of Process Parameters on Product Yields and Chemistry. *Frontiers in Sustainable Food Systems* **2021,** *5*.

10. Biswas, B.; Kumar, A.; Fernandes, A. C.; Saini, K.; Negi, S.; Muraleedharan, U. D.; Bhaskar, T., Solid base catalytic hydrothermal liquefaction of macroalgae: Effects of process parameter on product yield and characterization. *Bioresource Technology* **2020,** *307*, 123232.

11. Chen, W.-T.; Qian, W.; Zhang, Y.; Mazur, Z.; Kuo, C.-T.; Scheppe, K.; Schideman, L. C.; Sharma, B. K., Effect of ash on hydrothermal liquefaction of high-ash content algal biomass. *Algal Research* **2017,** *25*, 297-306.

12. Cheng, F.; Cui, Z.; Chen, L.; Jarvis, J.; Paz, N.; Schaub, T.; Nirmalakhandan, N.; Brewer, C. E., Hydrothermal liquefaction of high- and low-lipid algae: Bio-crude oil chemistry. *Applied Energy* **2017,** *206*, 278-292.

13. Gai, C.; Li, Y.; Peng, N.; Fan, A.; Liu, Z., Co-liquefaction of microalgae and lignocellulosic biomass in subcritical water. *Bioresource Technology* **2015,** *185*, 240-245.

14. Biller, P.; Ross, A. B., Potential yields and properties of oil from the hydrothermal liquefaction of microalgae with different biochemical content. *Bioresource Technology* **2011,** *102* (1), 215-225.

15. Maag, A. R.; Paulsen, A. D.; Amundsen, T. J.; Yelvington, P. E.; Tompsett, G. A.; Timko, M. T., Catalytic Hydrothermal Liquefaction of Food Waste Using CeZrOx. *Energies* **2018,** *11* (3).

16. Mishra, R. K.; kumar, V.; Kumar, P.; Mohanty, K., Hydrothermal liquefaction of biomass for bio-crude production: A review on feedstocks, chemical compositions, operating parameters, reaction kinetics, techno-economic study, and life cycle assessment. *Fuel* **2022,** *316*, 123377.

17. Sanderson, K., Lignocellulose: A chewy problem. *Nature* **2011,** *474* (7352), S12-S14.

18. Pereira, H., Chemical composition and variability of cork from Quercus suber L. *Wood Science and Technology* **1988,** *22* (3), 211-218.

19. Ahmadi, A.; Riahi, H.; Noori, M., Studies of the effects of environmental factors on the seasonal change of phytoplankton population in municipal waste water stabilization ponds. *Toxicological & Environmental Chemistry* **2005,** *87* (4), 543-550.

20. Benito, M.; Masaguer, A.; Moliner, A.; De Antonio, R., Chemical and physical properties of pruning waste compost and their seasonal variability. *Bioresource Technology* **2006,** *97* (16), 2071-2076.

21. Li, Z.; Zhou, H.; Zheng, L.; Wang, H.; Chen, T.; Liu, Y., Seasonal changes in bulk density-based waste identification and its dominant controlling subcomponents in food waste. *Resources, Conservation and Recycling* **2021,** *168*, 105244.

22. Roufou, S.; Griffin, S.; Katsini, L.; Polańska, M.; Van Impe, J. F. M.; Valdramidis, V. P., The (potential) impact of seasonality and climate change on the physicochemical and microbial properties of dairy waste and its management. *Trends in Food Science & Technology* **2021,** *116*, 1-10.

23. Tokmakov, A. A.; Kurotani, A.; Sato, K. I., Protein pI and Intracellular Localization. (2296-889X (Print)).

24. Tyufekchiev, M.; Ralph, K.; Duan, P.; Yuan, S.; Schmidt-Rohr, K.; Timko, M. T., Rapid Depolymerization of Decrystallized Cellulose to Soluble Products via Ethanolysis under Mild Conditions. *ChemSusChem* **2020,** *13* (10), 2634-2641.

25. Tyufekchiev, M. V. Reaction Engineering Implications of Using Water for the Conversion of Lignocellulosic Biomass. Worcester Polytechnic Institute, 2019.

CHAPTER 7

DEVELOPMENTS IN THE TRANSITION FROM BATCH TO CONTINUOUS PROCESSING FOR HYDROTHERMAL LIQUEFACTION

7.1 INTRODUCTION

To begin to combat climate change, waste-to-energy technologies are being explored for their ability to address two simultaneous problems. Hydrothermal liquefaction (HTL) is a waste conversion method suitable for converting wet-waste feeds to biocrude oil through the use of high temperature and pressure between 275 – 400 °C and 4 – 22 MPa.[1] The HTL process is useful due to its ability to handle inherently wet waste feeds without energy-intense and costly drying.[2] The HTL process, in addition to producing a usable biocrude, produces three byproduct phases including solid char, aqueous organic, and a CO_2 rich gas phase.[3]

The process of biomass and waste liquefaction contains inherent challenges in the transition from batch to continuous processing. While research efforts in bench-scale HTL have shown great promise in its ability to convert waste to energy, there remains a lack of large-scale continuous testing operations.[2] Additionally, small pilot scale reactors have been developed and tested in recent years, wherein operation of the Albany facility produced 52 barrels of product over the entire lifetime of the facility, highlighting the need for further research into continuous processing.[2, 4]

Some of the known challenges in the transition from batch to continuous HTL processing include temperature and pressure. While small-scale batch reactor research has indicated that

increased temperatures can improve biocrude yields, this further complicates the transition to continuous processing due to the requirement for additional back pressure to maintain a liquid water phase.[2, 5, 6] In addition to process complications, increased operating pressure and temperature can affect capital costs, requiring thicker tubing and pumps with higher operating limits. Additional considerations must be taken due to pumping capabilities of slurries. Since HTL works as a wet-waste technology, this means that the feedstock is a slurry mixture, in batch systems up to 30 wt% solids, however, research into continuous processing of waste has been able to achieve a maximum of 15 wt% solids, typically even lower than that.[2] In this way, research indicates that the major challenges to biocrude production in continuous processing is the feeding of wet biomass. In addition to the challenges present in continuous processing, there exist further considerations for batch processing including thermal transience, difficulty in decoupling temperature and pressure, and the lack of industrial applications.[7]

On the other hand, biocrude production is not the only challenge related to the transition from batch to continuous. As previously mentioned, HTL results in 3 byproduct phases that require separation and disposal. Currently, to dispose of the HTL aqueous phase it requires additional treatment to remove harmful chemicals before being sent to a wastewater treatment plant for processing and disposal.[8-10] The carbon-rich solid char also requires disposal through combustion or landfilling the material, which is a decrease in landfilled mass compared to the initial biomass waste, however, solid production within the reactor can result in clogging and requires separation from the remaining liquid phases.[11]

These identified challenges in regard to aqueous disposal are made more difficult by the requirement to separate product phases. It is customary in bench-scale HTL to use vacuum filtration to separate product phases in HTL.[1, 12, 13] In order to utilize this method in a continuous

reaction, this involves collecting all product in a large barrel before bringing it to a separate location for batch separation, which is costly and time consuming. This study aims to identify novel solutions to these problems by discussing the potential for in-line biocrude aqueous separation as well as introduce catalytic continuous upgrading as a method to reduce the organic content of the aqueous phase, thereby increasing the potential for direct disposal as well as improving overall energy recovery of the HTL process.

7.2 MATERIALS & METHODS

7.2.1 MATERIALS.

Materials used in continuous flow separation include the use of syringe pumps, capable of holding two 60 mL syringes, as well as a liquid-liquid separator developed and obtained from Zaiput Flow Technologies (Cambridge, MA). Solvents including hexane, toluene, tetrahydrofuran (THF), and methanol were all obtained from SigmaAldrich in purity of greater than 95%. Tubing was made of PTFE for flow experiments and a quartz cuvette was utilized in batch.

Materials utilized in the experimentation for the flow aqueous upgrading experiments included dichloromethane (DCM), purity > 98%. Catalysts were obtained from SigmaAldrich (hydroxyapatite, 1 mm particle size) and ZSM-5 catalyst was obtained from Zeolyst. Micro-reactors were conducted in stainless steel Hastelloy tubing capped with Swagelock fittings.

7.2.2 METHODOLOGY

Aqueous separation experiments were conducted in batch utilizing 50 mL glass vials to ensure that the receptacles could seal for proper mixing and to limit solvent evaporation. Flow experiments were conducted using the PTFE tubing identified in the materials section. UV-Vis wavelengths were screened and chosen to represent the typical wavelengths associated with carbon

in benzene, and carboxylic acid groups. Solvent ratios were identified and the amount of solvent and aqueous phase was determined based on maintaining a constant total volume of 10 mL.

Experiments for catalytic aqueous phase upgrading were conducted in micro-batch reactors in a sand bath. The sand bath temperature was set to the desired temperature and left to heat up until the desired temperature was reached and maintained for at least 30 minutes. During sand bath heat up, the reactors were prepared by filling them with the desired amounts of product and catalyst using a scale to ensure that measurements were taken of the initial empty reactor, with product, and fully closed for later gravimetric measurements. The reactors were then fully submerged in the sand bath and reaction time began when the internal temperature of the reactor reached the desired reactor temperature ± 5 °C, typically within 1-2 minutes. Reactors were shaken constantly in the sand bath using a rotary pump. After reaction, the reactors were immediately quenched in a water bath until they reached 30 °C and were left in the water bath for 30 minutes to ensure safety when handling and opening the reactor.

Reaction products were quantified through gravimetric analysis. Micro-reactors were first weighed after drying to ensure any residual water from the water bath was removed, and then the gaseous product was removed before re-weighing, allowing for a determination of the amount of gas produced. All liquid and solid products were then removed from the reactor into a vacuum filtration flask. The vacuum was turned on to draw out and separate the aqueous phase from the solids and oils. After the aqueous flask was weighed and transferred to another vial, acetone or DCM was used to dissolve and separate the biocrude from the solid phase and subsequently weighed. In reactions occurring with ZSM-5, aqueous and oil phases were separated via the use of a separatory funnel and a known amount of DCM.

Gravimetric analysis was also used for determination of product yields in the continuous reactions in the same method as described above. DI water was first flowed through the system at a flow rate of 5 – 10 mL/min to ensure the reactor was filled with liquid before setting the back pressure regulator to a pressure of 100 bar. The temperature for the pre-heater was then set to 180 °C and that of the heater to 550 °C, high enough to ensure the inside liquid temperature reached 300 °C. DI water flow rate was turned down to the operational flow rate (0.03 – 3.0 mL/min) to ensure that the liquid temperature at the proper flow rate remained constant. Heat up with DI water took 1 hour on average, before a valve was switched to flow aqueous phase through the system. Aqueous phase ran through the system without collection for two-times the length of time as would take to fill the entire system. Once this time was reached, the reaction time began and samples were collected every 15 minutes for analysis.

Aqueous phase analysis was conducted using the total organic carbon (TOC) reagent Hach kit from Hach and analyzed via the Hach laboratory spectrophotometer for water analysis (#LPV440.99.00012). 1 mL of aqueous phase was utilized for each of these TOC analyses. Carbon, nitrogen, and hydrogen were directly determined using an elemental analyzer (PerkinElmer, 2400 Series II), and oxygen was determined by difference, assuming negligible sulfur content. Biocrude and organic compositions were determined through GC-MS analysis utilizing an Agilent GC (8890), coupled with an Agilent MS (5977B) on a DB-5MS column (30m x 0.25mm x 0.25mm).

7.3 RESULTS & DISCUSSION

This work aims to quantify and reduce known challenges in the commercialization of hydrothermal liquefaction as a waste to energy process. In addition to challenges with scale-up, there remains additional setbacks in regards to the transition from batch to continuous processing,

including in-line product separation of the biocrude and aqueous phases, as well as ensuring maximum carbon recovery from byproduct phases. In this study, liquid-liquid membrane extraction is explored as an in-line product recovery technique to separate the biocrude and aqueous phases through a hydrophilic membrane. Additionally, a continuous packed bed reactor is designed and tested to recover carbon from the aqueous phase through reaction with a variety of catalysts to produce biocrude or specialty chemicals.

7.3.1 BIOCRUDE-AQUEOUS MEMBRANE SEPARATION

To begin to improve energy recovery from the HTL process, carbon must be diverted from the aqueous phase into the biocrude. For optimal carbon recovery, a suitable solvent that is not miscible with water must be selected. A series of solvents were selected to be screened including hexane, dichloromethane (DCM), toluene, tetrahydrofuran (THF), and methanol. **Figure F7-10** shows the results of this screening, wherein methanol produced the highest absorbance reading in UV-Vis, indicative of a higher carbon content, however, methanol also resulted in a single aqueous-organic phase.

Despite a low absorbance at 475 nm in the initial screening tests, hexane was chosen for UV-Vis calibrations due to detector limitations and the high miscibility of other solvents resulting in concentrations of carbon that were too high for accurate UV-Vis detection capabilities. In this way, **Figure 7-1** shows the results of the UV-Vis calibration using hexane in both batch (cuvette) as well as in flow utilizing PTFE tubing. Due to the differences in construction materials of the cuvette and tubing, each calibration is performed at a slightly different wavelength.

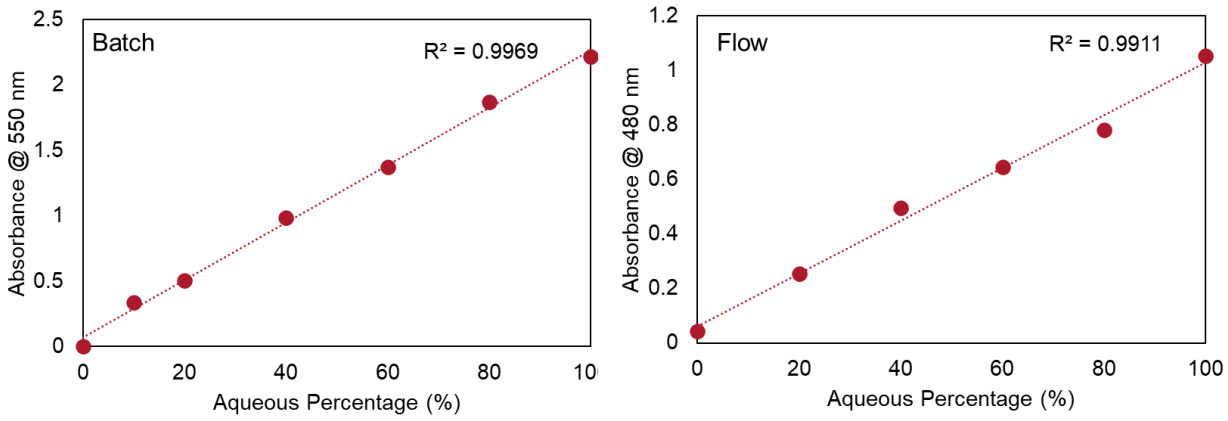

Figure 7-1. UV-Vis calibration curve for batch (cuvette) and flow (PTFE tubing) experiments for the separation of HTL aqueous phase with hexane.

For confirmation of the calibration, the molar absorption coefficient was calculated for each data point in the batch calibration. For a 'good' calibration, all molar absorption coefficients should be the same, within an error of ± 0.05. The results of this analysis (**Table F7-3**), indicate that this calibration is suitable for use in future experiments and for the determination of the separation efficiency for aqueous phase concentration. Further research in this area is required, however, to obtain an accurate representation of the effectiveness of solvents and membrane separation in HTL product purification. **Figure 7-2** showcases photographs of the product separation that occurs at differing ratios of solvent to aqueous phase, highlighting color differences in the hexane phase that are not visually apparent in the aqueous phase.

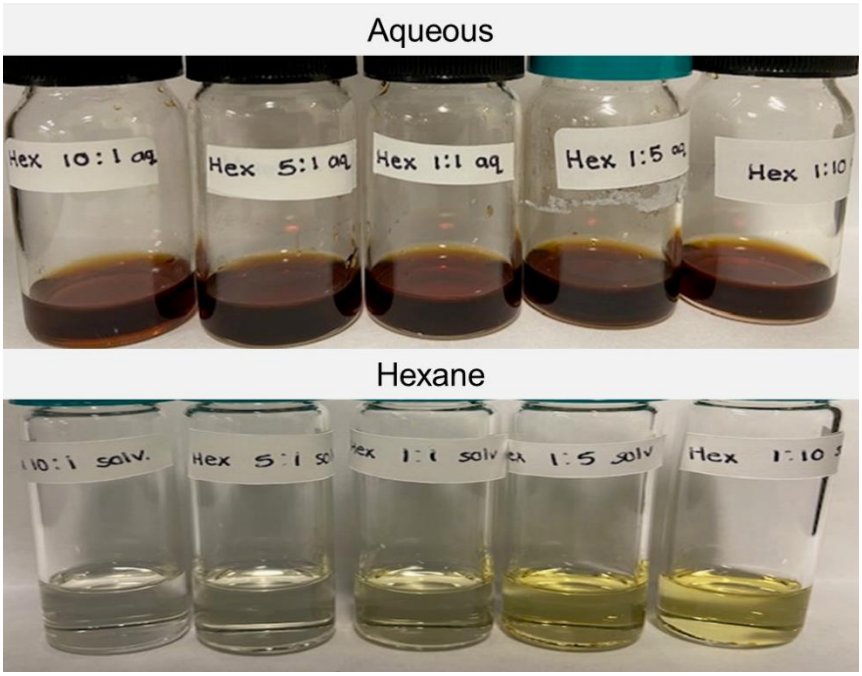

Figure 7-2. Photographs of the result of HTL aqueous phase extraction with hexane solvent. As the concentration of the solvent increases, the color decreases due to dilution effects.

In order to accurately use membrane separation as an in-line method for aqueous and biocrude extraction, solvents should be further explored to ensure complete dissolution of the biocrude in the solvent, and efforts should work to determine a suitable green solvent, due to the nature of the process. Furthermore, additional work should be completed in this area to determine the relationship between UV-Vis absorbance and the amount of carbon in the aqueous and solvent phases. This result can be obtained from calibration with total organic carbon (TOC) measurements of the aqueous phase and elemental analysis of the carbon in the biocrude. While this research was unable to progress to quantitative analysis of the membrane separator, the process flow diagram for such a system is highlighted in **Figure 7-3**.

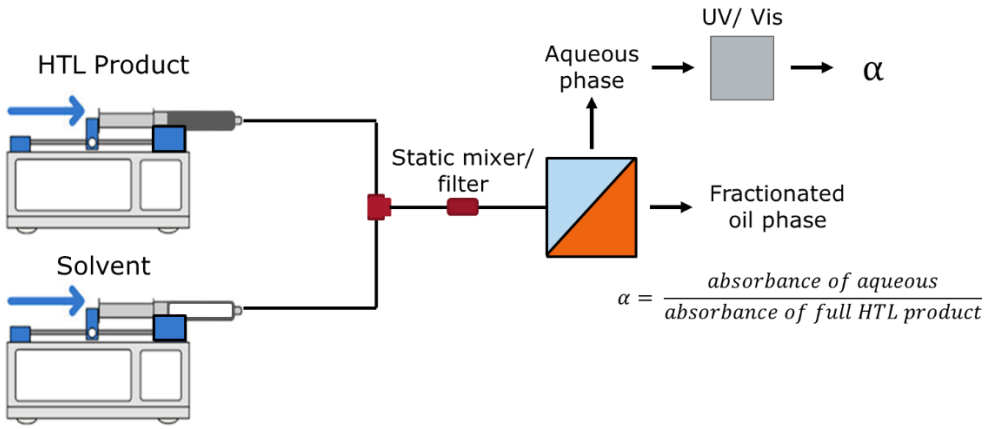

Figure 7-3. Process flow diagram for the isolation of carbon from HTL product phases using solvent and an in-line organic separation. Equation for α is included in the figure to ensure enhanced understanding.

In addition to solvent selection, one of the major challenges in in-line product separation is the presence of solids in the reactor that can clog the transfer lines as well as the membrane, potentially causing problems in continuous operation that require cleaning or replacement of PTFE tubing. An additional option to explore is the effect of pre-filtering before the liquid products go through the separator.

As always, commercialization is a concern in the transition from batch to continuous processing technologies for hydrothermal liquefaction. In order to ensure that in-line membrane separations are suitable for commercial use, it is imperative to understand the scalability of the process, in particular, what is the largest size of membrane separators available. The current unit houses a Zaiput membrane separator at the benchtop scale, if separators are not available in a size suitable for a commercial HTL plant, do they then have the potential to be operated in parallel and how does the need for additional units affect the capital cost and operating costs of the hydrothermal liquefaction plant. For this reason, it is recommended that further research into a)

commercial viability and technoeconomic analyses, b) green solvent capabilities, and c) solids loading and clog reduction methods be explored for the success of this process.

7.3.2 CONTINUOUS AQUEOUS UPGRADING

As mentioned previously, a significant fraction of carbon, up to 30%, ends up in the aqueous phase after separation. The majority of this carbon exists in the form of small, water-soluble molecules with K_{OW} values less than one. **Figure 7-4** highlights the average amount of carbon in the aqueous phase from a variety of food waste, lignocellulose, and lignin feedstocks. In this figure, it can be seen that a moderate-lipid food waste, and a high cellulose-content lignocellulose result in the greatest concentration of carbon in the aqueous phase. These two feeds have cellulose, or sugar, in common, wherein the sugars breakdown into small molecules such as glucose, which has a logP of -2.82, indicating its strong favorability towards the aqueous phase.

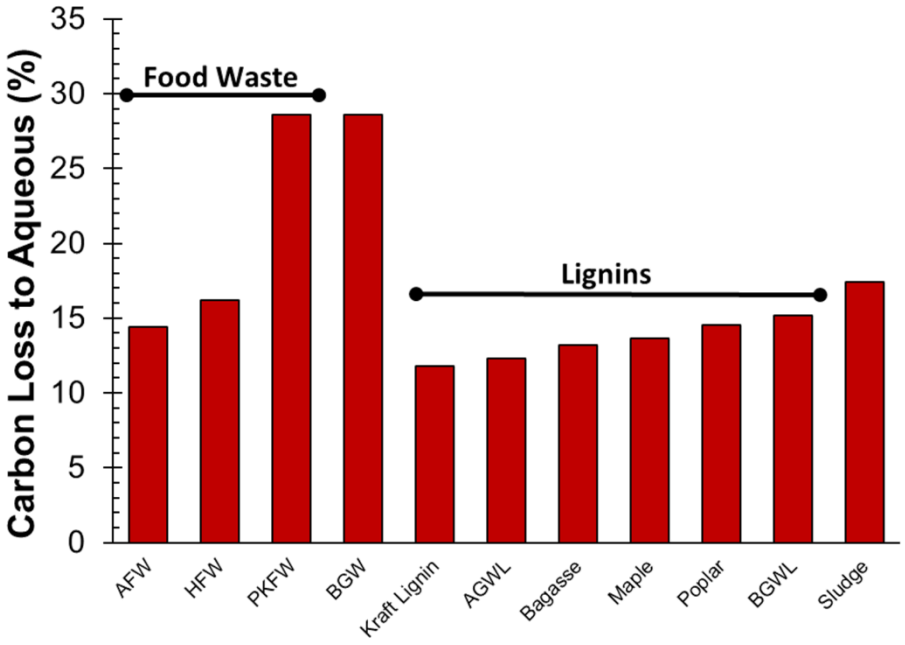

Figure 7-4. Percent carbon yield in the aqueous phase from hydrothermal liquefaction of a variety of feedstocks performed at 300 °C for 60 minutes.

In addition to the high concentration of overall carbon in the aqueous phase, it is important to understand the chemical composition to make informed hypotheses and decisions about remediation. Through analysis with GC-MS, it was determined that greater than 75% of analyzable aqueous phase molecules are carboxylic acids. In order to make the aqueous phase analyzable by GC-MS, the aqueous phase was first acidified with HCl to a pH of 3.5 before undergoing extraction with DCM. The resultant DCM phase was then placed in the GC-MS to determine chemical composition. This composition is shown in **Figure 7-5**, highlighting the high concentration of carboxylic acids, followed by nitrogen-containing compounds in the form of amides and heterocycles.

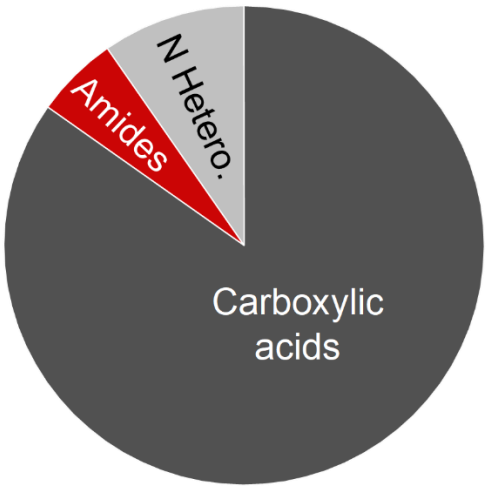

Figure 7-5. Pie chart showing the representative fractions of the aqueous phase carbon, as determined through aqueous acidification and separation using DCM before analysis with GC-MS.

Now that the carbon content of the aqueous phase is understood, it is important to choose the proper catalysts to explore. In this way, hydroxyapatite was chosen to produce biocrude, as hydroxyapatite has been shown to be effective in increasing biocrude production from food waste as well as serves as a suitable catalyst for *ex situ* catalytic HTL for aqueous carbon recovery in

batch. In addition to hydroxyapatite, the common zeolite ZSM-5 was chosen to produce specialty benzene, toluene, ethylbenzene, and xylene (BTEX) chemicals, due to its known effectiveness in converting carboxylic acids to BTEX.[14]

To begin to tackle this problem, the reactor system had to be designed. To achieve HTL conditions in flow, safety was an important consideration. To ensure safety, the reactor (**Figure 7-6**) was equipped with a number of pressure relief valves, pressure gauges, thermocouples for temperature monitoring, and was placed in a fume hood behind a blast shield. Pump operation was maintained at flow rates less than 5 mL/min, also working to ensure that any system leaks or failures would be easily contained.

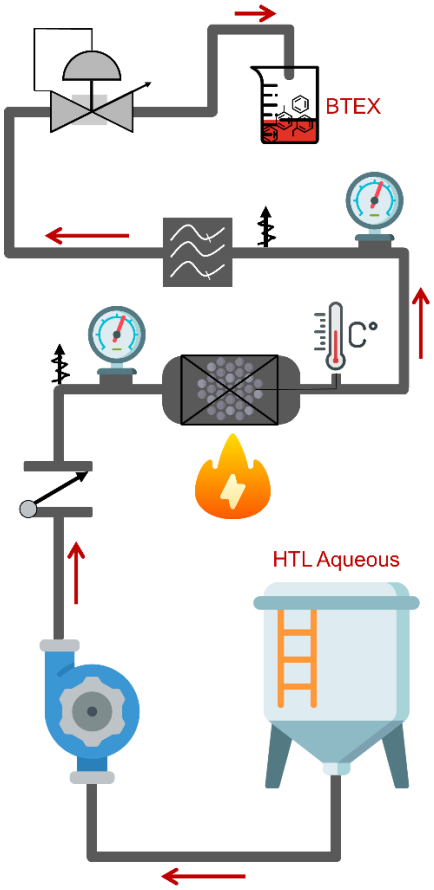

Figure 7-6. Process flow diagram for the continuous processing and upgrading of HTL aqueous phase through a packed bed reactor. Reactor is equipped with a pump, back pressure regulator and is made out of stainless steel for safety.

7.3.3 HYDROXYAPATITE EFFECTS ON AQUEOUS CARBON RECOVERY

Previous results displayed in Chapter 5 highlight the use of hydroxyapatite as a suitable catalyst for improved biocrude yields from hydrothermal liquefaction of food waste. Additionally, the idea of *ex situ* versus *in situ* catalysis was proposed as a method to reduce char build-up and catalyst deactivation. In this section, the idea of *ex situ* catalysis, i.e. using hydroxyapatite as a catalyst to produce biocrude from aqueous phase carbon, is transferred to use in a continuous set-up with varying HTL feedstocks.

While the use of HAP in batch systems resulted in decreases in aqueous phase carbon by 35% and therefore increases in biocrude carbon by the same margin, the continuous system struggled to produce comparable results. On a mass basis, continuous runs struggled to break 1% biocrude yields, due in part to the lack of solvent through the system, thereby causing a build-up of biocrude soluble products in the system, making it difficult to quantify catalyst turnover frequency and longevity. Mass results comparing the oil yields obtained from the continuous system in comparison to a micro-batch reactor are highlighted in **Figure 7-7**.

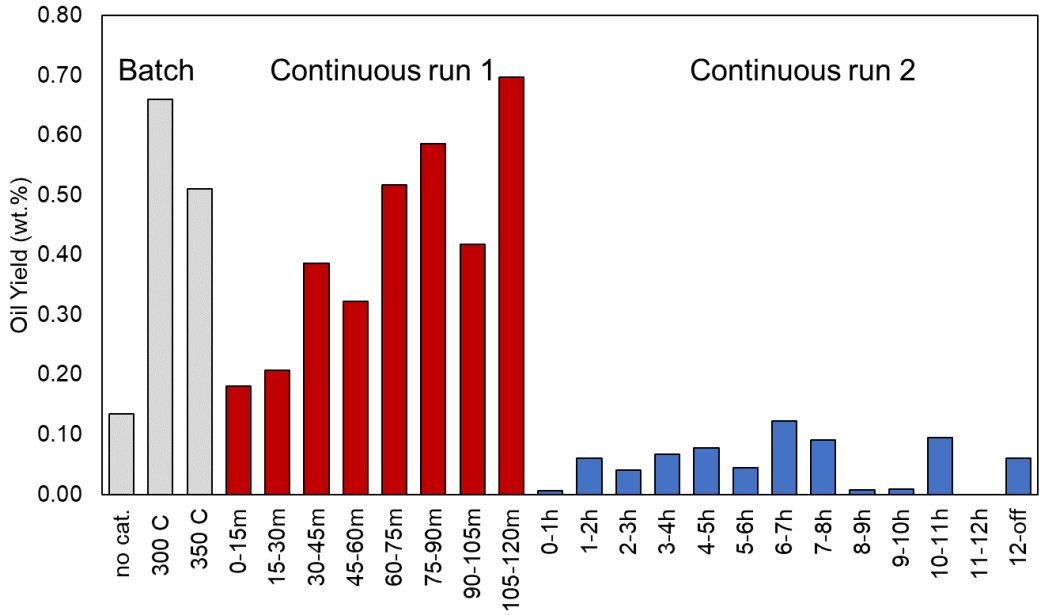

Figure 7-7. Mass yield results for the collection of biocrude obtained through catalytic aqueous-phase upgrading with hydroxyapatite. Continuous reactions were completed at a residence time of 15 minutes and maintained at a back pressure of 100 bar.

While all mass yields resulted in the production of biocrude, the continuous reactions resulted in lower biocrude yields than would be expected, due partially to the retained biocrude in the reactor. However, despite this loss, the total organic carbon in the aqueous phase decreased by 15.1% compared to the initial aqueous feed. **Table 7-1**, shown below, contains a summary of the

completed continuous runs with their total oil yields as well as their percent reduction of total organic carbon in the aqueous phase. In all experiments, the oil yield ranged from 0.01 – 0.41%. constituting a wide range of biocrude yields for the same feedstock and run conditions. Continuing with the previous analysis, it appears that the amount of biocrude trapped in the reactor varied throughout trials. Further research should aim to address these changes in biocrude entrapment, as well as determine a suitable solvent cleaning method to separate and determine biocrude yields.

Table 7-1. Biocrude yield and percent total organic carbon reduction in the aqueous phase from continuous runs of catalytic aqueous phase upgrading.

Date	Total Run Time	Oil Yield (%)	TOC Reduction (%)	Notes
3/17/2022	2 h	0.41	15.1	Sewage sludge aqueous, supercritical HTL, with K2CO3 and NaOH
4/27/2022	6 h	0.01	12.5	Sewage sludge aqueous
5/3/2022	6 h	0.10	0.1	Sewage sludge aqueous
5/4/2022	5 h	0.05	3.3	Pressure issues due to bubbles in line near end
5/12/2022	5 h	0.01	5.2	Wood aqueous, 1.5mL/min flow rate
5/17/2022	6 h	0.10	16.0	Wood aqueous
5/24/2022	5 h	0.06	8.2	Wood aqueous
5/25/2022	5 h	0.01	4.3	Wood aqueous, Catalyst re-use
Total Time	**52 hours**			

The continued poor yield results meant that additional considerations would need to be taken to accurately measure the oil yield as a function of time. In addition, previous work in Chapter 5 revealed the effect of hydroxyapatite catalyst on high-carbohydrate content feedstock.

With increasing lipid content, hydroxyapatite has a decreased effectiveness, corresponding to the poor performance with sewage sludge aqueous, which contained an initial lipid content greater than 20 wt%. Furthermore, the transition to wood-based aqueous phase would be expected to see an increase in biocrude produced from the aqueous phase, however, this is not what is seen in **Table 7-1,** instead, the average reduction in TOC is greater for wood than for sludge, an indication that while hydroxyapatite is more effective in the conversion of wood aqueous to biocrude, there remains the collection challenge wherein biocrude is trapped in the system, without a suitable recovery method.

7.3.4 BTEX PRODUCTION FROM HTL AQUEOUS

To further elucidate the potential of HTL aqueous to increase energy recovery and decrease HTL waste production, the common zeolite, ZSM-5, was used as a catalyst for the production of BTEX chemicals. As indicated by Page et al.[14] the use of ZSM-5 with a minority near-supercritical water phase results in the production of BTEX from carboxylic acids. As shown in **Figure 7-5** over 75% of the identifiable compounds in the aqueous phase from HTL of sewage sludge are carboxylic acids.

Proof of concept experiments were performed in micro-batch reactors, wherein the aqueous phase from sewage sludge, the bottom residue from distillation of sewage sludge aqueous, and wood aqueous phase were all tested in small sand bath reactors to confirm the production of BTEX. Reactions were performed at both 300 and 400 °C to explore the effect of temperature and near-supercritical water on BTEX production. **Table 7-2** highlights the TOC reduction in the resultant aqueous phase in addition to a simple metric stating whether BTEX compounds were identified in the dichloromethane (DCM)-soluble phase.

Table 7-2. Summary of the TOC reduction and presence of BTEX compounds from the treatment of the listed HTL aqueous phases at 300 or 400 °C for 15 minutes in the presence of ZSM-5.

	TOC Red. %	**BTEX?**
Sludge Aqueous Phase (400 C)	29.0	Yes
Sludge Aqueous Residue (400 C)	77.0	Yes
Sludge Aqueous Residue (300 C)	25.0	No

In addition to the presence or absence of BTEX chemicals, significant information can be obtained from visual observation of the samples. **Figure 7-8** contains images of unreacted sludge residue, the result of reacting entire sludge aqueous at 300 °C and the result of reacting the sludge residue at 400 °C. Each panel contains image(s) for the separation of phases for an aqueous and a DCM-soluble phase. In the leftmost panel, it can be seen that both the aqueous and DCM phases of the unreacted sludge are both dark in color and opaque, wherein they are not see-through. In addition, it is difficult to locate the line of demarcation between the phases, indicative of incomplete separations. The middle panel represents the reaction of sludge aqueous phase, without prior treatment, after reaction at 300 °C and DCM-aqueous separation. Compared to the panel at left, the aqueous fraction has undergone a color and opacity change, wherein the color has lightened from initial feed and one is able to identify the presence of residual solids within the aqueous phase. Lastly, the right panel shows the sample with the highest TOC reduction at a staggering 77%. This reduction in TOC correlates to the most transparent aqueous phase, and an extremely dark DCM-soluble phase. Further exploration into the product distribution within the DCM phase of these experiments are needed to determine the most promising reaction conditions.

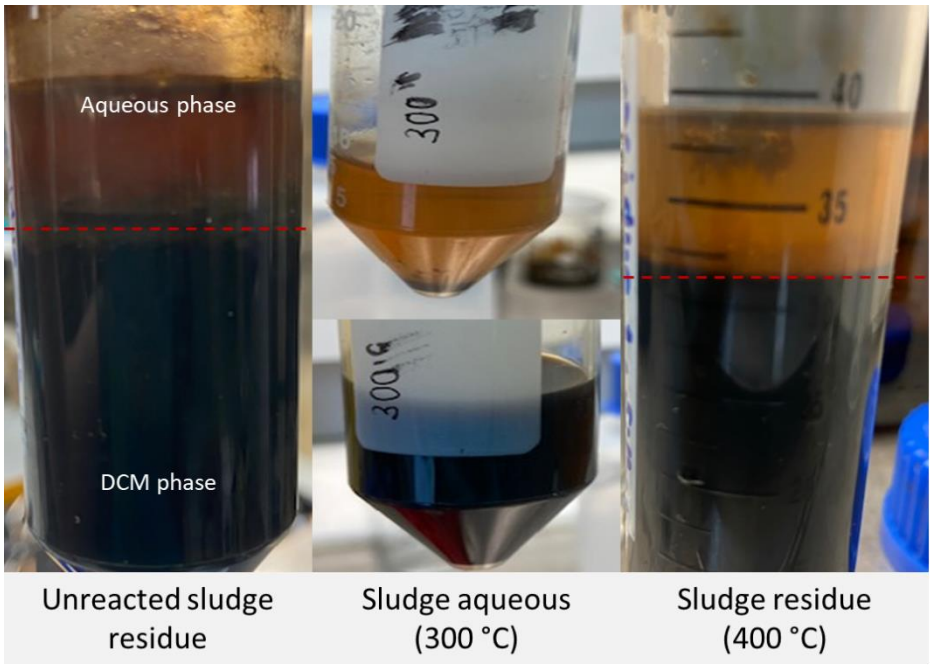

Figure 7-8. Photographs depicting the aqueous and DCM phases after liquid-liquid extraction. Left- unreacted residue from the distillation of HTL aqueous phase from sewage sludge. Middle- sewage sludge aqueous phase separation after reaction with ZSM-5 at 300 °C and 15 min reaction time. Right- sewage sludge aqueous residue from distillation after reaction with ZSM-5 at 400 °C and 15 min reaction time.

The last portion of this analysis includes identification and understanding of the composition of the DCM phase. In this way, all DCM phases were analyzed using GC-MS and the compounds identified with a similarity score greater than 80 were included to obtain the total abundance. Each compound was then lumped into one of the following 7 categories: nitrogenates, nitrogen heterocycles, carboxylic acids, xylene, ethylbenzene, toluene, and other aromatics. All BTEX and other aromatic compounds are colored in shades of green due to their desirability as products in **Figure 7-9**.

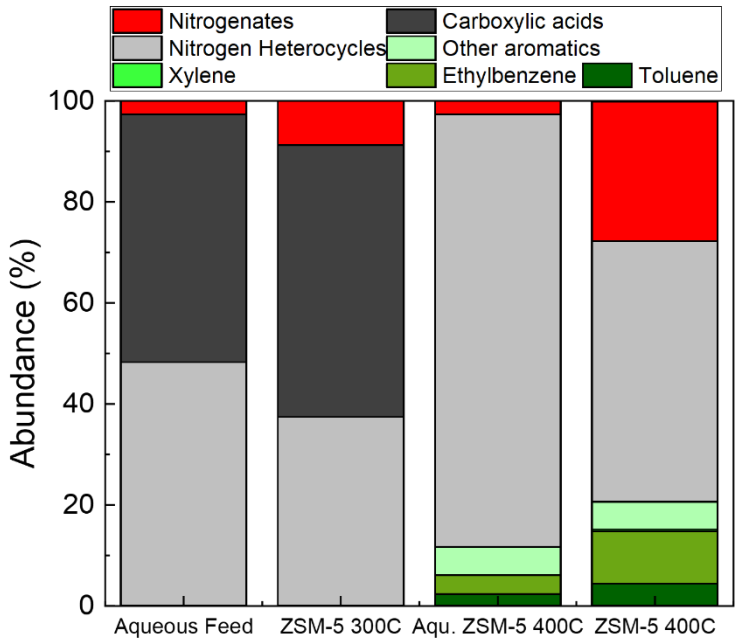

Figure 7-9. Percent abundance of the GC-MS intensity values for a range of aqueous reaction samples.

The abundance values presented in **Figure 7-9** are indicative of GC-MS response intensities calculated as a percentage of the total intensity of identified compounds. For future experimentation, a calibration curve will be obtained, and amounts quantified based on GC-FID confirmation. Despite the quantification considerations of **Figure 7-9**, the results presented here highlight the possibility of ZSM-5 at 400 °C to produce BTEX chemicals from HTL aqueous phase. In particular, no benzene was detected in either sample run at 400 °C, however, ethylbenzene was a major product, accounting for nearly 10% of the total abundance.

The results presented here in regard to the use of ZSM-5 as a catalyst for BTEX production from HTL aqueous phase show significant promise, however, further research should be conducted in this space to further strengthen the claims. Of utmost importance is to determine the effects on catalyst stability, as current research does not indicate that zeolites are especially stable in aqueous

environments, due to the loss of acid site activity.[14, 15] To begin to test the longevity of ZSM-5 in aqueous solutions, the continuous packed bed reactor constructed earlier has been modified to allow for liquid-free heat-up, wherein nitrogen gas is flowed through the system during the heating ramp and maintained at a back pressure of 185 bar. After the desired reaction temperature is achieved, valves will be opened to allow the aqueous phase to enter the reactor, thereby ensuring that the presence of water at room temperature does not affect catalyst lifetime. Previous research by Page et al. has indicated that ZSM-5 is stable in 15 wt% near-supercritical water at 400 °C for 30 minute reaction times for up to four uses in batch[14], highlighting the potential for this method to increase catalyst lifetime. Additionally, it will be important to ensure that the aqueous phase is sufficiently filtered before use in the continuous reactor so as to not cause clogging issues within the reactor, or more importantly, the pump.

As identified in **Figure 7-9**, the use of aqueous distillate residue resulted in two-times the production of BTEX abundance in the organic phase, potentially indicative of a maximum water-loading suitable for the reaction. This finding corroborates to previous literature, wherein 15 wt% was found as a local maximum water content for dodecane.[16] For this reason, future works should aim to explore the effect of water content on BTEX production and the use of distillation as a method to optimize water content in the bottom residues while ensuring recovery of light liquid products. In addition to catalyst reuse properties and optimal water content, it is also important to be able to determine the commercial feasibility and effectiveness of utilizing HTL aqueous to produce BTEX compounds. To this end, future aims should include an analysis of the technoeconomic viability of this aqueous phase reforming methodology.

7.4 CONCLUSIONS

The studies performed here reveal the effect of key byproduct phases on the transition from batch to continuous processing in hydrothermal conversion of waste. Determining methods for continuous biocrude – aqueous separation and aqueous carbon recovery are imperative to push HTL towards an economically viable commercial process. Specifically, bottlenecks were identified in determining optimal solvent selection for phase separation.

To ensure a cost-effective and environmentally friendly process, solvent selection must result in a high concentration of carbon in the organic phase with an inexpensive, green, and recoverable solvent. This work revealed the use of hexane as a suitable solvent with a linear UV-Vis response to changes in aqueous carbon concentration, that will be furthered by a true correlation to carbon content using total organic carbon. Furthermore, the collected calibration curves in both batch and flow operation mode revealed the linear response rate, as confirmed with a Beer's law analysis and calculation of the molar absorption coefficient. Future work in this area should aim to utilize full HTL product and therefore explore further solid remediation techniques.

Carbon recovery from the HTL aqueous phase was explored using two catalysts-hydroxyapatite and ZSM-5. While hydroxyapatite shows promise as a method to increase process carbon recovery as biocrude, method development must continue to ensure that biocrude is exiting the reactor and not trapped in the reactor. Additionally, the work presented herein highlights the feedstock dependence of hydroxyapatite effectiveness, as high-lipid content sewage sludge resulted in decreased biocrude yields compared to food waste. Future research with hydroxyapatite catalyst for aqueous biocrude production should focus on reactor design to optimize catalyst lifetime and ensure that dead volume is minimized within the reactor.

Lastly, the most promising aspect of this work includes the use of ZSM-5 to produce BTEX chemicals from carboxylic acids in HTL aqueous phase. This idea has been proposed for the first time in this work, wherein it was shown that BTEX production, specifically ethylbenzene and xylene as major products, are produced from the reaction of HTL aqueous phase and ZSM-5 at 400 °C in the presence of near-supercritical water. The work presented here has the potential to drastically alter the commercialization of HTL by providing an additional revenue product while simultaneously removing aqueous phase organics, thereby allowing for easier disposal.

The work presented here begins to explore the fate of byproduct phases in the transition from batch to continuous hydrothermal liquefaction processing. By furthering research efforts in these areas, two major commercialization challenges will be addressed, allowing for a more environmentally and economically-favorable process. These findings advance the realm of possibilities for maximizing process energy recovery and present, for the first time, the use of ZSM-5 to produce BTEX chemicals from HTL aqueous phase.

7.5 APPENDIX F

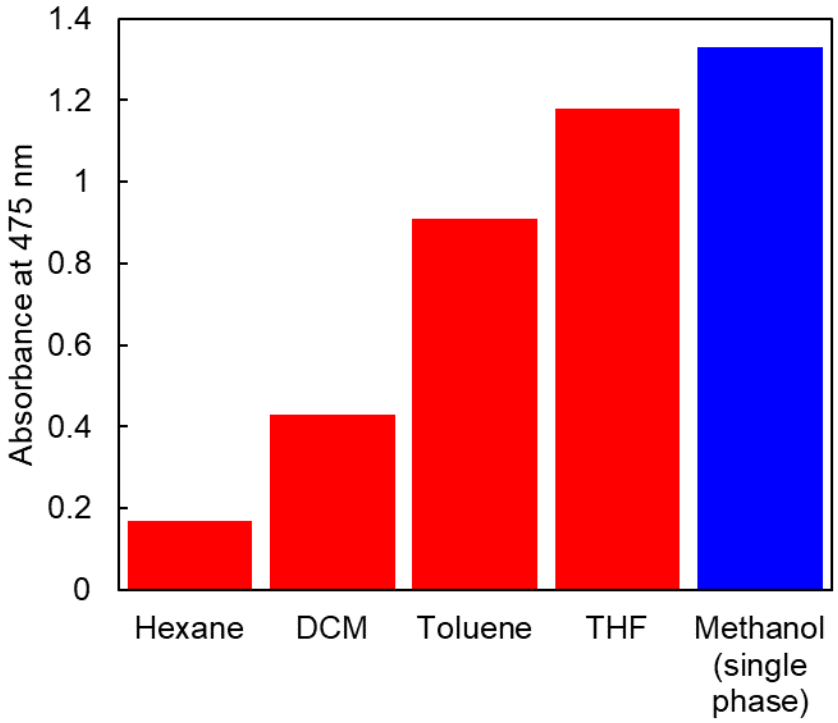

Figure F7-10. Results of the solvent screening experiments to determine the separation efficiency of HTL food waste aqueous phase in a variety of solvents. Hexane showed the lowest solubility in hexane, while methanol resulted in the greatest solubility- however, as a single phase.

Table F7-3. Aqueous phase concentration and the resultant molar absorption coefficient as determined by Beer's law calculation for the calibration standards of HTL aqueous phase in hexane.

Concentration (%)	Coefficient
0	0.020
10	0.034
20	0.025
40	0.025
60	0.023
80	0.023
100	0.022

7.6 REFERENCES

1. Akhtar, J.; Amin, N. A. S., A review on process conditions for optimum bio-oil yield in hydrothermal liquefaction of biomass. *Renewable and Sustainable Energy Reviews* **2011,** *15* (3), 1615-1624.

2. Elliott, D. C.; Biller, P.; Ross, A. B.; Schmidt, A. J.; Jones, S. B., Hydrothermal liquefaction of biomass: Developments from batch to continuous process. *Bioresource Technology* **2015,** *178*, 147-156.

3. Maag, A. R.; Paulsen, A. D.; Amundsen, T. J.; Yelvington, P. E.; Tompsett, G. A.; Timko, M. T., Catalytic Hydrothermal Liquefaction of Food Waste Using CeZrOx. *Energies* **2018,** *11* (3).

4. Goudriaan, F.; Naber, J. A.; Van de Beld, B.; Boerefijn, F. R.; Van der Wal, S.; Bos, G. M.; Zeevalkink, J. A. In *Thermal efficiency of the HTU Process for Biomass Liquefaction*, Netherlands, 2000-09-01; A.V. Bridgwater, Tyrol (Austria): Netherlands, 2000.

5. Biller, P.; Sharma, B. K.; Kunwar, B.; Ross, A. B., Hydroprocessing of bio-crude from continuous hydrothermal liquefaction of microalgae. *Fuel* **2015,** *159*, 197-205.

6. Gollakota, A. R. K.; Kishore, N.; Gu, S., A review on hydrothermal liquefaction of biomass. *Renewable and Sustainable Energy Reviews* **2018,** *81*, 1378-1392.

7. Castello, D.; Pedersen, T. H.; Rosendahl, L. A. Continuous Hydrothermal Liquefaction of Biomass: A Critical Review *Energies* [Online], 2018.

8. Alonso, D. M.; Bond, J. Q.; Dumesic, J. A., Catalytic conversion of biomass to biofuels. *Green Chemistry* **2010,** *12* (9), 1493-1513.

9. Chen, W.-T.; Haque, M. A.; Lu, T.; Aierzhati, A.; Reimonn, G., A perspective on hydrothermal processing of sewage sludge. *Current Opinion in Environmental Science & Health* **2020,** *14*, 63-73.

10. Leng, L.; Zhang, W.; Peng, H.; Li, H.; Jiang, S.; Huang, H., Nitrogen in bio-oil produced from hydrothermal liquefaction of biomass: A review. *Chemical Engineering Journal* **2020,** *401*, 126030.

11. Brewer, C. E.; Schmidt-Rohr, K.; Satrio, J. A.; Brown, R. C., Characterization of biochar from fast pyrolysis and gasification systems. *Environmental Progress & Sustainable Energy* **2009,** *28* (3), 386-396.

12. Barreiro, D. L.; Gómez, B. R.; Hornung, U.; Kruse, A.; Prins, W., Hydrothermal Liquefaction of Microalgae in a Continuous Stirred-Tank Reactor. *Energy & Fuels* **2015,** *29* (10), 6422-6432.

13. Cheng, F.; Tompsett, G. A.; Murphy, C. M.; Maag, A. R.; Carabillo, N.; Bailey, M.; Hemingway, J. J.; Romo, C. I.; Paulsen, A. D.; Yelvington, P. E.; Timko, M. T., Synergistic Effects of Inexpensive Mixed Metal Oxides for Catalytic Hydrothermal Liquefaction of Food Wastes. *ACS Sustainable Chemistry & Engineering* **2020,** *8* (17), 6877-6886.

14. Page, J. R.; LeClerc, H. O.; Smolitsky, P.; Esposito, J. P.; Theberge, D. P.; Zaker, A.; Maag, A. R.; Sabnis, S.; Ledford, E. B.; Coleman, J.; Fan, W.; Wang, S.; Bond, J. Q.; Castro-Dominguez, B.; Timko, M. T., Improving Yields and Catalyst Reuse for Palmitic Acid Aromatization in the Presence of Pressurized Water. *ACS Sustainable Chemistry & Engineering* **2022**.

15. Maag, A. R. Converting Biomass Feedstocks through Heterogeneous Catalysis: How Compressed Liquid Water Influences Catalytic Activity and Stability. Worcester Polytechnic Institute, 2019.

16. Guerra, P.; Zaker, A.; Duan, P.; Maag, A. R.; Tompsett, G. A.; Brown, A. B.; Schmidt-Rohr, K.; Timko, M. T., Analysis of coke formed during zeolite-catalyzed supercritical dodecane cracking: Effect of supercritical water. *Applied Catalysis A: General* **2020,** *590*, 117330.

CONCLUSIONS

The goal of this thesis was to 1) reveal enhanced knowledge of hydrothermal liquefaction molecular pathways and 2) apply the molecular-level understanding of pathways and sub-mechanisms to real-world feeds and conditions to obtain optimal biocrude yields. Motivated by the necessity to reduce fossil fuel usage and organic waste in landfills, this thesis takes a hypothesis-driven approach to identify bottlenecks and make recommendations towards future commercialization. The studies completed in this thesis attempted to answer the question of biocrude formation pathways and chemical differences in the complex system of waste-fed hydrothermal liquefaction.

Chapter 2 worked to develop a microkinetic model based on food waste model compounds that can accurately describe the fate of nitrogen in hydrothermal liquefaction. This chapter focused on the link between computational and experimental chemical analysis to determine nitrogen depolymerization and cross-coupling reactions in HTL. The curated reaction network containing 38 reaction steps and 47 species was compared to experimental HTL results to determine accuracy and found to fall in line with experimental results, confirming the use of model compounds in determination of complex chemistry. The advanced analytical technique of FT-ICR MS was used to further confirm model accuracy and allow for comparison between the model and experimental results, following Objective 1. Furthermore, the model was then used to determine optimal feedstock compositions and reaction temperatures that would serve to decrease nitrogen heterocycle formation in the biocrude, thereby improving the subsequent hydrotreating process in line with Objective 2.

The work completed in Chapter 3 provides insights into the chemical mechanisms that govern mixed-waste co-fed hydrothermal liquefaction. As has been discussed previously, the process of hydrothermal liquefaction is highly feedstock dependent. The use of real-world wastes in the process introduces additional process variability, wherein daily and seasonal changes in waste have the potential to drastically alter biocrude yields and composition. Chapter 3 used mixtures of food and lignocellulosic waste in three varying ratios in order to understand the impact on biocrude yield. Further characterization utilizing GC-MS, FT-ICR MS, and TGA were used in parallel to understand the fundamental chemical interactions at play between lignocellulose and food waste macromolecules. From this study, it was concluded that at equal ratios of food and lignocellulosic waste, the Maillard reaction is the dominant chemical pathway to the formation of nitrogen-oxygen compounds.

Chapter 4 took a step back from real-world, mixed-feed waste to understand the effects of lignin composition on biocrude structure and chemical pathways in HTL. To this end, five wood samples from a mixture of softwoods, agricultural woods, and hardwoods underwent co-solvent enhanced lignocellulose fractionation (CELF) to separate the cellulose and hemicellulose from lignin. The extracted lignin was then subject to hydrothermal liquefaction at 300 °C for 60 minutes before the resultant biocrude and char phases were subject to additional characterization. After carbon analysis on all product phases, it was seen that increased syringol content, representative of hardwood lignin, resulted in increased biocrude yield compared to softwood and agricultural wood lignins. Further characterization using GC-MS identified sufficient monomer content in the biocrudes, with apparent S/G ratios similar to those in the initial feedstock. Results from GC-MS sparked further interest in the biocrude composition and its ability to retain structural conformers from the initial feed. To further prove these trends, FTIR and FT-ICR MS were utilized to gain

insights into the bulk functionality and heavy fraction of the biocrudes. FTIR showcased the retention of syringol and guaiacol bands across feedstock, biocrude, and char phases- and indication of incomplete depolymerization or a lignin structural motif. Analysis of the biocrude heavy fraction via FT-ICR MS revealed shifts to higher-order oxygenates from increased S/G lignin, following a pattern towards the emergence of an abundance peak at lower molecular weight than in soft and agricultural woods.

Chapter 5 utilized the developed analytical framework to analyze the effect of a tunable, calcium phosphate mineral, hydroxyapatite, as a catalyst in food waste HTL. The developed framework included analysis via GC×GC and FT-ICR MS as analytical techniques, coupled with varying reactor operations coined *in situ* and *ex situ*. In this way, it was shown that hydroxyapatite can be used as a hydrothermally stable catalyst in food waste HTL to improve biocrude yields. Furthermore, the addition of HAP did not result in chemical changes to the biocrude, indicative of alterations in the chemical kinetics towards biocrude and aqueous solubility. This was further confirmed with FT-ICR MS analysis of both biocrude and aqueous phases. Additionally, the concept of an *ex situ* catalytic reactor was borrowed from pyrolysis literature and resulted in enhanced HAP lifetime due to negligible char formation on the catalyst. Moving forward, calcium phosphate-based catalysts can be utilized to improve biocrude yields from high-carbohydrate content feedstocks with minimal changes to biocrude quality or structure.

The work completed in Chapter 6 aims to reveal the effect of feedstock engineering and preconditioning as a key metric to understand the hydrothermal conversion of waste to biocrude. In this work, three primary parameters were explored including feedstock composition, pH dependence, and mechanochemical pretreatment. Lipid content was shown to play a significant role in biocrude production, resulting in an increase of 110% by increasing lipid content from 5%

to 40%. It is believed that the increase in biocrude yield is due to efficient extraction of lipid to biocrude, correlating to the corresponding decrease in char yield due to decreased carbohydrate repolymerization. Furthermore, this study determined the biocrude yields from lignocellulose as well as yields from lignocellulose that underwent ball-milling as a form of mechanochemical pretreatment. Ball-milling was found to increase biocrude yield by 63%, a stark improvement to the moderate performance of untreated lignocellulose. The remainder of this work aimed to reveal the mechanism in which biocrude yields were improved through a study of lignocellulose crystallinity and particle size distribution followed by an energy analysis to determine pretreatment efficiency.

Lastly, Chapter 7 focused on discovering new solutions towards challenges in hydrothermal liquefaction commercialization. Major challenges towards waste processing scale-up include transitioning from batch to continuous as well as the fate of carbon in byproducts. These challenges were addressed through the development of a liquid-liquid membrane separation process for isolation of carbon-rich organics from the resultant aqueous phase. Hexane, toluene, THF, and methanol were evaluated as solvents for use in the separation process, wherein methanol was quickly excluded due to its miscibility with water. Through the use of UV-Vis spectroscopy, linear calibrations were discovered relating transmittance and absorption response to carbon concentration. Moving forward, solids recovery before liquid separation will dominate the research space to ensure membrane longevity and sustainable continuous operation. Secondly, the use of hydroxyapatite and ZSM-5 catalysts were tested to determine effectiveness in capturing aqueous phase carbon as a usable product for additional energy recovery and water purification. Hydroxyapatite was shown to decrease aqueous phase carbon by 5 – 15%, recoverable as a biocrude oil with similar characteristics to that produced from initial hydrothermal liquefaction.

ZSM-5 resulted in the production of benzene, toluene, ethylbenzene, and xylene products from the reaction of HTL aqueous phase as well as from aqueous phase bottom distillates in appreciable quantities. Further work in this sphere should aim to quantify reaction kinetics and determine catalyst lifetime and reusability.

Overall, the goal of this thesis was to 1) reveal enhanced knowledge of hydrothermal liquefaction molecular pathways and 2) apply the molecular-level understanding of pathways and sub-mechanisms to real-world feeds and conditions to obtain optimal biocrude yields. Through detailed analysis into intermediate reaction chemistry, mixed-feed hydrothermal liquefaction, and catalyst use, the effect on molecular pathways was determined for a range of HTL process conditions. The chapters included in this thesis highlight how it has successfully advanced the scientific understanding of biocrude formation in hydrothermal liquefaction.

FUTURE DIRECTIONS AND PERSPECTIVES

The insight provided in this thesis in regard to hydrothermal liquefaction biocrude formation pathways enhanced the fundamental understanding of biocrude chemical composition from a variety of waste-based feedstocks. However, substantial work remains in advancing the fundamental knowledge related to chemical understanding of complex waste conversion mechanisms and pushing hydrothermal liquefaction towards commercialization. The transition to renewable fuel, specifically from HTL, continues to be plagued by three primary bottlenecks: fundamental chemical understanding, scale-up and continuous processing, and overall process economics.

From a fundamental perspective, biocrude maintains a high level of complexity that current analytical techniques cannot accurately deconvolute. Specifically, analytical bottlenecks towards understanding these complex chemical mechanisms lie in the use of individual techniques for chemical determination. For example, high resolution mass spectrometry, such as FT-ICR MS, cannot accurately determine chemical structure, whereas gas chromatography linked to mass spectrometry is limited by sample volatility. While the ability to couple a range of analyses exists, this method is limited by the availability of equipment and funds. To reduce this reliance on a suite of expensive analytical instruments, the future lies in the ability to determine structural information from FT-ICR MS and other high-resolution analytical techniques. This ability would have the potential to drastically increase chemical knowledge of these complex biocrude products, however, this ability does not currently exist, leading to the need to advance analytical chemistry. Current structural assignments in NMR, spectroscopy, and mass spectrometry based analyses are completed via the use of databases. Most of these assignments were determined through experiments with model compounds designed to isolate the desired structural information,

however, the field of analytical chemistry and its applications to complex chemical systems can be improved by coupling the analysis to computational chemistry and machine learning algorithms for superior structural prediction. In this way, with chemical knowledge from computational chemistry and the ability to correlate and predict variables with machine learning, future analytical work will be able to utilize knowledge of the starting material as well as the library of known chemical reactions and species to accurately correlate a single spectrum of a complex mixture to their chemical structures with ease.

The studies completed in this thesis, with the exception of those presented in Chapter 7, represent findings from batch hydrothermal liquefaction reactions. More specifically, reactions were carried out in a 300 mL stainless steel Parr reactor with average heating rates of 6 °C/min, representing total heat-up times in excess of 40 minutes. Recommendations for future experimentation involves transitioning to micro-batch and continuous reactor systems to allow for measurement of the intrinsic kinetics under a multitude of composition, temperature, solids loading, and catalytic environments. These intrinsic measurements can then be combined with reactor models that describe thermal and concentration gradients and layer them on top of kinetic measurements to predict performance and product distributions. This is particularly relevant in the transition from batch to flow where heat transfer rates can be increased by an order of magnitude and precise control over residence times and quenching allow for selectively optimizing product distributions. The transition to continuous reactor systems represents a paradigm shift towards fundamental understanding of commercial-scale processes as well as HTL reactor operation at the commercial scale.

From the applied perspective, biomass conversion through hydrothermal liquefaction is not limited solely by the chemical understanding of biocrude formation pathways due to the presence

of three high-yielding byproduct phases. For hydrothermal liquefaction to be economically viable, carbon loss to the aqueous and char phases must be limited and byproduct disposal managed. This management can include ensuring wastewater is within the limits of a wastewater treatment facility, or direct disposal to waterways. The current organic and metal content of HTL aqueous phase represents approximately 10%, on average, of the carbon in the system with total organic carbon levels between 8,000 – 20,000 ppm, drastically above the 50 ppm limit imposed for drinking water and the 300 ppm average for industrial wastewater entering a wastewater treatment facility. To improve the process efficiency of HTL, methods to reuse water and undergo low-cost organic separations are required. Methods for metal or organic precipitation out of solution may be desirable because precipitation methods will not require heating water, which is an energy intense process. In addition to the aqueous phase, the remaining solid char must also find an inexpensive, or commercially viable disposal option. With typical char yields accounting for 10 – 40% on a mass basis and applied at the scale of food waste in the U.S., the magnitude of char requires an application capable of utilizing up to 227,000 tons of char per day. While some specialty applications may exist, valorizing this stream by matching the scale is possible in agricultural, activated carbon, and sorbent applications. The fate of byproduct phases, however, is imperative towards producing an economical biocrude product.

In addition to byproducts, biocrude yield and ease of upgrading (i.e. heteroatom removal) play significant roles in process economics and the overall feasibility of this technology. The primary heteroatomic contaminants in biocrude consist of oxygen, nitrogen, and sulfur, each with their own unique challenges. Oxygen is typically considered the ‘easiest’ to remove, typically in the form of water, oxygen gas, or carbon dioxide with the addition of hydrogen. Nitrogen and sulfur, on the other hand pose unique challenges in their stability as well as the potential to poison

traditional hydrotreating catalysts. Research done by PNNL has found that the cost of hydrogen as well as the required catalyst adds approximately $1.10 per gallon of gasoline equivalent (GGE) to the bottom line of biofuel production. The greater the heteroatomic content of the biocrude, however, the more hydrogen that is required during upgrading which can increase the total economics of the process in a negative way, hence the need to understand the fate of heteroatoms in the biocrude.

In addition to heteroatoms, however, the overall biocrude yield plays a key role in the minimum fuel selling price. The variability of real-world feeds makes it difficult to predict biocrude outcomes on a continual year-round basis, thereby affecting process economics. As shown in Chapter 5, by doubling the biocrude yield, the MFSP decreases by nearly 60%. While continual increases in biocrude yield begin to have diminishing returns past ~40%, the seasonal variation in waste composition has the potential to drastically alter biocrude yields. Recently, work has been published which creates machine learned models to predict biocrude yields from feedstock composition information. Further work in this area is required to determine the robustness of HTL and its ability to withstand seasonal variations without sacrificing quality or process economics.

Beyond the economics of the process itself, however, is the challenge in obtaining investors and garnering public support. In most cases, it has proven extremely difficult to obtain buy-in from investors and to change the public's habits, especially regarding issues related to climate change and sustainability. While some towns and cities across the U.S. have implemented separate food waste disposal, such as areas of Boston, public buy-in is going to be regionally dependent. Additionally, for everyone to individually separate food waste, it can be expected that plastic, paper, and other contamination will find its way into the waste stream similar to that

currently found in glass and paper recycling streams. This contamination also has the potential to effect product yields and thereby economics. Commercialization of waste-fed hydrothermal liquefaction shows immense promise in creating a world without waste, however, the bottlenecks identified here must be understood and overcome.

To ensure the future success of waste to energy through hydrothermal liquefaction, researchers should also acknowledge that there is no universal solution that can be applied across the United States, let alone the world. Process optimization will be different based on geographical location due to population density, resource availability, and waste composition. For this reason, research efforts should be placed in developing model frameworks for individual waste to energy facilities across geographical regions. Model inputs should include feedstock properties, local wastewater disposal regulations, as well as local standards for equipment and cost of living. Desired model outputs would result in sufficient understanding of biocrude yields, composition, and approximate economic and environmental impacts. In order to achieve this level of understanding, however, there remains a great deal of work in obtaining sufficient, high-quality pilot-scale data for use in model development.